



# **Balkan** Journal of Electrical & Computer Engineering

An International Peer Reviewed, Referred, Indexed and Open Access Journal

[www.bajece.com](http://www.bajece.com)

Vol : 7  
No : 2  
Year : 2019  
ISSN : 2147 - 284X



It is abstracted and indexed in, Index Google Scholarship, the PSCR, Cross ref, DOAJ, Research Bible, Indian Open Access Journals (OAJ), Institutional Repositories (IR), J-Gate (Informatics India), Ulrich's, International Society of Universal Research in Sciences, DRJI, EyeSource, Cosmos Impact Factor, Cite Factor, SIS Scientific Indexing Service, IJIF, iijFactor. ULAKBİM-TR Dizin.

**General Publication Director & Editor-in-Chief**  
Musa Yılmaz, Batman University, Turkey.

**Vice Editor**  
Hamidreza Nazarpouya, University of California Riverside, USA

#### Editorial Board

Abdulkerim Öztekin (Turkey)  
Abhishek Shukla (India)  
Abidin Çalışkan (Turkey)  
Abraham Lomi (Indonesia)  
Aleksandar Georgiev (Bulgaria)  
Arunas Lipnickas (Lithuania)  
Audrius Senulis (Lithuania)  
Belle R. Upadhyaya (USA)  
Brijender Kahanwal (India)  
Chandar Kumar Chanda (India)  
Daniela Dzhonova-Atanasova (Bulgaria)  
Deris Stiawan (Indonesia)  
Emine Ayaz (Turkey)  
Enver Hatimi (Kosovo)  
Faruk Erken (Turkey)  
Gursel Alici (Australia)  
Hüseyin Acar (Turkey)  
Jan Izykowski (Poland)  
Javier Bilbao Landatxe (Spain)  
Jelena Dikun (Lithuania)  
Karol Kyslan (Slovakia)  
Kunihiko Nabeshima (Japan)  
Lambros Ekonomou (Greece)  
Lazhar Rahmani (Algerie)  
Marcel Istrate (Romania)  
Marija Eidukeviciute (Lithuania)  
Mehmet Emin Asker (Turkey)  
Milena Lazarova (Bulgaria)  
Muhammad Hadi (Australia)  
Muhamed Turkanović (Slovenia)  
Mourad Houabes (Algerie)  
Murari Mohan Saha (Sweden)  
Nick Papanikolaou (Greece)  
Ömer Faruk Ertuğrul (Turkey)  
Ramazan Tekin (Turkey)  
Reşat Çelikel (Turkey)  
Rumen Popov (Bulgaria)  
Tarek Bouktir (Algeria)  
Sead Berberovic (Croatia)  
Serhat Berat Efe (Turkey)  
Seta Bogosyan (USA)  
Savvas G. Vassiliadis (Greece)  
Suwarno (Indonesia)  
Tulay Adali (USA)  
Yogeshwarsing Calleecharan (Mauritius)  
YangQuan Chen (USA)  
Yasin Sönmez (Turkey)

#### Aim & Scope

The journal publishes original papers in the extensive field of Electrical-Electronics and Computer engineering. It accepts contributions which are fundamental for the development of electrical engineering, computer engineering and its applications, including overlaps to physics. Manuscripts on both theoretical and experimental work are welcome. Review articles and letters to the editors are also included.

Application areas include (but are not limited to): Electrical & Electronics Engineering, Computer Engineering, Software Engineering, Biomedical Engineering, Electrical Power Engineering, Control Engineering, Signal and Image Processing, Communications & Networking, Sensors, Actuators, Remote Sensing, Consumer Electronics, Fiber-Optics, Radar and Sonar Systems, Artificial Intelligence and its applications, Expert Systems, Medical Imaging, Biomedical Analysis and its applications, Computer Vision, Pattern Recognition, Robotics, Industrial Automation.



ISSN: 2147- 284X  
Vol: 7  
No : 2  
Year: April 2019

#### CONTENTS

- S. Karagöl, D. Yildiz;** Linear Block Coding and Discrete Wavelet Transform Based Audio Signal Transmission over AWGN .....**104-114**
- S.M. Çürük;** Impulsive Noise Models Used in Power Line Communications, .....**115-122**
- F. Asadi, K. Eguchi;** On the extraction of input and output impedance of PWM DC-DC converters, .....**123-130**
- M. Taştan;** Adaptive Notch Filter Bank Based Power Quality Analysis of an Ultra-High Frequency Induction Heating System, .....**131-136**
- E. Aydemir, F. Toslak;** Unlock A Device with Pressure and Rhythm Based Password, .....**137-142**
- R. Çelikel;** Speed Control of BLDC Using NARMA-L2 Controller in Single Link Manipulator, .....**143-148**
- M. İnci;** Performance Analysis of T-type Inverter Based on Improved Hysteresis Current Controller, .....**149-155**
- Y. Acar;** Subblock Aided OFDM with Index Modulation, .....**156-161**
- B. Ozmen, O.J. Olaleye;** Multispectral Palmprint Recognition Based on Multidirectional Transform, .....**162-170**
- J. Bala, O. Olaniyi, T. Folorunso, O.Arulogun;** Poultry Feed Dispensing System Control: A Case between Fuzzy Logic Controller and PID Controller, .....**171-177**
- U. Korkmaz;** Fate of Entanglement for Initial Separable States in Quantum Neural Network, .....**178-181**
- E. Taşçı;** A Meta-Ensemble Classifier Approach: Random Rotation Forest, .....**182-187**
- C. Şahin, M. Karaçor, A.E. Amaç;** Minimizing Mutually Coupled Switched Reluctance Machine's Stator Volume by Stator Yoke Optimization, .....**188-194**
- T. Ozcan, A. Basturk;** Lip Reading Using Convolutional Neural Networks with and without Pre-Trained Models, .....**195-201**
- O. Aydın;** Direction of Arrival Estimation in Multiple Antenna Arrays by Using Power Delay Profile for Random Access Performance in 5G Networks, .....**202-207**
- N. Kapucu;** An Approximate Error Expression for RQAM Scheme under  $\alpha$ - $\eta$ - $\mu$  Fading Conditions, .....**208-212**

#### BALKAN

#### JOURNAL OF

#### ELECTRICAL & COMPUTER ENGINEERING

(An International Peer Reviewed, Indexed and Open Access Journal)

#### Contact

Batman University  
Department of Electrical-Electronics Engineering  
Bati Raman Campus Batman-Turkey

**Web:** <http://dergipark.gov.tr/bajece>

<https://www.bajece.com>

**e-mail:** [bajece@hotmail.com](mailto:bajece@hotmail.com)

# Linear Block Coding and Discrete Wavelet Transform Based Audio Signal Transmission over AWGN and Rician Fading Channel

S. KARAGOL and D. YILDIZ

**Abstract**—Mobile communication has become an important part of our daily lives for voice communication, data sharing and access over the Internet. Mobile communication is an open network, so maintaining the privacy and reliability of data has always been anxiety. The reliability of the data against channel noise can be achieved by various error correction codes. The purpose of the channel coding process is to reduce the effect of some disruptive elements that the data is influenced in the transmission phase as much as possible. This procedure ensures that the data is delivered to the receiver with minimum error. In this study, a communication system was established in MATLAB environment for the transmission of five second audio signal. In this communication system, BER and MSE performances of four phase shift keying methods are obtained first. In the second phase of the study, the AWGN and Rician fading channels were individually coded with four different LBC types. Performance evaluation of these coding types was done with BER and MSE criteria. In the last part of the study, it was investigated which wavelet family is suitable for which level, in order to ensure audio transmission over AWGN and Rician fading channels with the least possible error. Four wavelet transform families at different levels were applied to the audio signal for LBC (7, 4), LBC (15, 8), LBC (17, 8) and LBC (23, 12) encoded channels, and the Mean Squared Error (MSE) performances were compared.

**Index Terms**—Audio Signals, Channel Coding, Linear Block Coding, Wavelet Transform.

## I. INTRODUCTION

TRADITIONAL ANALOG communication techniques do not perform well in mobile environments because appropriate techniques for reducing the effects of multi-path propagation fading have not been developed [1].

**S. KARAGOL**, is with Department of Electrical and Electronics Engineering, Ondokuz Mayıs University, Samsun, Turkey, (e-mail: [serap.karagol@omu.edu.tr](mailto:serap.karagol@omu.edu.tr))

<https://orcid.org/0000-0002-5750-1143>

**D. YILDIZ**, is with Department of Electrical and Electronics Engineering, Ondokuz Mayıs University, Samsun, Turkey, (e-mail: [dogan.yildiz@omu.edu.tr](mailto:dogan.yildiz@omu.edu.tr))

<https://orcid.org/0000-0001-9670-4173>

Manuscript received September 3, 2018; accepted March 26, 2019.

DOI: [10.17694/bajece.456774](https://doi.org/10.17694/bajece.456774)

Channel coding, also known as Forward Error Control (FEC) coding, can be defined as the detection and correction of bit errors in digital communication systems. Channel coding is performed on both transmitter and receiver. On the transmitter side, the channel coding is called the encoder. Here, extra bits (parity bits) are added to the raw data before modulation. On the receiver side, the channel coding is called the decoder. Channel coding allows the receiver to detect and correct errors caused by effects such as noise, parasite and fading that occur during transmission [2]. The key benefits of channel coding to communication systems are as follows: maximizing data transmission efficiency to provide high bit rate, low encoder / decoder complexity by limiting the size and cost of transceivers, minimizing the amount of energy required for transmission at the desired signal to noise ratio and thus achieving high Bit Error Rate (BER) performance. Lower-rate channel codes can usually correct more errors [3].

In recent years, many studies have been carried out using different channel coding methods in order to transmit data with the least possible loss. In [3], Dhaliwal et al. analyzed convolutional code's BER performance over Additive White Gaussian Noise (AWGN) channel using fixed Viterbi decoder, different code rates, different restriction lengths and Quadrature Phase Shift Keying (QPSK) modulation. In [4], Baviskar et al. proposed an adaptive Low Density Parity Control Code (LDPC) supported audio processing algorithm to transmit the speech signal over the wireless AWGN channel. Binary Phase Shift Keying (BPSK) technique have helped to achieve better BER performance. In [5], the robustness of the turbo decoding algorithm in a generalized Gaussian noise has been researched. In [6], Haque et al. studied the effect of various combined FEC codes on the performance of a wireless Orthogonal Frequency Division Multiplexing (OFDM) system. In this study, the authors used Reed-Solomon (RS) (255, 239, 8) encoder, Cyclic (15, 11) encoder, Bose-Chaudhuri-Hocquenghem (BCH) (127, 64) encoder and  $\frac{2}{3}$  and  $\frac{3}{4}$  encoders of convolutional coding for channel coding. QPSK, 8-PSK, 32-Quadrature Amplitude Modulation (32-QAM) and 64-QAM methods are used as the digital modulation method. In [7], Sidhu et al. evaluated the performance of multi-level linear block codes on Rayleigh fading channel. The error correction feature of linear block codes is controlled with different digital modulations. In [8], BER performance of  $2 \times 2$  Full-Rate Linear-Receiver Space

Time Block Code (FRLR-STBC) is evaluated. Using Appell and Gauss hypergeometric functions, new precise and asymptotic closed form BER formulas of BPSK-modulated FRLR-STBC are derived over Rayleigh fading channels, along with the corresponding coding gain and diversity order.

In the literature, Wavelet Transform (WT) is also used in some applications related to audio signal processing and channel coding. In [9], Romano et al. proposed a technique for analyzing and compressing speech signals using biorthogonal wavelet filters. This technique compared human voice with a typical Voice Over Internet Protocol (VoIP) encoding. This study has been emphasized how the wavelet filters can be suitable, especially in terms of the compression ratio, without causing significant degradation of the signal quality for the audiences. In [10], Kudumakis et al. investigated the performance of some different wavelet families for low bit rate coding of audio signals. For evaluating the coding gains of these wavelets, both octave and uniform sub-band coding schemes, fixed and dynamic bit-shares with entropy noiseless Huffman coding are used. In [11], Luo presented a new ultra-low latency wavelet voice encoder for real-time wireless transmission using non-overlapping short block processing and embedded coding. To investigate the correlation of the audio signal, a limited and minimized 2D fast lift WT is developed. In [12], Sinha et al. used a wavelet-based method that uses the median function threshold. By selecting a suitable main wavelet, a nearly unchanged signal quality and a flexible compression ratio are obtained and the performance of the proposed method is evaluated using various analysis methods. In [13], Sarnin et al. presented a performance evaluation of BPSK and QPSK techniques using error correcting code. BCH, Cyclic and Hamming codings are used as a coding method. Random data is passed through the AWGN channel and the BER is calculated. In [14], Bhatti recorded a speech signal of .wav format, represented by 8-kHz sampling frequency, 5-sec and 8 bits per sample in MATLAB environment. The audio signal is encoded in the AWGN channel using the Cyclic (17, 8) Coding Method. BPSK was used for the modulation of the audio signal. In [15], the authors used RS coding and Code Division Multiple Access (CDMA) methods, unlike the study [14].

In this study, a communication system was established in MATLAB environment for the transmission of 5 second audio signal. In this communication system, BPSK modulation is used in the remainder of the study, because the modulation analysis with good performance is performed first and the performance of BPSK modulation is obtained better than the other modulations. In the second phase of the study, the AWGN and Rician fading channels were individually coded with LBC (7, 4), LBC (15, 7), LBC (17, 8) and LBC (23, 12) respectively. Performance evaluation of these coding types was done with BER and MSE criteria. In the last part of the study, it was investigated which wavelet family is suitable for which level, in order to ensure audio transmission over AWGN and Rician fading channels with the least possible error. Four wavelet transform families at different levels were applied to the audio signal for four different types of LBC encoded channels, and the Mean Squared Error (MSE) performances were compared.

## II. AUDIO TRANSMISSION STEPS

In this study, the five-second length audio signal obtained from the external environment is passed through the steps of sampling, quantization and A/D conversion and then given to AWGN noisy (or AWGN noisy with Rician fading) LBC coded channel. In this section, the basic concepts used in the system for the transmission of the audio signal will be mentioned.

### A. Channel Coding

In the transmitter part of the digital communication system, the data like sound, image etc. produced by the source is converted into binary sequences with the shortest possible length, with no loss of information (or acceptable loss of information) with the aid of the source encoder. The binary  $k$ -bit sequences at the output of the source encoder are converted to  $n$ -bit sequences by adding  $n-k$  control bits with the aid of the channel encoder ( $n > k$ ). The intent of channel coding is to protect the data sequences from the disturbing effect of the channel. The coded arrays are then divided into blocks of a certain length. These sequences are then mapped to one of the elements of the signal set of the modulation to be used and modulated to give the channel. The type of modulation used varies depending on the channel's feature. On the receiver side, the demodulator allows distorted waves to be processed in the decoder due to disturbing effects in the channel. The channel and source decoders operate inversely to the channel and source encoders, respectively, to find the transmitted data and transfer it to the user. Because of the redundancy control bit insertion in the channel coding, the increase in sequence length reduces the data rate. One way to avoid this fall is to increase the modulation speed. The increase in modulation speed means to shorten the duration of the channel signal, which means that the bandwidth of the channel signal increases. Therefore, this can be done if the bandwidth of the channel is appropriate. The expansion of the signal set (for example, using 8-PSK modulation instead of 4-PSK) is another way of avoiding the drop in the transmission rate in band-limited channels. However, in this method, since the signs are closer to each other, the error performance of the system is reduced. Therefore, coding and modulation together in the design of efficient systems in terms of both error performance and bandwidth are now considered as a whole [16].

In this study, LBC is used for channel coding process and BPSK is used as modulation method.

### B. Linear Block Coding

LBC is an encoding method characterized by an  $(n, k)$  notation, where  $k$  is the length of the message vector and  $n$  is the length of the codeword, and LBC is a subclass of similarity control codes. Here, the encoder converts the message block of length  $k$  into a longer code word block. The code is a set of vectors created by vectors called code words.  $k$ -bit messages constitute  $2^k$  different message arrays, referred to as  $k$ -arrays. Blocks of  $n$  bits form  $2^n$  different arrays, expressed as  $n$ -arrays. As a result of the encoding process, each of the  $2^k$   $k$ -arrays is assigned to each of  $2^n$   $n$ -arrays. With a block code, each of the  $2^k$  message arrays is mapped to  $2^k$  different code words in the  $n$ -array. This mapping is an one to one correspondence.

$V_i$  and  $V_j$  are two separate code words from a set of  $(n, k)$  binary block codes. In order for any of these two words to be

linear, the necessary and sufficient condition is that  $V_i \oplus V_j$  is also a code vector at the same time. In general, a G generator matrix is defined as a  $k \times n$  matrix:

$$G = \begin{bmatrix} V_1 \\ V_2 \\ \vdots \\ V_k \end{bmatrix} = \begin{bmatrix} V_{11} & V_{12} & \dots & V_{1n} \\ V_{21} & V_{22} & \dots & V_{2n} \\ \vdots & \vdots & \dots & \vdots \\ V_{k1} & V_{k2} & \dots & V_{kn} \end{bmatrix} \quad (1)$$

m message vector is a  $1 \times k$  row vector consisting of k message bits:

$$m = [m_1 m_2 \dots m_k] \quad (2)$$

The U code vector is expressed as the product of the m and G sequences as follows:

$$U = mG \quad (3)$$

Hence, it can be said that the code vector of a message is a linear combination of the components of the G generator matrix. With a G generator matrix, a vector of length k is translated into a vector of length n. Here, the (n-k) bits are the parity bits. A systematic linear block code has a generator matrix in the form:

$$G = [P: I_k] \quad (4)$$

Here, since the unit matrix is not required to be stored, the systematic generator matrix will reduce the coding complexity. Eq. (5) could be obtained by combining Eq. (3) and (4).

$$U = [m_1 m_2 \dots m_k] \times \begin{bmatrix} P_{11} & P_{12} & \dots & P_{1,(n-k)} & 1 & 0 & \dots & 0 \\ P_{21} & P_{22} & \dots & P_{2,(n-k)} & 0 & 1 & \dots & 0 \\ \vdots & \vdots & \dots & \vdots & \vdots & \vdots & \dots & \vdots \\ P_{k1} & P_{k2} & \dots & P_{k,(n-k)} & 0 & 0 & \dots & 1 \end{bmatrix} \quad (5)$$

The systematic code vector can be expressed as follows.

$$U = \underbrace{[P_1 P_2 \dots P_{n-k}]}_{\text{parity bits}} \underbrace{[m_1 m_2 \dots m_k]}_{\text{message bits}} \quad (6)$$

The parity check matrix (H) provides us with a simple way to know if an error has occurred. It is necessary for decoding in receiver.  $GH^T$  has to be equal to zero. Since  $U = mG$ ,  $UH^T = 0$  condition will be provided for all valid codes. U can be said to be a code word generated by the G generator matrix if  $UH^T = 0$  is satisfied. The vector  $r = [r_1 r_2 \dots r_n]$  is the signal at the receiver and this vector is the consequent of the transmission of the  $U = [u_1 u_2 \dots u_n]$  vector over the channel. Eq. (7) gives the vector r.

$$r = U + e \quad (7)$$

Here the vector  $e = [e_1 e_2 \dots e_n]$  is the error vector. The syndrome of vector r is S and it is given with Eq. (8) [17].

$$S = rH^T \quad (8)$$

### C. Types of Channels

It is much more convenient to construct mathematical models that reflect the characteristics of transmission media during the

design of communication systems for the transmission of information over physical channels. Thus, this mathematical model of the channel can be used to design channel coders and modulators in transmitters and channel decoders and demodulators in receivers.

#### 1) AWGN Channel

One of the simplest mathematical models of a communication channel is the additive noise channel shown in Fig. 1. In this model, the transmitted signal  $s(t)$  is distorted by the additive noise process  $n(t)$ .

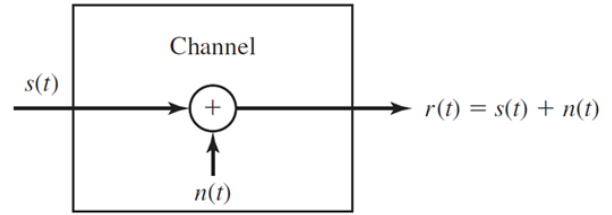


Fig. 1. The additive noise channel

Physically, additive noise process is produced by electronic components and amplifiers in the receiver end of the communication systems as well as in the case of transmission of radio signals. If the noise is mainly produced by the electronic components and the amplifier on the receiver side of the communication system, this noise can be characterized as thermal noise. This type of noise is statistically characterized as a Gaussian noise process. The mathematical model to be obtained for this channel is therefore called Additive White Gaussian Noise (AWGN) Channel. Since this channel model is a valid model for most of the physical communication channels and can be mathematically examined, it is a channel model that is often used in the analysis and design of communication systems. Channel attenuation components can easily be integrated into this model.

If a signal is attenuated during transmission along the channel, the received signal will be in the form of

$$r(t) = \alpha s(t) + n(t) \quad (9)$$

Here,  $\alpha$  represents the attenuation factor [18]. It can be said that a random X variable has a normal distribution if it has a probability density function (pdf) with  $\mu$  average and  $\sigma^2$  variance values as in the following Eq. (10) [19].

$$P(x) = \frac{1}{\sqrt{2\pi\sigma}} \exp\left[-\frac{(x - \mu)^2}{2\sigma^2}\right], \quad -\infty < x < \infty \quad (10)$$

#### 2) Rician Channel

The amplitude envelope of the small-scale faded channel is Rician distributed if there is a predominantly non-attenuated signal component (such as LOS) [20]. At the output of the envelope detector, the dominant signal causes the formation of a direct current component. The Rayleigh distribution is obtained when the dominant signal component in the Rician distribution is damped [21]. This channel can be seen in Fig. 2.

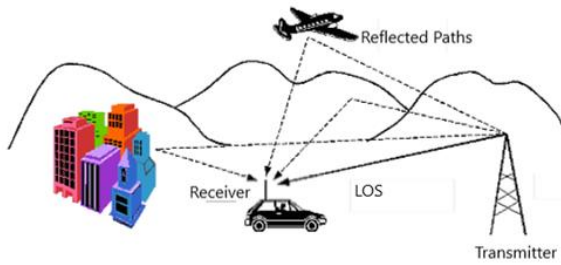


Fig. 2. Rician fading channel [22]

The Rician distribution is as follows.

$$P_{Rician}(r) = \frac{r}{\sigma^2} e^{-\frac{(r^2+A^2)}{2\sigma^2}} I_0\left(\frac{rA}{\sigma^2}\right), \quad A \geq 0 \text{ and } r \geq 0 \quad (11)$$

Here  $A$  – is the maximum value (envelope) of a dominant signal

$I_0(\cdot)$  – is the degree 0, first modified Bessel function

$\sigma^2$  – is the power of the perpendicular components of the channel's complex damping variable.

In Fig. 3, the Rician distribution is given for different  $A$  values [22].

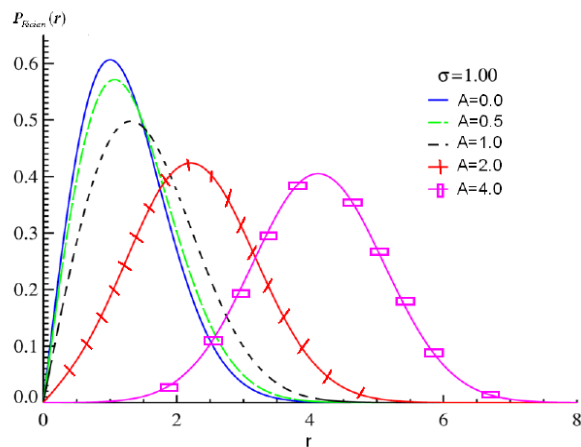


Fig. 3. Probability density function of Rician distribution [22]

The Rician distribution is usually expressed using the  $K$  parameter. The  $K$  parameter is calculated in dB:

$$K(dB) = 10 \log \frac{A^2}{2\sigma^2} [dB] \quad (12)$$

The average power of the Rician distribution is as follows:

$$\Omega = E[r^2] = A^2 + 2\sigma^2 = 2\sigma^2(1 + K) \quad (13)$$

Using these parameters, the probability density function can be rewritten as in Eq. (14).

$$P_{Rician}(r) = \frac{2r(K+1)}{\Omega} e^{-K-\frac{r^2(K+1)}{\Omega}} I_0\left(2r\sqrt{\frac{K(K+1)}{\Omega}}\right) \quad (14)$$

If  $K = 0$  is written in Eq. (14), the Rician distribution becomes the Rayleigh distribution. The increase in the value of the  $K$  parameter means that the effect of the fading in the channel is

reduced. In the case of  $K \rightarrow \infty$ , there is no fading in the channel and in this case, this channel is converged to the AWGN channel [22].

#### D. Wavelet Transform

Wavelets are small waves with an average value of 0, with a limited time interval. Wavelets are mathematical functions that localize a set of data or a function in both the frequency domain and the time domain. It can be said that the beginning of wavelet functions is Haar's thesis in 1909. In the 1930's, scale-varying functions were developed in physics, mathematics, seismology and electronics engineering. The broad concept of wavelet was introduced by Grossman and Morlet (1984) in the mid 80s [23].

WT gives successful results in data analysis where the Fourier transform is used ahead of time and some aspects are inadequate. For example, signals with alternating small or irregular details are generally better analyzed using wavelets compared to the conventional Fourier transform. WT is used extensively in one-dimensional and two-dimensional signal processing applications such as voice and audio signal processing, communication, geophysics, economics and medicine [24].

There are two types of wavelet analysis: Continuous Wavelet Transform (CWT) and Discrete Wavelet Transform (DWT). In CWT, the signal being processed is matched and transformed with the wavelet fundamental function in continuous frequency and time increases. The original signal is expressed as a weighted integral of the continuous basis wavelet function. If  $f(t)$  is a square integrable function of time,  $t$ , then the CWT of  $f(t)$  is defined as

$$W_{a,b} = \int_{-\infty}^{\infty} f(t) \frac{1}{\sqrt{|a|}} \psi^*\left(\frac{t-b}{a}\right) dt \quad (15)$$

where  $a, b \in \mathbb{R}, a \neq 0, \mathbb{R}$  - is the set of real numbers;

'\*' – denotes the complex conjugation; and the wavelet function is defined as

$$\psi_{a,b}(t) = \frac{1}{\sqrt{|a|}} \psi\left(\frac{t-b}{a}\right) \quad (16)$$

Here:  $a$  – is called the scaling parameter which captures the local frequency content;

$b$  – is called the translation parameter which localizes the wavelet basis function at time  $t = b$  and its neighborhood.

If the scale and translation parameters  $a$  and  $b$  are taken at discrete values, DWT is obtained. In this case, the parameters  $a$  and  $b$  are often based on powers of two and called dyadic scales and translations:

$$a_j = 2^j, b_{j,k} = k2^j \quad \text{for all } j, k \in \mathbb{Z} \quad (17)$$

In this situation, Eq. (15) becomes

$$\psi_{j,k}(t) = 2^{-\frac{j}{2}} \psi(2^{-j} \times (t - k)) \quad \text{for all } j, k \in \mathbb{Z} \quad (18)$$

The DWT discards all redundant information in CWT by employing a set of orthogonal basis functions. The multi-resolution decomposition formula for DWT of the original function as follows:

$$f(t) = \sum_{k=-\infty}^{\infty} c_k \Phi(t - k) + \sum_{k=-\infty}^{\infty} \sum_{j=-\infty}^{\infty} d_{j,k} \Psi(2^j \cdot t - k) \quad (19)$$

where  $\Phi(\cdot)$  – is the scaling function;  
 $d_{j,k}$  – are the wavelet coefficients  
 $c_k$  – are the scaling coefficients.

In the right hand side of Eq. (18), the first term represents an approximation to the general trend of the original function and the second term represents the local details in the original function. The wavelet coefficients  $d_{j,k}$  times the dilated and translated wavelet function can be interpreted as the local residual error between successive signal approximations at scales  $j-1$  and  $j$  and Eq. (20) is the detail signal at scale  $j$  [24].

$$r_j(k) = \sum_{k=-\infty}^{\infty} d_{j,k} \Psi(2^j \cdot t - k) \quad (20)$$

There are many wavelets in the literature proposed by different researchers. Daubechies (db), Symlet (sym), Coiflet (coif) and Biorthogonal (bior) wavelets are used in this study. Some types of these wavelets are shown in Fig. 4.

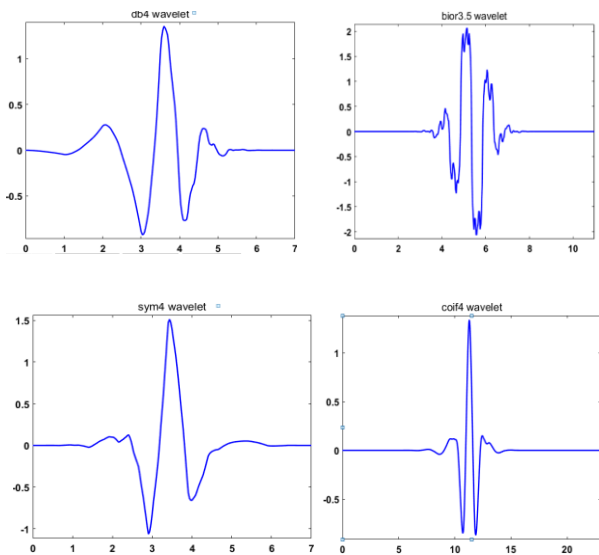


Fig. 4. Some types of Daubechies (db), Symlet (sym), Coiflet (coif) and Biorthogonal (bior) wavelets

### III. SIMULATION RESULTS

In this section, the performances of different coding types on different channels and in different conditions are obtained using MATLAB simulations. LBC (15,8) is used first to determine the performance of phase shift keying modulations. The created communication system is also explained for LBC (15, 8). Similar logic applies for other types of LBC encoding.

The speech signal (original audio signal) used in simulation is sampled at  $f_s = 8$  kHz frequency and recorded in MATLAB environment for 5 seconds with 8 bits resolution. The original audio signal is shown in Fig. 5.

In the second step, the amplitude values of -1 to 1 are shifted to the range of 0 to 255 and these values are expressed by the 8

bit binary number system. In the third step, the H parity check matrix and the G generator matrix are formed appropriately. The audio signal is encoded as a 40,000 x 8 matrix using these matrices. AWGN noise was first added in the fourth stage (then Rician fading). The S (7x15 matrix) syndrome test matrix, which will be used in the recovery phase of the audio signal, has been produced. Here, since the AWGN is added to the original audio signal at 0.8, the largest amplitude value increases from about 0.25 to about 1 and the smallest amplitude value decreases from about -0.25 to about -1.

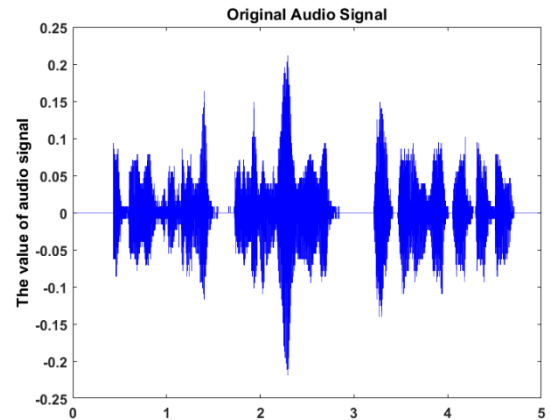


Fig. 5. Original audio signal

The difference between the signal obtained in the coding end resultant signal and the first original audio signal, namely error, is found for different modulation methods. In the course of determining the modulation with the best performance, AWGN channel and Rician fading channel are used for both coded and non-coded scenarios. BER-EbNo graphs for different EbNo values were traced and the performances of channel-coded and non-channel-coded modulation techniques were compared. For channel-coded scenario, LBC (15, 8) coding technique is used. Fig. 6 shows the performance without channel coding of the modulations and Fig. 7 shows the channel-coded performances of the modulations in AWGN channel.

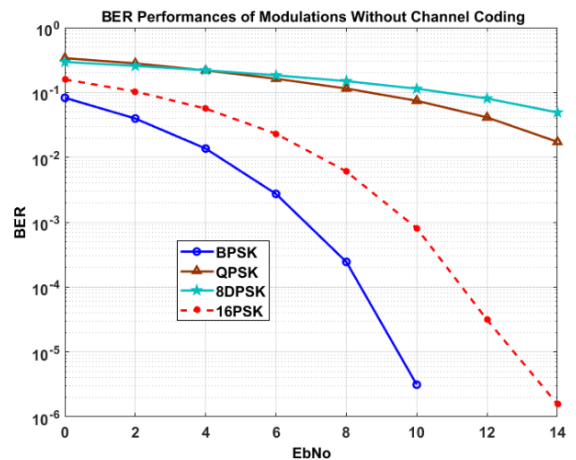


Fig. 6. BER performances of modulations without channel coding in AWGN channel

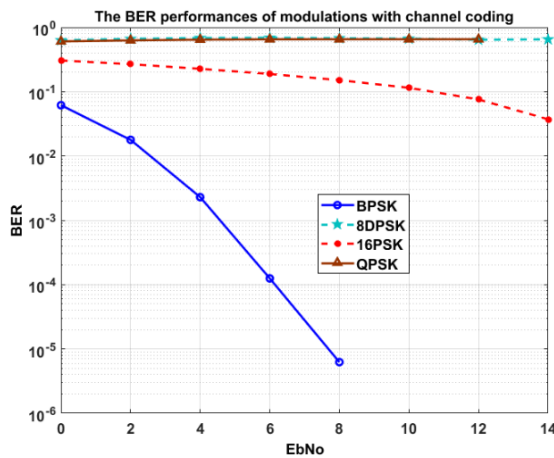


Fig. 7. BER Performances of modulations with channel coding in AWGN channel

Fig. 8 shows the non-channel-coded performances of the modulations and Fig. 9 shows the channel-coded performances of the modulations in Rician fading channel. For this simulation, K-factor =10 value is used.

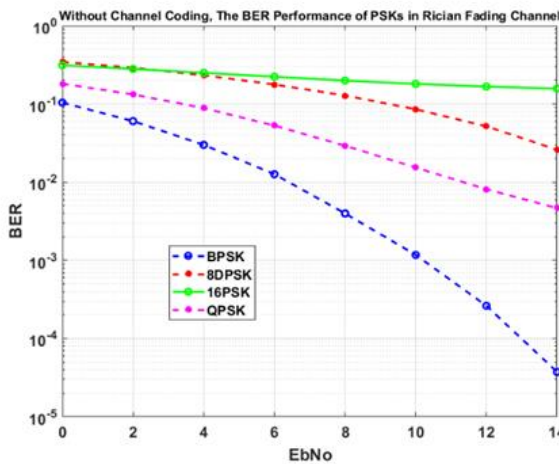


Fig. 8. BER performances of modulations without channel coding in Rician fading channel

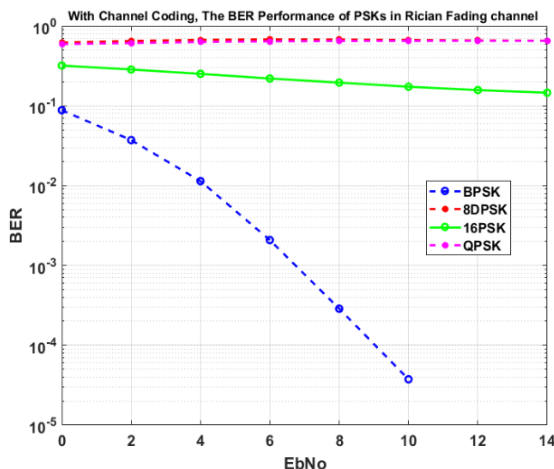


Fig. 9. BER performances of modulations with LBC (15,8) channel coding in Rician fading channel

The BER varies inversely with the signal to noise ratio. As can be seen from the figures, when the BER performances of the modulations are compared, the performance of the BPSK modulation is better than that of the other modulations for both channel coded and non-channel coded situations and for both of the channel types. The MSE performances of the modulations for AWGN channel and for LBC (15, 8) coded version are given in Table I.

TABLE I  
THE MSE PERFORMANCES OF THE MODULATIONS WITH LBC (15,8) CHANNEL CODING

Modulation	BPSK	8-DPSK	16-PSK	QPSK
MSE	1,49E-05	0,98169	0,041216	0,061413

For simulations done on the rest of the study, BPSK is used as modulation only because BPSK has good performance as the above figures and table show.

In the second phase of the study, the performance of different types of LBC codes on AWGN and Rician fading channels was investigated. For this purpose, firstly, MSE performance evaluation of LBC coding types in AWGN channel was performed. Table II shows the MSE performances of the LBC coding types in the AWGN channel. As can be seen in the table, the best MSE performance is achieved with the LBC (23, 12) coding type, which has a higher code length.

TABLE II  
THE MSE PERFORMANCES OF LBC CODING TYPES ON AWGN CHANNEL

LBC Coding Types			
LBC (7,4)	LBC (15,8)	LBC (17,8)	LBC (23,12)
0,003	1,49E-05	1,49E-05	5,77E-08

The BER performance of the LBC (23, 12) coding type is shown in Fig. 10. As can be seen from the figure, high BER performance is achieved even with very low EbNo values using LBC (23, 12).

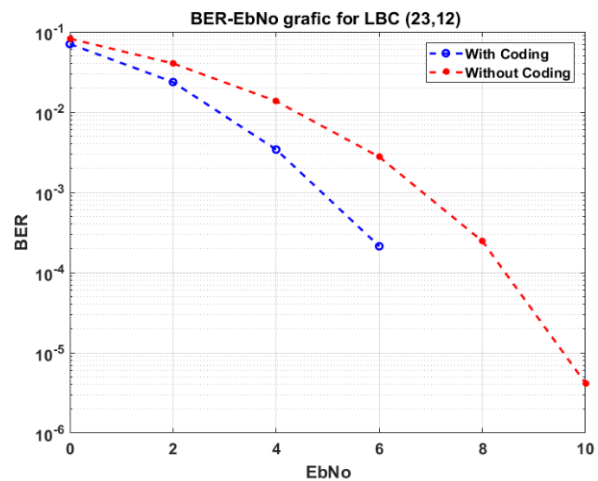


Fig. 10. BER performance of LBC (23,12) in AWGN channel

Secondly, MSE performance evaluation of LBC coding types in Rician fading channel was performed. Table III shows the

MSE performances of the LBC coding types in the Rician fading channel. As can be seen in the table, the best MSE performance is achieved with the LBC (23, 12) coding type same as AWGN channel. As seen in the table, the coding types in the Rician fading channel converge on the AWGN channel with different K-factor values.

In the Rician fading channel, a not-channel coded BER curve is also drawn in order to see the difference between the channel coded version and the not-channel coded version for the best MSE performance (LBC (23,12)). Fig. 11 shows the BER performance for the LBC (23, 12), K-factor = 14 case in Rician fading channel. Both not-coded and coded situations can be seen from the figure.

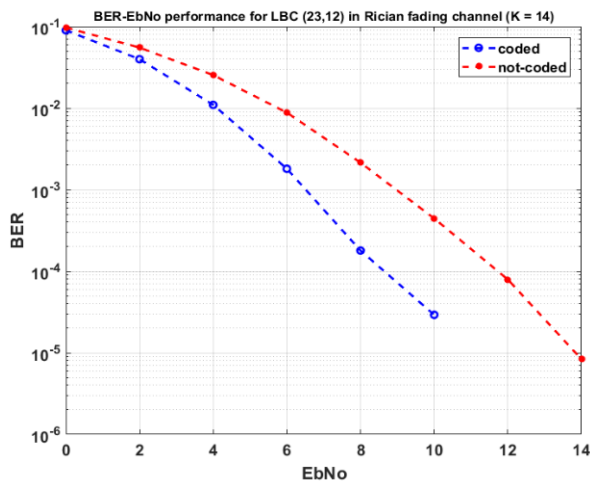


Fig. 11. BER performance of LBC (23,12) in Rician fading channel (K =14)

At the end of the study, four WT families at different levels were applied to the audio signal, and the performance of these families was first compared for the AWGN channel and then for the Rician fading channel. Using DWT, data compressed at different levels instead of the original data are put into the designed communication system and the performance obtained at the output is observed. For example, while the number of samples in the original dataset is 40,000, the number of samples in the dataset obtained from the first-level decompression is 20,000. In Table IV, the MSE performances of different wavelet transform families for LBC (15, 8) obtained by compression in different levels are given in the AWGN channel.

In these conditions, MSE performance was best obtained at db1 part of the Daubechies wavelet family at level 5, sym1 part of the Symlet wavelet family at the 5th level and bior1.1 part of the biorthogonal wavelet family at the 5th level. As can be seen, the MSE performance improves as the compression level increases.

The performances of different LBC species in Rician fading channels with different K-factor values was then obtained. These performances were obtained using DWT at the first, second, and third level compression levels, respectively. Table V, Table VI and Table VII show the performances of the wavelet families at these levels, respectively. As can be seen, as the code size increases, the K-factor value that converge to the AWGN channel of the Rician fading channel also increases.

And generally, as the DWT compression level increases, the K-factor value converging the AWGN value also shrinks. As the compression level increases, the MSE performance improves, and as a result no other compression levels need to be provided. The relationship between compression level and MSE for LBC (7, 4) is shown in Fig. 12.

#### IV. CONCLUSION

According to the obtained results, the LBC method is a suitable method which can be used for channel coding for both AWGN and Rician fading channels. For the channels and coding method considered, BER performance of 4 types of modulation is obtained for the best performance modulation detection. The BER performance of BPSK modulation is the best obtained from these modulations. The BER performance curve is obtained inversely proportional to the signal-to-noise ratio. The coding of the channel by the LBC method reduces the error effect of the channels in the transmitted signal. LBC (7, 4), LBC (15, 7), LBC (17, 8) and LBC (23, 12) used in this study and LBC (23, 12) was obtained as the best transmission performance from the LBC types studied for both of the channel types. The coding types in the Rician fading channel converge on the AWGN channel with different K-factor values.

At the end of the study, four WT families at different levels were applied to the audio signal, and the performance of these families was first compared for the different length LBC coded AWGN channels and then for the different length of LBC coded Rician fading channel. And generally, as the DWT compression level increases, the K-factor value converging the AWGN value also shrinks. As the compression level increases, the MSE performance improves. If both LBC (15, 8) and LBC (17, 8) performances are compared for both with wavelet and non-wavelet conditions, it can be said that the increase in the number of parity bits does not have much effect on the transmission performance. As a general evaluation, it can be said that Biorthogonal Wavelet family is the most suitable family among the families handled for audio transmission.

The difference between the original audio signal transmitted from the channels and the audio signal received at the receiver is not observed except for some acoustic differences. In order to obtain better performance as a result of voice transmission from the used channels by LBC method, sampling frequency can be increased and each sample can be represented by more bits. However, these increases will lead to a longer transmission of the audio signal from the channel.

TABLE III  
THE MSE PERFORMANCES OF LBC CODING TYPES ON RICIAN FADING CHANNEL

K-factor	LBC Types							
	LBC (7,4)		LBC (15,8)		LBC (17,8)		LBC (23,12)	
	not-coded	coded	not-coded	coded	not-coded	coded	not-coded	coded
1	0,1751	0,061	0,1547	0,088	0,1551	0,0794	0,1525	0,0977
2	0,0611	0,014	0,051	0,0165	0,0521	0,0136	0,052	0,0175
3	0,0213	0,005	0,0152	0,0036	0,0158	0,0031	0,016	0,0036
4	0,0094	0,003	0,0052	7,50E-04	0,0054	7,72E-04	0,005	8,31E-04
5	0,0053	0,003	0,0021	1,84E-04	0,0021	2,24E-04	0,0021	7,60E-05
6	0,004	0,003	6,48E-04	3,67E-05	7,88E-04	6,07E-05	7,82E-04	1,27E-05
7	0,0035	0,003	3,00E-04	2,21E-05	3,48E-04	5,66E-05	2,93E-04	3,87E-06
8	0,0032	0,003	1,77E-04	1,49E-05	9,81E-05	3,49E-05	1,67E-04	1,57E-06
9	<b>0,003</b>	<b>0,003</b>	1,77E-04	1,49E-05	9,34E-05	1,49E-05	4,10E-05	5,77E-08
10	0,0031	0,003	4,27E-05	1,49E-05	6,82E-05	1,49E-05	2,30E-05	5,77E-08
11			2,80E-05	1,49E-05	4,05E-05	1,49E-05	2,23E-05	5,77E-08
12			2,78E-05	1,49E-05	4,19E-05	1,49E-05	1,27E-05	5,77E-08
13			2,12E-05	1,49E-05	<b>1,49E-05</b>	<b>1,49E-05</b>	<b>5,77E-08</b>	<b>5,77E-08</b>
14			2,13E-05	1,49E-05	1,49E-05	1,49E-05	5,77E-08	5,77E-08
15			<b>1,49E-05</b>	<b>1,49E-05</b>				
16			1,49E-05	1,49E-05				

TABLE IV  
MSE PERFORMANCES OF WAVELET TRANSFORM FAMILIES

Wavelet Family		MSE Values				
		1st order	2nd order	3rd order	4th order	5th order
Daubechies	db1	4,22E-06	2,44E-06	1,02E-06	5,21E-07	<b>2,46E-07</b>
	db2	4,17E-06	2,02E-04	2,01E-04	2,01E-04	2,00E-04
	db3	4,15E-06	2,06E-06	3,83E-04	3,82E-04	3,82E-04
	db4	4,13E-06	1,83E-04	7,88E-04	7,87E-04	7,87E-04
	db5	4,11E-06	2,05E-06	9,93E-07	3,58E-04	3,58E-04
Symlet	sym1	4,22E-06	2,44E-06	1,02E-06	5,21E-07	<b>2,46E-07</b>
	sym2	4,17E-06	2,02E-04	2,01E-04	2,01E-04	2,00E-04
	sym3	4,15E-06	2,06E-06	3,83E-04	3,82E-04	3,82E-04
	sym4	4,14E-06	1,82E-04	7,90E-04	7,89E-04	7,89E-04
	sym5	4,14E-06	2,04E-06	9,99E-07	3,65E-04	3,65E-04
Coiflet	coif1	4,14E-06	2,06E-06	3,90E-04	3,89E-04	3,89E-04
	coif2	4,13E-06	1,82E-04	1,81E-04	6,86E-04	6,86E-04
	coif3	4,12E-06	2,06E-06	1,01E-06	4,99E-07	1,46E-04
	coif4	4,11E-06	1,78E-04	7,87E-04	7,87E-04	9,93E-04
	coif5	4,11E-06	2,06E-06	3,64E-04	9,52E-04	1,17E-03
Biorthogonal	bior1.1	4,22E-06	2,44E-06	1,02E-06	5,21E-07	<b>2,46E-07</b>
	bior1.3	4,19E-06	2,09E-06	5,44E-04	5,44E-04	5,43E-04
	bior1.5	4,16E-06	2,06E-06	1,01E-06	6,06E-04	6,06E-04
	bior3.1	3,49E-06	1,69E-04	1,68E-04	1,67E-04	1,73E-04
	bior3.3	3,48E-06	1,74E-04	7,49E-04	7,48E-04	7,48E-04
	bior3.5	3,44E-06	1,77E-04	1,76E-04	6,86E-04	6,86E-04

TABLE V  
THE MSE VALUES OBTAINED AFTER THE TRANSMISSION OF THE 1ST LEVEL WT COMPRESSED SIGNAL FROM THE RICIAN CHANNEL

Wavelet Family		LBC (7,4)	LBC (15,8)	LBC (17,8)	LBC (23, 12)
		MSE (K=10)	MSE (K=14)	MSE (K=14)	MSE( K=17)
Db	db1	0,0013	4,03E-06	4,03E-06	1,56E-08
	db2	0,0013	3,98E-06	3,98E-06	1,54E-08
	db3	0,0013	3,95E-06	3,95E-06	1,51E-08
	db4	0,0013	3,93E-06	3,93E-06	1,52E-08
	db5	0,0013	3,90E-06	3,90E-06	1,51E-08
Sym	sym1	0,0013	4,03E-06	4,03E-06	1,56E-08
	sym2	0,0013	3,98E-06	3,98E-06	1,54E-08
	sym3	0,0013	3,95E-06	3,95E-06	1,51E-08
	sym4	0,0013	3,92E-06	3,92E-06	1,52E-08
	sym5	0,0013	3,91E-06	3,91E-06	1,50E-08
Coif	coif1	0,0013	3,92E-06	3,92E-06	1,52E-08
	coif2	0,0013	3,92E-06	3,92E-06	1,51E-08
	coif3	0,0013	3,92E-06	3,92E-06	1,51E-08
	coif4	0,0013	3,92E-06	3,92E-06	1,48E-08
	coif5	0,0013	3,92E-06	3,92E-06	1,50E-08
Bior	bior1.1	0,0013	4,03E-06	4,03E-06	1,56E-08
	bior1.3	0,0013	3,99E-06	3,99E-06	1,52E-08
	bior1.5	0,0013	3,97E-06	3,97E-06	1,52E-08
	bior3.1	0,0011	3,26E-06	3,26E-06	1,27E-08
	bior3.3	0,0011	3,24E-06	3,24E-06	1,24E-08
	bior3.5	0,0011	3,21E-06	3,21E-06	<b>1,23E-08</b>

TABLE VI  
THE MSE VALUES OBTAINED AFTER THE TRANSMISSION OF THE 2ND LEVEL WT COMPRESSED SIGNAL FROM THE RICIAN CHANNEL

Wavelet Family		LBC(7, 4)	LBC(15, 8)	LBC(17, 8)	LBC(23, 12)
		MSE (K=7)	MSE (K=9)	MSE (K=9)	MSE (K=9)
Db	db1	7,28E-04	2,54E-06	2,54E-06	1,43E-08
	db2	8,12E-04	7,87E-05	7,87E-05	7,59E-05
	db3	7,37E-04	2,22E-06	2,22E-06	8,44E-09
	db4	7,97E-04	7,05E-05	7,05E-05	6,82E-05
	db5	7,32E-04	2,18E-06	2,18E-06	8,22E-09
Sym	sym1	7,28E-04	2,54E-06	2,54E-06	1,43E-08
	sym2	8,12E-04	7,87E-05	7,87E-05	7,59E-05
	sym3	7,37E-04	2,22E-06	2,22E-06	8,44E-09
	sym4	8,02E-04	7,26E-05	7,26E-05	6,98E-05
	sym5	7,26E-04	2,22E-06	2,22E-06	8,38E-09
Coif	coif1	7,30E-04	2,26E-06	2,26E-06	8,38E-09
	coif2	7,99E-04	7,16E-05	7,16E-05	6,89E-05
	coif3	7,32E-04	2,23E-06	2,23E-06	8,41E-09
	coif4	7,98E-04	7,13E-05	7,13E-05	6,90E-05
	coif5	7,32E-04	2,24E-06	2,24E-06	8,49E-09
Bior	bior1.1	7,28E-04	2,54E-06	2,54E-06	1,43E-08
	bior1.3	7,34E-04	2,22E-06	2,22E-06	9,29E-09
	bior1.5	7,32E-04	2,20E-06	2,20E-06	<b>8,32E-09</b>
	bior3.1	6,23E-04	6,33E-05	6,33E-05	6,17E-05
	bior3.3	6,33E-04	6,52E-05	6,52E-05	6,31E-05
	bior3.5	6,39E-04	6,67E-05	6,67E-05	6,48E-05

TABLE VII  
THE MSE VALUES OBTAINED AFTER THE TRANSMISSION OF THE 3RD LEVEL WT COMPRESSED SIGNAL FROM THE RICIAN CHANNEL

Wavelet Family		LBC (7,4)	LBC (15,8)	LBC (17,8)	LBC (23,12)
		MSE (K=6)	MSE (K=8)	MSE (K=8)	MSE (K=8)
Db	db1	0,00047	1,55E-06	1,55E-06	5,95E-09
	db2	0,00053	5,62E-05	5,62E-05	5,49E-05
	db3	0,00055	7,54E-05	7,54E-05	7,35E-05
	db4	0,00064	1,69E-04	1,69E-04	1,67E-04
	db5	0,00048	1,52E-06	1,52E-06	5,00E-05
Sym	sym1	0,00047	1,55E-06	1,55E-06	5,95E-09
	sym2	0,00053	5,62E-05	5,62E-05	5,49E-05
	sym3	0,00055	7,54E-05	7,54E-05	7,35E-05
	sym4	0,00065	1,71E-04	1,71E-04	1,70E-04
	sym5	0,00047	1,50E-06	1,50E-06	3,18E-08
Coif	coif1	0,00056	7,65E-05	7,65E-05	7,52E-05
	coif2	0,00051	4,75E-05	4,75E-05	9,61E-05
	coif3	0,00047	1,52E-06	1,52E-06	5,89E-09
	coif4	0,00064	1,73E-04	1,73E-04	1,72E-04
	coif5	0,00055	7,38E-05	7,38E-05	2,71E-04
Biort	bior1.1	0,00047	1,55E-06	1,55E-06	5,95E-09
	bior1.3	0,00058	1,07E-04	1,07E-04	1,06E-04
	bior1.5	0,00047	1,51E-06	1,51E-06	<b>5,84E-09</b>
	bior3.1	0,00046	3,99E-05	3,99E-05	3,85E-05
	bior3.3	0,00058	1,51E-04	1,51E-04	1,49E-04
	bior3.5	0,00047	4,33E-05	4,33E-05	4,17E-05

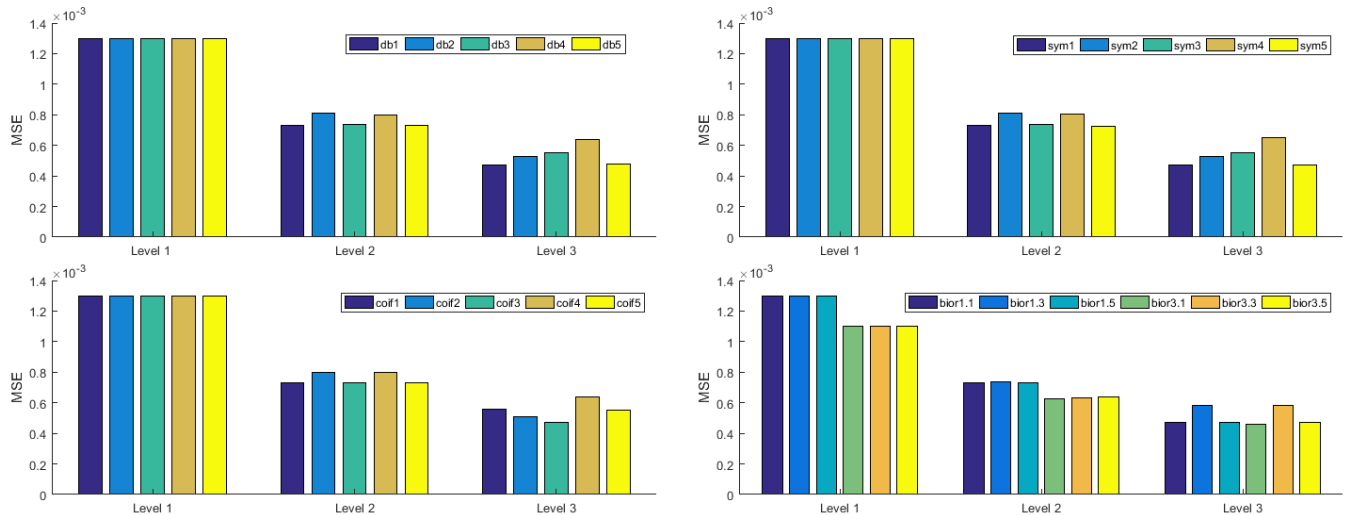
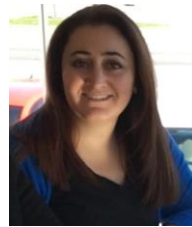


Fig. 12. Comparison of compression level and MSE for LCB(7,4) in Rician fading channel

## REFERENCES

- [1] N. Jacob, U. Sripathi, "Bit Error Rate Analysis of Coded OFDM for Digital Audio Broadcasting System, Employing Parallel Concatenated Convolutional Turbo Codes", in 2015 IEEE International Conference on Signal Processing, Informatics, Communication and Energy Systems (SPICES), IEEE, 2017. <https://doi.org/10.1109/SPICES.2015.7091461>
- [2] S. Faruque, Introduction to Channel Coding. In: Radio Frequency Channel Coding Made Easy, Springer Briefs in Electrical and Computer Engineering. Springer, Cham, 2016.
- [3] S. Dhaliwal, N. Singh, G. Kaur, "Performance analysis of convolutional code over different code rates and constraint length in wireless communication." I-SMAC (IoT in Social, Mobile, Analytics and Cloud)(I-SMAC), 2017 International Conference on. IEEE, 2017. <https://doi.org/10.1109/I-SMAC.2017.8058393>
- [4] J. Baviskar, A. Mulla, M. Gulati, P. Vaswani, A. Baaviskar, "LDPC based error resilient audio signal processing for wireless communication." Pervasive Computing (ICPC), 2015 International Conference on. IEEE, 2015. <https://doi.org/10.1109/PERVASIVE.2015.7087164>
- [5] T. Majoul, F. Raouafi, M. Jaidane, "Turbo decoding performance in non-Gaussian noise channels." Systems, Signals and Devices, 2009. SSD'09. 6th International Multi-Conference on. IEEE, 2009. <https://doi.org/10.1109/SSD.2009.4956730>
- [6] Md D. Haque, S. E. Ullah, Md R. Ahmed, "Performance evaluation of a wireless Orthogonal Frequency Division Multiplexing system under various concatenated FEC channel-coding schemes." Computer and Information Technology, 2008. ICCIT 2008. 11th International Conference on. IEEE, 2008. <https://doi.org/10.1109/ICCITECHN.2008.4802994>
- [7] K. K. Sidhu, G. Kaur, "Performance evaluation of multilevel linear block codes on Rayleigh fading channel." Electrical, Electronics, and Optimization Techniques (ICEEOT), International Conference on. IEEE, 2016. <https://doi.org/10.1109/ICEEOT.2016.7755080>
- [8] H. Lee, "Exact and asymptotic BER analysis of  $2 \times 2$  FRLR-STBC with BPSK modulation." Electronics Letters. 53(11) 2017: 720-722. <http://dx.doi.org/10.1049/el.2016.4194>
- [9] N. Romano, A. Scivoletto, D. Polap, "A real-time audio compression technique based on fast wavelet filtering and encoding." Computer Science and Information Systems (FedCSIS), 2016 Federated Conference on. IEEE, 2016.
- [10] P. E. Kudumakis, M. B. Sandler, "On the performance of wavelets for low bit rate coding of audio signals." Acoustics, Speech, and Signal Processing, 1995. ICASSP-95., 1995 International Conference on. Vol. 5. IEEE, 1995. <https://doi.org/10.1109/ICASSP.1995.479498>
- [11] G. Luo, "Ultra low delay wavelet audio coding with low complexity for real time wireless transmission." Intelligent Signal Processing and Communication Systems, 2005. ISPACS 2005. Proceedings of 2005 International Symposium on. IEEE, 2005. <https://doi.org/10.1109/ISPACS.2005.1595516>
- [12] A. K. Sinha, S. K. Dutta, B. Dev, Jaydipta, R. Ranjan, R. Kumari, "Wavelet based Speech Coding technique using median function thresholding." Electronics and Communication Systems (ICECS), 2014 International Conference on. IEEE, 2014. <https://doi.org/10.1109/ECS.2014.6892538>
- [13] S. S. Sarnin, N. F. Naim, W. N. S. W. Muhamad, "Performance evaluation of phase shift keying modulation technique using BCH code, Cyclic code and Hamming code through AWGN channel model in communication system." Information Sciences and Interaction Sciences (ICIS), 2010 3rd International Conference on. IEEE, 2010. <https://doi.org/10.1109/ICICIS.2010.5534715>
- [14] Bhatti, Ali Tariq, "Cyclic channel coding algorithm for original and received voice signal at 8 khz using ber performance through additive white gaussian noise channel." International journal of innovative science, engineering & technology (IJSET), 2(4), 843-852, 2015.
- [15] Bhatti, Ali Tariq, and Dr Jung H. Kim, "Implementation of reed-Solomon (rs) and cdma for signaling a voice through AWGN at 8 KHz sampling frequency using BPSK." International journal of advent research in computer and electronics (IJARCE), 2(8), 13-27, 2015.
- [16] E. Göse, "Zamanla değişen kanallarda turbo kodlama", PhD Thesis, Yıldız Technical University, Institute of Science and Technology, 2005.
- [17] B. Sklar, Digital Communications Fundamentals and Applications Second Edition, Prentice Hall P T R Upper Saddle River, New Jersey 07458, 2001.
- [18] J. Proakis, M. Salehi, Fundamentals of Communication Systems. Pearson Education, 2007.
- [19] P. R. Kamala, R. V. S. Satyanarayana, "Optimal linear block code modeling and performance analysis over various channels for use in wireless communications", Emerging Trends in Engineering, Technology and Science (ICETETS), International Conference on. IEEE, 2016. <https://doi.org/10.1109/ICETETS.2016.7603038>
- [20] B. Sklar, "Rayleigh fading channels in mobile digital communication systems. I. Characterization." IEEE Communications magazine 35(7), 90-100, 1997. <https://doi.org/10.1109/35.601747>
- [21] G. L. Stüber, Principles of mobile communication. Norwell, Mass, USA: Kluwer Academic, 1996.
- [22] A. Mahmutoğlu, "Uzay Zaman Blok Kodlarını Kullanan Röleli Sistemlerin Genelleştirilmiş Sönümlenmeli Kanallardaki Hata Performans Analizi", Diss. M. Sc. Thesis, İstanbul Technical University, Institute of Science and Technology, 2009.
- [23] Adeli, Hojjat, Ziqin Zhou, and Nahid Dadmehr. "Analysis of EEG records in an epileptic patient using wavelet transform." Journal of neuroscience methods 123(1), 69-87, 2003. [https://doi.org/10.1016/S0165-0270\(02\)00340-0](https://doi.org/10.1016/S0165-0270(02)00340-0)
- [24] A. Haşiloğlu, "Dalgacık dönüşümü ve yapay sinir ağları ile döndürmeye duyarlı doku analizi ve sınıflandırma" Turkish Journal of Engineering and Environmental Sciences (Turk J Engin Environ Sci.) 25, 405-413. 2001.

## BIOGRAPHIES



**SERAP KARAGOL** received the B.E. degree in Computer Engineering from the Karadeniz Technical University, Trabzon, Turkey, in 2002, and the M.S. and Ph.D. degrees in electrical engineering from North Carolina A&T State University, Greensboro, NC USA, in 2006 and 2011, respectively. She is currently an Assistant

Professor in the Department of Electrical and Electronics Engineering, Ondokuz Mayıs University, Samsun Turkey. She is engaged in teaching and conducting research in circuits and systems, signal processing, modeling, system identification and wireless sensors networks. She is the advisor for more than 10 M.S. and 3 Ph.D. students.



**DOGAN YILDIZ** born in Istanbul in 1989. He received the B.S. degree in Electrical-Electronics engineering and Mathematics from Fatih University, Istanbul, in 2013 and the M.S. degree in electrical-electronics engineering from Ondokuz Mayıs University, Samsun, in 2016.

Since 2013, he has been working as research assistant with the Electrical-Electronics Engineering Department in Ondokuz Mayıs University. His research interests include wireless sensor networks, localization, signal processing, telecommunication and applications, electromagnetic waves and electromagnetic radiation measurements.

# Impulsive Noise Models Used in Power Line Communications

S. M. ÇÜRÜK

**Abstract**— In a communication system, noise has always been considered as a serious cause of error. Although most common noises can be modeled by well-known Gaussian distributions, some communication systems experience other types of noise. Power Line Communication (PLC) is one of these systems which run on a difficult medium since it uses the preexisting power line network for transmission. PLC experiences several different types of human-made and natural noise which are mostly impulsive and cannot be modeled simply by Gaussian. Different statistical models are used for characterizing the impulsive noise of PLC systems in the literature. The purpose of this study is to go over the impulsive noise models previously presented in order to have a contribution to this hot topic. We point out the similarities and differences of the models, namely Middleton Class A, Bernoulli Gaussian and Alpha Stable statistical models. It is presented that all have heavy tails which make them appropriate for impulsive noise. Although Middleton Class A is more generic, Bernoulli Gaussian model is wide enough and can be preferable because of its compact simple form especially when analytical results are needed.

**Index Terms**— Alpha Stable distribution, Bernoulli Gaussian distribution, Impulsive Noise, Middleton Class A distribution.

## I. INTRODUCTION

THE noise is the main reason of errors occurred in data transmission and should be dealt with carefully for reliable communication. The common noise experienced in a communication system is the thermal noise and it can easily be modeled by a Gaussian distribution. Unfortunately, the effects of various human-made and/or natural noises are also observed in some communication systems, which are mostly impulsive and cannot be modeled by Gaussian density. A Power Line Communication (PLC) system is one of these systems.

PLC shares the installed power lines with various electrical sources for data transfer. Unfortunately, the power line medium is unsafe for communication and various noise types may be experienced. These noises are named as colored

background noise, narrowband noise, periodic asynchronous/synchronous impulsive noise and asynchronous impulsive noise [1]. Colored noise and narrowband noise are background noise and are modeled as Gaussian; but the rests are all impulsive and should be modeled exhaustively. The human-made noises such as switching (connection and removal of the sources) from the network, sudden power variations (changing speed of an ac motor etc.) or natural noises such as electromagnetic interference are all causes of impulsive noise in PLC. Impulsive noise is the more feared one because its prediction is not easy and its level could even be higher than the background noise.

For safe PLC, accurate models with true characteristics of impulsive noise are needed. Researches modeling the impulsive noise in different fields of communications, as well as in PLC, are present in literature. According to [1], the statistical properties of impulsive noise in a PLC system fit Alpha Stable distribution. The article [2] points out some features of impulse noise models, Middleton Class A, Bernoulli-Gaussian and Symmetric Alpha Stable. In [3] a new approach is applied to modeling of impulsive noise at the sources. In [4], the generalized Gaussian distribution is introduced as a suitable model after analyzing noise amplitude. [5] and [6] are interested in coping with impulsive noise which is modeled by Bernoulli Gaussian distribution. The authors in [7] used Middleton Class A noise model in their studies. Authors of [8] search the suitability of the Middleton Class A model for narrowband PLC noise. Frequency domain background and impulsive noises for broadband PLC systems are characterized in [9]. The authors of [10] compare Middleton Class A and Marcov-Middleton models. The authors of [11] modeled power line colored background noise, narrowband noise and burst noise. A simple mathematical representation of time variant and nonwhite noise for narrowband PLC is introduced in [12]. The authors in [13] give an easily implemented noise model for power line channel. Papers [14] and [15] are investigating statistical noise models.

We see it necessary to bring a general view of impulse noise models used in PLCs in order to sum up. A comparative study of the common models seen in the literature, namely Middleton Class A, Bernoulli Gaussian and Alpha Stable statistical models is given in the following sections.

SELVA MURATOĞLU ÇÜRÜK, is with Department of Electrical and Electronics Engineering of Iskenderun Technical University, Hatay, Turkey, (e-mail: [selva.curuk@iste.edu.tr](mailto:selva.curuk@iste.edu.tr)).

 <https://orcid.org/0000-0002-2195-7827>

Manuscript received September 5, 2018; accepted April 4, 2019.  
DOI: [10.17694/bajece.457393](https://doi.org/10.17694/bajece.457393)

## II. IMPULSIVE NOISE MODELS

In a communication system, impulsive noise is categorized into two groups: Human-made impulsive noise is caused by different sources, such as switching, dropouts or degradation of data, while naturally occurring impulsive noise is due to atmospheric phenomena and solar static. The human-made impulsive noise is described as trains of non-overlapping pulses while the impulsive noise due to nature is the random superposition of the pulses formed with the effects of the natural phenomena. Although impulsive noise duration is more than one sample long, it is relatively short compared to transmission.

The first detailed model of impulsive noise was given by Middleton [2], where impulsive noise was defined as randomly occurring sequences of pulses or impulses in time, with varying duration and intensity. Thus, in Middleton's model impulsive noise is a non-stationary, binary-state sequence of impulses with random amplitudes and random occurrence positions. Following, various studies have been done to fit the first order statistics of the noise to the known distributions, where Symmetric Alpha Stable and Bernoulli Gaussian models are the more featured ones in the literature. In this section, we examine the most popular models which appear more frequently in the literature for impulsive noise modeling.

### A. Gaussian Mixture Model

In a complex data, several different regions may be observed, some with high probabilities whereas the others with smaller probabilities. Such a multimodal data is modeled in terms of a mixture of several components, where each component has a simple parametric form, such as Gaussian. Thus, it is assumed that each data point belongs to one of the components and the distribution for each component is assigned separately.

A Gaussian Mixture model assumes all data are generated from a mixture of a finite number of Gaussian distributions with unknown parameters. According to this probabilistic model, random variable  $n_k$  has a distribution where the probability density function (pdf) is a weighted summation of different Gaussian distributions [7], i.e.,

$$p(n_k) = \sum_{m=0}^K P_m \cdot \mathcal{N}(n_k; \mu_m, \sigma_m^2) \quad (1)$$

$\mathcal{N}(n_k; \mu_m, \sigma_m^2)$  denotes Gaussian pdf with mean  $\mu_m$ , variance  $\sigma_m^2$  and  $P_m$  is mixing probability of the  $m$ -th Gaussian component which sums to 1, i.e.,

$$\sum_{m=0}^K P_m = 1, \quad 0 < P_m < 1 \quad (2)$$

Gaussian Mixture is the base of various distributions; Middleton Class A and Bernoulli Gaussian models are among them.

### B. Middleton Class A Model

Middleton has defined three statistical models depending on the bandwidth of impulsive noise and receiver and they have been widely used in electromagnetic and communication problems. (Class A noise has narrower bandwidth than that of the receiver; while Class B noise has larger bandwidth; and Class C noise is the sum of both noises.) In communication systems, as in PLC, Middleton Class A noise model is employed more widely compared to other two classes.

In Middleton Class A model,  $L$ , number of impulses in an observation period  $T_0$ , is assumed to obey a Poisson distribution. i.e., this model is a form of the Poisson model, with the impulse width is taken into account [2]:

$$P_{T_0}(L) = \frac{(\eta T_0)^L \cdot e^{-\eta T_0}}{L!} \quad (3)$$

where  $\eta$  is the average number of impulses per second ( $\eta T_0$  is the average number of impulses in the period  $T_0$ ). Then, the pdf of a Middleton Class A noise sample  $n_k$  is given as follows:

$$p(n_k) = \sum_{m=0}^{\infty} P_m \cdot \mathcal{N}(n_k; 0, \sigma_m^2) \quad (4)$$

$$P_m = \frac{A^m \cdot e^{-A}}{m!} \quad (5)$$

The non-Gaussian nature of the noise is measured by the parameter  $A$ . Impulsive index (non-structure index)  $A$  is the density of impulses in the observation period and is in the range  $A \in (0, \infty)$ . Lower  $A$  values mean fewer number of events, where the individual events dominate the instantaneous noise properties. As  $A$  gets larger, the noise becomes less structured and the statistics approach the Gaussian distribution as stated in Central Limit Theorem.

The Gaussian pdf  $\mathcal{N}(n_k; 0, \sigma_m^2)$  in (4) are zero mean with variance  $\sigma_m^2$  which is given by

$$\sigma_m^2 = \sigma_I^2 \cdot \frac{m}{A} + \sigma_g^2 \quad (6)$$

$\sigma_I^2$  is the variance of the impulse noise and  $\sigma_g^2$  is the variance of the background Gaussian noise. The  $m$ -th variance can be written equivalently as

$$\sigma_m^2 = \sigma_g^2 \cdot \left( \frac{m}{A\Gamma} + 1 \right) = \sigma^2 \cdot \left( \frac{m/A + \Gamma}{1 + \Gamma} \right) \quad (7)$$

The parameter  $\Gamma = \sigma_g^2 / \sigma_I^2$  is called the Gaussian factor and gives Gaussian to impulse noise power ratio.  $\sigma^2 = \sigma_g^2 + \sigma_I^2$  is the total power of noise. By adjusting the parameters  $A$  and  $\Gamma$ , the Middleton Class A density can cover a great variety of non-Gaussian noise densities. It would be noted that for an impulsive noise in PLC, generally  $\Gamma$  is in the range of  $[10^{-6}, 1]$  and  $A \in [10^{-2}, 1]$  [10].

### C. Bernoulli Gaussian Model

Another popular impulsive noise model is the Bernoulli Gaussian model. According to this model, the overall noise sample  $n_k$  may be expressed as [16]:

$$n_k = w_k + i_k \quad (8)$$

where  $w_k$  is the white Gaussian background noise and  $i_k$  is the impulsive noise sample given by

$$i_k = b_k \cdot g_k \quad (9)$$

$g_k$  is complex white Gaussian noise with mean zero and  $b_k$  is the Bernoulli process which means the arrival of impulsive noise has a probability

$$P(b_k) = \begin{cases} p, & b_k = 1 \\ 1-p, & b_k = 0 \end{cases} \quad (10)$$

In (10),  $p$  represents the impulsive bursts probability of occurrence.

The Bernoulli Gaussian noise model is described by the following pdf:

$$p(n_k) = (1-p) \cdot \mathcal{N}(n_k; 0, \sigma_g^2) + p \cdot \mathcal{N}(n_k; 0, \sigma_g^2 + \sigma_I^2) \quad (11)$$

where  $\mathcal{N}(n_k; 0, \sigma_m^2)$  represents the Gaussian pdf. Bernoulli Gaussian noise model is a Gaussian Mixture with two terms.

### D. Alpha Stable Model

The noise models discussed above are the most widely used ones, but Symmetric Alpha Stable distribution is also used for impulsive noise modeling in the literature. Central Limit Theorem states that, the normalized sum of independent and identically distributed random variables with finite variance converges to the Gaussian distribution as the number goes to infinity. Generalized Central Limit Theorem underlines that the sum converges to Alpha Stable distribution when the finite

variance limitation (it may be finite or infinite variance) drops. Alpha Stable distributions date back, but they have a limited usage because except for a few cases their pdfs cannot be expressed in closed-forms. Nowadays Alpha Stable distributions are being used more, as its usage in PLC noise models, since computation with powerful computers is possible.

An Alpha Stable random variable is defined by its characteristic function [1]:

$$\phi(u) = \begin{cases} \exp\left\{j\delta u - \gamma^\alpha |u|^\alpha \left(1 + j\beta \cdot \text{sign}(u) \cdot \tan\left(\frac{\pi\alpha}{2}\right)\right)\right\}, & \alpha \neq 1 \\ \exp\left\{j\delta u - \gamma |u| \left(1 - j\beta \cdot \frac{2}{\pi} \cdot \text{sign}(u) \cdot \ln|u|\right)\right\}, & \alpha = 1 \end{cases} \quad (12)$$

where the sign function is defined as

$$\text{sign}(u) = \begin{cases} 1, & u > 0 \\ 0, & u = 0 \\ -1, & u < 0 \end{cases} \quad (13)$$

Stability index  $\alpha$ , which is in the range of  $(0, 2]$ , is the characteristic exponent and controls the tail decays. Skewness parameter  $\beta$  takes on the values  $-1 \leq \beta \leq 1$ ; 0 for a symmetrical distribution,  $\beta > 0$  for right-skewed distributions and  $\beta < 0$  for left-skewed ones. Finally, scale parameter  $\gamma > 0$  is used to scale the random variable and shift parameter  $\delta \in \mathfrak{R}$  is used to control the location of the variable. The mean of an Alpha Stable distribution is  $\mu = \delta - \beta\gamma \cdot \tan(\pi\alpha/2)$  for  $\alpha > 1$ , but undefined for  $\alpha \leq 1$ . Similarly, the variance of the distribution is undefined for values of  $\alpha < 2$  but for  $\alpha = 2$ , the variance is  $\sigma^2 = 2\gamma^2$ .

The Gaussian distribution is a special case of Alpha Stable distributions when  $\alpha = 2$ . Although the value of  $\beta$  has no effect in this situation, it is usually written as  $\beta = 0$ . The other special cases are Cauchy distribution with  $\alpha = 1, \beta = 0$  and Lévy distribution with  $\alpha = 0.5, \beta = 1$ . Except for the Gaussian case, Alpha Stable distribution tail decay is slow and therefore they are considered for modeling of impulsive noise [1].

## III. SIMULATION RESULTS

Middleton Class A density can cover a great variety of densities by arranging its parameters. Fig. 1 gives the distribution pdfs for  $\Gamma = 0.01$  and various  $A$  values. For the sake of simplicity, in the simulations we will consider signals with total power 1. i.e.,  $\sigma^2 = \sigma_g^2 + \sigma_I^2 = 1$ , and this term will be omitted in (7). The number of terms in summation is selected to be high enough. As seen from the figure, the tails

are more pronounced compared to Gauss distribution, especially for  $A=0.5$  and  $A=1$ .

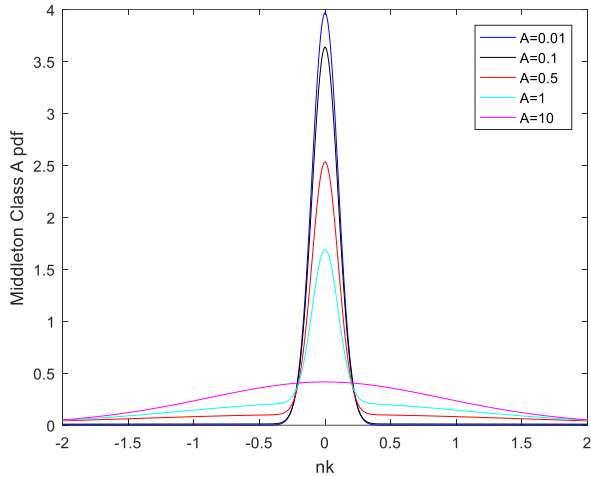


Fig. 1. Middleton Class A pdf,  $\Gamma = 0.01$ .

Middleton Class A density is a Gaussian Mixture but theoretically with infinite summation terms. Indeed this distribution can be approximated by the first few terms for obtaining a more simplified workable form, and still it may be sufficiently accurate [10]. As seen from (5), the mixing probability  $P_m$  decreases to zero as the term number  $m$  increases, with a speed depending on the value of selected  $A$ . Table 1 gives mixing probability  $P_m$  for  $A=0.01$ ,  $A=0.1$  and  $A=1$ . As it can be seen from the table, Middleton Class A pdfs can be approximated by 2 terms when  $A=0.01$ , 3 terms when  $A=0.1$  and 6 terms when  $A=1$ . Thus, for small  $A$  values (highly impulsive case), the model may be equal to Bernoulli Gaussian model with appropriate parameter selections.

TABLE I  
MIDDLETON CLASS A MODEL MIXING PROBABILITY ( $P_m$ )  
VALUES FOR  $A=0.01$ ,  $A=0.1$  AND  $A=1$

	$P_m$		
	$A=0.01$	$A=0.1$	$A=1$
$m = 0$	0.9900	0.9048	0.3678
$m = 1$	0.0099	0.0904	0.3678
$m = 2$	0.0000	0.0045	0.1839
$m = 3$	0.0000	0.0001	0.0613
$m = 4$	0.0000	0.0000	0.0153
$m = 5$	0.0000	0.0000	0.0030
$m = 6$	0.0000	0.0000	0.0005
$m = 7$	0.0000	0.0000	0.0000

For an approximated Middleton Class A pdf, the summation in (4) is limited by the first  $K$  terms where normalization follows, which results with a pdf given by

$$p(n_k) = \sum_{m=0}^{K-1} P_m' \cdot \mathcal{N}(n_k; 0, \sigma_m^2) \quad (14)$$

$$P_m' = \frac{P_m}{\sum_{m=0}^{K-1} P_m} \quad (15)$$

Fig. 2, Fig. 3, Fig. 4, Fig. 5 and Fig. 6 depict the pdfs of Middleton Class A distribution for several values of  $A$  and  $\Gamma$  in logarithmic scale. The logarithmic scale is preferred in plots to investigate the tails of the distributions thoroughly. It can be observed that when  $A=10$  (Fig. 2) the resulting pdfs are almost like the Gaussian ones, as expected, and the weight of  $\Gamma$  is hardly visible. There is an indistinct peak for very small  $\Gamma$  values. As  $A$  gets smaller, the peak becomes sharper and the tails fatter. For a fixed  $A$ , the value of  $\Gamma$  determines the width of the shoulders. Thus as it gets larger, the pdf is wider.

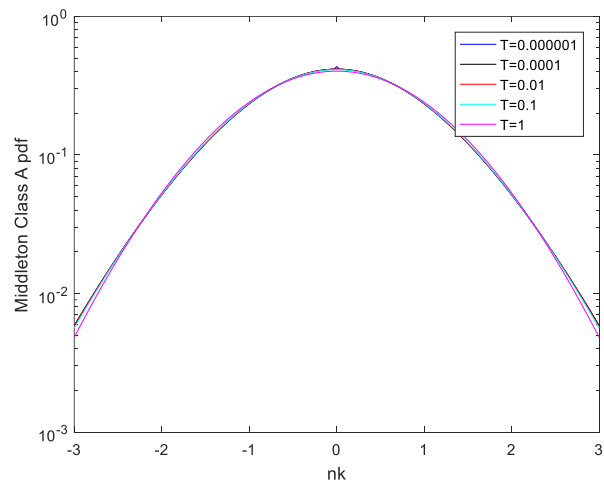


Fig. 2. Middleton Class A pdf,  $A = 10$ .

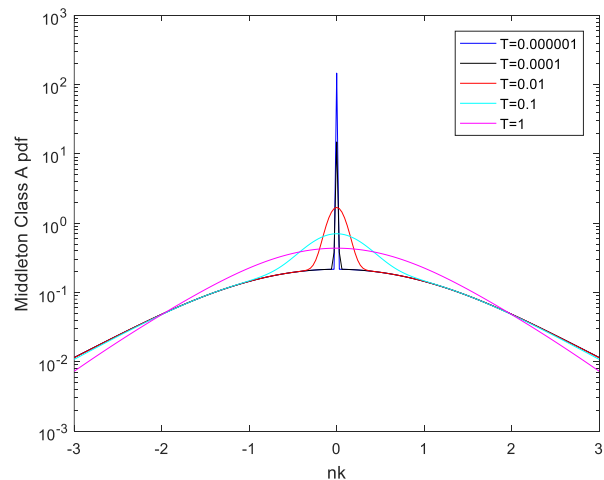


Fig. 3. Middleton Class A pdf,  $A = 1$ .

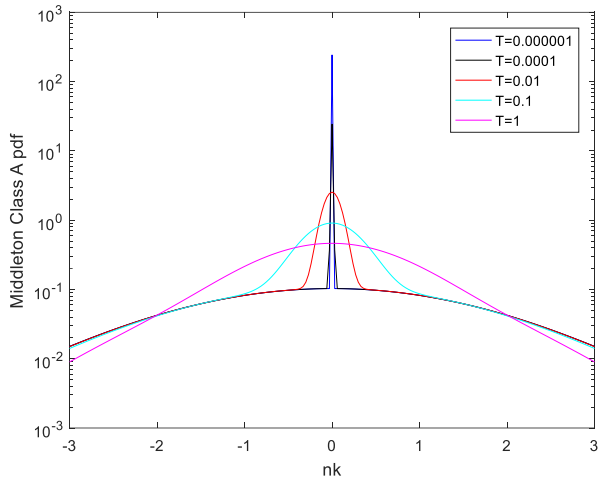


Fig. 4. Middleton Class A pdf,  $A = 0.5$  .

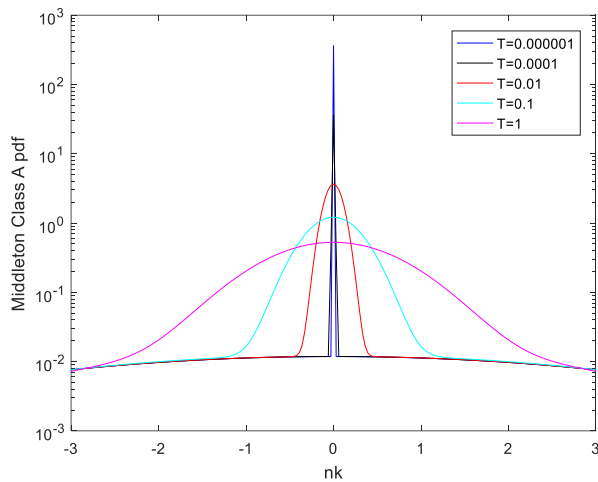


Fig. 5. Middleton Class A pdf,  $A = 0.1$  .

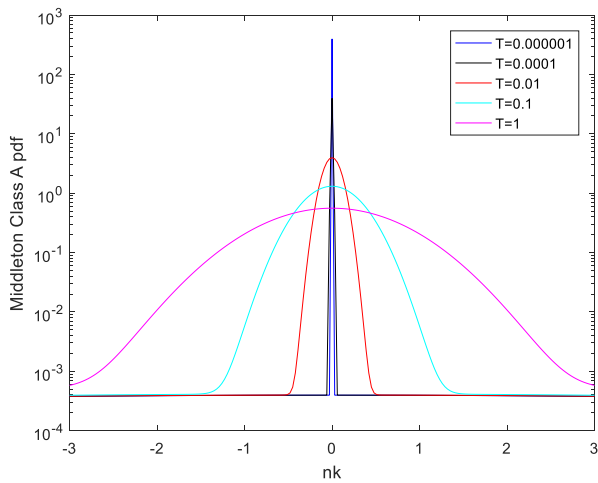


Fig. 6. Middleton Class A pdf,  $A = 0.01$  .

The Bernoulli Gaussian noise model has been frequently used for PLC impulsive noise in the literature. Fig. 7 gives the pdfs of Bernoulli Gaussian distribution for various probability

$p$  and  $\sigma_g^2 = 0.1$ . Again, for comparison, we consider the signals with  $\sigma_g^2 + \sigma_I^2 = 1$  in the simulations. As seen from the figure, similar to Middleton Class A distribution, it has heavy tails compared to Gaussian distribution, and as the probability of impulsive noise increases, the tails of pdfs become more pronounced.

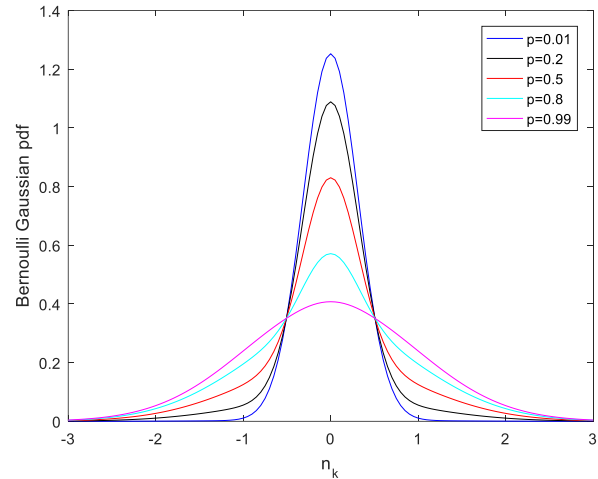


Fig. 7. Bernoulli Gaussian pdf,  $\sigma_g^2 = 0.1$  .

Fig. 8, Fig. 9, Fig. 10, Fig. 11 and Fig. 12 depict the pdfs of Bernoulli Gaussian distribution for several values of  $p$  and  $\sigma_g^2$  in logarithmic scale to investigate the tails of the distributions. It can be observed that when  $p = 0.99$  (Fig. 8) the resulting pdfs are almost like the Gaussian ones, and the influence of  $\sigma_g^2$  is very small. As  $p \rightarrow 0$ , the peak becomes sharper and the tails fatter as expected. For a fixed  $p$ , the value of  $\sigma_g^2$  determines the width of the shoulders.

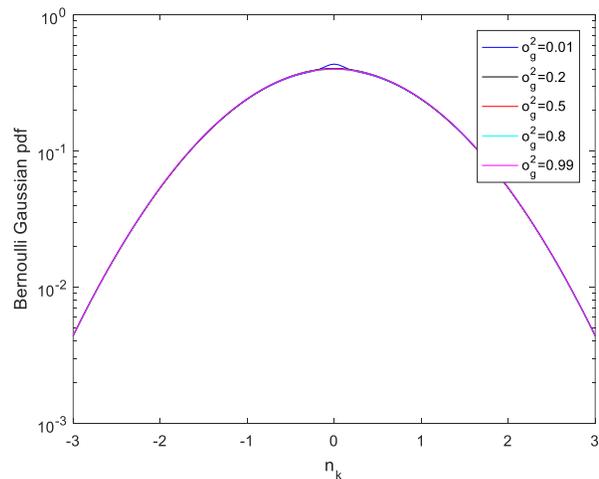


Fig. 8. Bernoulli Gaussian pdf,  $p = 0.99$  .

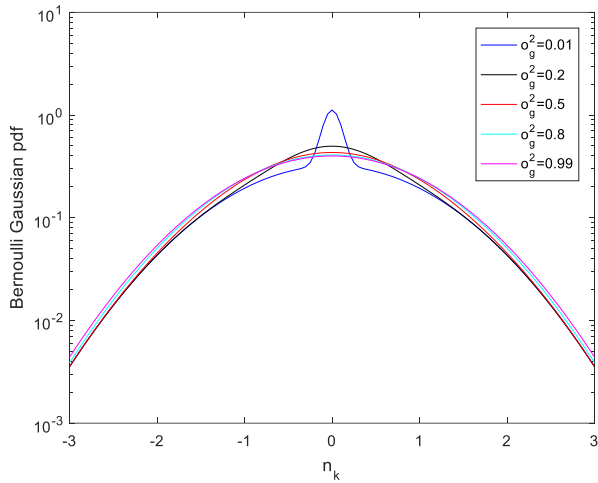


Fig. 9. Bernoulli Gaussian pdf,  $p = 0.8$ .

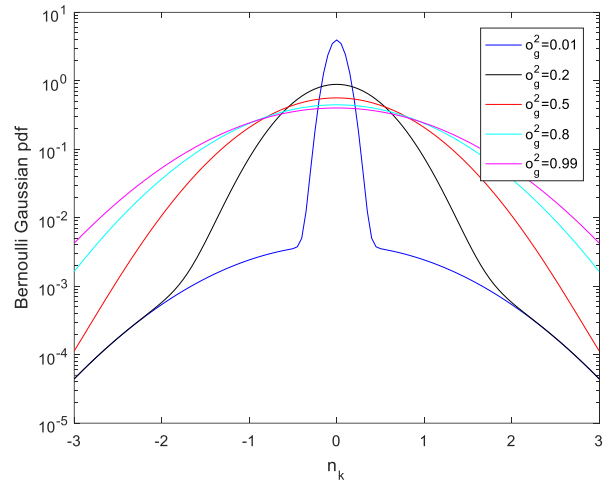


Fig. 12. Bernoulli Gaussian pdf,  $p = 0.01$ .

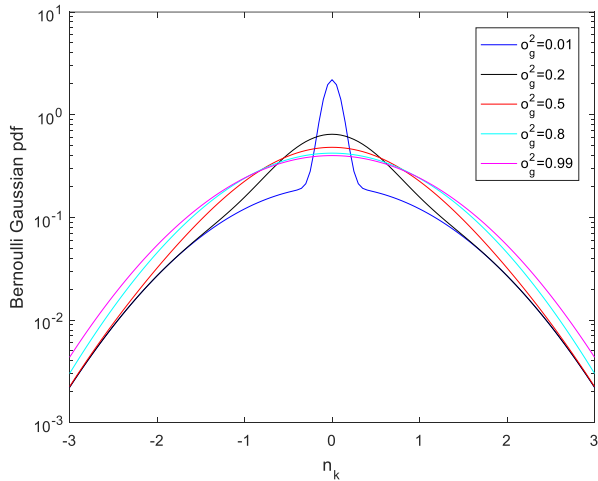


Fig. 10. Bernoulli Gaussian pdf,  $p = 0.5$ .

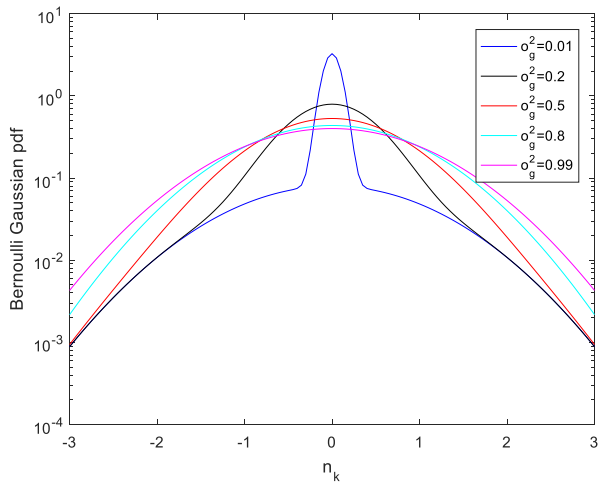


Fig. 11. Bernoulli Gaussian pdf,  $p = 0.2$ .

Bernoulli Gaussian distributions give very close results to the Middleton Class A distributions. But the Middleton Class A model has the advantage of having its parameters directly related to the physical channel. Another point is that since it can be arranged to contain more than two Gaussian distributions, Middleton Class A model is more powerful and can model wider class of data more precisely. It can easily be adjusted to approximate even the Bernoulli Gaussian model, by adjusting the parameters. But some researchers may prefer to use the simpler one, Bernoulli Gaussian impulsive noise model rather than the Middleton Class A noise model because it is more tractable, especially when analytic results are needed.

The Alpha Stable distribution pdfs are given in Fig. 13 for various skew values  $\beta$ , with  $\alpha = 0.5$ ,  $\gamma = 1$  and  $\delta = 0$ . As seen from the figure, right and left skewed distributions as well as symmetric ones can be obtained. Fig. 14, Fig. 15 and Fig. 16 give the pdfs of Symmetric Alpha Stable distributions for several values of  $\alpha$  and  $\gamma$  in logarithmic scale again. The lower  $\alpha$  values means the heavier tails especially for small  $\gamma$  values. As scale parameter gets higher, the tails are thicker after a while, for low  $\alpha$  values. It should be noted that the Alpha Stable pdfs has not shoulders as in the other two distributions, Middleton Class A and Bernoulli Gaussian.

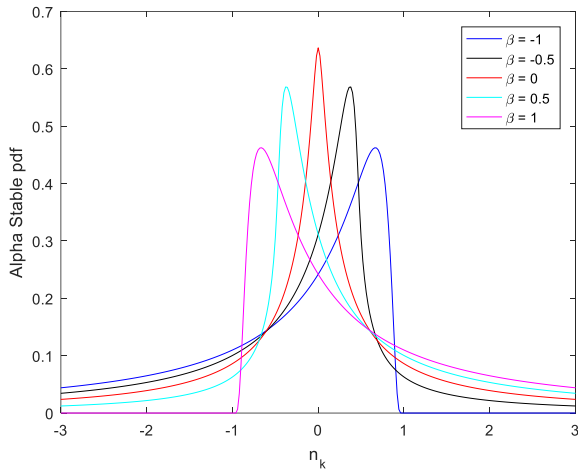


Fig. 13. Alpha stable pdf,  $\alpha = 0.5$ ,  $\gamma = 1$  and  $\delta = 0$ .

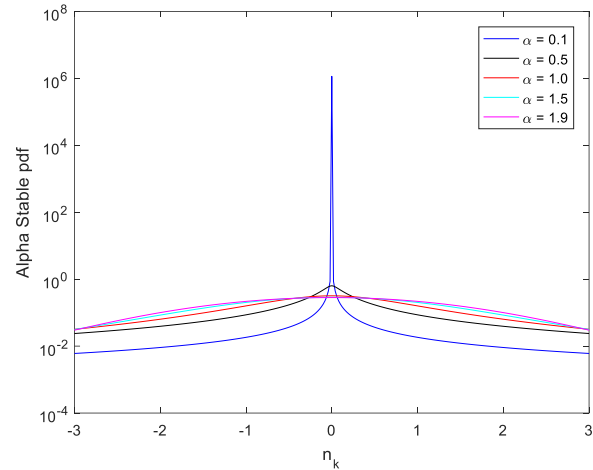


Fig. 16. Alpha stable pdf,  $\beta = 0$ ,  $\gamma = 1$  and  $\delta = 0$ .

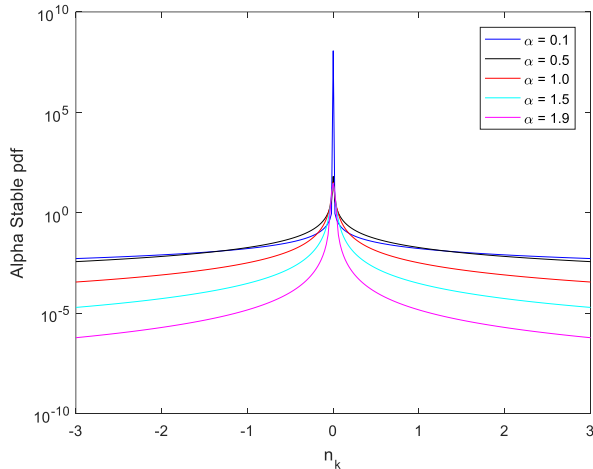


Fig. 14. Alpha stable pdf,  $\beta = 0$ ,  $\gamma = 0.01$  and  $\delta = 0$ .

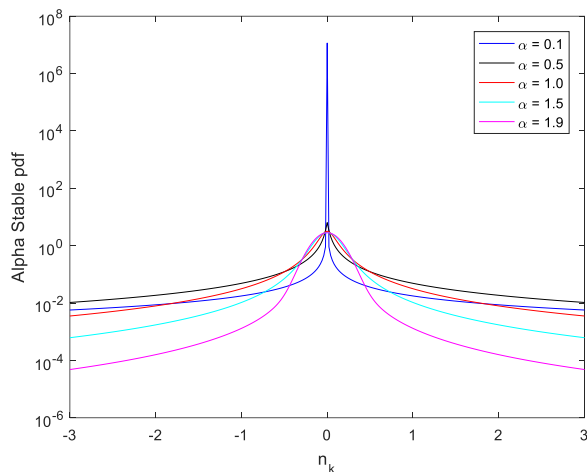


Fig. 15. Alpha stable pdf,  $\beta = 0$ ,  $\gamma = 0.1$  and  $\delta = 0$ .

IV. CONCLUSIONS

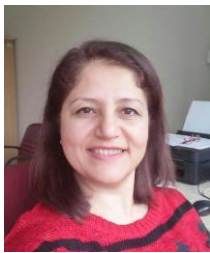
The three noise models, namely Middleton Class A, Bernoulli Gaussian and Alpha Stable models are used frequently in the literature for modeling the impulsive noise in PLC. In this study, we have investigated their probability density functions. Middleton Class A model has the advantage of selecting its parameters directly related to the physical channel. Further, the number of terms can be selected to be larger than two, which results with a more complicated but skilled model. It may model wider kind of data more precisely. Bernoulli Gaussian noise model is a multimodal distribution with two components. It can also model a wide range of data and its distribution is very close to Middleton Class A model, especially for heavy PLC impulsive noise case. Because of its simple form, Bernoulli Gaussian model can be preferable when calculation of analytic results is leading. Although it is not as powerful as the others, Alpha Stable model can also be used for impulse noise because of heavy tails. But it has a failure of having no closed form expression for its pdf. This is a handicap for analytic solutions.

REFERENCES

- [1] G. Laguna-Sanchez, M. Lopez-Guerrero, "On the use of Alpha-Stable distributions in noise modeling for PLC", IEEE Transactions on Power Delivery, Vol.30, No.4, 2015, pp.1863-1870.
- [2] T. Shongwe, A.J.H. Vinck, H.C. Ferreira, "A study on impulse noise and its models", SAIEE Africa Research Journal, Vol.106, No.3, 2015, pp.119-131.
- [3] H. Chaouche, F. Gauthier, A. Zeddou, M. Tlich, M. Machmoum, "Time domain modeling of powerline impulsive noise at its source", Journal of Electromagnetic Analysis and Applications, Vol.3, No.9, 2011, pp.359-367.
- [4] T. Guzel, E. Ustunel, H.B. Celebi, H. Delic, K. Mihcak, "Noise Modeling and OFDM Receiver Design in Power-Line Communication", IEEE Transactions on Power Delivery, Vol.26, No.4, 2011, pp.2735-2742.
- [5] Y. Himeur, A. Boukabou, "An adaptive recursive noise compensator for impulsive noise mitigation over OFDM power line communication", AEUE - International Journal of Electronics and Communications, Vol.70, No.1, 2016, pp.105-112.

- [6] G. Ndo, P. Siohan, M.H. Hamon, "Adaptive noise mitigation in impulsive environment: application to Power-Line Communications", *IEEE Transactions on Power Delivery*, Vol.25, No.2, 2010, pp.647-656.
- [7] J. Lin, M. Nassar, B.L. Evans, "Impulsive noise mitigation in Powerline Communications using Sparse Bayesian learning", *IEEE Journal on Selected Areas in Communications*, Vol.31, No.7, 2013, pp.1172-1183.
- [8] J.A. Cortes, A. Sanz, P. Estopinan, J.I. Garcia, "On the suitability of the Middleton class A noise model for Narrowband PLC", *International Symposium on Power Line Communications and its Applications*, 2016.
- [9] H. Meng, Y.L. Guan, S. Chen, "Modeling and analysis of noise effects on broadband power-line communications", *IEEE Transactions on Power Delivery*, Vol.20, No.2, 2005, pp.630-637.
- [10] F. Rouissi, H. Gassara, A. Ghazel, S. Najjar, "Comparative study of impulse noise models in the narrow band indoor PLC environment", *10th Workshop on Power Line Communications*, 2016.
- [11] Z. Zhang, Y. Sun, D. Wang, W. Xie, J. Liu, Y. Kuang, H. Ou, Q. Wang, Q. Lai, H.Y. Wang, B. Xu, Z. Liu, "Modeling and research of noise characteristics for low voltage Power Line Channel in OFDM communication system", *9th International Conference on Intelligent Human-Machine Systems and Cybernetics*, 2017, pp.116-120.
- [12] M. Katayama, T. Yamazato, H. Okada, "A mathematical model of noise in narrowband power line communication systems", *IEEE Journal on Selected Areas in Communications*, Vol.24, No.7, 2006, pp.1267-1276.
- [13] N. Andreadou, F.N. Pavlidou, "Modeling the noise on the OFDM Power-Line Communications system", *IEEE Transactions on Power Delivery*, Vol.25, No.1, 2010, pp.150-157.
- [14] F. Gianaroli, F. Pancaldi, G.M. Vitetta, "The impact of statistical noise modeling on the error-rate performance of OFDM Power-Line Communications", *IEEE Transactions on Power Delivery*, Vol.29, No.6, 2014, pp.2622-2630.
- [15] M.A. Sonmez, M.Bagriyanik, "Statistical model study for Narrowband Power Line Communication Noises", *8th International Conference on Electrical and Electronics Engineering*, 2013, pp.539-543.
- [16] K.M. Rabie, E. Alsusa, "Improved DPTE technique for impulsive noise mitigation over power-line communication channels", *AEUE International Journal of Electronics and Communications*, Vol.69, No.12, 2015, pp.1847-1853.

## BIOGRAPHIES



**SELVA MURATOĞLU ÇÜRÜK** received the B.S. degree from the Electrical and Electronics Engineering Department, Middle East Technical University (METU), Ankara, Turkey, in 1996, and the M.S. and Ph.D. degrees from the same university, in 1999 and 2008, respectively. She is currently at the Iskenderun Technical University.

Her research interests are wireless communication systems, digital communication theory, digital signal processing, multicarrier modulation and channel modeling.

# On the Extraction of Input and Output Impedance of PWM DC-DC Converters

F. ASADI, K. EGUCHI

**Abstract**— The buck, buck-boost and boost converter, are the most popular types of DC-DC converters. The input/output characteristics of these converters operating in Continuous Current Mode (CCM) is the object of considerations in this paper. The input impedance of converter helps the designer to select a suitable energy source for the converter. The internal impedance of selected input energy source must be quite lower than the input impedance of converter in order to avoid any voltage drop. The output impedance of DC-DC converters must be quite small in order to supply the load with high current demand. So, extraction of input/output characteristics of DC-DC converters is an important task and helps the designer to decide about the performance of system. Extraction of input/output characteristics is using pencil-and-paper analysis is quite tedious and error prone. This paper show how input/output impedance of DC-DC converters can extracted with the aid of MATLAB® programming. This paper can be used as a tutorial on the extraction of input/output impedance of DC-DC converters.

**Index Terms**— DC-DC converter, input impedance of DC-DC converters, output characteristics, Pulse Width Modulation (PWM).

## I. INTRODUCTION

The input impedance of a DC-DC converter is the impedance seen from the input DC source. The output impedance is defined as the output voltage response of converter for the excitation of current  $i_z$  at constant input voltage  $v_g$  and duty ratio  $D$ . In some descriptions, the output impedance includes the load conductance  $G$ , in other it does not.

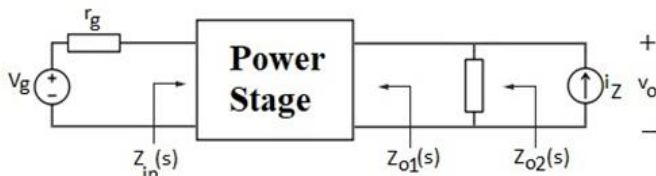


Fig. 1. Two variants of the output impedance of converter.

**FARZIN ASADI**, is with Department of Mechatronics Engineering, University of Kocaeli, Kocaeli, Turkey. (e-mail: [asadi.farzin@kocaeli.edu.tr](mailto:asadi.farzin@kocaeli.edu.tr)).

 <https://orcid.org/0000-0002-5928-0807>

**KEI EGUCHI**, is with Department of Information Electronics, Fukuoka Institute of Technology, Fukuoka, Japan. (e-mail: [eguti@fit.ac.jp](mailto:eguti@fit.ac.jp)).

 <https://orcid.org/0000-0002-1290-7975>

Manuscript received September 9, 2018; accepted March 28, 2019.  
DOI: [10.17694/bajece.468787](https://doi.org/10.17694/bajece.468787)

The input impedance of converter helps the designer to select the suitable input DC source. The input impedance of the converter must be much larger than the output impedance of the input DC source.

The output impedance of the converter is even more important than the input impedance. Output impedance must be as low as possible. Output impedance of the converter is especially important if the converter supplies a low-voltage, high-current load, with large values of output current slew rate. The most representative example of such a load is a processor in modern computer systems. The processor requires about  $1.0\text{ V}$  (or even less) and drawn current is typically over  $100\text{ A}$ . Current slew rates may approach  $300\frac{\text{A}}{\mu\text{s}}$  [1, 2]. According to the given numbers, the processor can be modelled as a  $10\text{ m}\Omega$  resistor (or lower). The output resistance of converter should be substantially lower than  $10\text{ m}\Omega$ , to ensure a good efficiency. Usually a buck converter is used to supply the processor. The output impedance of the buck converter supplying the processor (or other type of DC-DC converters) can be reduced with the aid of negative feedback. The relation between the open-loop output impedance ( $Z_{o,OL}$ ) and closed-loop output impedance ( $Z_{o,CL}$ ) is:

$$Z_{o,CL} = \frac{Z_{o,OL}}{1 + K_L} \quad (1)$$

where  $K_L$  is the loop gain [3, 4, 5].

The buck, buck-boost and boost converter, are the most popular types of converters. Their input/output characteristics are the object of considerations in this paper. A well-known reference such as [3] calculates the input/output impedance of converters for the ideal case only, i.e., a converter without parasitic element such as Equivalent Series Resistance (ESR) of capacitors/inductors. This paper extracts the input/output impedance in presence parasitic resistances.

The paper is organized as follows: The open-loop input/output impedance of buck, buck-boost and boost converters are derived with the aid of averaging and linearization in the second, third and fourth sections, respectively. The dependencies for averaged currents and voltages in converter are valid for low frequency range (i.e., below one-half of switching frequency). Finally, suitable conclusions are drawn.

## II. BUCK CONVERTER

Schematic of the PWM buck converter is shown in Fig. 2. The working principles of the buck converter can be found in standard text books such as [3] and [6].  $r_g, r_L$  and  $r_C$  show the

internal resistance of the input DC source, inductor ESR and capacitor ESR, respectively.

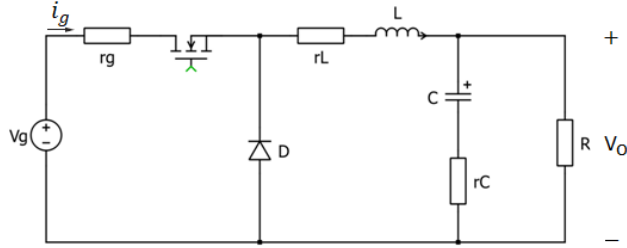


Fig. 2. Schematic of PWM buck converter.

When the MOSFET switch is closed, the diode is reverse-biased and the equivalent circuit of Fig. 3 applies.  $r_{ds}$  shows the MOSFET drain-source resistance.  $i_o$  is a fictitious current source added to the circuit in order to measure the output impedance ( $Z_o(s) = \frac{v_o(s)}{i_o(s)}$ ).

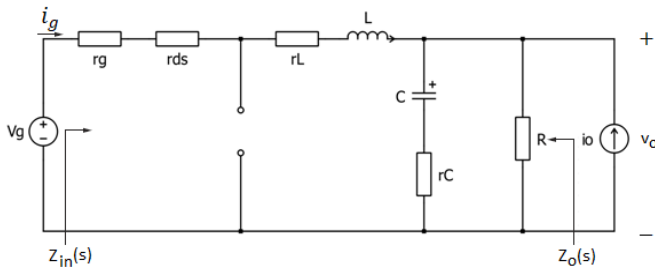


Fig. 3. Equivalent circuit of buck converter with closed MOSFET.

According to Fig. 3, the circuit differential equations can be written as:

$$\begin{cases} \frac{di_L(t)}{dt} = \frac{1}{L} \left( -\left( r_g + r_{ds} + r_L + \frac{R \times r_C}{R + r_C} \right) i_L - \frac{R}{R + r_C} v_C - \frac{R \times r_C}{R + r_C} i_o + v_g \right) \\ \frac{dv_C(t)}{dt} = \frac{1}{C} \left( \frac{R}{R + r_C} i_L - \frac{1}{R + r_C} v_C + \frac{R}{R + r_C} i_o \right) \end{cases} \quad (2)$$

$$i_g = i_L \quad (3)$$

$$v_o = r_C C \frac{dv_C}{dt} + v_C = \frac{R \times r_C}{R + r_C} i_L + \frac{R}{R + r_C} v_C + \frac{R \times r_C}{R + r_C} i_o \quad (4)$$

When the MOSFET is open, the diode becomes forward-biased to carry the inductor current and the equivalent circuit of Fig. 4 applies.  $r_D$  and  $V_D$  show the diode resistance and diode forward voltage drop, respectively.

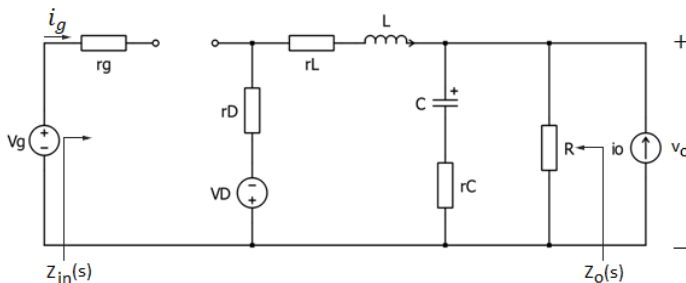


Fig. 4. Equivalent circuit of buck converter with open MOSFET.

According to Fig. 4, the circuit differential equations can be written as:

$$\frac{di_L(t)}{dt} = \frac{1}{L} \left( -\left( r_b + r_L + \frac{R \times r_C}{R + r_C} \right) i_L - \frac{R}{R + r_C} v_C - \frac{R \times r_C}{R + r_C} i_o - v_D \right) \quad (6)$$

$$\frac{dv_C(t)}{dt} = \frac{1}{C} \left( \frac{R}{R + r_C} i_L - \frac{1}{R + r_C} v_C + \frac{R}{R + r_C} i_o \right) \quad (7)$$

$$i_g = 0 \quad (8)$$

$$v_o = r_C C \frac{dv_C}{dt} + v_C = \frac{R \times r_C}{R + r_C} i_L + \frac{R}{R + r_C} v_C + \frac{R \times r_C}{R + r_C} i_o \quad (9)$$

State Space Averaging (SSA) is one of the most important tools to study the dynamics of converters operating in CCM. Foundation of SSA was laid down in [7] and later extended in [8, 9, 10], as well as many other publications. Theory of SSA has been studied in many text books for instance see [10] and [11].

SSA has two important steps: averaging and linearization. The SSA procedure can be summarized as follows [11]:

**Step 1-** Circuit differential equations are written for different working modes (i.e on/off state of semiconductor switches).

**Step 2-** Equations are time averaged over one period.

**Step 3-** Steady state operating points are calculated by equating the derivative terms to zero.

**Step 4-** The averaged equations are linearized around the steady state operating point found in the third step.

Applying the SSA to the Equations (2)-(9) leads to 6 different transfer functions:  $\frac{i_g(s)}{d(s)}$ ,  $\frac{i_g(s)}{v_g(s)}$ ,  $\frac{i_L(s)}{i_o(s)}$ ,  $\frac{v_o(s)}{d(s)}$ ,  $\frac{v_o(s)}{v_g(s)}$  and  $\frac{v_o(s)}{i_o(s)}$ . Open-loop input and output impedance of the converter is extracted with the aid of  $\frac{1}{i_g(s)}$  and  $\frac{v_o(s)}{i_o(s)}$ , respectively.

Applying the aforementioned steps manually is tedious and error prone (especially if the converter order is high). MATLAB® can be very helpful to do the mathematical machinery of SSA. The program shown in appendix (program 1) extracts the small signal transfer functions of a buck converter with component values as shown in Table 1.

Table I.

The buck converter parameters (see Fig. 2).

	Nominal Value
Output voltage, vo	20 V
Duty ratio, D	0.4
Input DC source voltage, Vg	50 V
Input DC source internal resistance, rg	0.01 Ω
MOSFET Drain-Source resistance, rds	40 mΩ
Capacitor, C	100 μF
Capacitor ESR, rC	0.05 Ω
Inductor, L	400 μH
Inductor ESR, rL	50 mΩ
Diode voltage drop, vD	0.7 V
Diode forward resistance, rD	10 mΩ
Load resistor, R	20 Ω
Switching Frequency, Fsw	20 kHz

The program gives the following results (OL sub script stands for Open Loop):

$$\frac{v_o(s)}{d(s)} = 6316.8 \frac{s + 2 \times 10^5}{s^2 + 813.4s + 2.503 \times 10^7} \quad (10)$$

$$Z_{in,ol}(s) = \frac{v_g(s)}{i_g(s)} = 0.0025 \frac{s^2 + 813.4s + 2.503 \times 10^7}{s + 498.8} \quad (11)$$

$$Z_{o,ol}(s) = \frac{v_o(s)}{i_o(s)} = 0.049875 \frac{(s + 2 \times 10^5)(s + 190)}{s^2 + 813.4s + 2.503 \times 10^7} \quad (12)$$

Bode diagram of control-to-output transfer function, open loop input impedance and open loop output impedance are shown in Fig. 5, 6 and 7, respectively.

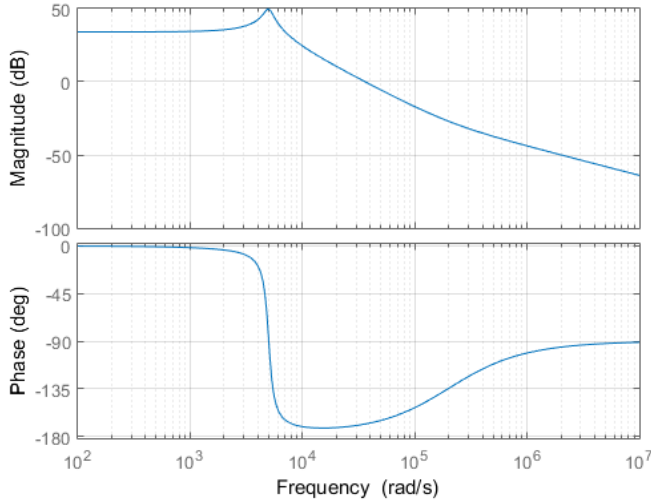


Fig. 5. Control-to-output transfer function of studied buck converter.

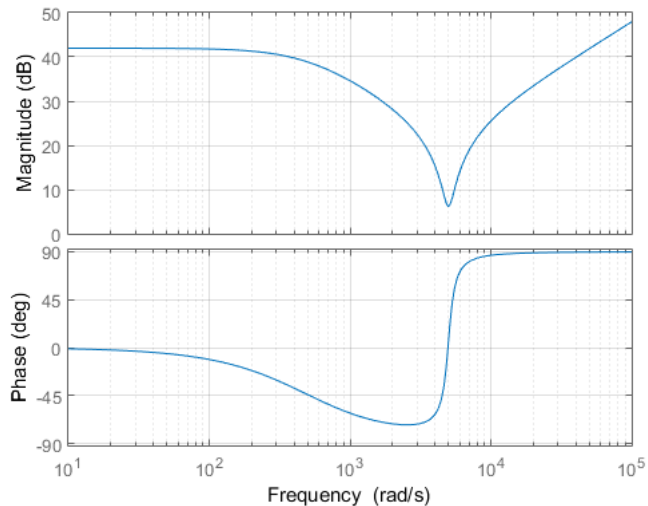


Fig. 6. Open loop input impedance of studied buck converter.

Fig. 7. Open loop output impedance of studied buck converter. The block diagram shown in Fig. 8 can be drawn for the studied buck converter. We want to study the effect of feedback on output impedance.

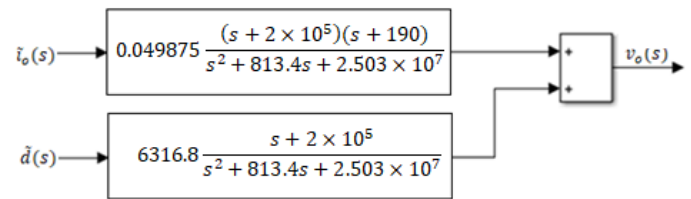
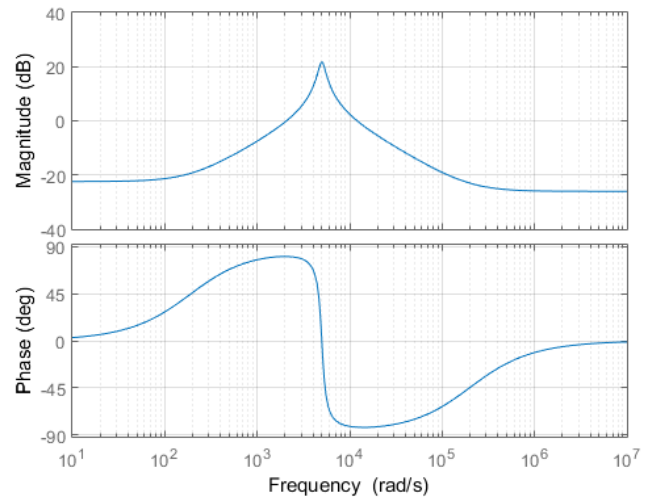


Fig. 8. Dynamical model of the studied buck converter. Input voltage variations are ignored. Consider a simple feedback loop as shown in Fig. 9.

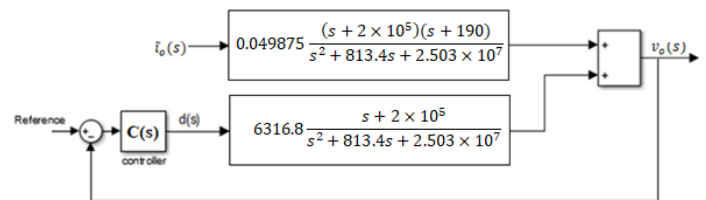


Fig. 9. Voltage Mode (VM) control of the studied buck converter.

Assume that the controller is a simple I-type controller ( $C(s) = \frac{4.85}{s}$ ). Fig. 10, shows the step response of the closed loop.

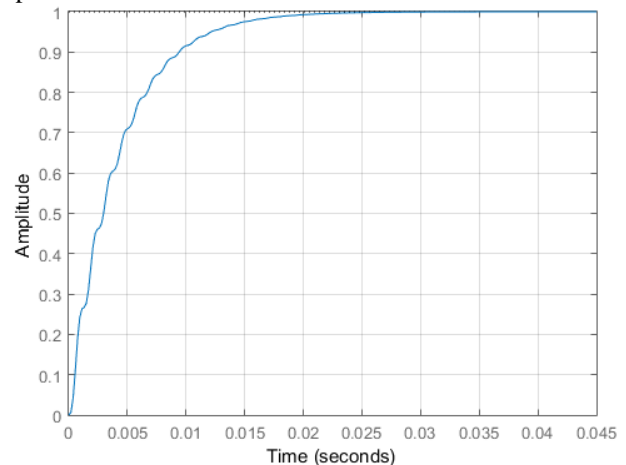


Fig. 10. Step response of closed-loop control system shown in Fig. 9 with  $C(s) = \frac{4.85}{s}$ .

According to Fig. 9, the closed loop output impedance ( $Z_{o,CL}(s)$ ) is:

$$Z_{o,CL}(s) = Z_{o,OL}(s) \times \frac{1}{1 + C(s) \times \frac{v_o(s)}{d(s)}} \quad (13)$$

$$Z_{o,CL}(s) = 0.049875 \times \frac{(s + 2 \times 10^5)(s + 190)}{s^2 + 813.4s + 2.503 \times 10^7} \times \frac{1}{1 + \frac{4.85 \times 6316.8 \times (s + 2 \times 10^5)}{s^2 + 813.4s + 2.503 \times 10^7}}$$

$$= \frac{0.04988s^5 + 10^4s^4 + 1.13 \times 10^7s^3 + 2.515 \times 10^{11}s^2 + 4.744 \times 10^{13}s}{s^5 + 1627s^4 + 5.075 \times 10^7s^3 + 4.687 \times 10^{10} + 6.323 \times 10^{14}s + 1.534 \times 10^{17}} \quad (14)$$

Fig. 11, is a comparison between the open-loop output impedance ( $Z_{o,OL}(s)$ , Equation (12)) and closed-loop output impedance ( $Z_{o,CL}(s)$ , Equation (14)). The closed loop output impedance is reduced at low frequency portion of the graph. Reduction of output impedance is one of the desired properties of feedback control.

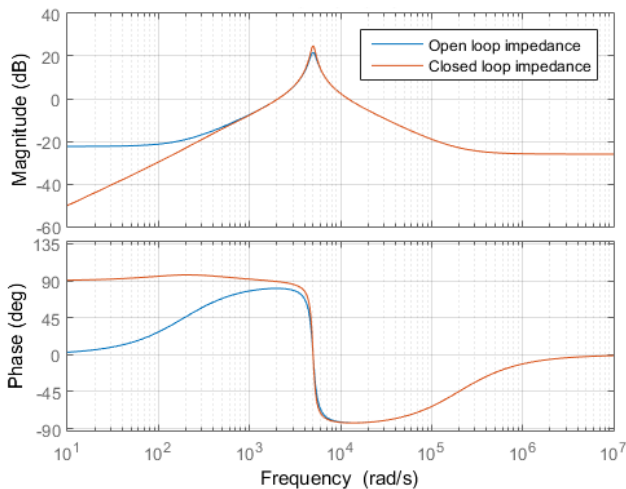


Fig. 11. Comparison of open-loop output impedance with closed-loop output impedance for the studied buck converter.

There are many efforts presented in the literature to achieve satisfactory output impedance of PWM DC-DC converters, especially buck type. The methods can be categorized into two groups:

- Sophisticated design of control loops in the converter [13, 14, 15, 16]
- Modifications of the basic structure of the power stage [17-18].

The starting point of the first method is the precise description of the converter, in particular the use of accurate formulas for open-loop output impedance. The program given in appendix can be helpful for this purpose [19].

### III. BUCK-BOOST CONVERTER

Schematic of the buck-boost converter is shown in Fig. 12.

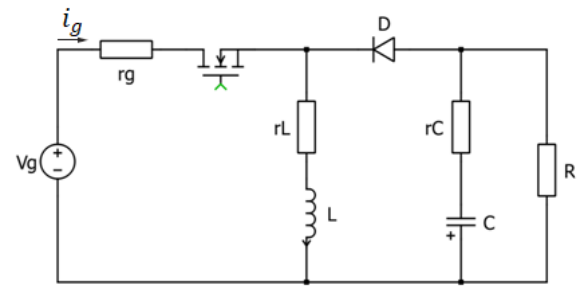


Fig. 12. Schematic of PWM buck-boost converter. When the MOSFET is closed, the diode is reverse biased.

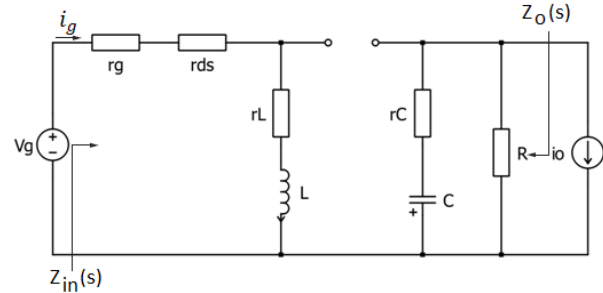


Fig. 13. Equivalent circuit of buck-boost converter with closed MOSFET.

According to Fig. 13, the circuit differential equations can be written as:

$$\left( \frac{di_L(t)}{dt} = \frac{1}{L} \left( -(r_g + r_{ds} + r_L) i_L + v_g \right) \right) \quad (15)$$

$$\left( \frac{dv_C(t)}{dt} = \frac{1}{C} \left( \frac{R}{R + r_C} i_o - \frac{1}{R + r_C} v_C \right) \right) \quad (16)$$

$$i_g = i_L \quad (17)$$

$$v_o = \frac{R}{R + r_C} v_C + \frac{R \times r_C}{R + r_C} i_o \quad (18)$$

When the MOSFET switch is opened, the diode becomes forward-biased.

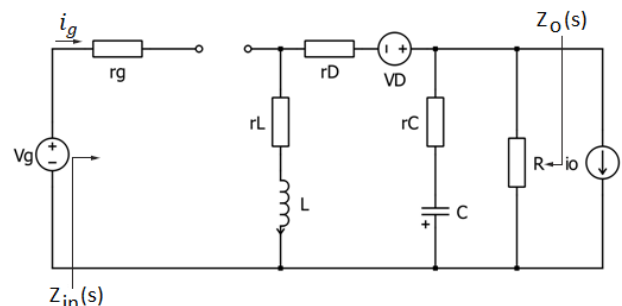


Fig. 14. Equivalent circuit of buck-boost converter with open MOSFET.

According to Fig. 14, the circuit differential equations can be written as:

$$\left( \frac{di_L(t)}{dt} = \frac{1}{L} \left( - \left( r_D + r_L + \frac{R \times r_C}{R + r_C} \right) i_L - \frac{R}{R + r_C} v_C - \frac{R \times r_C}{R + r_C} i_o - v_D \right) \right) \quad (19)$$

$$\left( \frac{dv_C(t)}{dt} = \frac{1}{C} \left( \frac{R}{R + r_C} i_L - \frac{1}{R + r_C} v_C + \frac{R}{R + r_C} i_o \right) \right) \quad (20)$$

$$i_g = 0 \quad (21)$$

$$v_o = \frac{R \times r_c}{R + r_c} i_L + \frac{R}{R + r_c} v_c + \frac{R \times r_c}{R + r_c} i_o + V_D \quad (22)$$

The program shown in appendix (program 2) extracts the small signal transfer functions of a buck-boost converter with component values as shown in Table 2.

Table II.

The buck-boost converter parameters (see Fig. 12).

	Nominal Value
Output voltage, $v_o$	-16 V
Duty ratio, D	0.4
Input DC source voltage, $V_g$	24 V
Input DC source internal resistance, $r_g$	0.1 $\Omega$
MOSFET Drain-Source resistance, $r_{ds}$	40 m $\Omega$
Capacitor, C	80 $\mu$ F
Capacitor ESR, $r_c$	0.05 $\Omega$
Inductor, L	20 $\mu$ H
Inductor ESR, $r_L$	10 m $\Omega$
Diode voltage drop, $v_D$	0.7 V
Diode forward resistance, $r_D$	10 m $\Omega$
Load resistor, R	5 $\Omega$
Switching Frequency, $F_{sw}$	100 kHz

The program gives the following results:

$$\frac{v_o(s)}{d(s)} = -0.94123 \frac{(s + 1.267 \times 10^5)(s - 1.168 \times 10^5)}{s^2 + 7560s + 2.332 \times 10^8} \quad (23)$$

$$Z_{in}(s) = \frac{v_g(s)}{i_g(s)} = 0.000125 \frac{s^2 + 7560s + 2.332 \times 10^8}{s + 2475} \quad (24)$$

$$Z_o(s) = \frac{v_o(s)}{i_o(s)} = 0.049505 \frac{(s + 2.5 \times 10^5)(s + 4194)}{s^2 + 7560s + 2.332 \times 10^8} \quad (25)$$

Bode diagram of control-to-output transfer function, open loop input impedance and open loop output impedance are shown in Fig. 15, 16 and 17, respectively.

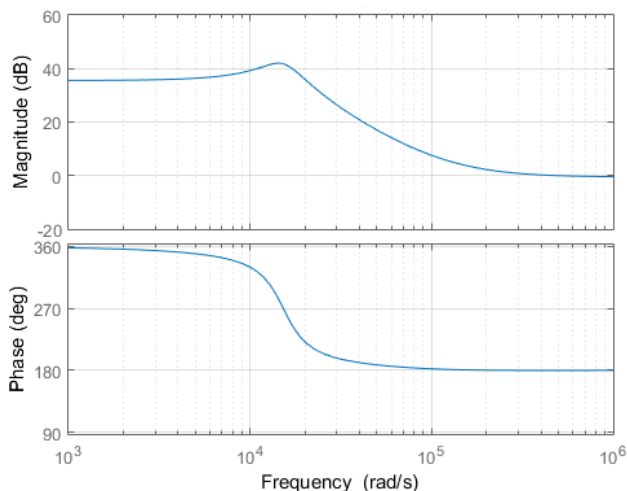


Fig. 15. Control-to-output transfer function of studied buck-boost converter.

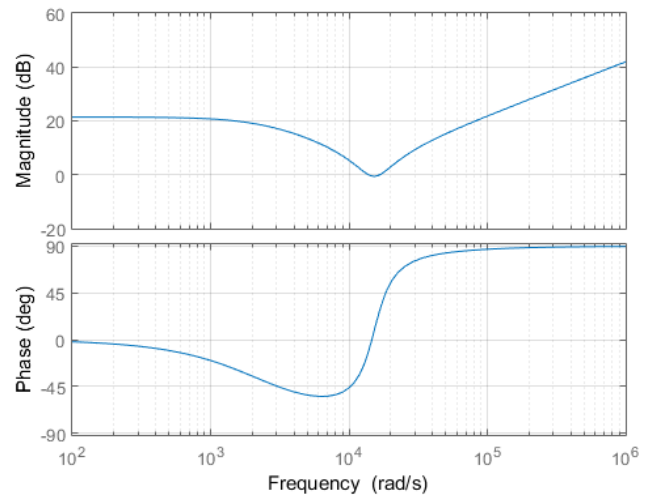


Fig. 16. Open loop input impedance of studied buck-boost converter.

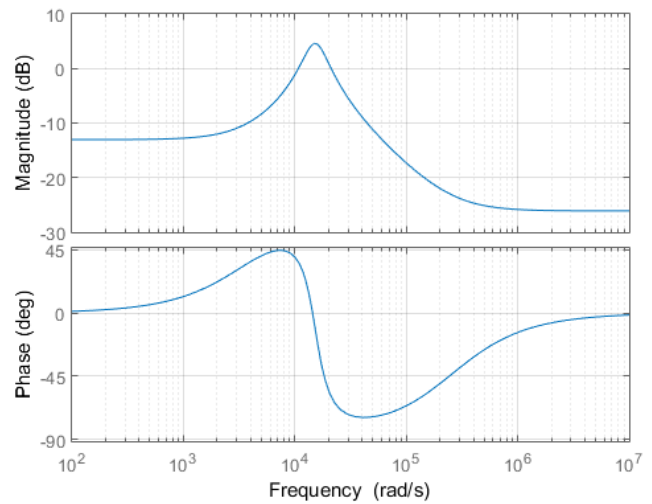


Fig. 17. Open loop output impedance of studied buck-boost converter.

#### IV. BOOST CONVERTER

Schematic of boost converter is shown in Fig. 18.

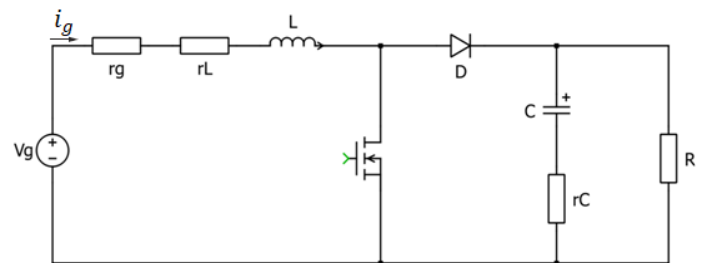


Fig. 18. Schematic of PWM boost converter.

When the MOSFET is closed, the diode is reverse biased.

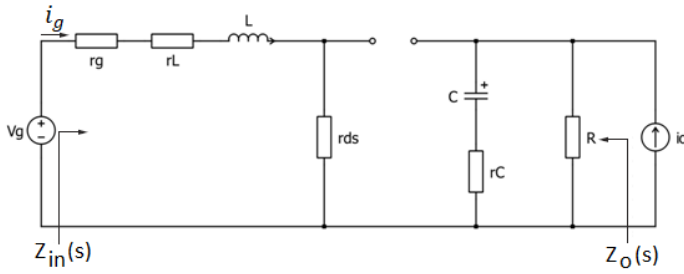


Fig. 19. Equivalent circuit of boost converter with closed MOSFET.

According to Fig. 19, the circuit differential equations can be written as:

$$\frac{di_L(t)}{dt} = \frac{1}{L}(-r_g + r_{ds} + r_L)i_L + v_g \quad (26)$$

$$\frac{dv_C(t)}{dt} = \frac{1}{C}\left(-\frac{1}{R+r_C}v_C + \frac{R}{R+r_C}i_o\right) \quad (27)$$

$$i_g = i_L \quad (28)$$

$$v_o = \frac{R}{R+r_C}v_C + \frac{R \times r_C}{R+r_C}i_o \quad (29)$$

When the MOSFET switch is opened, the diode becomes forward-biased. Fig. 20, shows the equivalent circuit for this case.

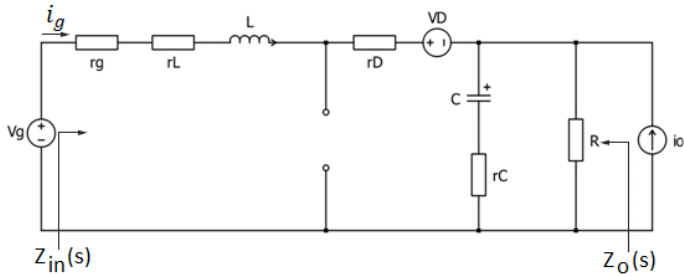


Fig. 20. Equivalent circuit of boost converter with open MOSFET.

According to Fig. 20, the circuit differential equations can be written as:

$$\frac{di_L(t)}{dt} = \frac{1}{L}\left(-\left(r_g + r_L + r_D + \frac{R \times r_C}{R+r_C}\right)i_L - \frac{R}{R+r_C}v_C - \frac{R \times r_C}{R+r_C}i_o + v_g - v_D\right) \quad (30)$$

$$\frac{dv_C(t)}{dt} = \frac{1}{C}\left(\frac{R}{R+r_C}i_L - \frac{1}{R+r_C}v_C + \frac{R}{R+r_C}i_o\right) \quad (31)$$

$$i_g = i_L \quad (32)$$

$$v_o = \frac{R \times r_C}{R+r_C}i_L + \frac{R}{R+r_C}v_C + \frac{R \times r_C}{R+r_C}i_o \quad (33)$$

The program shown in appendix (program 3) extracts the small signal transfer functions of a boost converter with component values as shown in Table 3. Switching Frequency is 25 kHz.

Table III. The boost converter parameters (see Fig. 18).

	Nominal Value
Output voltage, vo	30 V
Duty ratio, D	0.6
Input DC source voltage, Vg	12 V
Input DC source internal resistance, rg	0.1 Ω
MOSFET Drain-Source resistance, rds	40 mΩ
Capacitor, C	100 μF
Capacitor ESR, rC	0.05 Ω
Inductor, L	120 μH
Inductor ESR, rL	10 mΩ
Diode voltage drop, vD	0.7 V
Diode forward resistance, rD	10 mΩ
Load resistor, R	50 Ω

The program gives the following results:

$$\frac{v_o(s)}{d(s)} = -0.007199 \frac{(s + 2 \times 10^6)(s - 6.703 \times 10^4)}{s^2 + 1367s + 1.356 \times 10^7} \quad (34)$$

$$Z_{in}(s) = \frac{v_g(s)}{i_g(s)} = 0.00012 \frac{s^2 + 1367s + 1.356 \times 10^7}{s + 200} \quad (35)$$

$$Z_o(s) = \frac{v_o(s)}{i_o(s)} = 0.049995 \frac{(s + 2 \times 10^6)(s + 1160)}{s^2 + 1367s + 1.356 \times 10^7} \quad (36)$$

Bode diagram of control-to-output transfer function, open loop input impedance and open loop output impedance are shown in Fig. 21, 22 and 23, respectively.

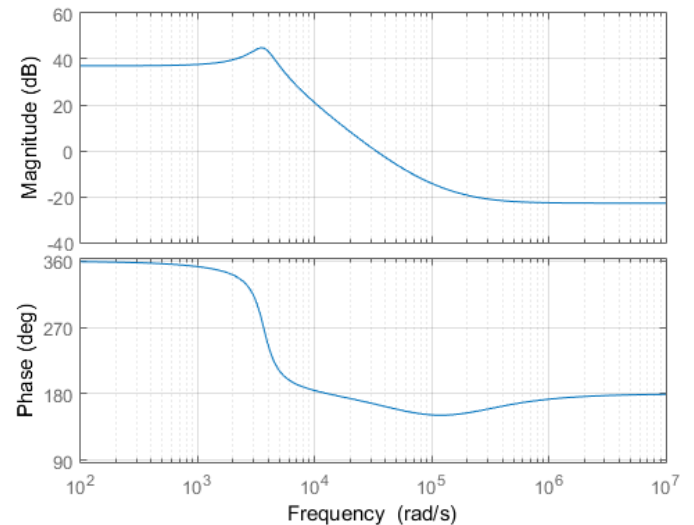


Fig. 21. Control-to-output transfer function of studied boost converter

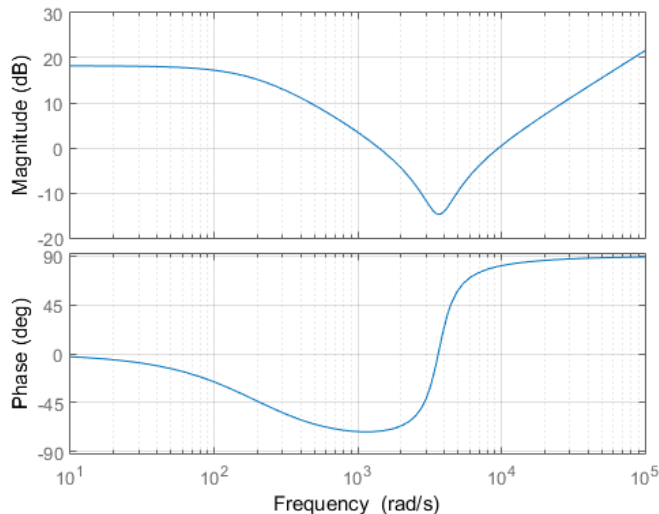


Fig. 22. Open loop input impedance of studied boost converter.

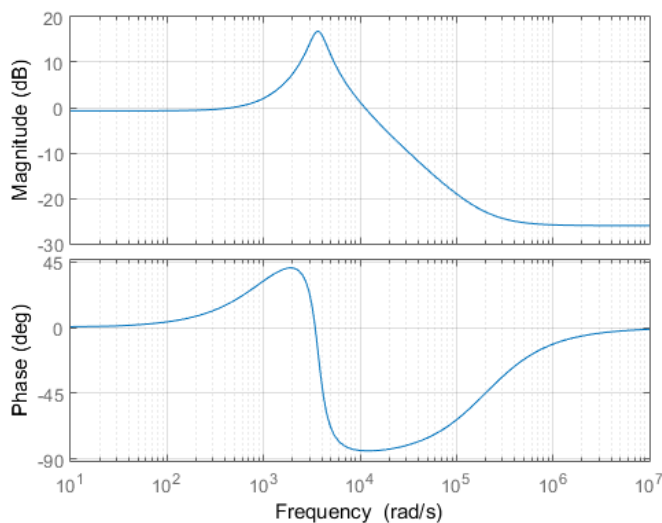


Fig. 23. Open loop output impedance of studied boost converter.

The programs given in appendix calculates the steady state operating point of the converters as well. The steady state operating point for studied boost converter is  $I_L = 1.438 \text{ A}$  and  $V_C = 28.76 \text{ V}$ .  $I_L$  and  $V_C$  show the average inductor current and average capacitor voltage, respectively.

The average current drawn from the input DC source is the same as the average current of inductor. So, the input DC source sees the converter as a  $\frac{12 \text{ V}}{1.438 \text{ A}} = 8.35 \Omega$  load. If we substitute  $s = 0$  in the Equation (35), we obtain the  $8.15 \Omega$  which is quite close to the expected value. The DC gain of obtained input impedance (at  $s = 0$ ) can be checked in a similar way for other type of converters.

## V. CONCLUSION

Input/output characteristics of DC-DC converters are important parameters. The input impedance helps the designer to select the suitable input source. The output impedance of the converter shows whether the converter can supply the output load successfully or not.

This paper studied the input/output characteristics of buck, buck-boost and boost converters. MATLAB programming is used to do the mathematical machinery. Input/output characteristics of other types of converters can be extracted in a similar way shown in the paper. The control to output transfer function of power electronics converters is used to design the control loop of converter. The Buck converter has a minimum phase control to output transfer function while the Boost and Buck-Boost converters have non-minimum phase control to output transfer functions. The feedback control of power converters affect the output impedance of converter. The output impedance of converter decreases with the aid of feedback control as shown in the second section of paper.

## REFERENCES

- [1] Voltage Regulator Module (VRM) and Enterprise Voltage Regulator-Down (EVRD), 11.1 Design Guidelines, Intel Corp.,2009.
- [2] R.P. Singh and A.M. Khambadkone, "A Buck-derived topology with improved step-down transient response", IEEE Trans. on Power Electronics 23 (6), 2855–2866 (2008).
- [3] R.W. Erickson and D. Maksimovic, Fundamentals of Power Electronics, 2-nd Ed., Kluwer, Berlin, 2002.
- [4] K. Yao, M. Xu, Y. Meng, and F.C. Lee, "Design considerations for VRM transient response based on the output impedance", IEEE Trans. on Power Electronics 18 (6), 1270–1277 (2003).
- [5] R. Ahmadi, D. Paschedag, and M. Ferdowsi, "Closed loop input and output impedances of DC-DC switching converters operating in voltage and current mode control", IECON 36-th Annual Conf. IEEE Industrial Electronic Society 1, 2311–2316 (2010).
- [6] M.K. Kazimierzczuk, Pulse-Width Modulated DC – DC Power Converters, J. Wiley, London, 2008.
- [7] Middlebrook RD, Cuk S. A general unified approach to modeling switching-converter power stages. Int. J. Electronics Theoretical and Experimental.1977.p. 521–550.
- [8] Tymerski R, Vorperian V. Generation, classification and analysis of switched-mode DC-DC converters by the use of converter cells. Telecommunications Energy Conference. 1986. p. 181-195.
- [9] Chen J, Ngo K.D.T. Alternate forms of the PWM switch model in discontinuous conduction mode. IEEE Trans. Aerosp. Electron. Syst. 2001.p. 754-758.
- [10] Sun J, Mitchell DM, Greuel MF, Krein PT, Bass RM. Average modeling of PWM converters in discontinuous modes. IEEE Trans. Power Electron. 2001.p. 482–492.

- [11] Asadi F, Eguchi K. Dynamics and control of DC-DC converters, San Rafael: Morgan and Claypool; 2018. p. 89-145.
- [12] Suntio T. Dynamic profile of switched mode converter: modeling, analysis and control. New Jersey: John Wiley & Sons. 2009. p. 17-37.
- [13] D. Chen, F.C. Lee, and S.J. Chen, "Evaluation of various Adaptive Voltage Positioning (AVP) schemes for computer power sources", J. Chinese Institution of Engineers 30 (7), 1137-1143 (2007).
- [14] M. Lee, D.C. Huang, K. Chih-Wen, and L. Ben Tai, "Modeling and design for a novel adaptive voltage positioning (AVP) scheme for multiphase VRM", IEEE Trans. on Power Electronics 23 (4), 1733-1742 (2008).
- [15] S. Xiao, W. Qiu, G. Miller, T.X. Wu, and I. Batarseh, "Adaptive modulation control for multiple-phase voltage regulators", IEEE Trans. on Power Electronics 23 (1), 495-499 (2008).
- [16] J.A. Qahouq and V.P. Arikatla, "Power converter with digital sensorless adaptive voltage positioning control scheme", IEEE Trans. on Industrial Electronics 58 (9), 4105-4116 (2011).
- [17] R.P. Singh and A.M. Khambadkone, "A Buck-derived topology with improved step-down transient response", IEEE Trans. on Power Electronics 23 (6), 2855-2866 (2008).
- [18] Y. Birbir, and M. Yilmaz. "Optimal Speed Application on the Universal Motor by Means of Microcontroller." WSEAS Transactions on Power Systems 1.11 (2006): 1903.
- [19] M.E. Asker, and H. Kilic. "Modulation Index and Switching Frequency Effect on Symmetric Regular Sampled SPWM." European Journal of Technique 7.2 (2017): 102-109.

ICICIC2017 Best Paper Award, ICICIC2016 Best Paper Award, ICEEI2016 Excellent Oral Presentation Award, ICIAE2016 Best Presentation Award, ICEESE2016 Best Presenter Award, ICIAE2015 Best Presentation Award, ICPEE2014 Excellent Oral Presentation Award, iCABSE2014 Excellent Paper Award, KKU-IENC2014 Outstanding Paper Award, ICEEN2014 Excellent Paper Award, JTL-AEME2013 Best Paper Award, ICTEEP2013 Best Session Paper Award, 2010 Takayanagi Research Encourage Award, 2010 Paper Award of Japan Society of Technology Education, ICICIC2009 Best Paper Award, and ICINIS2009 Outstanding Contribution Award. He is a senior member of IEEJ and a member of INASS, and JSTE. His research interests include nonlinear dynamical systems, intelligent circuits and systems, and low-voltage analog integrated circuits.

## BIOGRAPHIES



**FARZIN ASADI** is with the Department of Mechatronics Engineering at the Kocaeli University, Kocaeli, Turkey. He has published 30 international papers and 10 books. He is on the editorial board of 6 scientific journals as well. His research interests include switching converters, control theory, robust control of power electronics converters, and robotics.



**KEI EGUCHI** is with the Department of Information Electronics at the Fukuoka Institute of Technology, Fukuoka, Japan. He received ICICIC2018 Best Paper Award, IETNR-18 Oral Best Paper Award,

# Adaptive Notch Filter Bank Based Power Quality Analysis of an Ultra-High Frequency Induction Heating System

M. TAŞTAN

**Abstract**— Widespread use of the semiconductor switching elements of power electronics in energy systems has brought about various power quality problems. One of these significant power quality problems is the harmonics, which occur in power systems. Harmonics are generated predominantly by induction systems, arc furnaces, welding machines, static frequency converters and motor converter drivers. In this study, a power quality analysis is proposed with a Phase-Locked Loop (PLL) based Digital Adaptive Notch Filter (ANF) for the 900 KHz Ultra-High Frequency Induction Heating System (UHFIHS), which is widely used in the industry. In this proposed method, firstly the power signal is synchronized with the fundamental frequency using PLL, and then the harmonic frequency components of the signal is obtained by the ANF. Finally, challenging factors behind the harmonic analysis, such as fundamental frequency shifting, spectral leakage and leakage effect are eliminated and thus a precise and reliable power quality analysis is conducted.

**Index Terms**— power quality, power system harmonics, phase locked loops, adaptive filter, electromagnetic induction.

## I. INTRODUCTION

THE RESPONSIBILITY of institutions that produce, transfer and distribute electric power, which is one of the most significant energy sources, is to ensure uninterrupted, economical, quality and highly reliable delivery of energy to the consumers. Certain devices which are connected to energy systems, and especially those with semiconductor switching elements, such as induction heating systems, arc furnaces, welding machines, static frequency converters and motor converter drivers, cause a variety of problems like shortening in the lifetime, voltage fluctuations, flickers, and more importantly, harmonics [1], [2].

Induction heating systems are normally used for fast heating applications of magnetic materials. These systems are also used for various other purposes, such as forging, melting,

hardening, sintering and welding. Induction is one of the fastest heating systems in today's technology [3]. It has already been identified that heat treatment processes which are carried out with the UHFIHS is more cost-efficient than the other practices [4]. Moreover, the treatments carried out with the UHFIHS is faster than those performed with conventional heating systems [5]. Fast Fourier Transformation (FFT) [6], [7], [8] is widely used in harmonic analysis due to its efficiency in measurement. However, certain factors such as the incorrect selected sampling window, frequency resolution that is restricted by the windowing function and fundamental frequency deviation may result in aliasing, spectral leakage, and picket-fence effect [9], [10], [11]. All these problems cause errors in measurements of the harmonic analysis. In addition to the methods based on the Fourier Transformation, the Prony Method [12], [13], ESPRIT [14], PLL-based Methods [15], Kalman Filter [16], [17], ANN Analysis [18], Wavelet Transform Method [19], ANF [20] and similar others are also commonly used in harmonic analysis. Errors in calculation of fundamental frequency values in harmonic analyses, which are performed for non-linear loads such as induction and arc furnaces [21], result in imprecision in harmonic frequency components as well. Miscalculated fundamental frequency may cause the emergence of interharmonics, which do not exist in the signal under normal conditions. For this reason, there are a number of different methods in use to ensure proper calculation of fundamental frequency or synchronization with the fundamental frequency. PLL is among the most common methods used for this purpose. In addition, the software based PLL structure used in the proposed method is proven to be superior to the other PLL structures [22]. In this study, current and voltage data are collected for heat treatments performed with a 900 KHz induction heating system with 2.8 kW power. With the PLL based digital ANF proposed for this study, the frequency and amplitude value of each harmonic component is separately calculated and the power quality analysis of the UHFIHS is performed with a high level of reliability.

The main contributions of this paper are as follows:

- The study shows that induction heating systems cause a high amount of harmonic distortion.
- The spectral leakage effect caused by the interharmonics is prevented and it makes harmonic calculation with great accuracy.

M. TAŞTAN, is with Department of Electronic and Automation University of Manisa Celal Bayar, Turgutlu, Manisa, Turkey, (e-mail: [mehmet.tastan@cbu.edu.tr](mailto:mehmet.tastan@cbu.edu.tr)).

 <https://orcid.org/0000-0002-2306-6008>

Manuscript received December 16, 2018; accepted Feb 26, 2019.

DOI: [10.17694/bajece.498021](https://doi.org/10.17694/bajece.498021)

II. PROPOSED METHOD

Estimation of the fundamental frequency is critical for harmonic analysis. Even a minor deviation in fundamental frequency estimation may cause significant calculation errors in results of the analysis. PLL is a closed-loop servo system, which continuously tracks the output signal in order to minimize phase errors between the input and the output signals. PLL aims to lock the frequency and phase of the feedback signal,  $x(k)$ , to the phase and frequency of the input signal,  $V(t)$ . The used PLL structure is identical to the PLL structure developed in [22]. The structure of the proposed

software-based PLL is given in Fig.1. This PLL structure consists of four blocks, namely, Phase Detector (PD), Frequency Divider (FD), PI and Voltage-Controlled Oscillator (VCO). The proposed PLL's superiority over the other structures widely used in the literature, such as EPLL [23] and pPLL [24], and its success against certain disturbances such as phase shifting, amplitude changing and multizero crossing, are proven as it is revealed by the real-time experiments given in [25].

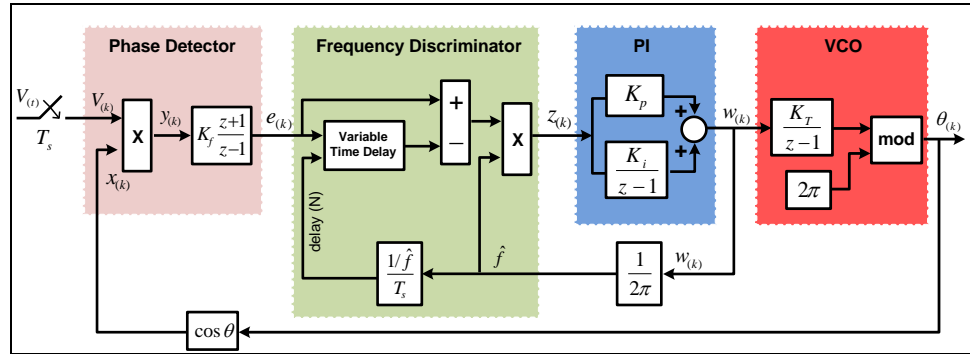


Fig.1. The Phase-Locked Loop (PLL) Block Diagram

PLL locks up the fundamental component ( $\omega_0$ ) of the power signal in input, and generates the signals specified as integer power of  $\omega_0$ , which are  $\sin\omega_0, \sin2\omega_0, \sin3\omega_0, \dots, \sin n\omega_0, \cos\omega_0, \cos2\omega_0, \cos3\omega_0, \dots, \cos n\omega_0$  in output. Changes in fundamental frequency of the power sign are tracked by the PLL's digital tracker sensitively. Frequencies of  $\sin n\omega_0/\cos n\omega_0$  generated by the PLL can track changes in

fundamental frequency even under other disturbances than the harmonics. The discrete-time transfer function for the notch filter proposed in this study and the frequency response analysis are given in [22]. In parallel with the block diagram given in Fig.2, the transfer function of the notch filter which damps the angular frequency,  $\omega_0$ , is shown in Equation 1 below:

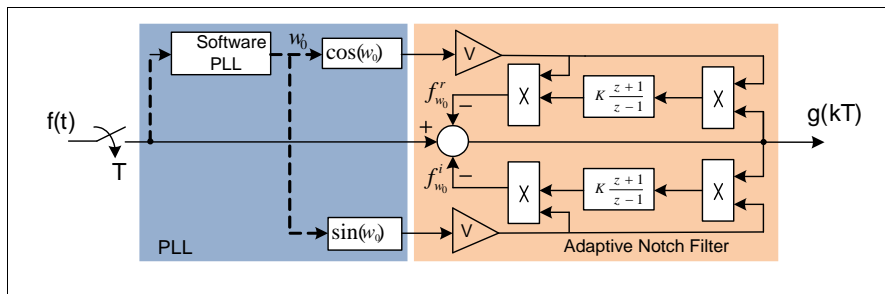


Fig.2. Digital Adaptive Notch Filter Block Diagram

$$H(e^{j\omega T}) = \frac{\cos\omega_\Delta T + jsin\omega_\Delta T - 1}{\{1 + 2KV^2\}\{\cos\omega_\Delta T + jsin\omega_\Delta T\} + 2KV^2 - 1} \quad (1)$$

where T is the sampling time,  $\omega_0$  is the angular frequency of the reference signal for  $\omega_\Delta = \omega - \omega_0$ ,  $\omega$  is the angular frequency of the signal  $f(t)$ , V is the amplitude of  $\sin\omega_0$  and  $\cos\omega_0$  reference signals, and K represents the integrator factor. According to Equation 1,  $|H(e^{j\omega T})| = 0$  is the equation for the angular frequency  $\omega = \omega_0$  in  $f(t)$  input signal. This means that the  $\omega_0$  component in  $f(t)$  signal is suppressed in the output. The filter bandwidth is not affected by peripheral

factors. The equation for the bandwidth is  $BW = V^2K$ , and the value of bandwidth can be altered by changing V and K values. Keeping the bandwidth in a short range prevents leakage of interharmonics, particularly those close to harmonic frequency components. Experimental studies for disturbances such as phase shifting, frequency deviation, multizero crossing and voltage sag, which emerge either separately or simultaneously, have proven that the proposed ANF is highly efficient in each of these situations [25]. As it is seen in Fig.3, the structure of the proposed method for power quality analysis consists of a software-based PLL and a digital

ANF.  $X(t)$ , which is applied as an input to the software-based interharmonic distortions, frequency deviation, change in amplitude values, phase shifting and multizero crossing, in addition to the harmonics. The ANF bank is composed of number “n” of adaptive notch filters with adjustable suppression frequency. In this study, 25 notch filters are used in total until the 25th harmonic. In each ANF, relevant components of the input signal,  $(\omega_0, \omega_1, \dots, \omega_n)$ , are suppressed. The  $n\omega_0/\cos n\omega_0$  signal frequencies, which are applied to the

PLL, may include different disturbances such as notch filter, are also used as the notch filter's suppression frequency. When the fundamental frequency of the signal applied to the notch filter input changes, the suppression frequency also changes. In each filter output, the components of the input signal,  $A_n \sin n\omega_0 / B_n \cos n\omega_0$  are suppressed. When the input signal of each filter output is subtracted from  $x(t)$ , the frequency component  $(\omega_n)$ , which is suppressed by the notch filter, is obtained.

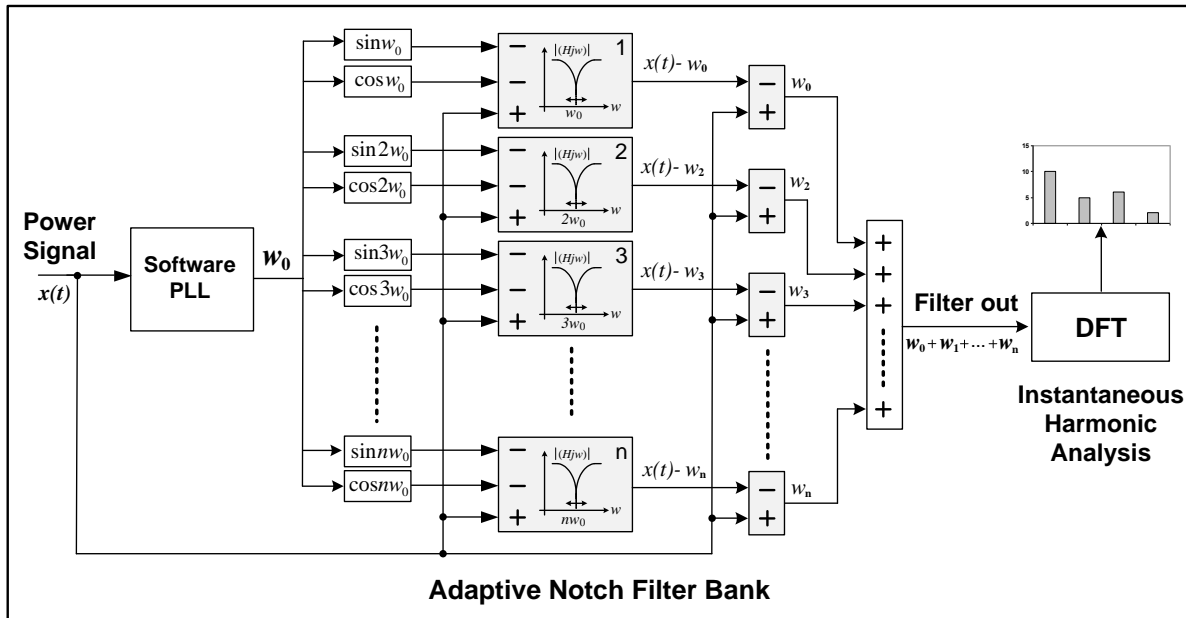


Fig.3. Structure of the PLL Based Adaptive Notch Filter Bank

In this way, each filter produces proper outputs without the impact of interharmonics or other disturbances. The sum total of all notch filter outputs gives the total value of harmonic signals that exist in the input signal. This signal, which is the sum total of the harmonics obtained in the ANF output, is subjected to a DFT calculation in accordance with the IEC standards. In this way, the amplitude values, phase angles and frequencies of the harmonics in the signal can separately be calculated in a more precise and accurate way.

### III. EXPERIMENTAL RESULTS

The current and voltage data of the experimental studies are recorded by the LabVIEW™ 8.5 graphical interface creator over the National Instruments PCI 6221 data acquisition card, with a sampling frequency equal to  $f_s=5000$  samples/s. The process is performed in accordance with the IEC 61000-4-30 and IEC 62053-21 standards. Fig.4 shows the visual front panel of the LabVIEW™ based measurement system.

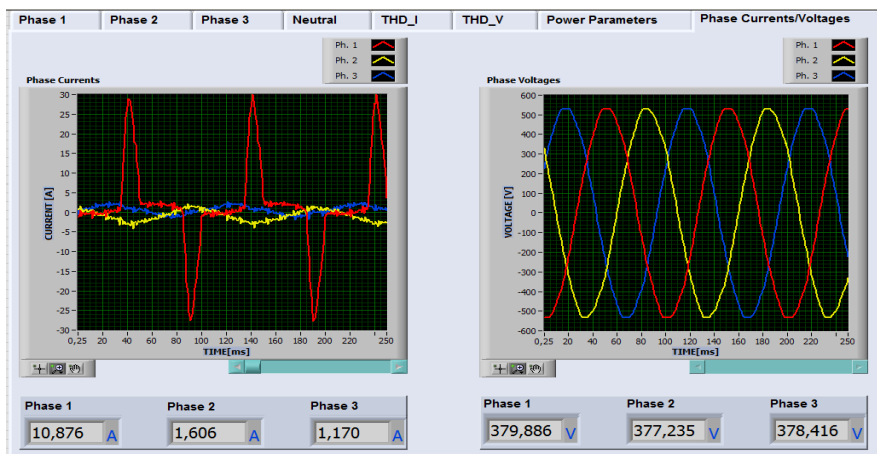


Fig.4. Front panel of the LabVIEW™ based measurement system.

Fig.5 shows the block structure of the data acquisition system. The data obtained through this data acquisition system is filtered by passing through the PLL based ANF bank, which is prepared in MATLAB/Simulink. The fundamental frequency component,  $(\omega_0)$ , and the signal that represents the total sum

of harmonics,  $(\omega_0+\omega_1 + \dots + \omega_n)$ , are subjected to the DFT analysis in accordance with the IEC 61000-4-7 standards. The amplitude values of the fundamental component and the harmonic components are obtained as a result of this analysis.

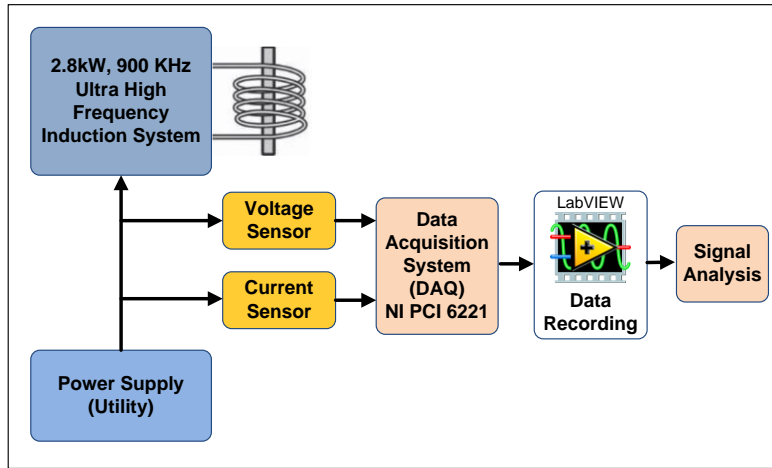


Fig.5. LabVIEW™ Based Data Acquisition System

Following the calculation of amplitude values of aforementioned components, values of other harmonic components are calculated taking the fundamental component as 1 Pu. The Total Harmonic Distortion (THD) is measured with the formula given in Equation 2. The Total Harmonic Distortion of the current is calculated with the equation below; Where;

$$[THD]_I(\%) = 100x \frac{\sqrt{\sum_{h=2}^{\infty} I_h^2}}{I_1} \tag{2}$$

- [THD]<sub>I</sub> : Total Harmonic Distortion of the current,
- I<sub>h</sub> : Effective value of n. order of harmonic in the load current,
- I<sub>1</sub> : Effective value of the load current in the fundamental frequency,
- h : Harmonic order.

Total harmonic distortion for the current can also be explained as the ratio of the active value of harmonic components to the active value of the fundamental component.

Coefficients of the software-based PLL and ANF used in the proposed method are given in Table 1.

TABLE I  
PLL AND ADAPTIVE NOTCH FILTER COEFFICIENTS

PLL		Adaptive Filter	
Coefficient	Value	Coefficient	Value
K <sub>i</sub>	1800	k <sub>i</sub>	0.0085
K <sub>p</sub>	60	k <sub>v</sub>	0.125
K <sub>t</sub>	1.0	T <sub>s</sub>	50µs
T <sub>s</sub>	50µs		

The analysis of this power signal, which involves the fundamental component and harmonic components obtained in the filter output, is conducted with the DFT method suggested by IEC. The DFT analysis took N=1000 samples as the reference for t=0.2s, and used T=10/f windows with 5 Hz resolution for f=50 Hz, as suggested in IEC 61000-4-7.

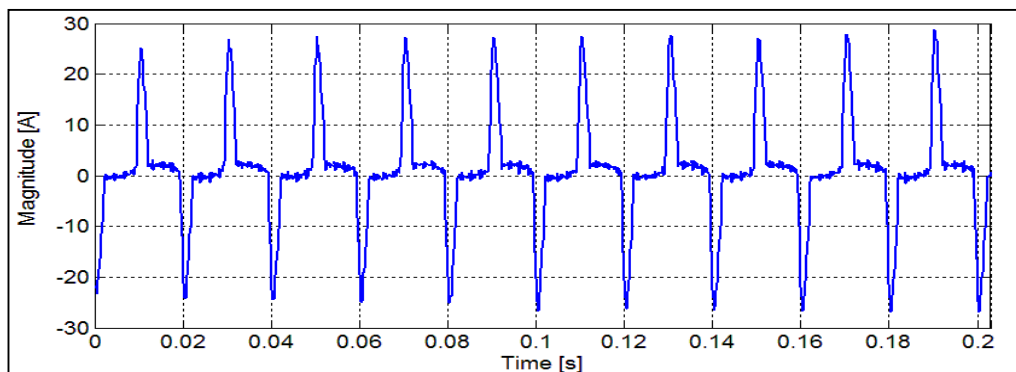


Fig.6. t=0.2s Induction System Current Signal

Fig.6 shows the sampling frequency current signal ( $f_s=5000$ ) of a heat treatment taken from the induction system. This current signal has 10 periods and  $T=0.2s$  sampling time, as

required for DFT analysis. It is seen in its structure that the signal includes a large number of harmonic components in a position far from the sinusoidal structure.

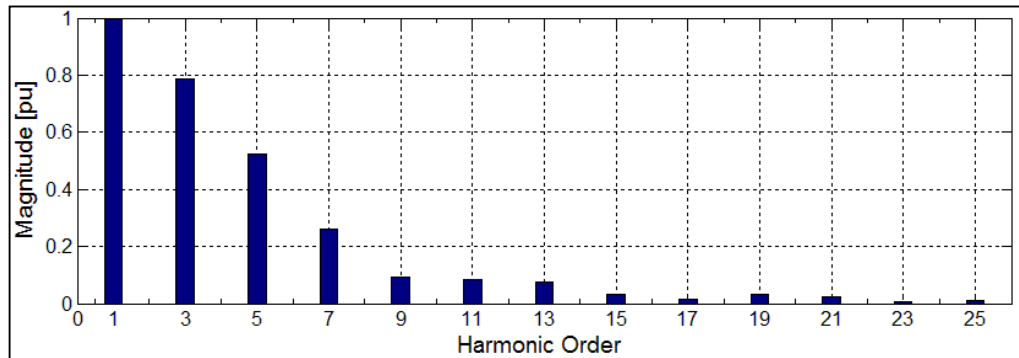


Fig.7. DFT Frequency Spectrum for Current Signal

Fig.7 shows DFT frequency spectrum of the current signal. When the DFT frequency spectrum is analyzed, it is seen that

the 3rd, 5th, and 7th harmonic components are fairly higher than 10 %, while the others are below 10 %.

TABLE II  
EFFECTIVE HARMONIC CURRENT AND HARMONIC RATIOS (%)

Harmonic Order [n]	Harmonic Current [A]	Harmonic Ratios [%]	Harmonic Order [n]	Harmonic Current [A]	Harmonic Ratios [%]
1	7.688	100	15	0.246	3,21
3	6.048	78,68	17	0.101	1,32
5	4.018	52,27	19	0.253	3,30
7	2.006	26,10	21	0.181	2,36
9	0.709	9,23	23	0,038	0,35
11	0.635	8,27	25	0.127	1,16
13	0.581	7,57	THD%		99,22 %

Table 2 includes harmonic current values and harmonic ratios. Only the 3rd harmonic component's amplitude is equal to 78,68% of the fundamental component's amplitude value. The THD percentage of the UHFIHS after all calculations is found as 99,22%.

#### IV. CONCLUSIONS

This study performs a power quality analysis with the proposed PLL-based digital ANF for a 900 KHz UHFIHS with 2.8 kW power. A notch filter bank is created using sufficient number of notch filters in the PLL-based measurement system. Due to the superiority of the software-based PLL, the synchronization with the fundamental frequency is performed properly. The filter bank is adaptive to deviation in fundamental frequency of the signal and the filter's bandwidth is adjustable. Keeping the bandwidth in a short range prevents leakage of interharmonics, particularly those close to harmonic frequency components. With this proposed method, all components until the 25th harmonic ( $\omega_0, \omega_3, \dots, \omega_{25}$ ), which exist in the current signal, are separately suppressed by the ANF. The signals obtained in each ANF output are subtracted from the input signal,  $x(t)$ , to calculate the frequency component, ( $\omega_n$ ), of each harmonic. In this way, the leakage effect caused by the interharmonics is prevented

and the signal is subjected to a DFT analysis. As a result, frequency and amplitude values of all harmonic components are calculated in a proper, precise and accurate way, in accordance with the IEC standards. The proposed method is found highly successful as it doesn't cause problems like spectral leakage and picket-fence effect, which may lead to calculation errors in FFT and DFT. As a result of the calculations, the total harmonic distortion in the UHFIHS is obtained as 99,22%. This percentage shows a significantly high level of harmonic distortion in the given UHFIHS. Such systems must necessarily be supported with appropriate filter designs that can suppress the target harmonic components. Otherwise, the systems that produce such high-value harmonics can negatively affect other devices connected to the same power supply and result in breakdowns and even permanent damages in these devices.

#### REFERENCES

- [1] E. Fuchs and M. A. Masoum. *Power quality in power systems and electrical machines*. Academic press, 2011.
- [2] X. Wang, F. Blaabjerg, Harmonic stability in power electronic based power systems: concept, modeling, and analysis. *IEEE Transactions on Smart Grid*, 2018.
- [3] U. Çavdar, "Mechanical properties of hot forged ANSI 1050 steel," *Materials Testing*, vol.56, no.3, pp. 208-212, 2014.

- [4] H. Gokozan, M. Taştan, S. Taskin, P.S. Cavdar and U. Cavdar, "Comparison of electrical energy consumption for different material processing procedures," *Materials Testing*, vol. 58, no. 11-12, pp. 1009-1013, 2016.
- [5] M. Taştan, H. Gökozan, S. Taştin and U. Çavdar, "Comparative energy consumption analyses of an ultra high frequency induction heating system for material processing applications," *Revista de metalurgia*, vol. 51, no. 3, pp. 46, 2015.
- [6] S. Taskin and H. Gokozan, "Determination of the spectral properties and harmonic levels for driving an induction motor by an inverter driver under the different load conditions," *Elektronika ir Elektrotechnika*, vol. 108, no. 2, pp. 75-80, 2011.
- [7] P. K. Ray, P. S. Puhan and G. Panda, "Real time harmonics estimation of distorted power system signal," *International Journal of Electrical Power & Energy Systems*, vol. 75, pp. 91-98, 2016.
- [8] A. Dalcalı and M. Akbaba, "Detection of the space harmonics of the shaded pole induction motor," *Journal of Engineering Research*, vol. 5, no. 4, 2018.
- [9] T. Jin, Y. Chen and R. C. Flesch, "A novel power harmonic analysis method based on Nuttall-Kaiser combination window double spectrum interpolated FFT algorithm," *Journal of Electrical Engineering*, vol. 68, no. 6, pp. 435-443, 2017.
- [10] D. Belega, D. Petri and D. Dallet, "Impact of harmonics on the interpolated DFT frequency estimator. *Mechanical Systems and Signal Processing*, vol. 66, pp. 349-360, 2016.
- [11] Y. Xia, Y. He, K. Wang, W. Pei, Z. Blazic and D. P. Mandic, "A complex least squares enhanced smart DFT technique for power system frequency estimation," *IEEE Transactions on Power Delivery*, vol. 32, no. 3, pp. 1270-1278, 2017.
- [12] H. Wen, J. Zhang, W. Yao and L. Tang, "Fft-based amplitude estimation of power distribution systems signal distorted by harmonics and noise," *IEEE Transactions on Industrial Informatics*, vol. 14, no. 4, pp. 1447-1455, 2018.
- [13] J. Khodaparast and M. Khederzadeh, "Dynamic synchrophasor estimation by taylor-prony method in harmonic and non-harmonic conditions," *IET Generation, Transmission & Distribution*, vol. 11, no. 18, pp. 4406-4413, 2017.
- [14] S. K. Jain and S. N. Singh, "Exact model order ESPRIT technique for harmonics and interharmonics estimation," *IEEE Transactions on Instrumentation and Measurement*, vol. 61, no. 7, pp. 1915-1923, 2012.
- [15] Y. F. Wang and Y.W. Li, "Three-phase cascaded delayed signal cancellation PLL for fast selective harmonic detection," *IEEE Transactions on industrial electronics*, vol. 60, no. 4, pp. 1452-1463, 2013.
- [16] S. K. Singh, N. Sinha, A. K. Goswami and N. Sinha, "Several variants of Kalman Filter algorithm for power system harmonic estimation," *International Journal of Electrical Power & Energy Systems*, vol. 78, pp. 793-800, 2016.
- [17] A. Bagheri, M. Mardaneh, A. Rajaei and A. Rahideh, "Detection of grid voltage fundamental and harmonic components using Kalman filter and generalized averaging method," *IEEE Transactions on Power Electronics*, vol. 31, no. 2, pp. 1064-1073, 2016.
- [18] H. Gokozan, S. Taskin, S. Şeker and H. Ekiz, "A neural network based approach to estimate of power system harmonics for an induction furnace under the different load conditions," *Electrical Engineering*, vol. 97, no. 2, pp. 111-117, 2015.
- [19] F. Vatanserver and A. Ozdemir, "An alternative approach for calculating/measuring fundamental powers based on wavelet packet transform and its frequency sensitivity analysis," *Electrical Engineering*, vol. 91, no. 8, pp. 417-424, 2010.
- [20] I. Askarian, S. Eren, M. Pahlevani and A. M. Knight, "Digital Real-Time Harmonic Estimator for Power Converters in Future Micro-Grids," *IEEE Transactions on Smart Grid*, vol. 9, no. 6, pp. 6398-6407, 2018.
- [21] Y. E. Vatankulu, Z. Şentürk and O. Salor, "Harmonics and Interharmonics Analysis of Electrical Arc Furnaces Based on Spectral Model Optimization With High-Resolution Windowing," *IEEE Transactions on Industry Applications*, vol. 53, no. 3, pp. 2587-2595, 2017.
- [22] A. Özdemir, I. Yazici and C. Vural, "Fast and robust software-based digital phase-locked loop for power electronics applications," *IET Generation, Transmission & Distribution*, vol. 7, no. 12, pp. 1435-1441, 2013.
- [23] S. Luo and F. Wu, "Improved Two-Phase Stationary Frame EPLL to Eliminate the Effect of Input Harmonics, Unbalance, and DC Offsets," *IEEE Transactions on Industrial Informatics*, vol. 13, no. 6, pp. 2855-2863, 2017.
- [24] S. Golestan, M. Monfared, F. D. Freijedo and J. M. Guerrero, "Design and tuning of a modified power-based PLL for single-phase grid-connected power conditioning systems," *IEEE Transactions on Power Electronics*, vol. 27, no. 8, pp. 3639-3650, 2012.
- [25] A. Özdemir, M. Taştan, "PLL based digital adaptive filter for detecting interharmonics," *Mathematical Problems in Engineering*, 2014.

## BIOGRAPHIES



**Mehmet TAŞTAN**, was born in Afyon, Turkey, in 1977. He received the M.S. degrees in electric and electrical engineering from the University of Niğde Ömer Halisdemir, in 2002 and the Ph.D. degree in electric and electrical engineering from Sakarya University, in 2014. His studies include harmonic analysis in power systems, power quality, microcontrollers and signal processing.

# Unlock A Device with Pressure and Rhythm Based Password

E. AYDEMİR, F. TOSLAK

**Abstract**— When people open their doors, they usually use the keys they carry in their pockets. As an alternative to these used keys, it is possible to open the doors which are authorized with RFID-enabled key holders or ID cards. But it seems that different alternatives have not been developed much. Moreover, none of them carries the sensory understanding dimension of the person and it is not possible to determine whether or not the entrance request has been made by that person. In this study, both the identification of the person and the opening of the door are ensured by considering both the stroking rhythm and the stroke force of a buttoner placed in the door. Thus, it is possible to open the door according to the person's identity and authority without carrying any object beside it, and it will have a unique original value. The milliseconds between each stroke for the stroke of the quill are recorded in the generated database. Comparison is made with the data obtained in the next stroke and the person is used for verification. In addition, the pressure data of the person is also kept in the database for each stroke and compared. In the study, the data of two different people were recorded in the system and the information of the people using the subjective button was recorded. Then, in addition to these two different people, a total of 15 people, including 13 different people, were allowed to use the system. In total, 50 door opening requests data were recorded and 87.5% success rate was obtained.

**Index Terms**— Rhythm, Pressure, Button, Password, Door Lock, Key Stroke.

## I. INTRODUCTION

MANY DIFFERENT methods are used by people to unlock any locked device. Some of them are performed by carrying a device on people. For example, key, card, RFID keychain. Biometric solutions are also used to unlock locked devices. Fingerprint, face recognition, eye recognition, speech recognition and keystrokes are some of these. Carrying a device on people will be reduce in the future because of forgetting, loosing and being damaged reasons.

**EMRAH AYDEMİR**, is with Department of Computer Engineering, Kirsehir Ahi Evran University, Kirsehir, Turkey, (e-mail: [emrah.aydemir@ahievran.edu.tr](mailto:emrah.aydemir@ahievran.edu.tr)).

 <https://orcid.org/0000-0002-8380-7891>

**FERHAT TOSLAK**, is with Department of Computer Technologies, Kirsehir Ahi Evran University, Kirsehir, Turkey, (e-mail: [ferhattoslak@ahievran.edu.tr](mailto:ferhattoslak@ahievran.edu.tr)).

 <https://orcid.org/0000-0003-1054-379X>

Manuscript received December 25, 2018; accepted February 06, 2019.

DOI: [10.17694/bajece.502550](https://doi.org/10.17694/bajece.502550)

The applications such as fingerprint, face recognition and eye retina, which are among the biometric solutions, cannot become widespread because they do not want to share their most special knowledge in various places. Likewise, in systems with critical data, software is used to protect confidential data and to provide locking. This software is used in computers and mobile devices and other special devices. These software use drag, move, enter PIN code, enter password, drawing pattern, fingerprint, face and voice recognition methods.

In this study, the key stroke dynamics within the biometric solutions developed among the unlocking systems was developed. An extra feature of the key stroke is considered and the stroke intensity is taken into consideration. In this way, it will not be necessary for people to carry any objects in the opening of the locked devices, and people who worry in the very special information held in fingerprint, eye and face recognition systems will be eliminated. In the literature there is also a patent that includes a comparison with a code generated from variations between hit force and stroke times in touch or touch systems [1]. Here, the person will be asked to stroke a button with a rhythm that he / she chooses. The time between each of these strokes and the force of each stroke will provide to unlock the locked system. Thus, the key stroke dynamics system in the literature will be improved and become safer and more effective. In addition, with just one button, the operation and reliability of this system will be tested and presented to the literature.

## II. KEYSTROKE DYNAMICS

Computer users use their own unique rhythm while typing text with the keyboard. This method is called keystroke dynamics [2]. This method assumes that every person has the use of a keyboard in unique rhythm, just like the differences in characters in signatures. Keystroke dynamic is the data processing method that analyzes the typing in keyboard inputs. Stroke and pulling moments are considered. With the data of these moments, various algorithms are generated as a result of the calculation [4, 5]. Fig. 1 shows the graph of the key stroke and release times on the keyboard when writing the same text ("Computer") of the same person at different times. The similarity of keystroke dynamics can be easily seen from the graph. Fig. 2 shows the status of the keystroke dynamics that occur at the time when different people write the same text. Although the text is the same, it can be seen that it contains many differences.

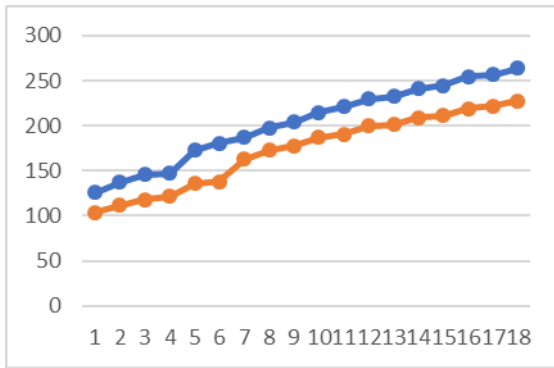


Fig 1. Same person writing the same text.

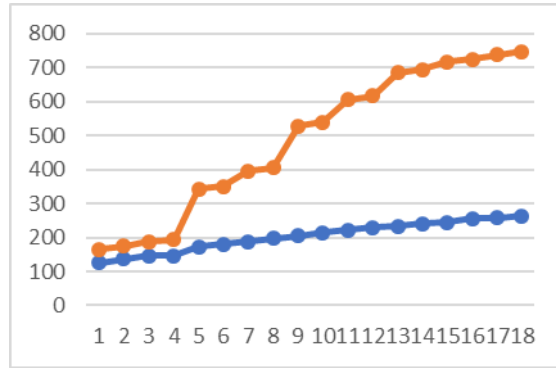


Fig 2. Different people writing the same text

Compared to other physical and biometric solutions, keystroke dynamics methods are not the most reliable identification method. Keystroke dynamics will be insufficient to become an independent biometric authentication factor. But using both the traditional applications and keystroke dynamics method will increase the security level of the unlocking systems [6]. The usability of the rhythm factor applied to mouse clicks has been investigated and it has been seen that it may be a secondary identification factor for general password applications [7, 8]. Providing a value indicating the reliability of the rhythm-based password to the user will also be useful in increasing the user's own reliability [9]. In addition to the existing password entries, the input rhythm of a given word is also used to increase the password security [10].

III. FORCE SENSITIVE KEYSTROKE DYNAMICS

The force-sensitive keystroke dynamics is a data processing method that analyzes the user's keystroke dynamics via a keyboard or a button, as well as the pressure values generated by the keystroke. Fig. 3 and Fig. 4 shows the pressure values for the force-sensitive keystroke dynamics and the time-to-break data. Even though two different people try the same rhythms, the data is different. Therefore, considering the pressure values in the keystroke dynamics, it is thought that the security level will increase even more and the person will be better acquainted.

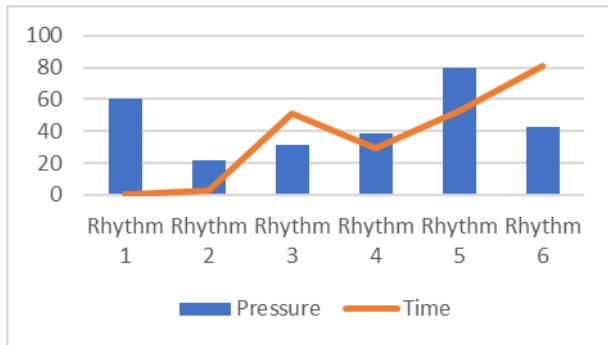


Fig 3. Pressure and time values of person A

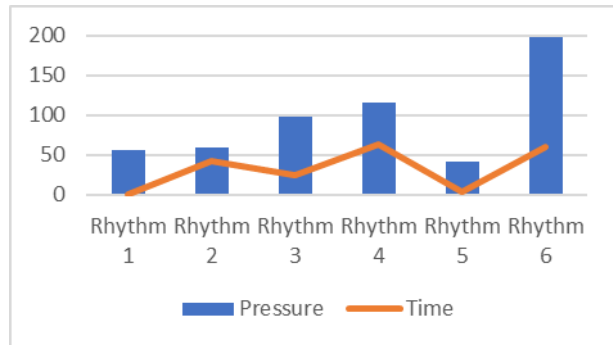


Fig 4. Pressure and duration values of Person B.

IV. DOOR LOCK DESIGN WITH FORCE SENSITIVE BUTTON

In this study, a button is designed to apply the force-sensitive keystroke dynamics method. Under this button there is a sensor that measures the pushing force and returns the pressure value. A resistor is connected to this sensor and connected to the LattePanda device with other connections. The LattePanda device comes with Windows 10 64 bit installed and also with Arduino software installed. Fig. 5 below shows the connections visually.

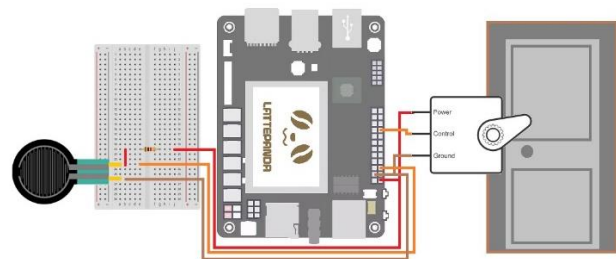


Fig 5. Door Lock Design with Force Sensitive Button.

The pressure values from Arduino were obtained with a program written in C#. One timer was added to receive data from Serialport, and the data on one port per millisecond was read and processed. The button pressure values come from the port. Data were processed with the following formulas considering the incoming values and the time of arrival.

$$\bar{t}_j = \frac{\sum_{i=1}^n t_i - t_{i-1}}{n} \tag{1}$$

$$\bar{P}_j = \frac{\sum_{i=1}^n P_i}{n} \tag{2}$$

$n$ =number of attempts

$t$ =duration of stroke

$\bar{t}$ = average stroking time

$j$ =number of rhythms

$P$ =value of pressure

$\bar{P}$ =average pressure

$\bar{P}_j$ = average pressure for rhythm  $j$ .

$\bar{t}_j$ =  $j$ . average duration for rhythm  $j$ .

In each stroke, the pressure and time values are obtained from the designed embedded system. Each stroke here is called rhythm. Values are kept in tables in a created database. The person definitions table records the highest-pressure value of each person and the duration of that stroke. Finger stroke begins to be read by the force applied to the first stroke of the finger, and as the pressure exerted by the finger on the unit area increases, the amount of force is increased. The highest force value was taken into consideration. Before registering these datas, the person is asked to try at least three times for the special stroke. The average of these trials is kept in the person definitions table. Here the number of attempts made by the person must be directly proportional to the consistency of his / her own special stroke. In other words, the higher the number of trials, the closer the values should be printed. All input requests are recorded in a table regardless of whether the entry is successful or not. Fig. 6 below shows the structure of the tables.

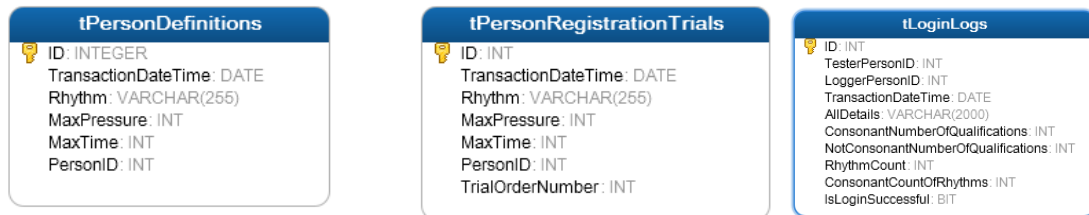


Fig 6. Database Table Designs

Here, the pressure values rise from the first touch of the finger to the completion of the touch. Therefore, the highest value between the values is the actual value of the stroke. Similarly, the time information is obtained from the first touch of the finger when stroking time is obtained but the time information is taken into consideration when the maximum pressure value is reached.

First of all, the records with the same number of rhythms are filtered from the input information registered in the input requests. Then comparisons are made with the pressure and duration information in each of these rhythms. A maximum of 25% difference between each is acceptable. If the difference is higher, a failure occurs and other conditions continue to be compared. A maximum of 10% failure is expected in the total number of events. If a higher failed situation is obtained, no entry is allowed.

V. RESULTS

In the study, identification data of two people were recorded and transactions were made. In addition to the real people, 13 people tried to do the same by attempting the identification stroke of these two people. This total of 13 people has made 29 attempts. The real people made 21 attempts. Table I below shows the data for this situation.

TABLE I  
OVERVIEW OF DATA

Informations	Number
Number of total people	15
Number of real people	2
Real People Trial Count	21
Other people Trial Count	29

Two people recorded their strokes dynamics primarily in the system. While there are five rhythms in the strokes dynamics of an EA-coded person, there are four rhythms in the strokes dynamics of an FT-coded person. The data and data generated from these strokes are as follows on Table II and Fig. 7.

TABLE II  
The Force-sensitive Stroke Dynamics Data of the People Registered to the System

Rhythm	Intensity	Duration	Name of Person
1. rhythm	89	0	EA
2. rhythm	56	73	EA
3. rhythm	87	31	EA
4. rhythm	87	50	EA
5. rhythm	134	81	EA
1. rhythm	74	0	FT
2. rhythm	105	53	FT
3. rhythm	99	52	FT
4. rhythm	45	123	FT

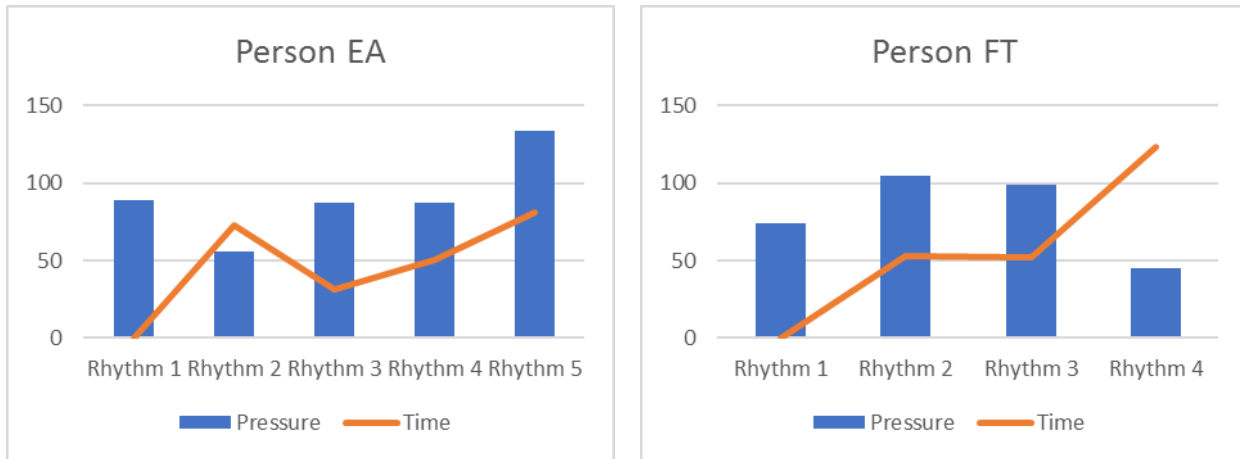


Fig 7. Force Sensitive Stroke Dynamics Data Chart of Registered People in the System.

The key strokes dynamics of two people with EA and FT codes differ from each other in terms of intensity and duration, while the number of rhythms is five in one and four in the other. Therefore, it is checked whether the number of rhythm matches. The number of rhythms is not negative and the

demand is negative. The Table III shows the data of people attempting to login. These data include both natural people and strokes, and try to match the results. In addition, several people tried to teach how they stroked and experimented.

TABLE III  
Trial Data of People

ID	Person Who Try	Real Person	Process Date	Number of Correct Attributes	Number of Incorrect Attributes	Number of Rhythm	Number of People who Match Rhythm	Input Success Status.
1002	EA	EA	03.04.2018 10:29	8	1	5	1	1
1003	FT	FT	03.04.2018 11:17	7	0	4	1	1
1004	FT		03.04.2018 11:17	0	0	5	1	0
1005	FT		03.04.2018 11:18	0	0	5	1	0
1007	FT		03.04.2018 11:19	0	0	6	0	0
1008	FT		03.04.2018 11:20	0	0	5	1	0
1009	FT		03.04.2018 11:21	0	0	8	0	0
1010	FT	FT	03.04.2018 11:21	6	1	4	1	1
1011	FT		03.04.2018 11:22	0	0	5	1	0
1013	EA	EA	03.04.2018 11:23	9	0	5	1	1
1014	FT		03.04.2018 11:25	0	0	6	0	0
1017	FT		03.04.2018 12:37	0	0	5	1	0
1018	FT	FT	03.04.2018 12:38	6	1	4	1	1
1019	EA		04.04.2018 11:09	0	0	5	1	0
1020	EA	EA	04.04.2018 11:09	8	1	5	1	1
1021	EA	EA	04.04.2018 11:11	9	0	5	1	1
1022	KAK		04.04.2018 11:12	0	0	5	1	0
1023	KAK		04.04.2018 11:13	0	0	5	1	0
1024	KAK	EA	04.04.2018 11:13	8	1	5	1	1
1025	MÖ		04.04.2018 11:14	0	0	5	1	0
1026	HÇ		04.04.2018 11:16	0	0	5	1	0
1027	IY	EA	04.04.2018 11:16	8	1	5	1	1
1028	EA	EA	04.04.2018 11:17	9	0	5	1	1
1029	FA		04.04.2018 11:17	0	0	5	1	0
1030	FA		04.04.2018 11:18	0	0	4	1	0
1031	FA	EA	04.04.2018 11:18	8	1	5	1	1
1032	EA	EA	04.04.2018 11:19	8	1	5	1	1
1033	FT		04.04.2018 11:20	0	0	8	0	0
1034	ŞÖ		04.04.2018 14:44	0	0	2	0	0
1035	ŞÖ		04.04.2018 14:45	0	0	3	0	0
1036	BT		04.04.2018 14:45	0	0	5	1	0
1037	BT		04.04.2018 14:45	0	0	5	1	0
1038	EA	EA	04.04.2018 14:46	8	1	5	1	1
1039	HCP		04.04.2018 15:09	0	0	8	0	0
1041	EA	EA	04.04.2018 15:10	8	1	5	1	1
1042	HCP		04.04.2018 15:10	0	0	5	1	0

When the above table is examined, it has been seen that the total of 50 attempts from 32 attempts failed due to various reasons such as rhythm incompatibility. EA-coded person's own attempt to perform an experiment with eight deviations in a part of the success of the rhythm despite the high level of deviation despite the failure seems to be failing. This means that 87.5% success has been achieved. Again, FT coded person's three of the three attempts were successful. However, as a result of the EA-coded person's strokes dynamics, all of the 22 entry attempts of the people were able to capture the number of rhythms and failed because they could not approach the sensitivity and intensity of the stroke. 10 experiments did not catch the number of rhythms. Six people were shown the accuracy and severity of strokes and their experiments were successful.

## VI. CONCLUSION

Various methods such as voice, face recognition and fingerprint reading used in the data entry offer distinctive access to people. However, the use of such systems may not be sufficient because of cost and being insufficient alone the result of some disadvantages. In this study, the password entry in the access systems which are actively used today is taken into consideration. These password entries are made through a touch screen or physical key systems of numerical or alphabetical values. In this study, it is discussed to unlock a locked system with a single button, considering both the stroking force and the rhythms generated by the times between the strokes. As a result of the study, it was seen that the people who registered in the system had repeated their stroking style very well and others could not achieve success either because of the stroke time or the stroke force. It is seen some people achieve success by looking carefully or being thought and some people did not achieve success although they were thought several times. In the literature, there is a patent intended rhythmized strokes which considered the keystroke duration differences. [11]. In this patent study, similar to the study here, the vector graphics consisting of time between keys are compared and processed. However, the impact force is not considered. In addition, another application of the study with a single button with the stroke rhythm validation study was performed and 83.2% accuracy was achieved. 19.4% of those who hear the stroking, copied successfully the shape of the stroke [12]. In this study, the accuracy rate is 87.5%. In another study, a similar situation was adapted to mobile applications and proved to be very reliable [13, 14]. Again, in mobile applications, the error rate was reduced from 13% to 4% by applying rhythm-based keystroke dynamics to the password entries [15]. The system presented in this study may not be as cheap as relying only on the rhythm of keystroke dynamics because of the need for extra hardware [16-17], but it appears to directly affect the reliability coefficient.

It would be useful to apply this study to more diverse user groups and to test for more recorded force-sensitive keystroke dynamics when there are contact data. It is thought that the comparison of different studies to be made by changing the threshold value and the reliability of such studies will be compared.

## REFERENCES

- [1] G.J. Anderson. U.S. Patent No. 6,509,847. Washington, DC: *U.S. Patent and Trademark Office*. 2003.
- [2] Y. Zhong, Y. Deng, A.K. Jain. "Keystroke dynamics for user authentication", 2012 IEEE Computer Society Conference on Computer Vision and Pattern Recognition Workshops (CVPRW 2012). Rhode Island, USA, 2012.
- [3] M.S. Obaidat, B. Sadoun. "Keystroke dynamics-based authentication. Biometrics". *US: Springer*, 1996, pp 213-229.
- [4] R. Giot, M. El-Abed, C. Rosenberger. "Keystroke dynamics with low constraints svm based passphrase enrollment". In *Biometrics: Theory, Applications, and Systems*, 2009. BTAS'09. IEEE 3rd International Conference on IEEE. 2009.
- [5] S.S. Bender, H.J. Postley. U.S. Patent No. 7,206,938. Washington, DC: *U.S. Patent and Trademark Office*. 2007.
- [6] P.S. Teh, A.B.J. Teoh, C. Tee, T.S. Ong. "Keystroke dynamics in password authentication enhancement". *Expert Systems with Applications*, vol. 37. 12, 2010, pp 8618-8627.
- [7] T.Y. Chang, C.J. Tsai, Y.J. Yang, P.C. Cheng. "User authentication using rhythmic click characteristics for non-keyboard devices". In *Proceedings of the 2011 International Conference on Asia Agriculture and Animal IPCBEE*, Singapore, 2011.
- [8] T.Y. Chang, Y.J. Yang, C.C. Peng. "A personalized rhythm click-based authentication system". *Information Management & Computer Security*, vol. 18. 2, 2010, pp 72-85.
- [9] D.L. Ashbrook, F.X. Lin, S.M. Whtie. *U.S. Patent Application No. 13/092,383*, 2012.
- [10] Y.V. Fedorova, T.R. Ruddy, M.S. Nunuparov. U.S. Patent No. 7,536,556. Washington, DC: *U.S. Patent and Trademark Office*, 2009.
- [11] G.R. Hird. *U.S. Patent Application No. 13/484,836*, 2013.
- [12] J.O. Wobbrock. "Tapsongs: tapping rhythm-based passwords on a single binary sensor". In *Proceedings of the 22nd annual ACM symposium on User interface software and technology*. New York, USA, 2009.
- [13] Y. Chen, J. Sun, R. Zhang, Y. Zhang. "Your song your way: Rhythm-based two-factor authentication for multi-touch mobile devices". In *Computer Communications (INFOCOM)*, 2015 IEEE Conference on. Kowloon, Hong Kong, 2015.
- [14] J.D. Lee, Y.S. Jeong, J.H. Park. "A rhythm-based authentication scheme for smart media devices". *The Scientific World Journal*, vol. 2014, 2014.
- [15] S.S. Hwang, S. Cho, S. Park. "Keystroke dynamics-based authentication for mobile devices". *Computers & Security*. vol. 28. 1-2, 2009, pp 85-93.
- [16] T. Tuncer, and Y. Sönmez. "Block based data hiding method for images." *European Journal of Technique* 7.2 (2017): 85-95.
- [17] F. Cherifi, B. Hemery, R. Giot, M. Pasquet, C. Rosenberger. "Performance evaluation of behavioral biometric systems". In *Behavioral Biometrics for Human Identification: Intelligent Applications*, 2010, pp 57-74.

## BIOGRAPHIES

**EMRAH AYDEMİR** Elazığ, in 1987. He received the M.S. degrees in computer teaching from the University of Elazığ Firat, in 2012 and the Ph.D. degree in informatics from Istanbul University, Turkey, TR, in 2017.



From 2012 to 2015, he was an Expert with the Istanbul Commerce University. Since 2017, he has been an Assistant Professor with the Computer Engineering Department, Kirsehir Ahi Evran University. He is the author of three books, more than 10 articles, and more than 40 conference presentation. His research interests include artificial intelligence, microcontroller, database and software.



**FERHAT TOSLAK** Karaman, in 1987. He received the B.S. in computer teaching from the University of Suleyman Demirel, Isparta, in 2010 and he is student in computer engineering from Inonu University, Turkey, TR.

From 2011 to 2016, he was a Research Assistant with the Sirnak University. Since 2016, he has been a Lecture with the Computer Technology Department, Kirsehir Ahi Evran University.

# Speed Control of BLDC Using NARMA-L2 Controller in Single Link Manipulator

R. CELIKEL

**Abstract**—The BLDC motors are widely used in industrial applications. The load characteristic and controller are important to obtain optimum performance in the speed control of the BLDC motor because some problems are occurred in speed control of nonlinear loads which is used the conventional control methods. The single link manipulator used in robotic applications is a nonlinear system for control algorithms. The load of motor is determined on considering the conversion ratio of the reducer box. In this study, a single link manipulator system consist of BLDC motor, reducer gearbox and robot arm is controlled by using NARMA-L2 controller as known modern control method in used the control of the nonlinear systems. The NARMA-L2 controller is based on neural network. The single link manipulator system is analyzed by using MATLAB/Simulink environment. The speed control of the BLDC motor is performed in conditions the constant and nonlinear load. The results show that the speed control of BLDC motor is performed the high performance in nonlinear loads.

**Index Terms**—BLDC motor, Neural networks, NARMA-L2 controller, Single link manipulator.

## I. INTRODUCTION

THE BRUSHLESS direct current (BLDC) motors are widely used in industrial applications such as automotive technology, appliances, medical, industrial automation equipment, and aerospace application. The BLDC motors are used owing to their low weight, high power density, high efficiency, and high reliability [1].

The some problems such as steady state error, high overshoot and control response error are occurs in the speed control of the nonlinear loads. Nowadays, there are many industrial systems with non-linear parameters such as single link manipulator which is most basic part in robotic systems. It is difficult to achieve a nonlinear manipulator load using conventional control methods with high-speed tracking. The conventional control methods have been applied to various types of manipulators in the literature [2]. The nonlinear parameters of the single link manipulator load can be explicitly defined. These parameters are the gravitational

**R. CELIKEL**, is with Department of Electrical Engineering University of Batman University, Batman, Turkey, (e-mail: [resat.celikel@batman.edu.tr](mailto:resat.celikel@batman.edu.tr)).

 <https://orcid.org/0000-0002-9169-6466>

Manuscript received January 8, 2019 accepted March 18, 2019.  
DOI: [10.17694/bajece.510170](https://doi.org/10.17694/bajece.510170)

force, the mass of the load, the position of the manipulator and the viscous friction. The modern control method is used to the control of nonlinear systems. The real-time applications using Nonlinear Autoregressive Moving Average (NARMA-L2) control method has been performed for a single link manipulator [3-4].

An adaptive control method has been developed for the small signal inputs that NARMA is unsuccessful and situations where NARMA model is unknown [5]. The NARMA-L2 controller has been used to control of the induction motors. The three-phase induction motor has been controlled by using PID, fuzz logic and NARMA-L2 control methods and the obtained results have been compared [5-8]. The simulation of the induction motors' control has been performed by using PI, NARMA-L2 and fuzzy logic and more high performance has been obtained by using NARMA-L2 controller method than others control methods [9].

At the same time, NARMA-L2 controller has been used to control the speed of the different motor types. The speed control of DC motor has been performed using PID and the NARMA-L2 controllers and the results obtained have been compared among themselves [10]. The NARMA-L2 controller has been used to many applications apart from motor control applications. NARMA-L2 controller and PID controller have been used for control of the scaled-model helicopters. The superiority performance of the NARMA-L2 controller is demonstrated by the simulation [11].

In another study, a pendulum has been connected to the flywheel and a gyroscope inverter pendulum (GIP) has been performed. The real-time application of the GIP control has been achieved using NARMA-L2 controller [12]. A novel adaptive NARMA-L2 controller has been implemented to control of the nonlinear systems and the novel controller has been based on support vector regression (SVR). Against the measurement noises and uncertainty of the system parameters have been analyzed the controller durability. As a result of, the proposed control method is quite successful in suppressing measurement noise and uncertainty of the system parameters [13]. The synergy control has been proposed for a robot arm to follow a certain orbit. This control consists of a combination of the NARMA-L2 and the PD controller and has been obtained a very high performance [14].

The control of unmanned aerial vehicles is quite difficult due to the dynamic of the vehicle has a non-linear structure. The NARMA-L2 controller has been used to control the unmanned aircraft and the controller successful has been shown in simulation results [15]. A simulation has been performed to analyze instant changes of the two-area power system, which has been controlled by using PID, fuzzy logic

and NARMA-L2 controller. The controller performance has been compared in different situation [16].

A new MIMO ANFIS-based NARMA-L2 controller has been proposed and compared with other PI, PID, Fuzzy, GA and PSO controlled Fuzzy logic controls. The superiority of the proposed method in low tracking error and time response behaviors has been demonstrated by the simulation [17].

The NARMA-L2 controller has been implemented to obtain the optimum performance from maximum power point tracking algorithm which is used in photovoltaic water pump system. The performance of the PID and NARMA-L2 controller has been compared and superiority performance of the NARMA-L2 controller has been shown in simulation environment [18]. GA-adjusted Fuzzy system controller and NARMA-L2 controller have been implemented by using a simulation study for 5-degree of freedom robotic system. The simulation of the system has been performed in MATLAB/Simulink environment and obtained results have been compared [19].

In this study, the speed control of the BLDC motor is performed by using NARMA-L2 controller in MATLAB/Simulink environment at conditions constant load and nonlinear load. A single link manipulator is used as the nonlinear load. This manipulator is driven by a dc gear-motor. The nonlinear load and inertia of the manipulator is degraded to the motor side. Thus, the angular position control of the motor is obtained similar to the real system. The results are analyzed by using MATLAB / Simulink environment.

## II. MODELLING OF SINGLE LINK MANIPULATOR

The control of electric motors is quite difficult in nonlinear loads. The conventional control methods are caused some problems in nonlinear loads such as steady state error and failure to adapt at unexpected situations. Nowadays, the nonlinear control methods are preferred to obtain high performance in control of the nonlinear loads. A single-link manipulator is widely used as the basis for studies in the robotic system control. The single link manipulator is nonlinear loads for the BLDC motor. In this study, a single link manipulator is used to control the speed of the BLDC motor.

Today BLDC motors are preferred as actuators, especially for the movement of industrial robot arms. The most important reason of this motor are preferred; high efficiency, high power/volume density, stable operation, lack of brushes and physical commutator and good dynamic response. The speed of the BLDC motors used in robotic applications can sometimes up to 20.000 rpm. The output speed of the gearbox is reduced and its torque is increased by using a step-down gearbox between the robot arm and the motor, assuming that the output power of the gearbox is equal to the output power of the motor. The single link manipulator is shown in Fig. 1.

The drive of BLDC motors are preferred six-step switching due to simple structure. In this technique, two phase windings are in connection at any time. It can be expressed by the equations of the conventional DC motor when a BLDC motor is controlled by a six-step switching technique. The voltage and torque of motor are obtained as shown Eq. (1) and Eq. (2), respectively.

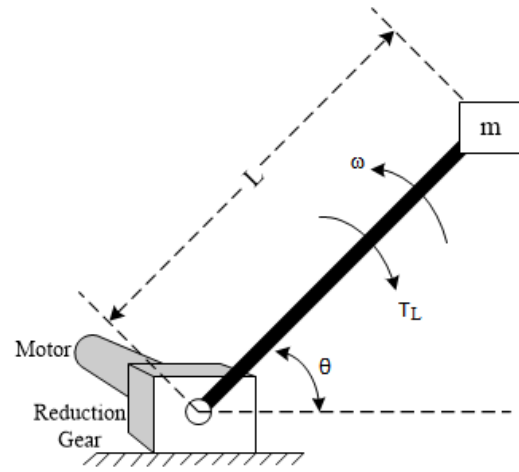


Fig.1. Single-link manipulator

$$V = i_s R_s + L_s \frac{di_s}{dt} + E_z, \quad E_z = K_e \omega_m \quad (1)$$

$$T_m = T_L + J_m \frac{d\omega_m}{dt} + B_m \omega_m, \quad T_m = K_t i_s \quad (2)$$

where  $V$  is the motor voltage,  $i_s$  is the motor current,  $R_s$  is motor winding resistance,  $L_s$  is winding inductance of the motor,  $K_e$  is speed constant,  $\omega_m$  is motor angular velocity,  $T_m$  is the developed torque by the motor,  $T_L$  is load torque,  $J_m$  is inertia of the motor,  $B_m$  is friction coefficient of the motor,  $K_t$  is torque constant of the motor.

The load torque applied to motor is given in Eq. (3). The ratio of the gearbox connected to single link manipulator is taken into account when the load torque is calculated. The conversion ratio of the gearbox is given as shown in Eq. (4). The motor speed can be derived from the position of the motor as shown in Eq. 5. The load torque of the single-link manipulator and the developed torque from the motor shaft are given in Eq. (6) and Eq. (7), respectively.

$$T_L = \left(\frac{1}{u}\right)^2 \left(\frac{1}{2}mL^2\right) \frac{d^2\theta}{dt^2} + \left(\frac{1}{u}\right)^2 B_L \frac{d\theta}{dt} + \left(\frac{1}{u}\right) mgL \cos\theta \quad (3)$$

$$u = \frac{\omega_m}{\omega_L} \quad (4)$$

$$\omega_m = \frac{d\theta}{dt} \quad (5)$$

$$T_m = \left(\frac{1}{u}\right)^2 \left(\frac{1}{2}mL^2\right) \frac{d\omega_m}{dt} + \left(\frac{1}{u}\right)^2 B_L \omega_m + \left(\frac{1}{u}\right) mgL \cos\theta + J_m \frac{d\omega_m}{dt} + B_m \omega_m \quad (6)$$

$$T_m = \left[ \left( \frac{1}{u} \right)^2 \left( \frac{1}{2} mL^2 \right) + J_m \right] \frac{d\omega_m}{dt} + \left[ \left( \frac{1}{u} \right)^2 B_L + B_m \right] \omega_m + \left( \frac{1}{u} \right) mgL \cos\theta \tag{7}$$

where  $\omega_L$  is angular velocity of the load,  $B_L$  is the friction coefficient of the load,  $u$  is the ratio of the gearbox,  $m$  is the mass of the load,  $L$  is the arm length,  $g$  is the force of gravity.

III. DESIGN OF NARMA-L2 CONTROLLER

Artificial Neural Network (ANN) based control methods are popular due to their skills, learning, and approach in control of nonlinear systems. These control methods are frequently used in the control and identification of dynamic systems in recent years. One of the most suitable methods is NARMA-L2 controller for controlling time-dependent and nonlinear systems. NARMA-L2 controller consists of two steps such as determination of the system to be controlled and design of system control.

The behavior of the nonlinear discrete time system is examined in the system determination step is shown in Eq. 8.

$$y(k+d) = N(y(k), y(k-1), \dots, y(k-n+1), u(k), u(k-1), \dots, u(k-m+1)) \tag{8}$$

where  $u(k)$  and  $y(k)$  are system input and system output, respectively.  $m$  and  $n$  are the measured delay values of the inputs and outputs, respectively.  $d$  is relative degrees. Multilayer neural networks can be used to define  $N$  nonlinear function.

If the system follows a reference, the nonlinear controller can be shown as Eq. 9. Neural network training can be used to determine the  $G$  function that minimizes the mean square error using the back-propagation algorithm. In this case, the NARMA-L2 controller can be obtained as in Eq. 10.

$$u(k) = G(y(k), y(k-1), \dots, y(k-n+1), y_r(k+d), u(k-1), \dots, u(k-m+1)) \tag{9}$$

$$\hat{y}(k+d) = f[y(k), y(k-1), \dots, y(k-n+1), u(k-1), \dots, u(k-m+1)] + g[y(k), y(k-1), \dots, y(k-n+1), u(k-1), \dots, u(k-m+1), u(k)] \tag{10}$$

The advantage of this form of reference system outputs can be solved for the control input that causes the tracking. The obtained controller is shown in Eq. 11.

$$u(k) = \frac{y_r(k+d) - f[y(k), y(k-1), \dots, y(k-n+1), u(k-1), \dots, u(k-m+1)]}{g[y(k), y(k-1), \dots, y(k-n+1), u(k-1), \dots, u(k-m+1)]} \tag{11}$$

However, it is not practical to define the input that depends on the output. For this reason, Eq. 12 is used for system definition for  $d \geq 2$ .

$$y(k+d) = f[y(k), y(k-1), \dots, y(k-n+1), u(k), u(k-1), \dots, u(k-n+1)] + g[y(k), y(k-1), \dots, y(k-n+1), u(k), u(k-1), \dots, u(k-n+1), u(k+1)] \tag{12}$$

The NARMA-L2 controller is obtained as shown in Eq. 13.

$$u(k+1) = \frac{y_r(k+d) - f[y(k), \dots, y(k-n+1), u(k), \dots, u(k-n+1)]}{g[y(k), \dots, y(k-n+1), u(k), \dots, u(k-n+1)]} \tag{13}$$

The general form of the NARMA-L2 controller is illustrated in Fig. 2 as the simplest structure. The hidden layer also has only one neuron. However, more neurons are needed in practice. At the same time, the number of delayed inputs is also important because the degree of the system model is unknown. The NARMA-L2 controller must be connected to the system as shown in Fig. 3 after the training process is completed. The DC motor and the system parameters used in this study are given in Table I.

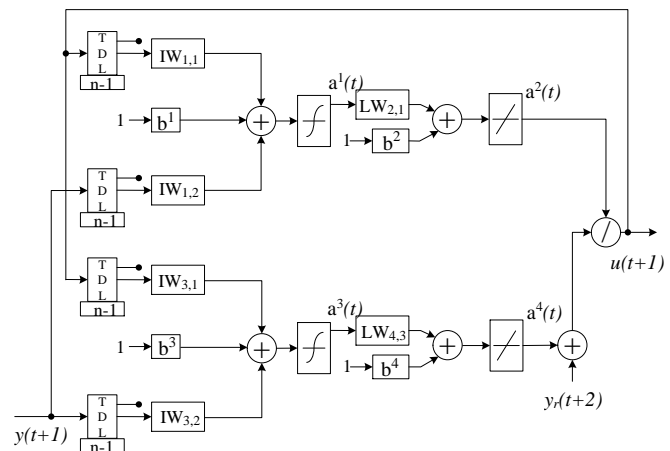


Fig.2. The simplest form of NARMA-L2 controller

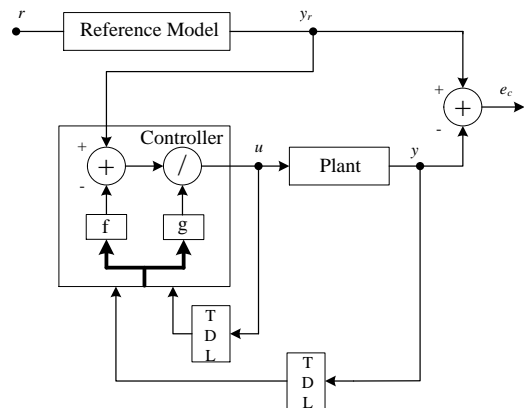


Fig.3. The block diagram of NARMA-L2 controller connected the system

TABLE I  
THE PARAMETERS OF THE DC MOTOR AND THE SYSTEM

Symbol	Unit	Parameter	Value
$V$	V	Nominal voltage	48
$R$	$\Omega$	Terminal resistance	1.03
$L$	mH	Terminal inductance	0.204
$i_s$	A	Nominal current	4.06
$K_t$	mNm/A	Torque constant	44.8
$K_e$	rpm/V	Speed constant	213
$\omega_m$	rpm	Nominal speed	9250
$T_m$	mNm	Nominal torque	170
$J_m$	kgm <sup>2</sup>	Torque of the total inertia	0.0000101
$B_m$	Nms/rad	Friction constant of the motor	~0
$B_L$	Nms/rad	Friction constant of the payload	0.0001
$m$	kg	Mass of the payload	1
$g$	m/s <sup>2</sup>	Gravitational force	10
$L$	m	Length of manipulator arm	1
$u$		Conversion ratio of reduction gear	100

IV. SIMULATION RESULTS

The simulation is performed by using MATLAB/Simulink environment. In this study, the size of hidden layers is determined as 20, the number of delay inputs is taken as 3 and the number of delay outputs is taken as 2. These data are usually obtained by performing simulation study. The sample time of the network is 0.001s and the number of data input and output trained by neural network is 10000 in this time. The results of the system identification and neural network training in MATLAB/Simulink environment are shown in Fig.4. The system input and output, NN output and the error between system output and NN output are given in Fig. 5.

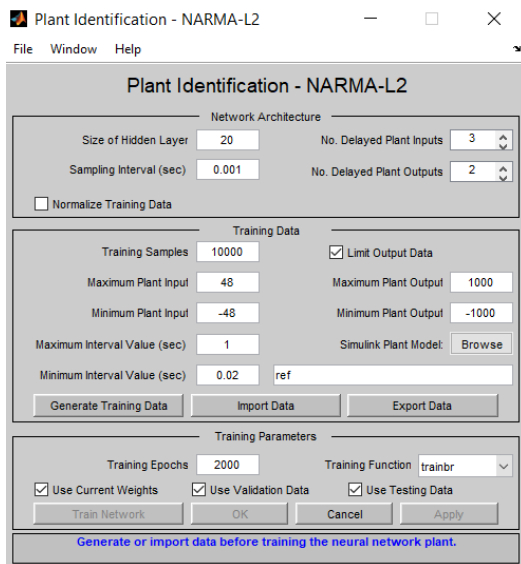


Fig.4. The plant identification of the NARMA-L2 and NN training in MATLAB/Simulink environment

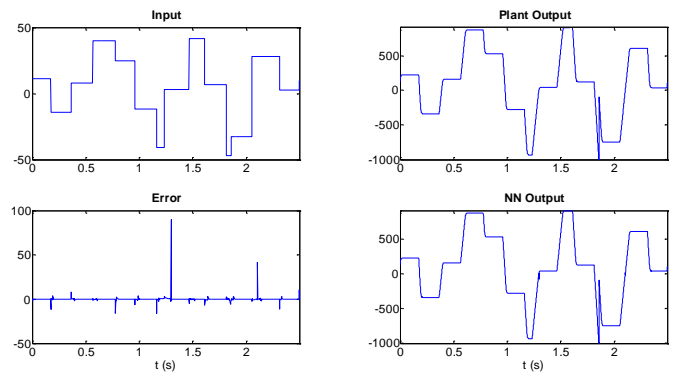


Fig.5. The system input, the plant output, the NN output and error between plant output and NN output after the NN training

A speed control simulation of a DC motor, gear and single-link manipulator reduced by dc motor in MATLAB/Simulink environment is performed as illustrated in Fig.6. At the same time, the simulation is performed to control the speed of dc motor under constant load by using NARMA-L2 controller.

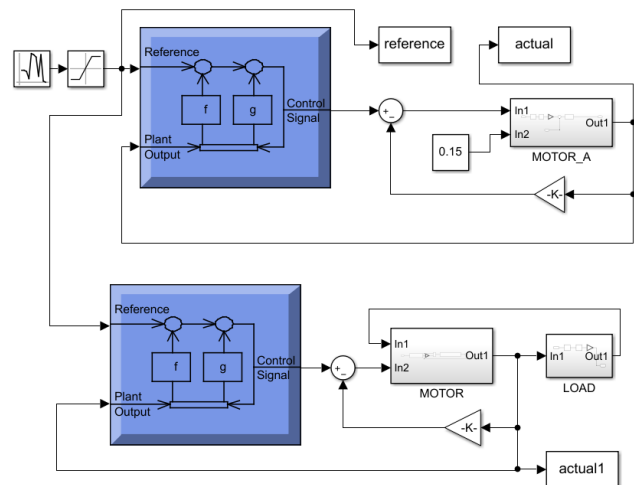


Fig.6. The control of motor by using NARMA-L2 in condition single-link manipulator load and constant load.

The desired speed of the motor is applied in the reference input in radians as shown in Fig. 7. The speed of the manipulator connected to the output of the gear is as low as the conversion ratio. The torque of the single-link manipulator is applied to the motor as a load. The gearbox conversion ratio is included in the system when the motor load torque is calculated.

Fig. 7 shows the results of the simulation. The simulation results showed that the motor speed is tracked to the various reference inputs as desired.

In Fig.7, the load applied the motor is given as 0.15 Nm. The motor speed is track the reference speed with a low error. The overshoot is almost zero in transient response. In addition to, the speed of motor is catch the reference speed without oscillation. The motor speed of the single link manipulator is shown in Fig. 8.

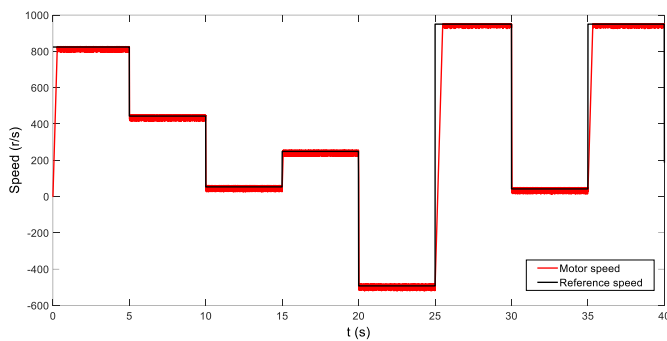


Fig.7. The motor speed under constant load.

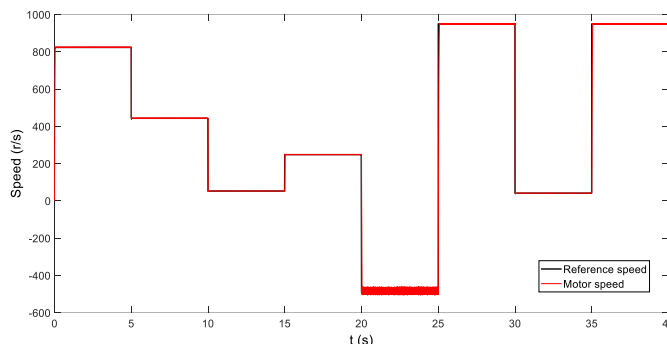
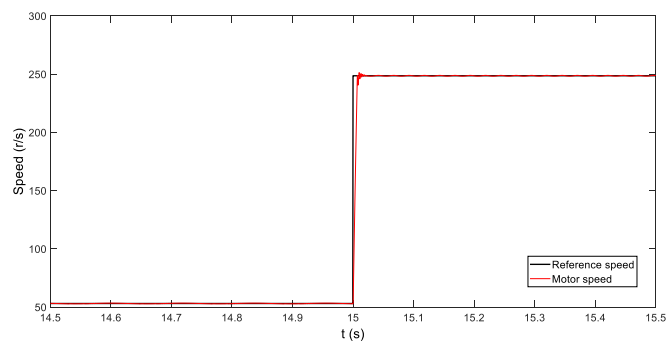


Fig.8. The motor speed under single link manipulator load.

The gearbox conversion ratio and other system parameters is consider while the torque applied to the motor is calculate. The simulation of motor load is performed by using Table 1. The speed of the motor tracks the reference speed approximately zero overshoot and very quickly, as seen in Figure 8. This demonstrates the success of the NARMA-L2 controller in controlling the nonlinear systems. Fig. 9 shows the motor speed reaching up to reference speed between 14.5<sup>th</sup> and 15.5<sup>th</sup> seconds.

Fig.10. The result of simulation between 14.5<sup>th</sup> and 15.5<sup>th</sup> seconds.

## V. CONCLUSION

The single link manipulator is nonlinear system due to nonlinear loads. The control of the nonlinear loads is performed by using nonlinear control methods because the conventional control methods is insufficient in the control of this loads. NARMA-L2 controller is the nonlinear control method which is used neural network. In this study, the speed of a single link manipulator has been controlled by using NARMA-L2 controller. The controlled system consists of a dc

motor, a reducer gearbox connected between the motor and a single-link manipulator. Different speed values are applied to the NARMA\_L2 controller input as reference for 40 seconds. The simulation has been performed under condition both constant load and single link manipulator load. As a result of the simulation study, the speed of the motor is tracked by high accuracy with reference speed in both load condition. This study showed that the NARMA controller could be used in both constant loads and nonlinear loads such as single link manipulator.

## REFERENCES

- [1] R. Çelikel, M. Özdemir, and Ö. Aydoğmuş, "Implementation of a flywheel energy storage system for space applications," *Turkish J. Electr. Eng. Comput. Sci.*, Vol.25, 2017, pp. 1197–1210.
- [2] J.Y.S. Luh, "Conventional Controller Design for Industrial Robots—A Tutorial," *IEEE Trans. Syst. Man Cybern.*, Vol.SMC-13, No. , 1983, pp.298–316.
- [3] Wahyudi, S.S. Mokri, and A.A. Shafie, "Real time implementation of NARMA L2 feedback linearization and smoothed NARMA L2 controls of a single link manipulator," *Proc. Int. Conf. Comput. Commun. Eng. 2008, ICCCE08 Glob. Links Hum. Dev.*, pp.691–697, 2008.
- [4] S.S. Mokri, H. Husain, W. Martono, A. Shafie, U.K.M. Bangi, and S. De, "Real Time Implementation of NARMA-L2 Control of a Single Link Manipulator Faculty of Engineering , Kulliyah of Engineering , International Islamic University of Malaysia , 50728 , Kuala Lumpur , Malaysia," *Am. J. Appl.*, Vol.5, No.12, 2008, pp. 1642–1649.
- [5] O. Adetona, S. Sathananthan, and L.H. Keel, "Robust adaptive control of nonaffine nonlinear plants with small input signal changes," *IEEE Trans. Neural Networks*, Vol.15, No.2, 2004, pp.408–416.
- [6] M. George and K. Prasad Basu, "NARMA-L2 controlled variable frequency three-phase induction motor drive," *Eur. J. Sci. Res.*, Vol.70, No.1, 2012, pp. 98–111.
- [7] T.D. Dongale, T.G. Kulkarni, S.R. Ghatage, and R.R. Mudholkar, "Implementation and Comparative study of Three Phase Induction Motor Control Using PID Controller , Fuzzy Logic and Neural Network Techniques," *International Journal of Science and Research*, 2012, pp. 271–275.
- [8] I. Iulia and A. Mihail, "Design of NARMA-L2 Neural controller for an Induction Motor ' s Speed Control," *Journal of Computer Science & Control Systems*, Vol.6, No.2, 2013, pp. 18–22.
- [9] H. Abu-Rub and A. Awwad, "Artificial neural networks and fuzzy logic based control of AC motors," *Int. Electr. Mach. Drives Conf. (IEMDC 2009)*, No.1, 2009., pp. 1575–1580.
- [10] M. Alhanjouri, "Speed control of DC motor using artificial neural network," *International Journal of Science and Research*, Vol.6, No.2, 2012, pp. 2104–2148.
- [11] M.R. Khaldi, A. El, and H. Hassan, "State estimation based optimal control and NARMA-L2 controllers of a scaled-model helicopter," *IFAC, 2009, Vol.2, No. PART 1*.
- [12] F. Chetouane and S. Darenfed, "Neural network NARMA control of a gyroscopic inverted pendulum," *Eng. Lett.*, Vol.16, August, 2008, pp.1–6.
- [13] K. Uçak and G. Öke Günel, "A novel adaptive NARMA-L2 controller based on online support vector regression for nonlinear systems," *Neural Process. Lett.*, Vol.44, No.3, 2016, pp. 857–886.
- [14] J. Kananai, "Stiff PD and Narma L2 synergy control for a nonlinear mechanical system," *Eur. J. Sci. Res.*, Vol.77, No.3, 2012, pp. 350–361.
- [15] Y. Jiang, D. Neculescu, and J. Sasiadek, "Robotic unmanned aerial vehicle trajectory tracking control," *IFAC, 2006, Vol.39, No.15*.
- [16] S.A. Azeer, R. Ramjug-Ballobin, and S.Z. Sayed Hassen, "Intelligent controllers for load frequency control of two-area power system," *IFAC-Papers On Line*, 2017, Vol.50, No.2, pp.301–306.
- [17] Y. Al-Dunainawi, M.F. Abbod, and A. Jizany, "A new MIMO ANFIS-PSO based NARMA-L2 controller for nonlinear dynamic systems," *Eng. Appl. Artif. Intell.*, Vol.62, November, 2016, pp. 265–275.
- [18] A.M. Kassem, "MPPT control design and performance improvements of a PV generator powered DC motor-pump system based on artificial neural networks," *Int. J. Electr. Power Energy Syst.*, Vol.43, No.1, 2012, pp. 90–98.

- [19] V. Bhatia, V. Kalaichelvi, and R. Karthikeyan, "Comparison of GA tuned fuzzy logic and NARMA-L2 controllers for motion control in 5-DOF robot," *Int. J. Comput. Appl.*, Vol.39, No.2, Apr. 2017, pp. 69–78.

#### BIOGRAPHY



**RESAT CELIKEL** was born in 1980. He received B.S, M.S and PhD degrees from Firat University, Elazığ, Turkey. He has been working as an Assist. Prof. Dr. at Batman University. His current interests are BLDC motors, flywheel energy storage, FPGA, motor drive.

# Performance Analysis of T-type Inverter Based on Improved Hysteresis Current Controller

M. İNCİ

**Abstract**—This paper presents an improved hysteresis current control method for five level T-type inverter. The proposed method is based on four hysteresis levels and performed to generate switching signals of fundamental transistors in T-type inverter. By using generated signals through hysteresis controller, bidirectional switch in T-type inverter is triggered through the logical way. The system is detailed in analytical expression and exhibited to generate five voltage levels at the output of inverter. The improved technique is based on an error signal between the output current and the reference value. Therefore, the proposed modulation technique achieves the following output current at the desired value and ensures high-efficiency conversion ratio at the output. In order to show the validity of the proposed method, the controller is compared with conventional sinusoidal pulse width modulated T-type inverter. In performance results, it is obvious that the proposed method provides a lower total harmonic distortion in comparison with conventional method.

**Index Terms**—Hysteresis current controller, T-type inverter, Comparison, Total harmonic distortion, Sinusoidal pulse width modulation.

## I. INTRODUCTION

IN INDUSTRIAL APPLICATIONS, inverters are known as power electronic converters which convert dc electrical power into ac electrical power. These converters exist in different implementations such as renewable energy integration, custom power devices, industrial and home appliances in different power ranges [1, 2]. In order to convert dc power into ac power, traditional inverters cause high switching losses, electromagnetic interferences and high total harmonic distortion (THD) [3-5]. An alternative solution is the utilization of multilevel inverter to minimize the disadvantages of conventional inverters [6]. Multilevel inverters have high-efficiency conversion ratio, low electromagnetic interferences and low power losses in energy conversion implementations compared to conventional inverters [7-9]. Because they have more smooth voltage waveforms with an increased number of

voltage levels compared to classical inverters[10]. Besides, they require low-rated filters thereby diminishing the entire system dimension. These inverters also reduce the THD level at output voltage thus increasing the power quality of the entire system [11, 12].

Conventional inverters are generally preferred for low power applications. But, the usage of these inverters becomes difficult to apply owing to the high voltages that the switching devices must block [13-15]. In this case, the solution is to use multilevel inverters. In these conditions, multilevel inverters replace conventional inverters. The most common multilevel inverter topologies are cascaded H-bridge, diode clamped and flying capacitors [16, 17]. Also, there are several switches reduced multilevel inverter topologies in addition to H-bridge, diode clamped and flying capacitors. Among switch reduced multilevel inverters, T-type inverter is an alternative solution which generates five levels with fewer components [18, 19]. There are different modulation techniques to generate a more smooth output voltage with less THD. Sinusoidal pulse width modulation, space vector modulation, selective harmonic elimination and hysteresis pulse width modulation are common techniques in the literature [20, 21]. However, conventional T-type inverters use conventional sinusoidal based PWM methods in order to convert dc voltage to ac voltage. For this purpose, in this paper, hysteresis-band controller with current feedback is firstly integrated with five level T-type inverter. The study also evaluates the performance of T-type based on hysteresis controller according to THD, efficiency and voltage output. Also, the performance results of hysteresis band controller is compared to spwm.

## II. T-TYPE INVERTER

Fig. 1 introduces the circuit scheme of a five-level T-type inverter. This structure consists of four mono-directional switches (S1, S2, S3 and S4), one bidirectional switch and two dc sources per phase [22]. The presented bidirectional switch includes two back-back mono-directional switches and triggered simultaneously. For higher voltage levels, topology requires more bidirectional switches and dc voltage sources [23].

To generate five voltage levels by using T-type inverter, two dc-link capacitors (of each  $V_{dc}/2$ ) are used per phase. In the operation of the inverter, S1-S4 and S2-S3 are turned on to generate  $V_{dc}$  and  $-V_{dc}$  levels, respectively [24]. The switching states to generate all voltage levels are given in Table 1. The equivalent circuits of T-type inverter during

MUSTAFA İNCİ, is with Department of Mechatronics Engineering, Iskenderun Technical University, Hatay, Turkey, (e-mail: mustafa.inci@iste.edu.tr)

 <https://orcid.org/0000-0002-0900-5946>

Manuscript received January 8, 2019; accepted March 26, 2019.  
DOI: [10.17694/bajece.510412](https://doi.org/10.17694/bajece.510412)

switching states are introduced in Fig. 2. In the first state, S1 and S4 are turned on and the output voltage is equal to +Vdc. In this state, the operation of T-type inverter is similar to the positive cycle of conventional H-bridge inverter and the current follows the path from S1 and returns from S4 [18, 23]. In State 2, bidirectional switch S5 and S4 are closed and the voltage value is half the dc voltage in positive. The current flows through C2 and S4 in order to complete full path. In the third stage, bidirectional switch S5 and S3 are turned on to generate negative half dc voltage at load [25]. In this condition, the current flows through C1-S3-S5 and the direction of current is opposite to state 2. In the fourth stage, S2 and S3 are turned on and the output voltage is obtained as the inverse voltage of dc source [26]. This is the negative cycle operation of conventional H-bridge inverter. In state 5 and state 6, S2-S3 and S1-S3 are respectively turned on to obtain zero voltage at the load.

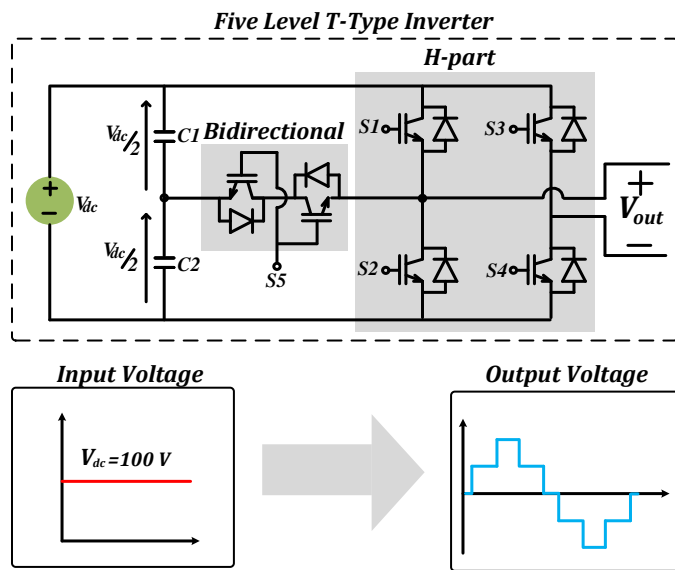


Fig.1. The circuit scheme of five level T-type inverter

TABLE I  
THE SWITCHING STATES OF FIVE-LEVEL T-TYPE INVERTER  
OUTPUT VOLTAGE

S1	S2	S3	S4	S5	Vout
1	0	0	1	0	+Vdc
0	0	0	1	1	+Vdc/2
0	0	1	0	1	-Vdc/2
0	1	1	0	0	-Vdc
0	1	0	1	0	0
1	0	1	0	0	0

For a resistive-inductive load connected T-type inverter, the relationship of voltage and current at load-side is given as [27]:

$$V_{out} = Ri_{load} + L \frac{di_{load}}{dt} \quad (1)$$

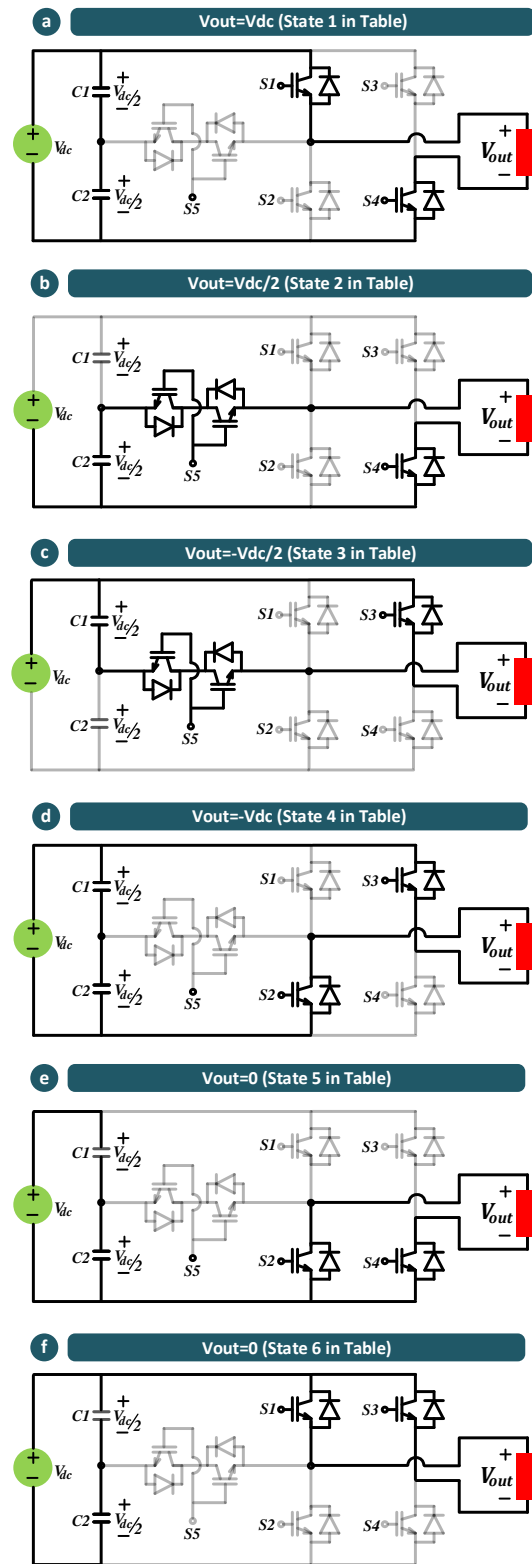


Fig. 2 The switching states and equivalent circuits of T-type inverter

Rearranging the (1), the equations can be written in the new form:

$$\Delta i_{load} = i_{load}^* - i_{load} \quad (2)$$

$$V_{out} = R i_{load} + L \frac{\Delta i_{load}}{dt} \quad (3)$$

Assuming the value of resistance is very small, we can write the reference voltage in (4):

$$V_{ref} = L \frac{\Delta i_{load}}{dt} \quad (4)$$

In the final arrangement, it is clear that the output voltage is controlled by the small change of load current, as introduced in (5) and (6) [27].

$$L \frac{\Delta i_{load}}{dt} = L \frac{di_{load}^*}{dt} - V_{out} \quad (5)$$

$$L \frac{\Delta i_{load}}{dt} = V_{ref} - V_{out} \quad (6)$$

### III. THE PROPOSED CONTROLLER

In switching of T-type inverters, spwm based controller methods are used to generate switching signals [28]. However, these methods cannot achieve the following output current at the desired value. For this purpose, in this paper, hysteresis-band controller with feedback current is improved and designed for five-level T-type inverter. The hysteresis controller defines the states of the switching devices in an inverter to make current follow its reference value. In the implementation of the hysteresis controller, the switching is accomplished through a maximum error band of current ( $\Delta i$ ) [29, 30]. This method is based on instantaneous feedback current control in which the load current permanently tracks the reference current within hysteresis band values [31].

Figure 3 clarifies the working fundamentals of the hysteresis-band controller based on current error. In classical hysteresis band controller, it consists of two hysteresis bands: upper and lower. When the current exceeds upper band, the switching signals are produced and the switch is turned on. If the value of current passes to the lower-band, the switching signal turns off. In the proposed controller scheme, four hysteresis values are determined, and it is compared with the actual current error signal. When the current exceeds a pre-defined hysteresis band, the switching signals are produced and the switches are turned on or turned off according to a rational rule. The scheme of proposed hysteresis current controlled T-type inverter is introduced in Fig. 4. The expression of the scheme is expressed below.

In T-type inverter, when S1 and S4 are in conduction mode, the slope of current is positive and describe as follows:

$$\frac{di}{dt} = \frac{V_{dc} - V_m \sin(\omega t + \theta)}{L} \quad (7)$$

When S5 and S4 are in conduction mode, the slope of current is positive and the output voltage is equal to  $+V_{dc}/2$ . It is described as:

$$\frac{di}{dt} = \frac{V_{dc}/2 - V_m \sin(\omega t + \theta)}{L} \quad (8)$$

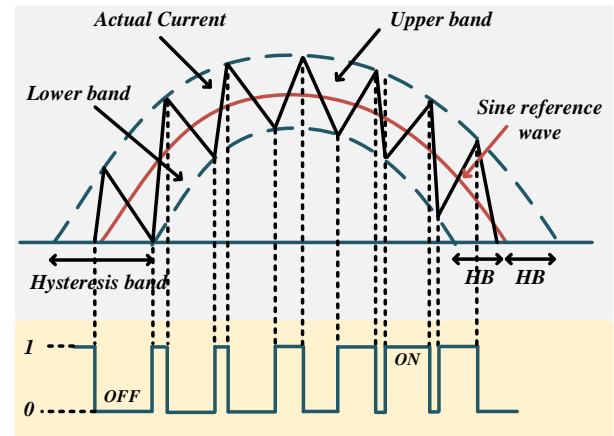


Figure 3. A classical presentation of conventional hysteresis current controller

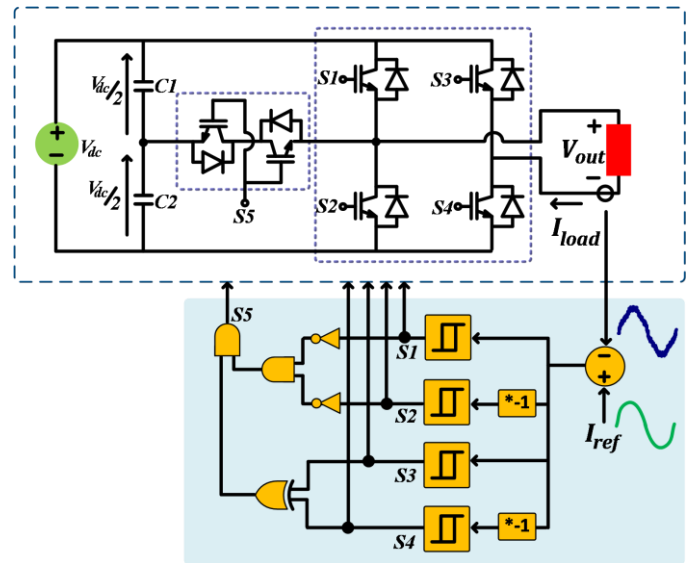


Fig. 4 The proposed hysteresis controller for five-level T-type inverter

In conduction states of S5 and S2, the slope of current is negative and the output voltage is equal to  $-V_{dc}/2$ . It is described as:

$$\frac{di}{dt} = \frac{-(V_{dc}/2 + V_m \sin(\omega t + \theta))}{L} \quad (9)$$

In which,  $V_{dc}$  is dc input voltage,  $V_m \sin(\omega t + \theta)$  is instantaneous load voltage and  $L$  is inductance value. The similar relation when the S2-S3 is turned on and it is written as follows:

$$\frac{di}{dt} = \frac{-(V_{dc} + V_m \sin(\omega t + \theta))}{L} \quad (10)$$

In hysteresis-controller, current ripples and switching frequency are dependent on the depth of the band. For instance, switching at high frequency and low ripple is obtained by very small band value. Also, an optimal band that provides stabilization between harmonics ripples and switching losses is fascinating. Figure 5 presents the illustration of hysteresis band modulation technique for five-

level T-type inverter. In the controller, the error signal is applied at the input of comparator with hysteresis bands.

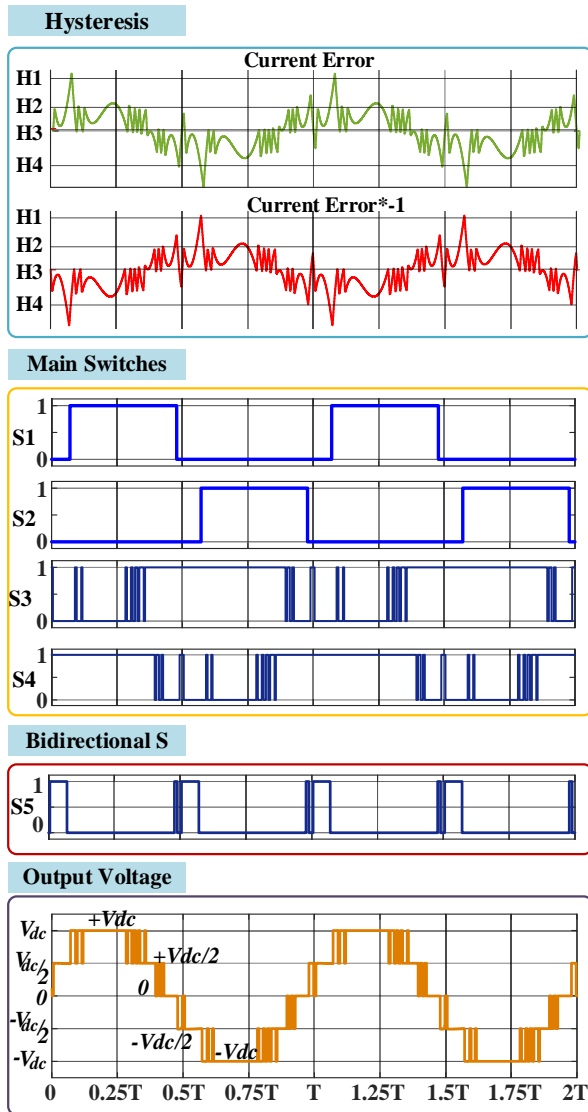


Fig. 5 Illustration of improved hysteresis-band current control based T-type inverter

According to the hysteresis rule of T-type inverter, the conditions for S1, S2, S3 and S4 are:

The switching states of S1 are given as:

$$S_1 = \begin{cases} i_{load}^* - i_{load} > H1 \rightarrow ON \\ i_{load}^* - i_{load} < H4 \rightarrow OFF \end{cases} \quad (11)$$

The switching states of S2 are expressed as:

$$S_2 = \begin{cases} i_{load}^* - i_{load} < H1 \rightarrow ON \\ i_{load}^* - i_{load} > H4 \rightarrow OFF \end{cases} \quad (12)$$

The switching states of S3 are defined as:

$$S_3 = \begin{cases} i_{load}^* - i_{load} > H2 \rightarrow ON \\ i_{load}^* - i_{load} < H3 \rightarrow OFF \end{cases} \quad (13)$$

The switching states of S4 are defined as:

$$S_4 = \begin{cases} i_{load}^* - i_{load} < H2 \rightarrow ON \\ i_{load}^* - i_{load} > H3 \rightarrow OFF \end{cases} \quad (14)$$

where H1, H2, H3 and H4 define the levels of hysteresis controller.

The switching of bidirectional S5 is achieved by logical gates according to the logic table. The switch is turned-on or turned-off according to the below rule:

$$S_5 = \overline{S1}S2(S3S4 + \overline{S3}S4) \quad (15)$$

Bidirectional (S5) signal is derived according to the karnaugh-map rule by using Table 1.

#### IV. PERFORMANCE RESULTS

The proposed modulation strategy is modeled and tested in the Simulink environment. In the tested system, one bidirectional and four mono-directional switches are triggered to generate the output voltage. For this purpose, 100 V dc voltage is used at the input of inverter and 3 ohm resistor is used as a load. Performance results are obtained with and without output filter. The system parameters of the designed model is given in Table 2.

TABLE II  
THE SYSTEM PARAMETERS OF THE DESIGNED CIRCUIT

System parameters	Value
Input voltage	100 Vdc
Output voltage frequency	50 Hz
Transistor	MOSFET
Number of transistors	Six (6)
DC-link capacitors	100 uF
Load resistor	2 ohm
Load inductor	2.2 mH
Filter	Lf=1 mH Lc=1 uF

In the performance stage, hysteresis current controller is performed for two conditions of hysteresis bands. Also, a performance comparison is given in order to show the effectiveness of the proposed method. In the first case study, the hysteresis bands are selected in a wide range. The values of hysteresis are 0.8, 0.3, 0 and -0.5 for H1, H2, H3 and H4, respectively. By this way, the waveforms of switching states and output voltage are introduced in Fig. 6. It is clear that T-type inverter generate five voltage levels through a proposed hysteresis current controller method.

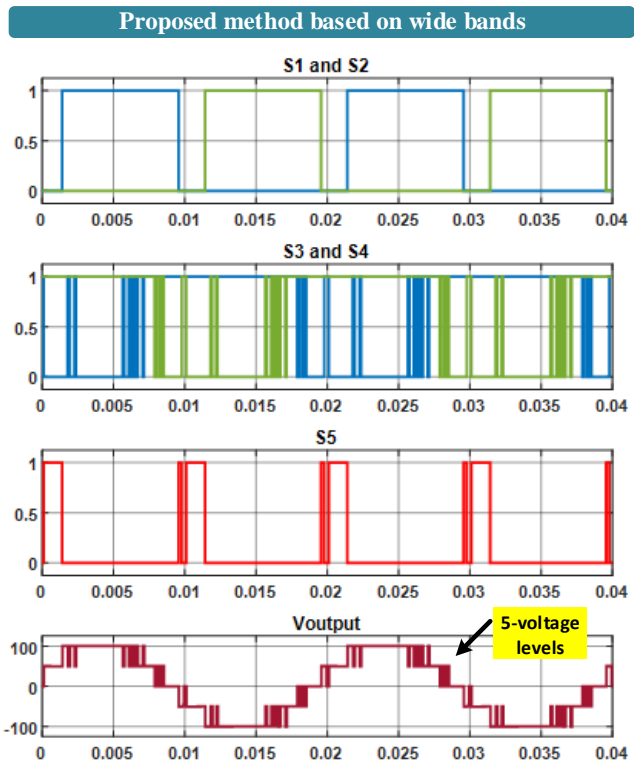


Fig. 6 Switching signals and output voltage at wide-range hysteresis band

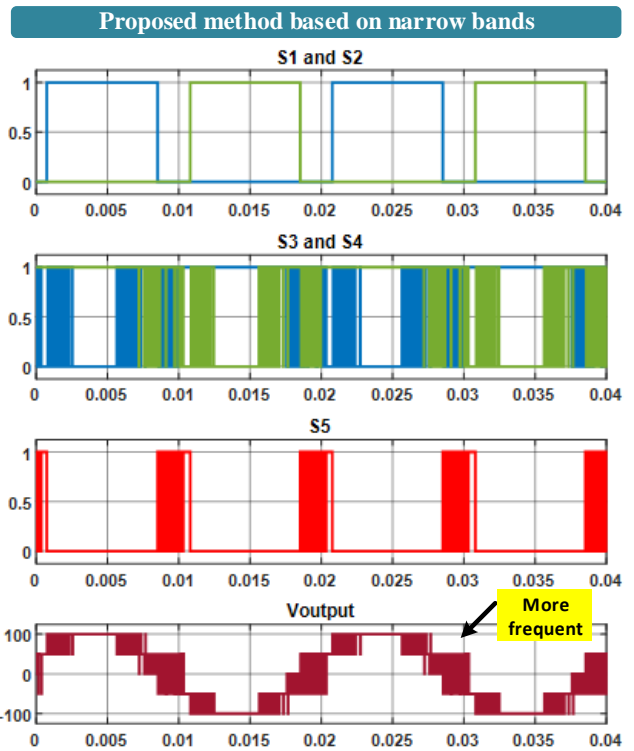


Fig. 7 Switching signals and output voltage at narrow-range hysteresis band

In the second case study, T-type inverter with control based on Hysteresis control is performed in narrowband values. The values of hysteresis bands are respectively 0.8, 0.3, 0 and -0.5 for H1, H2, H3 and H4. In this state, the frequency of the narrowest switching pulse is measured as 10 kHz. The switching states and square-wave output voltage waveforms are presented in Figure 7. It is obvious that the switching frequency of the inverter is higher in comparison of first case.

When the LC filter is used at the output of the inverter, the voltage and current filtered become in sinusoidal form. The waveforms of voltage and current after the filtering are presented in Figure 8. In this case, the performance results are taken for narrowband based hysteresis current controller method.

In performance assessment, THD values of spwm and proposed hysteresis current controller are compared. The harmonic spectrums of both spwm and the proposed method are given in Figure 9. It presents individual harmonic components up to 1 kHz. The switching frequency of each method is selected as 10 kHz for comparison. The comparison results show that THD value by using conventional spwm is 2.97 percent. However, the proposed method can achieve to reduce lower THD values. THD value by using the proposed method is shown as 1.21 percent.

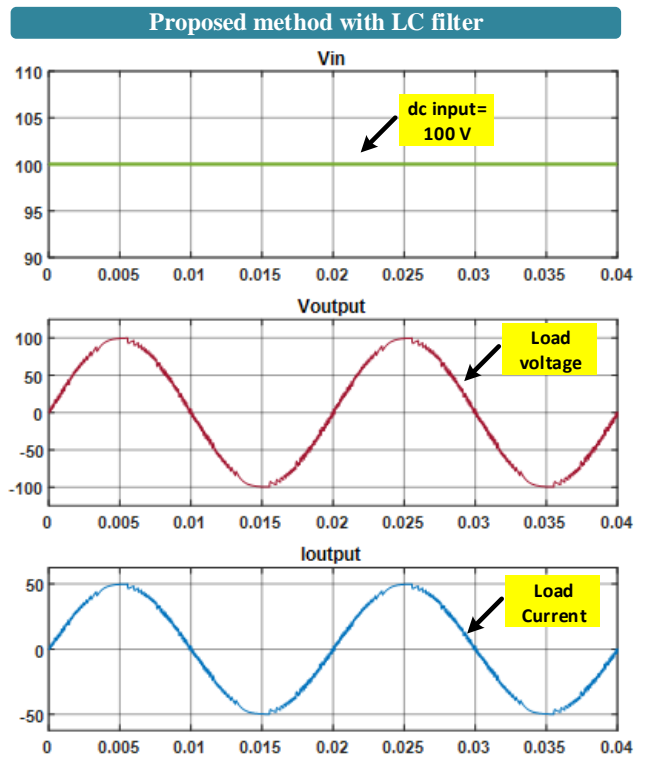


Fig. 8 The waveforms of filtered input/output voltages and output current under narrow hysteresis band control

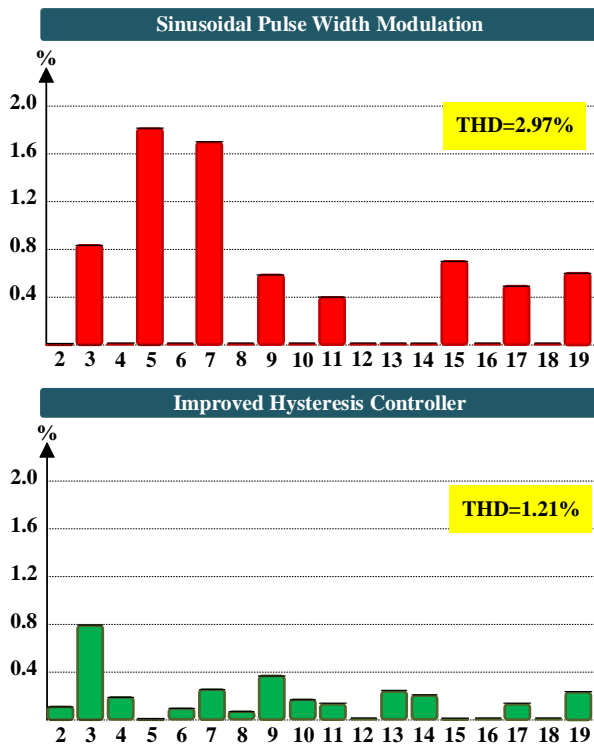


Fig. 9 THD comparison of conventional spwm and improved hysteresis controller at 10 kHz

Table III presents the THD value according to spwm and hysteresis methods. Also, the magnitudes of fundamental and individual harmonic components are given.

TABLE III THD VALUE, HARMONIC INDIVIDUAL PERCENTAGES AND PHASE DEGREES FOR SPWM AND HYSTERESIS METHODS

THD	Spwm		Hysteresis	
	Percentage	Degree	Percentage	Degree
No	2.97%		1.21%	
1	100	-0.8	100	-0.1
2	0.07	86.5	0.22	117.4
3	0.85	-37.4	0.79	207.6
4	0.07	82.9	0.35	-27.1
5	1.83	-17.2	0.06	70.7
6	0.07	79.4	0.17	248.9
7	1.72	-10.8	0.32	226.5
8	0.07	75.9	0.15	60
9	0.54	9.4	0.37	75.8
10	0.07	72.4	0.21	-83.2
11	0.40	16.3	0.16	81.1
12	0.07	68.9	0.06	205.6
13	0.04	-69.6	0.25	-77.3
14	0.06	65.5	0.21	18
15	0.70	198.6	0.04	-59.1
16	0.06	62.1	0.15	-68.3
17	0.51	268.7	0.27	-49.1
18	0.06	58.7	0.06	159.6
19	0.62	-45.1	0.26	121.7

CONCLUSION

In this paper, hysteresis current controller is improved and adapted for five-level T-type inverter. In the proposed controller scheme, the main switches (S1, S2, S3 and S4) are triggered through hysteresis current controller modulation strategy. In order to generate these switching signals, the error

signal between the actual load current and the reference signal is used as hysteresis input. The error signal and its inverted signals are compared with four hysteresis levels in order to generate switching signals of S1, S2, S3 and S4. In triggering of the bidirectional switch, the logical procedure is realized according to the truth table of T-type inverter. The proposed hysteresis controller with feedback current is tested and switching signals are generated for different hysteresis band values. According to the different hysteresis band values, it is obvious that the switching frequency changes in kHz levels. Also, the performance results of the proposed method are compared to conventional spwm technique implemented in T-type inverter. The comparison results show that THD of hysteresis current controlled T-type inverter is lower than spwm controlled inverter. In this way, it presents that proposed modulation strategy shows excellent results for ac-dc voltage conversion in T-type inverter.

REFERENCES

- [1] K. Zeb, W. Uddin, Muhammad A. Khan, Z. Ali, M. U. Ali, N. Christofides, *et al.*, "A comprehensive review on inverter topologies and control strategies for grid connected photovoltaic system," *Renewable and Sustainable Energy Reviews*, vol. 94, pp. 1120-1141, 2018/10/01/ 2018.
- [2] K. Matsui, Y. Kawata, and F. Ueda, "Application of parallel connected NPC-PWM inverters with multilevel modulation for AC motor drive," *IEEE Transactions on Power Electronics*, vol. 15, no. 5, pp. 901-907, 2000.
- [3] A. Sinha, K. Chandra Jana, and M. Kumar Das, "An inclusive review on different multi-level inverter topologies, their modulation and control strategies for a grid connected photo-voltaic system," *Solar Energy*, vol. 170, pp. 633-657, 2018/08/01/ 2018.
- [4] X. Guo and W. Chen, "Control of multiple power inverters for more electronics power systems: A review," *CES Transactions on Electrical Machines and Systems*, vol. 2, no. 3, pp. 255-263, 2018.
- [5] M. S. Irfan, A. Ahmed, and J. Park, "Power-Decoupling of a Multiport Isolated Converter for an Electrolytic-Capacitorless Multilevel Inverter," *IEEE Transactions on Power Electronics*, vol. 33, no. 8, pp. 6656-6671, 2018.
- [6] J. G. Subaman, "4 - Multilevel inverters: an enabling technology," in *Hybrid-Renewable Energy Systems in Microgrids*, A. H. Fathima, N. Prabakaran, K. Palanisamy, A. Kalam, S. Mekhilef, and J. J. Justo, Eds. ed., Woodhead Publishing, 2018, pp. 61-80.
- [7] K. Thakre, K. B. Mohanty, and A. Chatterjee, "Reduction of circuit devices in symmetrical voltage source multilevel inverter based on series connection of basic unit cells," *Alexandria Engineering Journal*, 2018/11/15/ 2018.
- [8] M. Ahmed, A. Sheir, and M. Orabi, "Asymmetric cascaded half-bridge multilevel inverter without polarity changer," *Alexandria Engineering Journal*, 2017/09/12/ 2017.
- [9] E. Babaei, M. F. Kangarlu, M. Sabahi, and M. R. A. Pahlavani, "Cascaded multilevel inverter using sub-multilevel cells," *Electric Power Systems Research*, vol. 96, pp. 101-110, 2013/03/01/ 2013.
- [10] Y. Suresh and A. K. Panda, "Investigation on stacked cascade multilevel inverter by employing single-phase transformers," *Engineering Science and Technology, an International Journal*, vol. 19, no. 2, pp. 894-903, 2016/06/01/ 2016.
- [11] J. Jamaludin, S. Syamsuddin, N. A. Rahim, and H. W. Ping, "Control of switch-sharing-based multilevel inverter suitable for photovoltaic applications," *Journal of the Franklin Institute*, vol. 355, no. 3, pp. 1018-1039, 2018/02/01/ 2018.
- [12] N. Prabakaran and K. Palanisamy, "Analysis and integration of multilevel inverter configuration with boost converters in a photovoltaic system," *Energy Conversion and Management*, vol. 128, pp. 327-342, 2016/11/15/ 2016.
- [13] S. Mariethoz, "Systematic Design of High-Performance Hybrid Cascaded Multilevel Inverters With Active Voltage Balance and

- Minimum Switching Losses," *IEEE Transactions on Power Electronics*, vol. 28, no. 7, pp. 3100-3113, 2013.
- [14] A. Ruderman, "About Voltage Total Harmonic Distortion for Single- and Three-Phase Multilevel Inverters," *IEEE Transactions on Industrial Electronics*, vol. 62, no. 3, pp. 1548-1551, 2015.
- [15] A. Shukla, A. Ghosh, and A. Joshi, "State Feedback Control of Multilevel Inverters for DSTATCOM Applications," *IEEE Transactions on Power Delivery*, vol. 22, no. 4, pp. 2409-2418, 2007.
- [16] J. Venkataramanaiah, Y. Suresh, and A. K. Panda, "A review on symmetric, asymmetric, hybrid and single DC sources based multilevel inverter topologies," *Renewable and Sustainable Energy Reviews*, vol. 76, pp. 788-812, 2017/09/01/ 2017.
- [17] A. Chen and X. He, "Research on Hybrid-Clamped Multilevel-Inverter Topologies," *IEEE Transactions on Industrial Electronics*, vol. 53, no. 6, pp. 1898-1907, 2006.
- [18] A. Narendrababu, N. Yalla, and P. Agarwal, "A modified T-type single phase five-level inverter with reduced switch voltage stress," *2018 International Conference on Power, Instrumentation, Control and Computing (PICC)*, 2018, pp. 1-5.
- [19] K. Lee, H. Shin, and J. Choi, "Comparative analysis of power losses for 3-Level NPC and T-type inverter modules," *2015 IEEE International Telecommunications Energy Conference (INTELEC)*, 2015, pp. 1-6.
- [20] M. M. Harin, V. Vanitha, and M. Jayakumar, "Comparison of PWM Techniques for a three level Modular Multilevel Inverter," *Energy Procedia*, vol. 117, pp. 666-673, 2017/06/01/ 2017.
- [21] H. Athari, M. Niroomand, and M. Ataei, "Review and Classification of Control Systems in Grid-tied Inverters," *Renewable and Sustainable Energy Reviews*, vol. 72, pp. 1167-1176, 2017/05/01/ 2017.
- [22] H. P. Vemuganti, D. Sreenivasarao, and G. S. Kumar, "Improved pulse-width modulation scheme for T-type multilevel inverter," *IET Power Electronics*, vol. 10, no. 8, pp. 968-976, 2017.
- [23] P. Singh, S. Tiwari, and K. K. Gupta, "A new topology of transistor clamped 5-level H-Bridge multilevel inverter with voltage boosting capacity," *2012 IEEE International Conference on Power Electronics, Drives and Energy Systems (PEDES)*, 2012, pp. 1-5.
- [24] N. Abd Rahim, M. F. M. Elias, and W. P. Hew, "Transistor-Clamped H-Bridge Based Cascaded Multilevel Inverter With New Method of Capacitor Voltage Balancing," *IEEE Transactions on Industrial Electronics*, vol. 60, no. 8, pp. 2943-2956, Aug 2013.
- [25] G. E. Valderrama, G. V. Guzman, E. I. Pool-Mazun, P. R. Martinez-Rodriguez, M. J. Lopez-Sanchez, and J. M. S. Zuniga, "A Single-Phase Asymmetrical T-Type Five-Level Transformerless PV Inverter," *Ieee Journal of Emerging and Selected Topics in Power Electronics*, vol. 6, no. 1, pp. 140-150, Mar 2018.
- [26] M. Anzari, J. Meenakshi, and V. T. Sreedevi, "Simulation of a transistor clamped H-bridge multilevel inverter and its comparison with a conventional H-bridge multilevel inverter," *2014 International Conference on Circuits, Power and Computing Technologies [ICCPCT-2014]*, 2014, pp. 958-963.
- [27] W. Huaisheng and X. Huifeng, "A Novel Double Hysteresis Current Control Method For Active Power Filter," *Physics Procedia*, vol. 24, pp. 572-579, 2012/01/01/ 2012.
- [28] F. Wang, Y. Wang, L. J. Hang, and C. M. Wang, "Five-level inverter for solar system and its self-adaptive pulse-width modulation strategy," *IET Power Electronics*, vol. 9, no. 1, pp. 102-110, Jan 20 2016.
- [29] L. Malesani, P. Mattavelli, and P. Tomasin, "Improved constant-frequency hysteresis current control of VSI inverters with simple feedforward bandwidth prediction," *IEEE Transactions on Industry Applications*, vol. 33, no. 5, pp. 1194-1202, 1997.
- [30] D. S. Oh and M. J. Youn, "Automated adaptive hysteresis current control technique for a voltage-fed PWM inverter," *Electronics Letters*, vol. 26, no. 24, pp. 2044-2046, 1990.
- [31] A. Fereidouni, M. A. S. Masoum, and K. M. Smedley, "Supervisory Nearly Constant Frequency Hysteresis Current Control for Active Power Filter Applications in Stationary Reference Frame," *IEEE Power and Energy Technology Systems Journal*, vol. 3, no. 1, pp. 1-12, 2016.

## BIOGRAPHIES



MUSTAFA İNCİ received the B.S. and M.S. degrees in Electrical-Electronics engineering from the Çukurova University, Adana, in 2011 and 2013 the Ph.D. degree in mechanical engineering from Çukurova University, Adana, Turkey, in 2017.

From 2011 to 2018, he was a Research Assistant with the Çukurova University. Since 2018, he has been an Assistant Professor with the Mechatronics Engineering Department, İskenderun Technical University. He is the author of more than 10 articles, and more than 20 conference papers. His research interests include grid integration of renewable energy systems and advanced power electronic converters.

# Sub-block Aided OFDM with Index Modulation

Y. ACAR

**Abstract**—Recently, orthogonal frequency division multiplexing (OFDM) with index modulation (IM) has been appeared as a novel method for future wireless communication systems. However, such a mechanism has low spectral efficiency since some sub-carriers are not activated in order to implicitly convey information. In this paper, a subblock dependent approach, called sub-block aided OFDMIM (SA-OFDM-IM) technique, is proposed for spectral efficiency enhancement of the OFDM-IM method with lower complexity. The simulation results illustrate that the proposed SA-OFDM-IM and well known OFDM-IM have same bit error rate (BER) performance while SA-OFDMIM has 40% more spectral efficiency with low complexity.

**Index Terms**— Orthogonal frequency division multiplexing (OFDM), index modulation (IM), spatial modulation (SM).

## I. INTRODUCTION

MULTIPLE-ANTENNA techniques constitute a key technology for next-generation fixed and mobile wireless communication systems [1]. Their performance is related to some restriction such as the spacing between transmitter and receiver antennas [2], [3], inter-antenna synchronization (IAS) at the transmitter and also inter-channel interference (ICI) [4], [5]. To circumvent these problems, Mesleh *et al.* proposed spatial modulation (SM) as a low computational complexity alternative to well known MIMO systems [6]. The SM technique is using the indices of transmit antennas to carry extra data, in addition to the 2 dimensional  $M$ -ary signal constellations. To show the potential benefits of SM, several experimental studies have done and it has shown that SM scheme is an alternative to the plain MIMO systems [7]. Consequently, the SM is promising transmission technique that has a very flexible structure and provides low complexity with high spectral efficiency [8].

Orthogonal frequency division multiplexing (OFDM) is being used by wireless communications systems such as the world wide interoperability for microwave access (WiMAX), long term evolution (LTE), IEEE 802.11 (Wi-Fi), etc. [9], [10], [11], [12]. As, OFDM has become the very popular multi-carrier modulation method, it continues to be widely studied. Following this trend, the index modulation (IM)

concept which is inspired by SM has draw attention as a promising technique for the new-generation wireless communication systems in the last decade [13]. It has many significant advantages such as reduced peak-to-average power ratio (PAPR), better bit-error-rate (BER), energy efficiency, higher robustness against the inter-carrier interference (ICI) etc. [13], [14], [15].

In [16] and [17] MIMO-OFDM-IM technique is proposed by combining MIMO and OFDM-IM transmission methods. In [18] sub-carrier block interleaving is proposed for OFDM-IM to enhance its error performance. The bit error probability of OFDM-IM is analytically derived in [19]. Recently, generalization of OFDM-IM has been proposed by extending the index domain to include quadrature and inphase dimensions [20]. For more details on these studies, the concerned readers are referred to [21].

In spite of its advantages mentioned above, there is still limitation to the operation of OFDM-IM in wireless communications. The OFDM-IM scheme cause a decrease in data rate due to its unused subcarriers. To solve this difficulty, this paper proposes a new OFDM-IM with improved spectral efficiency and low complexity through integrating a new constellation design using sub-block. It is also shown that proposed SA-OFDM-IM performs same performance with traditional OFDM while SA-OFDM-IM has more spectral efficiency with low complexity.

The remain of this study is given as; Section II demonstrates the principle of proposed SA-OFDMIM scheme. Section III introduces the receiver part of the SA-OFDM-IM. The computational complexity and simulation results are given in Section IV and Section V, respectively. Finally, conclusion is presents in Section VI.

## II. PROPOSED SA-OFDM-IM METHOD

In [13], sub-carriers were partitioned into  $g$  subblocks which have  $n$  sub-carriers. In each sub-blocks only  $k$  out of these  $n$  sub-carriers are active, and the remains are inactive. The total number of transmitted data bits for OFDM-IM system is calculated as

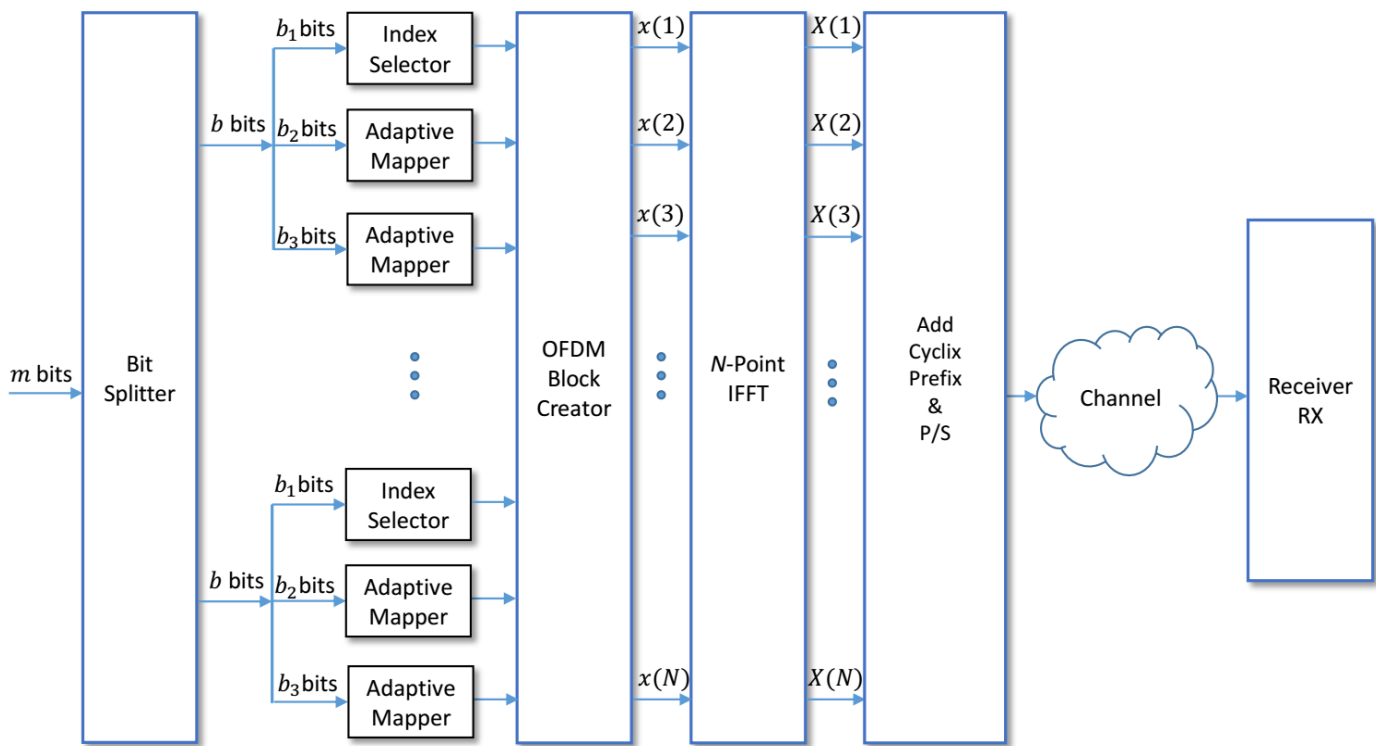
$$m_m = \lfloor \log_2(C(n, k)) \rfloor g + k \log_2(M)g. \quad (1)$$

**Yusuf ACAR**, is with Department of Electrical and Electronic Engineering, Istanbul Kültür University, Bakırköy, Istanbul, 34156, Turkey, (e-mail: y.acar@iku.edu.tr).

 <https://orcid.org/0000-0002-3956-1097>

Manuscript received January 17, 2019; accepted March 26, 2019.

DOI: [10.17694/bajece.514324](https://doi.org/10.17694/bajece.514324)



A LOOK-UP TABLE FOR SYMSBOL PAIRS GIVE IN FIG.1 (b)

Fig.1. Block diagram of the proposed scheme

where  $M$  represents the modulation size,  $\lfloor \cdot \rfloor$  is the floor operation and  $C(n,k)$  shows the binomial number. It is clear that, unused sub-carriers cause the low spectral efficiency. In this work, sub-block aided OFDM-IM (SA-OFDM-IM) is proposed, to gain a high spectral efficiency rate without degrading BER performance and maintaining same power consumption.

Block diagram of the proposed scheme is given in Fig. 1. To take advantage of sub-blocks (not subcarriers), we design the new constellation scheme as shown in Fig. 2. We split all symbols in a pairs. For example, in Fig. 2 (b), there are two shifted binary phase shift keying (BPSK) symbol pairs  $(\{x_1^1, x_1^2\}, \{x_2^1, x_2^2\}) \in S_a$  hence there are two BPSK symbol pairs i.e.  $M = 2$ . Similarly, symbol pairs in Fig. 2 (c) are given as  $(\{x_1^1, x_1^2\}, \{x_2^1, x_2^2\}, \{x_3^1, x_3^2\}, \{x_4^1, x_4^2\}) \in S_b$ , thus  $M$  is 4.

TABLE I  
A LOOK-UP TABLE FOR SYMSBOL PAIRS GIVE IN FIG.1 (a)

Bits	Symbol Pairs
[0]	$\{x_1^1, x_1^2\}$
[1]	$\{x_2^1, x_2^2\}$

We simply assign the information bits in each symbol pairs as given in Tables I-II for proposed constellation diagram. Then, for each sub-block, we used these symbol pairs according to incoming information bits. For instance, if

TABLE II

Bits	Sub-block Indices	Sub-block Symbols
[0,0]	{2,3}	$[x_i^j, x_i^j, 0, 0]$
[0,1]	{3,2}	$[0, x_i^j, x_i^j, 0]$
[1,0]	{4,3}	$[0, 0, x_i^j, x_i^j]$
[1,1]	{4,1}	$[x_i^j, 0, 0, x_i^j]$

TABLE II  
A LOOK-UP TABLE FOR SYMSBOL PAIRS GIVE IN FIG.1 (b)

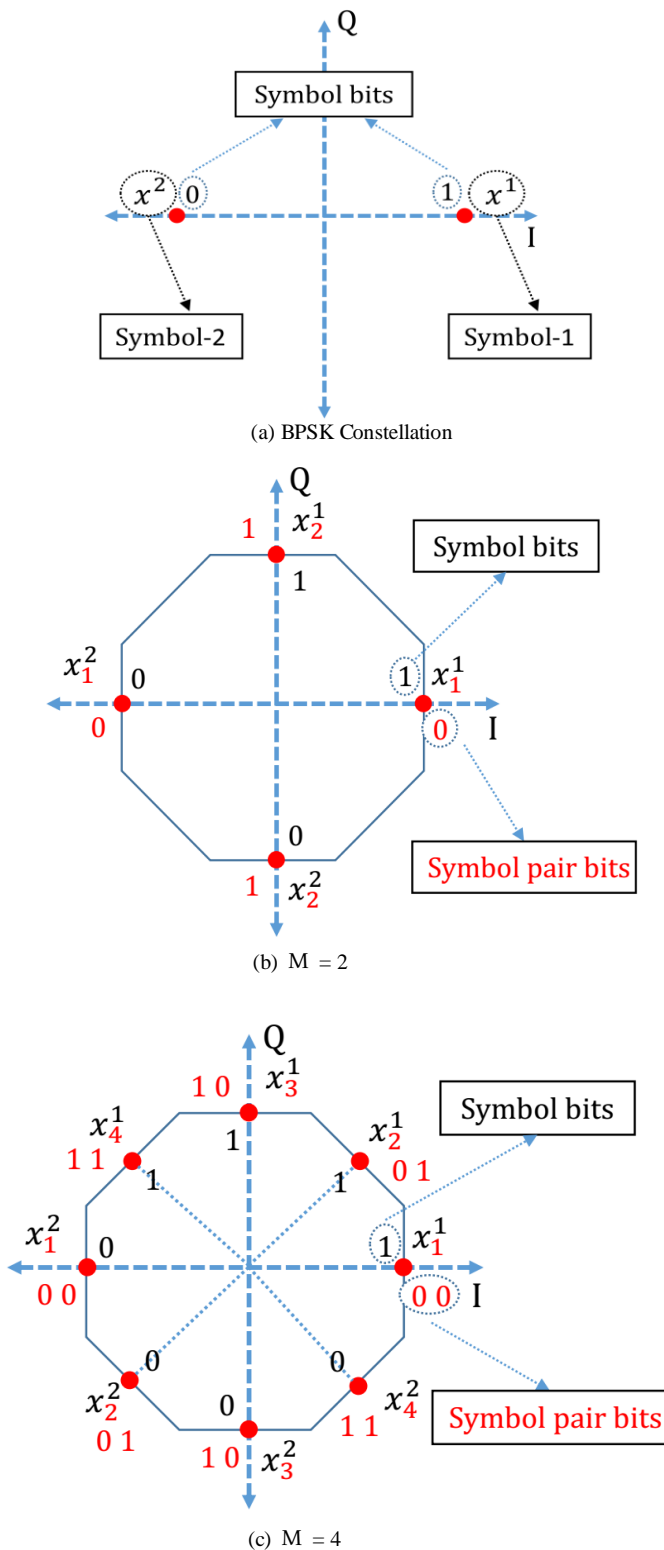


Fig.2. Proposed constellation diagram for total number of symbol pairs for (b) M = 2 and (c) M = 4

The total transmitted bits of proposed scheme can be determined as

$$m_{SA} = \lfloor \log_2(C(n, k)) \rfloor g + k \log_2(M)g + \log_2(M)g$$

$$= m_{IM} + \log_2(M)g. \tag{2}$$

Therefore, in the proposed system, in contrast to OFDM-IM, all sub-block within the whole OFDM symbol are used to carry additional bits. If the SAOFDM-IM and existing OFDM-IM techniques are compared, the total number of data bits, *i.e.* spectral efficiency of the SA-OFDM-IM technique is greater than that of the existing OFDM-IM schemes. For example, OFDM-IM has  $m_{IM}=256$  bits for BPSK modulation while SA-OFDM-IM has  $m_{SA}=320$  bits for  $M = 2$ . Using sub-block also increases the frequency diversity gain in addition to the diversity gain brought by IM.

In the proposed system, incoming bits are divided into  $b = m_{SA}/g$  bits. Hence, each sub-block contains  $b$  bits. In the each sub-block, the  $b$  bits are split into three parts as  $b = b_1 + b_2 + b_3$  for different goals. The first part,  $b_1$  bits, is used to determine the sub-carrier index as given in Table III. The second part,  $b_2$  bits, is used by symbol pairs as given Tables I-II. Finally,  $b_3$  bits is used by modulated symbol  $x_i^j, j = 1, 2, i = 1, \dots, M$ .

Fig. 3 shows an illustrative frame structure of the proposed scheme where total number of sub-carrier  $N = 16, n = 4$  and  $k = 2$ . We give two example below for better understating.

**Example 1:**

Assume that incoming bits are [0 1 0 0 1 0] for first sub-block as shown in Fig. 3. The first two bits [0 1] show the sub-carriers index, (*i.e.*, in transmission second and third sub-carriers will be activated) then other two bits [0 0] are denote the symbol pair index  $\{x_i^1, x_i^2\}, i = 1, \dots, M$  where  $M = 4$  and  $i = 1$  as given in Table II. The last two bits [1 0] are for the symbol bits of  $x_1^1 \rightarrow [1]$  and  $x_1^2 \rightarrow [0]$ .

**Example 2:**

In this example, incoming bits are [1 0 1 0 0 1] for fourth sub-block. The first two bits [1 0] illustrate that in transmission fourth and third sub-carriers will be activated. Other two bits [1 0] are assigned the symbol pair index  $\{x_i^1, x_i^2\}, i = 1, \dots, M$  where  $M = 4$  and  $i = 3$ . Finally, last two bits [0 1] are for the symbol bits of  $x_3^1 \rightarrow [1]$  and  $x_3^2 \rightarrow [0]$ .

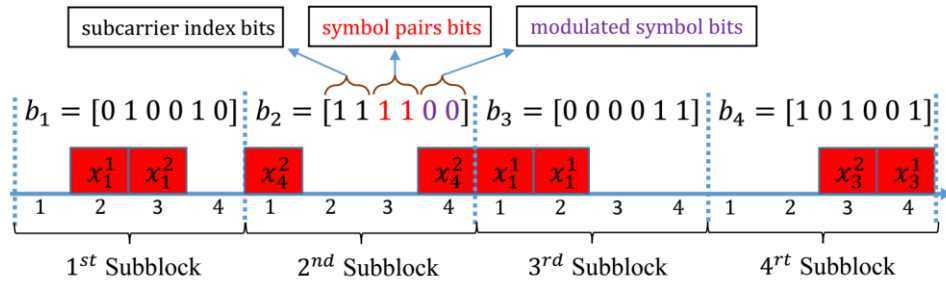


Fig.3. An illustrative frame structure of the proposed scheme with  $N = 16$ ,  $n = 4$  and  $k = 2$

By concatenating these  $g$  sub-blocks,  $\mathbf{x}_F$  can be transmitted symbols of the SA-OFDM-IM method :

$$\mathbf{x}_F = \left[ x_i^j(1), x_i^j(2), \dots, x_i^j(N) \right], \quad (3)$$

$$j = 1, 2, \quad i = 1, \dots, M$$

Then, after applying IFFT, the OFDM symbol given as:

$$\mathbf{x}_T = \frac{N}{\sqrt{Z}} \mathbf{W}_N^H \mathbf{x}_F \quad (4)$$

where  $\mathbf{W}_N$  is the FFT matrix with  $\mathbf{W}_N^H \mathbf{W}_N = \mathbf{M} \mathbf{I}_N$ ,  $Z = kg$  is the number of active sub-carriers, and  $N/\sqrt{Z}$  term is used for the normalization  $E\{x_T^H x_T\} = N$ .

At the receiver, the received signal is given as

$$y_F(f) = h_F(f)x(f) + w_F(f) \quad (5)$$

where  $w_F(f)$  and  $h_F(f)$  are the noise samples and the channel fading coefficients in the frequency domain, respectively.

### III. MAXIMUM LIKELIHOOD (ML) DETECTOR

We investigate ML detector to estimate the information from the received symbols for proposed scheme. Owing to channel impulse response knowledge, in order to estimate the modulated symbols ( $\hat{x}_{i,\beta}^j$ ) and the active indices ( $\hat{I}_\beta$ ) in each sub-block. Then, estimation of the data symbols and active indices are calculated as follows:

$$\left( \hat{I}_\beta, \hat{x}_{i,\beta}^j \right) = \arg \min_{I_\beta, x_{i,\beta}^j} \sum_{\gamma=1}^k \left| y_F^\beta(i_{\beta,\gamma}) - h_F^\beta(i_{\beta,\gamma}) x_{i,\beta}^j(\gamma) \right|^2 \quad (6)$$

$$j = 1, 2, \quad i = 1, \dots, M$$

where  $y_F^\beta(i_{\beta,\gamma})$ ,  $i_{\beta,\gamma}$ , and  $h_F^\beta(i_{\beta,\gamma})$  show the received symbols, the indices corresponding to active indices set of  $I_\beta = \{i_{\beta,1}, \dots, i_{\beta,k}\}$ , and the channel coefficients for the sub-

lock  $\beta$ , respectively.  $x_{i,\beta}^j$ ,  $j = 1, 2$ ,  $i = 1, \dots, M$  denotes the vector of modulated signals from designed two dimensional constellation alphabets in Fig. 2. To obtain the transmitted information bits on each sub-block, receiver uses these two estimates,  $\hat{x}_{i,\beta}^j$  and  $\hat{I}_\beta$ , in the Tables I - II by an inverse mapping process.

### IV. COMPUTATIONAL COMPLEXITY (CC) COMPARISON

The CC of the ML detector for exiting OFDMIM is  $\sim O(rM^k)$  where  $r$  denotes the number of possible realizations of the selected active indices and  $M$  is modulation order. It is obvious that, the CC of exiting OFDM-IM with BPSK is  $\sim O(r2^k)$ . As seen in Fig. 2, the proposed method uses BPSK and  $\pi/2$  rotated form of BPSK. Hence, the CC of proposed method for the ML detector with  $M = 2$  is  $\sim O(2r2^k)$ . Consequently, the CC of the SAOFDM-IM is  $\sim O(Mr2^k)$  while OFDM-IM is  $\sim O(rM^k)$ . It is clear that the CC of our proposed scheme is much lower than OFDM-IM scheme with the higher modulation size.

### V. SIMULATION RESULTS

The BER performance of the proposed technique is evaluated for new constellation design with  $M = 2$  and  $M = 4$  by assuming frequency selective Rayleigh channels with length  $N_L$ . The total number of sub-carriers in one block is set to  $n = 4$ . The SNR is described as  $E_b/N_0$  where  $N_0$  is the noise power and  $E_b$  is energy per bit.

The BERs of OFDM-IM and proposed system are given in Figs. 4-5 as functions of the SNR for  $N = 256$  and  $N = 1024$ , respectively. As shown in from Fig. 4, the proposed method with  $M = 2$  achieves almost same performance of the well known OFDM-IM with BPSK and  $N = 256$ . In that case, the total number of data bits transmitted by the proposed method is  $m_{sa} = 320$  while OFDM-IM is  $m_{im} = 256$  bits. Moreover, proposed method with  $M = 2$  and OFDM-IM with QPSK modulation scheme have same number of bits as  $m_{sa} = m_{im} = 384$  while proposed method has better

performance. We also use log likelihood receiver (LLR) for OFDM-IM systems for QPSK modulation to compare with the proposed scheme.

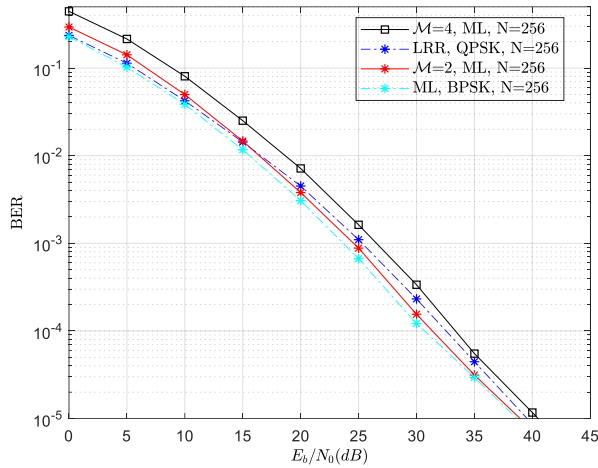


Fig.4. BER performances of proposed SA-OFDMIM scheme and exiting OFDM-IM with  $N = 256$ ,  $k = 2$  and  $n = 4$

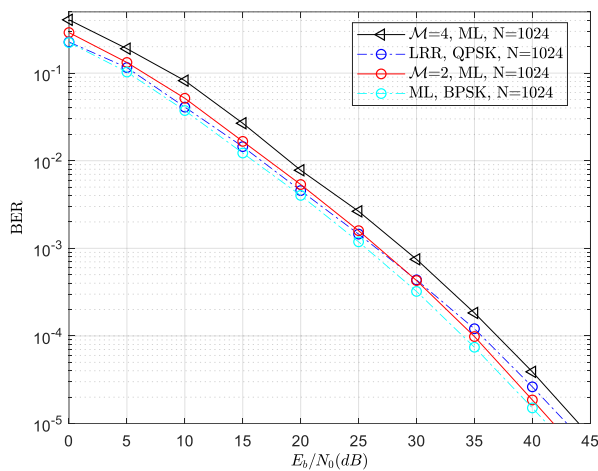


Fig.5. BER performances of proposed SA-OFDMIM scheme and exiting OFDM-IM with  $N = 1024$ ,  $k = 2$  and  $n = 4$

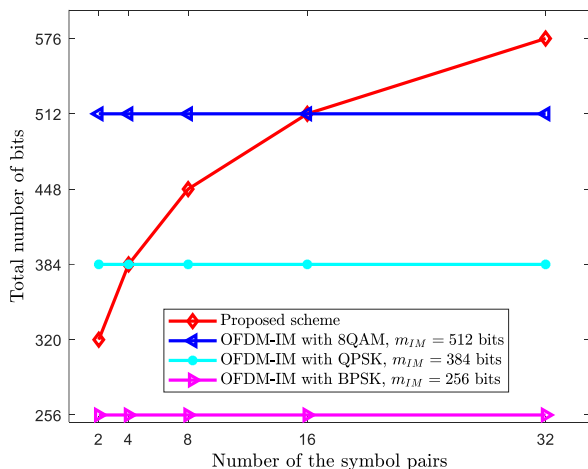


Fig.6. Total number of bits with  $N = 256$ ,  $n = 4$  and  $k = 2$

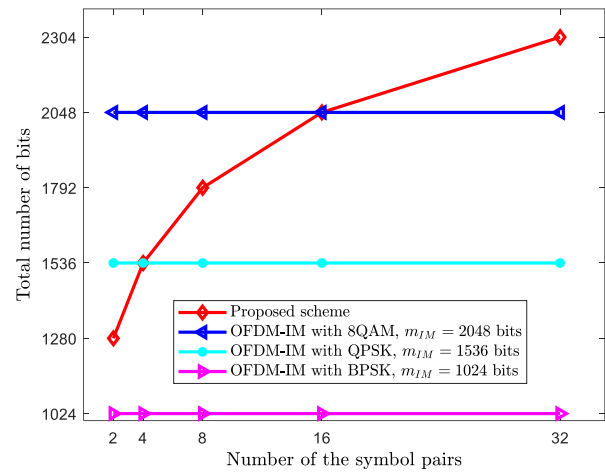


Fig.7. Total number of bits with  $N = 1024$ ,  $n = 4$  and  $k = 2$

Figs. 6-7 depicts the impact of increasing the number of the BPSK symbol pairs  $M$  on the spectral efficiency of the proposed technique for  $N = 256$  and  $N = 1024$ , respectively. The spectral efficiency of the proposed method has a high positive correlation with the number of symbol pairs  $M$ .

As illustrated in Fig. 7, the total number of bits carry by the proposed scheme with  $M = 2$  is  $m_{sa} = 1280$  while OFDM-IM with BPSK is  $m_{IM} = 1024$  bits. As a result, the spectral efficiency of the proposed method is 40% higher than OFDM-IM system, while both of them has the same performance and complexity.

## VI. CONCLUSIONS

High spectral efficiency is one of the challenge issue in the next generation wireless communication systems such as 5G, 6G etc. In this work, to obtain the high spectral efficiency of the OFDM-IM method, new constellation diagrams are designed for each sub-blocks. The bit error rate and total number of bits for proposed method are investigated and the computational complexity is given. Results show that using the proposed constellations in each subblock a high spectral efficiency is achieved with same BER performance and tolerable complexity compared to currently known OFDM IM. In future, this work might be extended to multiple-input multiple-output (MIMO) scheme to increase spectral efficiency more.

## REFERENCES

- [1] N. Panwar, S. Sharma, and A. K. Singh, "A survey on 5g: The next generation of mobile communication," *Physical Communication*, vol. 18, 2016, pp. 64–84.
- [2] A. Sibille, C. Oestges, and A. Zanella, *MIMO: from theory to implementation*, Academic Press, 2010.
- [3] C. Oestges and B. Clerckx, *MIMO wireless communications: From real-world propagation to space-time code design*, Academic Press, 2010.
- [4] S. Ahmadi, *LTE-advanced: A practical systems approach to understanding 3GPP LTE releases 10 and 11 radio access technologies*. Academic Press, 2013.
- [5] A. V. Nikitin, "On the interchannel interference in digital communication systems, its impulsive nature, and its mitigation," *EURASIP Journal on Advances in Signal Processing*, Vol.2011, No.1, 2011, pp. 137.
- [6] R. Mesleh, H. Haas, C. W. Ahn, and S. Yun, "Spatial modulation - A new low complexity spectral efficiency enhancing technique," in *Proc. Conf. Commun. Netw. China, Beijing, China, Oct. 2006*, pp. 1–5.
- [7] N. Serafimovski, A. Younis, R. Mesleh, P. Chambers, M. Di Renzo, C.-X. Wang, P. M. Grant, M. A. Beach, and H. Haas, "Practical implementation of spatial modulation," *IEEE Trans. Veh. Technol.*, Vol.62, No.9, 2013, pp. 4511–4523.
- [8] M. Di Renzo, H. Haas, and P. M. Grant, "Spatial modulation for multiple-antenna wireless systems: a survey," *IEEE Commun. Mag.*, Vol.49, No.12, pp. 182–191, December 2011.
- [9] J. G. Andrews, A. Ghosh, and R. Muhamed, *Fundamentals of WiMAX: understanding broadband wireless networking*, Pearson Education, 2007.
- [10] S. Sesia, M. Baker, and I. Toufik, *LTE-the UMTS long term evolution: from theory to practice*, John Wiley & Sons, 2011.
- [11] E. Dahlman, S. Parkvall, and J. Skold, *4G: LTE/LTE-advanced for mobile broadband*. Academic press, 2013.
- [12] B. P. Crow, I. Widjaja, J. G. Kim, and P. T. Sakai, "IEEE 802.11 wireless local area networks," *IEEE Communications magazine*, Vol.35, No.9, 1997, pp. 116–126.
- [13] E. Başar, Ü. Aygözü, E. Panayırıcı, and H. V. Poor, "Orthogonal frequency division multiplexing with index modulation," *IEEE Transactions on Signal Processing*, Vol.61, No.22, 2013, pp. 5536–5549.
- [14] M. Wen, B. Ye, E. Basar, Q. Li, and F. Ji, "Enhanced orthogonal frequency division multiplexing with index modulation," *IEEE Trans. Wireless Commun.*, Vol.16, No.7, 2017, pp. 4786–4801.
- [15] N. Ishikawa, S. Sugiura, and L. Hanzo, "Subcarrier-index modulation aided ofdm-will it work?" *IEEE Access*, Vol.4, 2016, pp. 2580–2593.
- [16] E. Başar, "Multiple-input multiple-output OFDM with index modulation," *IEEE Signal Processing Letters*, Vol.22, No.12, 2015, pp. 2259–2263.
- [17] B. Zheng, M. Wen, E. Basar, and F. Chen, "Multiple-input multiple-output OFDM with index modulation: Low-complexity detector design," *IEEE Transactions on Signal Processing*, Vol.65, No.11, 2017, pp. 2758–2772.
- [18] Y. Xiao, S. Wang, L. Dan, X. Lei, P. Yang, and W. Xiang, "OFDM with interleaved subcarrier-index modulation," *IEEE Communications Letters*, Vol.18, No. 8, 2014, pp. 1447–1450.
- [19] Y. Ko, "A tight upper bound on bit error rate of joint OFDM and multi-carrier index keying," *IEEE Communications Letters*, Vol.18, No.10, 2014, pp. 1763–1766.
- [20] R. Fan, Y. J. Yu, and Y. L. Guan, "Generalization of orthogonal frequency division multiplexing with index modulation," *IEEE transactions on wireless communications*, Vol.14, No.10, pp. 5350–5359, 2015.
- [21] E. Başar, M. Wen, R. Mesleh, M. Di Renzo, Y. Xiao, and H. Haas, "Index modulation techniques for next-generation wireless networks," *IEEE Access*, Vol.5, 2017, pp. 693–746.

## BIOGRAPHY



**YUSUF ACAR** received the B.S.E. degree (with honors), M.S.E. degree and Ph.D. degrees in Electrical and Electronics Engineering from Istanbul University, Istanbul, Turkey, in 2008, 2011 and 2015, respectively. In 2015, he joined the Department of Electrical and Electronics Engineering, Istanbul Kültür

University as an Assistant Professor.

He was a researcher at the Purdue University Fort Wayne (PFW), USA, between the September 2017 and September 2018. His general research interests cover communication theory, estimation theory, statistical signal processing, and information theory. His current research activities are focused on software-defined platforms.

# Multispectral Palmprint Recognition Based on Multidirectional Transform

B. OZMEN and O. J. OLALEYE

**Abstract**—Multispectral palmprint recognition is one of the most useful biometric techniques due to features obtained from different spectral resolutions/wavelengths. In this paper, we propose a multidirectional transform-based feature encoding plan for reliable and robust representation and matching of multispectral palm images. The method extracts the region of interest (ROI) for palmprint images captured with non-contact sensors. The registered ROI of each band is newly downsampled using DWT. This approach allows us to take more lines into consideration for interpolation. A undecimated dual-tree complex wavelet transform based multidirectional feature encoding plan is then newly applied since it provides better shift invariance and directional selectivity. Finally, a binary code matching strategy with score level fusion is used to compute matching for efficient identification. The experimental results obtained on CASIA and PolyU datasets show that the presented method gives better results in the blurring binary code matching case than state-of-the-art methods and provides comparable performance in the non-blurring binary code matching.

**Index Terms**—Feature Extraction, Image Recognition, Matching, Multispectral Encoding, Pattern Analysis, Wavelet Transforms.

## I. INTRODUCTION

BIOMETRICS IS THE method used to recognize individuals based on one or more authentic physical and/or behavioral traits [1]. Palmprint recognition has attracted much attention from researchers [2]–[6] due to its ease of use, high speed, robustness, reliability and affordability. 3D imaging can be used to improve the accuracy of the palmprint system and ability to detect spoof attacks [7]. However, improper tools and the cost of the systems make it difficult to use. Multispectral imaging can be one solution [8]–[10]. It captures an image in a range of spectral bands.

**B. OZMEN**, is with Department of Electrical & Electronics Engineering, European University of Lefke, Lefke, Northern Cyprus, TR-10 Mersin, Turkey, (e-mail: [bozmen@eul.edu.tr](mailto:bozmen@eul.edu.tr)).

 <https://orcid.org/0000-0002-3608-394X>

**O. J. OLALEYE**, is with Department of Electrical & Electronic Engineering, Cyprus International University, Haspolat - Lefkoşa, Northern Cyprus, TR-10 Mersin, Turkey, (e-mail: [olaleyeolayinka30@gmail.com](mailto:olaleyeolayinka30@gmail.com)).

 <https://orcid.org/0000-0003-0692-0847>

Manuscript received January 28, 2019; accepted April 22, 2019.  
DOI: [10.17694/bajece.518050](https://doi.org/10.17694/bajece.518050)

Specific features of each palm can be obtained from different spectral bands so that we have enough information to enhance its accuracy. The antispoofing capability of palmprint systems can be improved.

The unique patterns that can be seen with the naked eye are the principal lines, the fine edges and the wrinkles [11]. Standard imaging devices can capture these superficial features. High-wavelength scanners can capture the fine ridges that can be used for inert palmprint identification in forensics [12]. The wrinkles and principal lines captured with low-wavelength sensors are well-suited for security applications such as client identification or authentication [13]. The subsurface vein pattern is extra information presented in the human palm. The subsurface vein pattern is unrelated to the palm lines. Standard imaging sensors cannot identify such features. Infrared imaging can capture subsurface features due to its capability to penetrate the skin. Multispectral palmprint recognition can be used to investigate the subsurface and superficial features of a palm. Multispectral imaging captures images at multiple wavelengths. These complementary features (veins and palm lines) allow for increased discrimination between persons. These features of palm images are important to improve performance where user cooperation is moderate, such as secure access gates, personality records and workplace entry.

Multispectral palm pictures can be captured by using monochromatic camera under spectrally changing illumination [14], [15]. Hand movement is restricted by contact device but increases user admissibility issues due to hygiene. Nevertheless, biometrics which are captured with non-contact sensors are more useful and socially more sufficient [16], but create the problem of Rotation-Scale-Translation (RST) variations. The movement of the palm is the reason for these misalignments. Landmark detection and ROI extraction must be applied to solve this problem. A robust feature extraction strategy is required for precise recognition of line-like edges, because of the multi-modal nature of the palm. In addition, multi-modal feature extraction results with many features cause slow matching time and require large storage resources. These challenges can be solved with a feature encoding plan and matching technique.

This paper presents a new multidirectional transform-based feature encoding strategy for reliable and robust representation and matching. A reliable method is applied to extract ROI from non-contact palmprint images; a robust directional and multiscale feature encoding method is proposed for multispectral palmprint images; and an effective binary code matching strategy is used for matching process and compact storage of multidirectional components. Presented approach is

compared with state-of-the-art methods by using different experimental setups.

## II. RELATED WORKS

Using multispectral images, biometrics like the iris [17], face [18], [19] and fingerprint [20] have been researched for improved precision in the past decade. Researchers have now turned their attention to multispectral palmprint recognition [14], [15], [21]-[32]. Palmprint recognition techniques can be categorized as texture-based coding methodologies, line-like feature finders and subspace learning strategies [33]. The combination of these three classes is possible. Edge detectors can be used to extract palm lines in line detection-based methodologies. A palmprint verification method by utilizing principal lines is presented in [34]. The principal palm lines were separated by using a modified finite Radon transform. However, recognition based on only palm lines was inadequate [27]. Palm lines can be extracted by line detection. However, line detection is not suitable for extraction of palm veins due to their broad structure and low contrast.

The global characteristics of the palm can be captured by using subspace projection. Subspace projection strategies incorporate Eigen-palm [35], which reflects palm images to a PCA space, or Fisher-palm [36] which reflects to a LDA space. However, such subspace projection is not well suited to preserve and model finer local details. In [37], Laplacian palm representation is proposed by fusing palmvein and palmprint images. In that work, Laplacian palm representation is used to preserve local characteristics while reflecting onto subspace unlike Eigen-palm [35] and Fisher-palm [36]. Multispectral palmprint images are represented as quaternion PCA and employed quaternion PCA to get features. For recognition, a nearest neighbor classifier is used. The quaternion model was not as effective as state-of-the-art techniques in representing multispectral palm images and were found to have low recognition accuracy. The subspace learned from incorrect align palms cannot create an exact representation of every identity.

The methods based on orientation encode and extract the directional lines. Those methods have shown state-of-the-art performance in palmprint recognition [11]. The Competitive Code (CompCode) [38], the Ordinal Code (OrdRepr) [39] and the Derivative of Gaussian Code (DoGRepr) [40] can be examples of the orientation-based methods. In the generic form of the methods based on orientation coding, each directional subband is identical to a certain orientation of lines. The orientation-based code is formed from the dominant orientation index, extracted from each of the directional subbands. A directional bank of Gabor filters is used to extract the orientation of palm lines in CompCode [38]. Coefficients of the directional subbands are encoded into a binary code. Then, the results are matched directly by applying the Hamming distance. The OrdRepr [39] studies the ordinal relationship of lines. This method compares reciprocally orthogonal filter pairs to get feature orientation at a point. The DoGRepr [40] uses vertical and horizontal derivative filters to extract feature orientation. The coefficients of the orientation-based methods can be binarized for effective storage and fast matching compared to other representations

that need floating point data storage and calculations. Another critical part of multispectral palmprints is the way to combine the spectral bands. The multispectral palmprints have been examined with feature, data, rank-level combination and score.

Multiresolution transform techniques such as wavelets and curvelets are used to fuse multispectral palmprint images. A three-scale wavelet transform methodology is used for fusion multispectral palmprint images in [14] and then they applied CompCode for feature extracting and matching. The results showed that the wavelet combination of multispectral palm images is valuable for blurred palm images. In [32], different image fusion methods are used. The OLOF was one of those representations for multispectral palmprint recognition. The best recognition accuracy was accomplished when the curvelet was used for band combination. A wavelet-based band combination and a Gabor wavelet-based feature representation for multispectral palm pictures are presented in [28]. Feature selection was done using Ant Colony Optimization (ACO) [41] to reduce the dimensionality and classified by SVM and normalized correlation. However, Gabor wavelet-based fusion did not give better results than the curvelet combination with OLOF [32] for palmprint recognition. A joint palmline strategy is proposed in [27] to have multispectral palmprint recognition. Different feature encoding techniques were designed for palmline and palmvein. Later, score-level fusion was used to compute the final match. This approach showed more promising results than a feature- and/or rank-level fusion. In addition, single palmprint image representation may be extended to multispectral cases. However, features in different bands such as lines and veins might not be preserved [27]. A comparative study presented in [12] showing that local orientation-based features are the recommended option for palmprint image feature extraction.

This paper proposes a new multidirectional transform-based feature extraction considering multispectral palmprint recognition. UDTCWT is used to represent coefficients since it gives superior performance with directionality and shift invariance properties than UDWT and DTCWT. A two-level filtering strategy is presented to obtain more robust and useful multidirectional features than those of orientation-based methods that use a directional filterbank. The idea presented in [42] is used for the binary matching strategy. Three orientation-based techniques [38] [39] [40] are implemented and compared with the presented method considering different experimental setups. The scheme of the presented method is depicted in Fig. 1.

The rest of this paper is organized as follows. In Section III, we explain a solid procedure for ROI extraction from multispectral pictures produced by means of non-contact sensors. The proposed feature extraction method and applied binary code matching and coordinating procedures are discussed in Section IV. In Section V, we introduce a point-by-point trial examination to assess the precision of the multispectral palmprint image analysis. We investigate the impact of different parameters. We perform verification and identification tests in different trial settings using two standard multispectral palmprint databases and compare the proposed

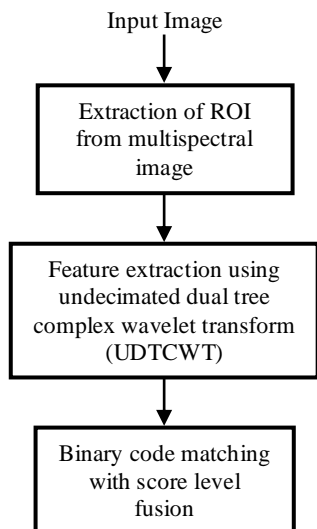


Fig. 1. Schematic diagram for the presented method.

method with the state-of-the-art methods. Conclusions are given in Section VI.

### III. REGION OF INTEREST EXTRACTION

For feature extraction and matching, it is necessary to extract a specific portion from the palmprint image which is known to be ROI extraction. There are many advantages to applying ROI extraction processes to the images captured from non-contact sensors. One of these advantages is to be used to eliminate translation, scale and rotation of palm vein images. ROI extraction process also extracts the most useful area in the images. It reduces the amount of data without missing much useful information. This process affects the speed and the quality of the feature extraction and matching processes. The ROI extraction method introduced in [42] is used.

Since each band of the multispectral images is sequentially captured, minor hand movements cannot be eliminated. Therefore, the maximization of mutual information explained in [32] is used for inter-band registration of the ROIs. The strategy was effective for registering multispectral palm images. Once the registration of ROIs for each band is completed, it is resized to  $128 \times 128$  pixels with bicubic interpolation and then downsampled to  $32 \times 32$  pixels using the discrete wavelet transform rather than the method used in [42]. This re-sampling step shows better performance than bicubic interpolation because it reduces the noisy regions and inconsistent lines while taking more lines or points into consideration for interpolation. This approach reduces the amount of required storage in the final feature. The required time and final stage storage are also reduced in case of extraction and matching processes. Process for extraction of ROI is shown in Fig. 2.

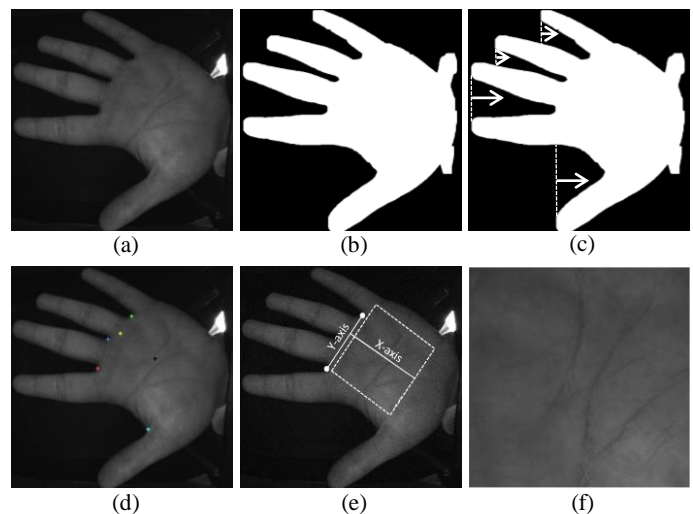


Fig. 2. Extraction of ROI from sample image. (a) Input image (b) Pre-processed binary image (c) Starting search for mid-points (d) Overlay extracted landmarks and reference points on input image (e) Location of ROI (f) Extracted ROI.

### IV. MULTISPECTRAL PALMPRINT IMAGE ANALYSIS

#### A. Directional Feature Encoding

The undecimated dual tree complex wavelet transform (UDTCWT) [43] is an improved expansion of DTCWT. Two different form UDTCWT is presented in [43]. One of them is termed as U1DT-CWT, which provides exact shift invariance properties with the advantage of having one-to-one map in each subband with the same directional selectivity as DTCWT, since downsampling and upsampling of the filters are removed like a simple UDWT. Having a consistent size in all scales is an important relationship in the applications such as image denoising and image fusion. The second form of UDTCWT is termed as U2DT-CWT, which is retaining sub-sampling after the first level to reduce overcompleteness. However, sub-bands are not same size as input image in this form. In this paper, we use the shift invariance, one-to-one map in each subband and directional selectivity properties of the U1DT-CWT [43] for directional feature encoding in palmprint images.

A biorthogonal set of filters ( $B_f$ ) is used at the first scale to be convolved with an ROI  $I \in \mathbb{R}^{m \times n}$ . This step helps us to capture the details in the palm and allows robust information to be passed on to the subsequent stage.

$$\rho = I * B_f \quad (1)$$

The filtered component ( $\rho$ ) of the input image is processed by the  $q$ -step filters ( $D_f^i$ ) which comprise six complex directional subbands.

$$\Psi^i = \rho * D_f^i \quad (2)$$

Where:  $\Psi^i$  – indicates six set of directional complex subbands,  $i = 1, 2, \dots, 6$ . The combination of biorthogonal and  $q$ -step filter decomposition stages lets us determine the

capability of the system to capture line-like features. Usually, both the vein and line characteristics appear as black intensities in a palm. This corresponds to a negative filter response. The minimum peak response among all directional subbands is selected at a specific point. Assume  $\Psi_{x,y}^i$  represents the coefficient at point  $(x, y)$  in the  $i^{\text{th}}$  directional subband where  $i = 1, 2, \dots, 6$ . We use a similar rule to the competitive rule [38]. The dominant orientation in each  $(x, y)$  is encoded.

$$C = \arg_i \min(\Psi^i) \quad (3)$$

where  $C$  – denotes the UIDT-CWT coefficients that represents  $I$ . Note that  $C$  is calculated for all subbands of the multispectral picture of a palm.

### B. Binary Encoding

The binary encoding process presented in [42] is used to calculate one-to-many matching in palm image identification. The binary hash table method is applied to equation (3). The coefficients of the UIDT-CWT in equation (3) is then binarized. It should be noted that palmprint features are non-rigid, so it is not possible to have an exact 1:1 correspondence between all the directions of two palmprint pictures captured at different instances of time. Consequently, it is intuitive to set multiple orientations to a hash location  $(x, y)$  based on its neighborhood. The blurring depends on a specific neighborhood rather than a single pixel and robustly catches crossover line orientations. Less blurring occurs in a few number of points matched with high confidence. Conversely, high-level blurring will result in large numbers being matched with low confidence.

The maximum score within all translations is defined as the final match. The class of inquiry palm is identified by the  $n^{\text{th}}$  image in the gallery which corresponds to the highest match as defined in [42]:

$$Class = \arg_n \max(S_{t_x, t_y}^{Q_n}) \quad (4)$$

Here:  $S_{t_x, t_y}^{Q_n}$  – is a match score. The bands are differently translated to determine the best possible combination [42]. In the matching process, each band is matched individually. The resulting scores are combined. Floating point comparisons are not needed for final decision, because a matching score is always an integer.

## V. EXPERIMENTAL RESULTS

### A. Databases

Two publicly available datasets are used for experiments: the CASIA [44] and PolyU [45]. Both datasets have low resolution (less than 150 dpi) multispectral palmprint images and that is stored as 8-bit images per band. ROIs of the PolyU database are already extracted by the method presented in [13].

2D Undecimated Dual Tree Complex Wavelets

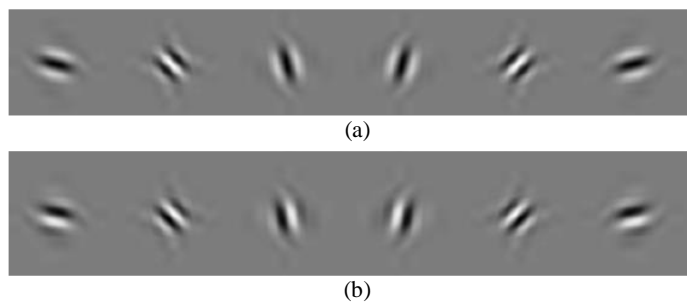


Fig. 3 Impulse response of 2D complex-valued wavelet filters. (a) Real part (b) Imaginary part.

The ROIs of the CASIA databases are not extracted and we apply landmark localization with ROI extraction strategy discussed in Section 3 in order to extract them. CASIA databases are captured by using a non-contact sensor and contains too many RST variations.

### B. Parameter Selection

The effect of various parameters is studied such as ROI size, number of scales in the presented method, influence of binary encoding with blurring and non-blurring neighborhood. All parameters except the analysis of a specific parameter are kept fixed. This experimental analysis is carried out by using a sample set of the PolyU multispectral palmprint database comprising exact number of images from the first and second sessions. Optimal parameters found for PolyU databases are applied for the CASIA database.

#### 1) Dimension of ROI

The length and thickness of the palmprint features vary. The most discriminative data can be lost with a small ROI. Moreover, unnecessary details and features can be included with a larger ROI. Different size of ROI regions with square sets such as (16,16), (32,32), ..., (128,128) are empirically tested. Minimum EER is found at (32,32). ROI size of (32,32) is used in all our experiments.

#### 2) Scale Setting

UIDT-CWT results in six complex directional subbands in the orientation of  $\pm 15^\circ, \pm 45^\circ, \pm 75^\circ$ . The six directional subbands for the impulse response of the filters are illustrated in Fig. 3. We consider only the real parts of the directional complex subbands, since the most promising feature for low-resolution image is in the real part. Different scale sizes are tested. Empirical tests show that scale 2 gives minimum EER. Therefore, two-scale decomposition is used in all experiments.

#### 3) Matching with Blurring Neighborhood

The given palm is not a fixed object. Therefore, hash table blurring is applied to prevent minor misalignments. Moreover, too much blurring can result in false matches. The lowest ERR is obtained with four-adjoint blur neighborhood.

4) Filter Selection

Biorthogonal sets of filters must be chosen for the first scale [43] and NDAntonB2 filter is used. In the remaining scales, q-step filters can be applied [43], [44]. NDdualfilt1 filter is used in the remaining scales.

C. Validity of Experiments

The PolyU and CASIA databases are used to perform the experiments. In both cases, half of the sample for each identity was obtained in one session and the other half was obtained in another. We used session-based Sets as discussed in [11] to observe recognition performance. We ran five experiments to evaluate the method in real life scenarios. The analyses of the experiments continued by matching:

- Set 1: session regardless of the individual bands.
- Set 2: palmprints (multispectral) from the first session.
- Set 3: palmprints (multispectral) from the second session.
- Set 4: palmprints (multispectral) of the first session to the second session.
- Set 5: palmprints (multispectral) regardless of the session.

For the recognition experiments, the ROC curves are used to show variations between False Acceptance Rate (FAR) to the False Rejection Rate (FRR). The Genuine Acceptance Rate (GAR) at 0.1% FAR and the Equal Error Rate (EER) are selected to evaluate the recognition performance of the presented method. The presented method is compared with three state-of-the-art techniques: CompCode, DoGRepr and OrdRepr. We use our implementation for these three techniques since their code is not public. Table 1 gives the number of genuine and imposter matches for each sets. We apply four-adjoint blur neighborhood for gallery binary hash table encoding. Furthermore, the matching process is carried out by score-level band fusion.

TABLE I  
GENUINE AND IMPOSTER MATCHES CONSIDERED IN EACH SET.

		Experiments		
		Set 2&3	Set 4	Set 1&5
CASIA	Gen.	600	1,800	3,000
	Imp.	179,100	358,200	716,400
PolyU	Gen.	7,500	18,000	33,000
	Imp.	4,491,000	8,982,000	17,964,000

1) Set 1

This set analyzes the discriminant capability of individual bands as depicted in Fig. 4. Table 2 compares individual bands of palm performance of the PolyU and CASIA database for the presented code with blurring and non-blurring case. For the PolyU database, the 660nm band gives the best performance for blurring and non-blurring. A major reason for this could be that the 660nm wavelength mostly catches both the line and vein features which make this band more

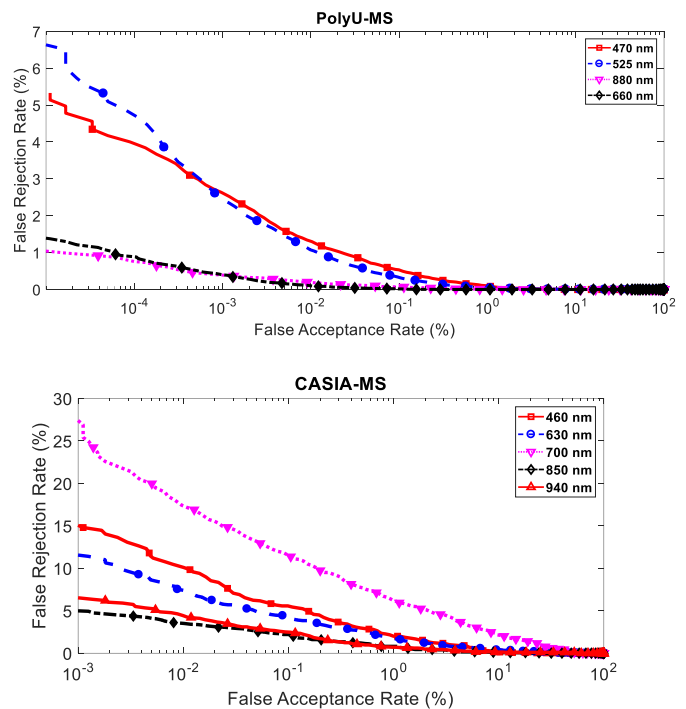


Fig. 4. Individual bands considered with blurring effect for PolyU and CASIA databases by proposed method in Set 1.

TABLE II  
PERFORMANCE OF THE INDIVIDUAL BANDS FOR THE PROPOSED METHOD.

Band		PolyU		CASIA		
		Blur	Non-blur	Band	Blur	Non-blur
470 nm	GAR(%) EER (%)	99.47 0.2766	99.07 0.3820	460 nm	94.45 1.6484	93.64 1.7821
525 nm	GAR(%) EER (%)	99.67 0.2028	99.35 0.2880	630 nm	95.84 1.3907	96.09 1.3628
660 nm	GAR(%) EER (%)	99.98 0.0381	99.93 0.0842	700 nm	87.48 3.8757	90.83 2.8488
880 nm	GAR(%) EER (%)	99.93 0.0754	99.88 0.1118	850 nm	97.80 0.8000	98.30 0.6427
	GAR (%) EER (%)			940 nm	97.52 0.7642	97.90 0.6538

discriminative. For the CASIA database, the most discriminant data is available in the 850nm and 940nm bands which give the best results with and without consideration of the blurring effect.

2) Set 2

Set 2 examines the variability in the palmprint information obtained in the first session. Fig. 5 analyzes the ROC curves of the proposed method with three techniques on the CASIA and PolyU databases.

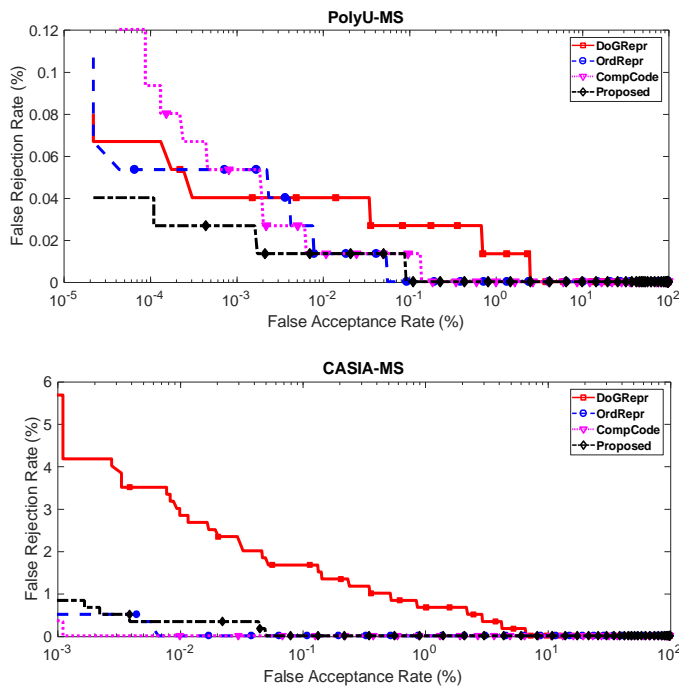


Fig. 5. Multispectral palmprints obtained in first session with blurring effect for PolyU and CASIA databases in Set 2.

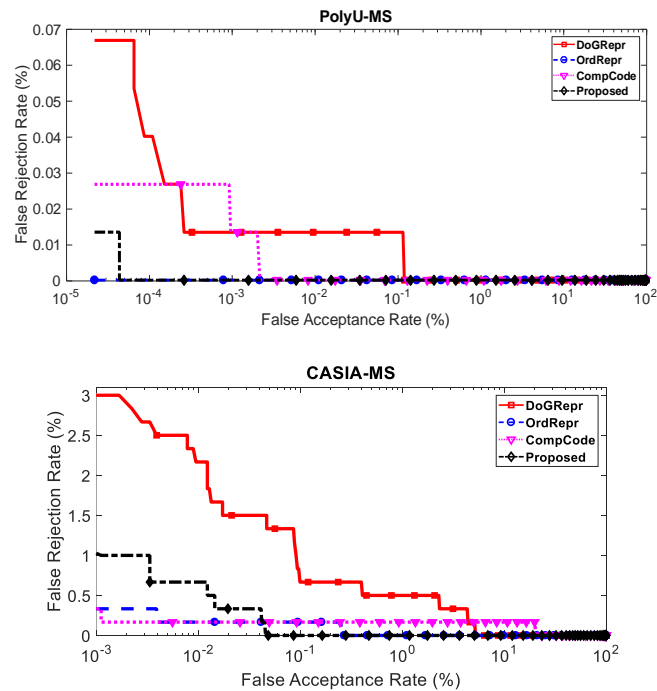


Fig. 6. Multispectral palmprints gained in second session with blurring effect for PolyU and CASIA.

3) Set 3

Set 3 investigates the variability in the palmprint information gained in the second session as depicted in Fig. 6. In this set we investigate the intra-band variations compare the results obtained in Set 2. Furthermore, only the palmprints obtained in the second session are matched.

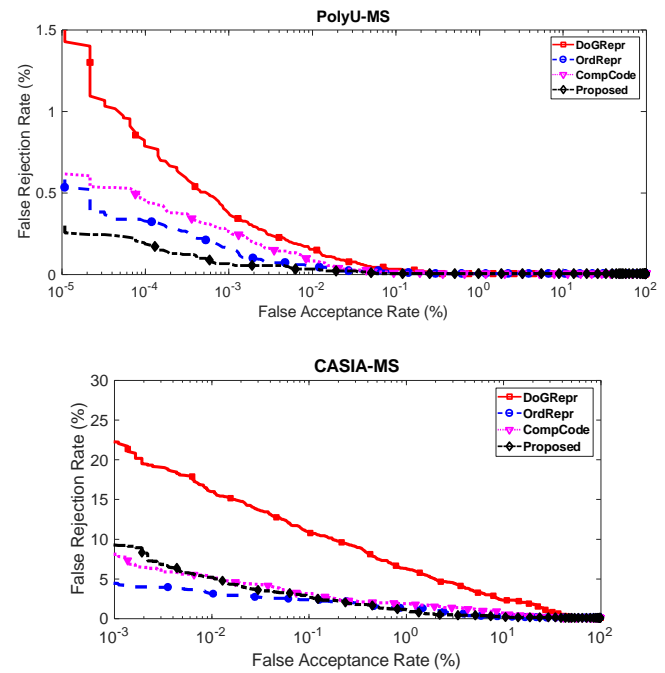


Fig. 7. Multispectral palmprints of the first session to the second session with blurring effect for PolyU and CASIA databases in Set 4.

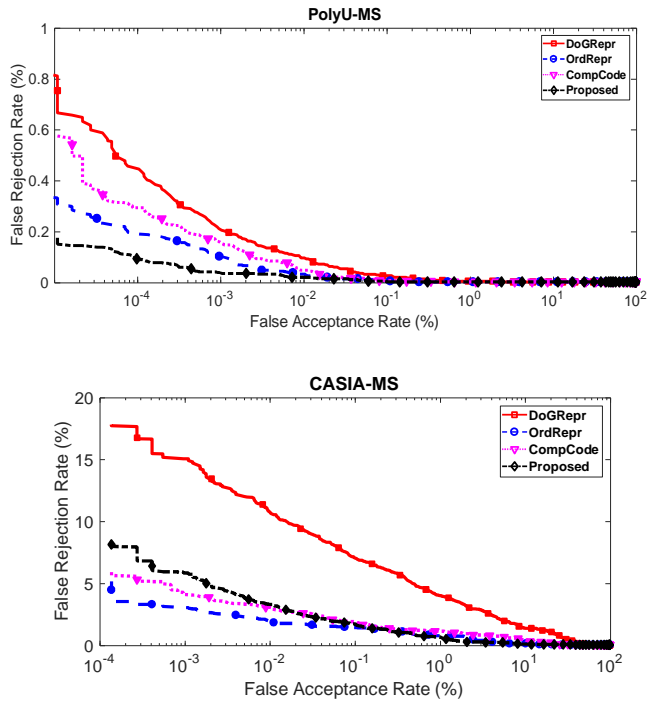


Fig. 8. Multispectral palmprints regardless of the session with blurring effect for PolyU and CASIA databases in Set 5.

4) Set 4

Set 4 is used to test a real-life scenario where there is a variation in image quality and/or human behavior over time. According to this, all images from the first session are matched to all images of the second. Fig. 7 compares the ROC curves of the proposed code with three methods. It should be mentioned that there is a performance degeneration of other methods compared to Set 2 and Set 3 because of the difficulty

TABLE III  
VERIFICATION EXPERIMENTS FOR SET 2 TO SET 5 WITH  
BLURRING.

CASIA Database					
Methods		Set 2	Set 3	Set 4	Set 5
DoGRepr	EER (%)	0.8333	0.5000	3.8889	2.8667
	GAR (%)	98.33	99.33	89.18	92.97
OrdRepr	EER (%)	0.0067	0.1667	1.2222	0.7667
	GAR (%)	100.00	98.83	97.72	98.60
CompCode	EER (%)	0.0011	0.1667	1.6111	1.1000
	GAR (%)	100.00	98.83	96.94	98.13
Proposed	EER (%)	0.0512	0.0455	1.0154	0.6874
	GAR (%)	100.00	100.00	97.42	98.30
PolyU Database					
Methods		Set 2	Set 3	Set 4	Set 5
DoGRepr	EER (%)	0.0353	0.0134	0.0462	0.0402
	GAR (%)	99.97	99.99	99.97	99.98
OrdRepr	EER (%)	0.0134	0.000	0.0208	0.0182
	GAR (%)	100.00	100.00	99.99	100.00
CompCode	EER (%)	0.0134	0.0022	0.0278	0.0212
	GAR (%)	99.99	100.00	99.99	99.99
Proposed	EER (%)	0.0134	0.0000	0.0167	0.0148
	GAR (%)	100.00	100.00	100.00	100.00

TABLE IV  
VERIFICATION EXPERIMENTS FOR SET 2 TO SET 5 WITH  
NON-BLURRING.

CASIA Database					
Methods		Set 2	Set 3	Set 4	Set 5
DoGRepr	EER (%)	0.3225	0.3333	2.4444	1.6813
	GAR (%)	99.00	99.67	93.22	95.67
OrdRepr	EER (%)	0.0234	0.1667	0.7015	0.5333
	GAR (%)	100.00	99.83	98.22	98.90
CompCode	EER (%)	0.0295	0.1667	1.3000	0.8667
	GAR (%)	100.00	99.83	97.17	98.27
Proposed	EER (%)	0.0926	0.1667	0.8889	0.7262
	GAR (%)	100.00	99.83	97.44	98.43
PolyU Database					
Methods		Set 2	Set 3	Set 4	Set 5
DoGRepr	EER (%)	0.0267	0.0025	0.0278	0.0242
	GAR (%)	100.00	100.00	100.00	100.00
OrdRepr	EER (%)	0.0400	0.0000	0.0225	0.0221
	GAR (%)	99.97	100.00	99.98	99.98
CompCode	EER (%)	0.0267	0.0006	0.0207	0.0182
	GAR (%)	99.99	100.00	100.00	100.00
Proposed	EER (%)	0.0359	0.0013	0.0500	0.0364
	GAR (%)	99.99	100.00	99.97	99.98

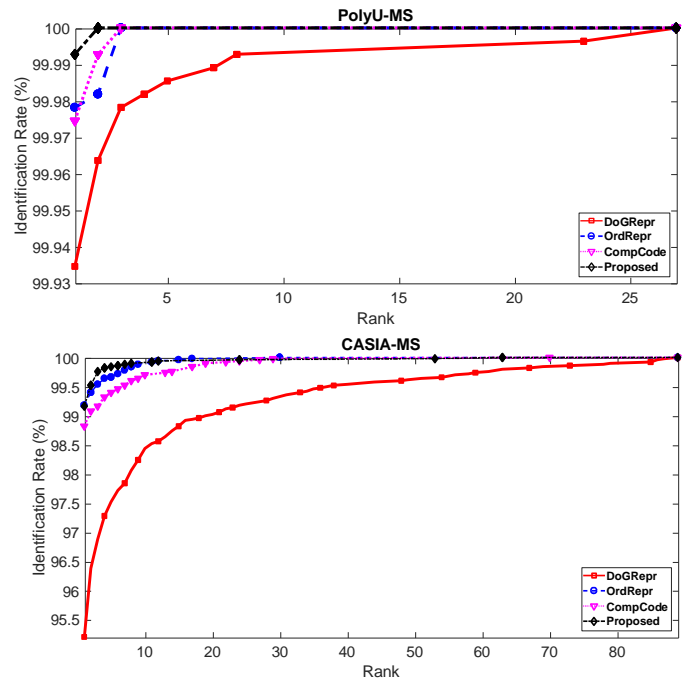


Fig. 9. Identification performance with CMC curves.

of the scenario. However, degeneration of the proposed method is much less than of other methods on PolyU database, which indicates the robustness of the proposed method to the image variability.

5) Set 5

Set 5 analyzes the overall recognition performance which allows comparison of existing methods with the proposed method on the same database. This set is termed to be “all versus all” in the literature since all images in that database are compared to all other images. The proposed method is compared with three other methods in Fig. 8 considering this scenario. The proposed method outperforms all other methods on the PolyU database and gives comparable results on the CASIA database.

D. Comparison with State-of-the-Art Methods

The results obtained in Set 2 to Set 5 are given in Table 3. The proposed method gives the best results in the PolyU database compared to the three state-of-the-art methods for blurring case. Furthermore, the proposed method outperforms in some sets considering the CASIA database. It should be noted that OrdRepr has more comparable results than the other methods for blurring case on the CASIA database. In Table 4, the propose method still gives a very good comparable result although it might not give the best results in some cases compared to the other state-of-the-art methods in the CASIA database. Since the palm images were acquired with the use of contact-based sensors in the PolyU database, all methods produce better EER performance. The EER performance of CompCode and DoGRepr deteriorated and produce the worst results of all other methods in the CASIA database with blurring. At the same time, the presented method gives much

better EER performance with blurring.

### E. Validity of Experiments

Identification experiments are performed by using fivefold cross validation and identification rates at rank-1 and reported with the Cumulative Match Characteristics (CMC) curves. We randomly choose one multispectral palm image per subject to set the gallery and all other images as test samples in each fold. In this way, a single multispectral palm image in the gallery is used for identification for any test sample subject. Then, the average identification rates are computed over fivefold. We use this protocol for both databases. Fig. 9 gives the CMC curves to compare the performance of the proposed method with other three state-of-the-art methods with blurring effect. The identification performances are given in Table 5 and Table 6 for the blurring and non-blurring case, respectively. Both tables indicate that the proposed method gives the best and results compared to the three state-of-the-art methods.

## VI. CONCLUSION

This paper presents a new multidirectional and multiscale analysis based on UDTCWT for feature encoding by applying a binary hash table matching procedure for palm image recognition. Newly, a simple DWT is also used to extract the ROIs rather than the usual method that uses bicubic interpolation to reduce noisy regions and inconsistent lines. With this approach, the performance of the three state-of-the-art methods are compared. The proposed multidirectional and multiscale feature extraction method provides robust and effective palmprint representation and matching compared to three of the state-of-the-art methods. Furthermore, the matching speed is increased by using the score-level-fusion method for effective palmprint recognition. Results obtained in the experimental part show that the proposed method gives the best results for blurring case and comparable results for non-blurring case when compared with the state-of-the-art methods. UDT-CWT based feature encoding can be easily applied to line-like features and can be extended to other types of biometrics.

### REFERENCES

- [1] D. D. Zhang, *Automated Biometrics—Technologies and Systems*, Boston: Kluwer Academic Publishers, pp. 3-18, 2000.
- [2] T. Connie, A. Jin, M. Ong, D. Ling, "An automated palmprint recognition system", *Image Vis. Computation.*, vol. 23, no. 5, pp. 501–505, May 2005.
- [3] A. Kong, D. Zhang, M. Kamel, "Palmprint identification using feature-level fusion", *Pattern Recog.*, vol. 39, no. 3, pp. 478–487, Mar. 2006.
- [4] A. Kong, D. Zhang, "Competitive coding scheme for palmprint verification", in *Proc. Int. Conf. Pattern Recog.*, 2004, pp. 520–523.
- [5] W. Jia, D. Huang, D. Zhang, "Palmprint verification based on robust line orientation code", *Pattern Recog.*, vol. 41, no. 5, pp. 1504–1513, May 2008.
- [6] A. Kumar, D. Zhang, "Personal recognition using hand shape and texture", *IEEE Trans. Image Process.*, vol. 15, no. 8, pp. 2454–2461, Aug. 2006.

TABLE V

CORRELATION OF RANK-1 RECOGNITION RATES AND STANDARD DEVIATIONS ON THE CASIA AND POLYU DATABASES FOR BLURRING. IDENTIFICATION RATES ARE AVERAGED OVER 5-FOLD.

Methods	CASIA (%)	PolyU (%)
DoGRepr	95.20 ± 0.81	99.98 ± 0.02
OrdRepr	99.18 ± 0.15	100.00 ± 0.01
CompCode	98.82 ± 0.22	99.99 ± 0.02
Proposed	99.16 ± 0.26	100.00 ± 0.01

TABLE VI  
CORRELATION OF RANK-1 RECOGNITION RATES AND STANDARD DEVIATIONS ON THE CASIA AND POLYU DATABASES FOR NON-BLURRING. IDENTIFICATION RATES ARE AVERAGED OVER 5-FOLD

Methods	CASIA (%)	PolyU (%)
DoGRepr	97.46 ± 0.34	99.95 ± 0.07
OrdRepr	99.60 ± 0.25	99.99 ± 0.02
CompCode	99.04 ± 0.36	99.99 ± 0.01
Proposed	99.30 ± 0.19	99.97 ± 0.04

- [7] S. Schuckers, "Spoofing and anti-spoofing measures", *Inf. Secure. Tech. Rep.*, vol. 7, no. 4, pp. 56–62, Dec. 2002.
- [8] R. Rowe, K. Nixon, S. Corcoran, "Multi spectral fingerprint biometrics", in *Proc. Inf. Assurance Workshop*, 2005, pp. 14–20.
- [9] J. Park, M. Kang, "Multispectral iris authentication system against counterfeit attack using gradient-based image fusion", *Opt. Eng.*, vol. 46, no. 11, pp. 117003-1–117003-14, Nov. 2007.
- [10] R. Singh, M. Vatsa, A. Noore, "Hierarchical fusion of multispectral face images for improved recognition performance", *Inf. Fusion*, vol. 9, no. 2, pp. 200–210, Apr. 2008.
- [11] D. Zhang, W. Zuo, F. Yue, "A comparative study of palmprint recognition algorithms", *ACM Computing Surveys (CSUR)*, vol. 44, no. 1, pp. 2:1–2:37, Jan. 2012.
- [12] A. Jain, J. Feng, "Latent palmprint matching", *IEEE Trans. on Pattern Anal. Mach. Intell.*, vol. 31, no. 6, pp. 1032–1047, Oct. 2009.
- [13] D. Zhang, W. Kong, J. You, M. Wong, "Online palmprint identification", *IEEE Trans. on Pattern Anal. Mach. Intell.*, vol. 25, no. 9, pp. 1041–1050, Sept. 2003.
- [14] D. Han, Z. Guo, D. Zhang, "Multispectral palmprint recognition using wavelet-based image fusion", in *Proc. Int. Conf. on Signal Processing*, 2008, pp. 2074–2077.
- [15] Y. Hao, Z. Sun, T. Tanet, "Comparative studies on multispectral palm image fusion for biometrics", in *Proc. Asian Conf. on Computer Vision*, Springer, pp. 12–21, 2007.
- [16] A. Jain, A. Ross, S. Prabhakar, "An introduction to biometric recognition", *IEEE Trans. on Circuits and Systems for Video Technology*, vol. 14, no. 1, pp. 4–20, Jan. 2004.
- [17] C. Boyce, A. Ross, M. Monaco, L. Hornak, X. Li., "Multispectral iris analysis: A preliminary study", in *Proc. Computer Vision and Pattern Recognition Workshops (CVPRW)*, July 2006.
- [18] W. Di, L. Zhang, D. Zhang, Q. Pan, "Studies on hyperspectral face recognition in visible spectrum with feature band selection", *IEEE Transactions on Systems, Man, and Cybernetics - Part A: Systems and Humans*, vol. 40, no. 6, pp. 1354–1361, 2010.
- [19] Z. Pan, G. Healey, M. Prasad, B. Tromberg, "Face recognition in hyperspectral images," *IEEE Trans. on Pattern Anal. Machine Intelligence*, vol. 25, no. 12, pp. 1552–1560, Dec. 2003.
- [20] R. Rowe, U. Uludag, M. Demirkus, S. Parthasaradhi, A. Jain, "A multispectral whole-hand biometric authentication system", in *IEEE Biometrics Symposium*, 2007, pp. 1–6.

- [21] A. Meraoumia, S. Chitroub, A. Bouridane, "An efficient palmprint identification system using multispectral and hyperspectral imaging", in *Modeling Approaches and Algorithms for Advanced Computer Applications*, vol. 488, pp. 155–164, 2013.
- [22] M. Bounneche, L. Boubchir, A. Bouridane, B. Nekhoul, and A. AliCherif, "Multi-spectral palmprint recognition based on oriented multiscale log-Gabor filters", *Neurocomputing*, vol. 205, pp. 274–286, Sept. 2016.
- [23] N. Luo, Z. Gang, W. C. Song, "Multispectral palmprint recognition by feature level fusion", in *Recent Advances in Computer Science and Inf. Engineering*, Springer, vol. 128, pp. 427–432, 2012.
- [24] S. Mistani, S. Minaee, E. Fatemizadeh, "Multispectral palmprint recognition using a hybrid feature", vol. abs/1112.5997, Dec. 2011.
- [25] Y. Abermi, L. Boubchir, B. Daachi, "Multispectral palmprint recognition: A state-of-the-art review", in *Int. Conf. on on Telecommunications and Signal Processing (TSP)*, 2017, pp. 793–798.
- [26] A. Tahmasebi, H. Pourghasem, H. Mahdavi-Nasab, "A novel rank level fusion for multispectral palmprint identification system", in *Proc. Int. Conf. on Intelligent Computation and Bio-Medical Instr. (ICBMI)*, 2011, pp. 208–211.
- [27] D. Zhang, Z. Guo, G. Lu, L. Zhang, Y. Liu, W. Zuo, "Online joint palmprint and palmvein verification", *Expert Systems with Applications*, vol. 38, no. 3, pp. 2621–2631, March 2011.
- [28] D. Kisku, P. Gupta, J. Sing, C. Hwang, "Multispectral palm image fusion for person authentication using ant colony optimization", in *Proc. Int. Works. on Emerging Tech. and Challenges for Hand-Based Biometrics (ETCHB)*, 2010, pp. 1–7.
- [29] Z. Guo, D. Zhang, L. Zhang, W. Liu, "Feature band selection for multispectral palmprint recognition", in *Proc. Int. Conf. on Pattern Recog. (ICPR)*, 2010, pp. 1136–1139.
- [30] D. Zhang, Z. Guo, G. Lu, L. Zhang, W. Zuo, "An online system of multispectral palmprint verification", *IEEE Trans. on Instrumentation and Measurement*, vol. 59, no. 2, pp. 480–490, Feb. 2010.
- [31] X. Xu, Z. Guo, "Multispectral palmprint recognition using quaternion principal component analysis", in *Proc. Int. Workshop on Emerging Tech. and Challenges for Hand-Based Biometrics (ETCHB)*, 2010, pp. 1–5.
- [32] Y. Hao, Z. Sun, T. Tan, C. Ren, "Multispectral palm image fusion for accurate contact-free palmprint recognition", in *Proc. Int. Conf. on Image Process.*, 2008, pp. 281–284.
- [33] A. Kong, D. Zhang, M. Kamel, "A survey of palmprint recognition", *Pattern Recog.*, vol. 42, no. 7, pp. 1408–1418, July 2009.
- [34] D. Huang, W. Jia, D. Zhang, "Palmprint verification based on principal lines", *Pattern Recog.*, vol. 41, no. 4, pp. 1316–1328, April 2008.
- [35] G. Lu, D. Zhang, K. Wanga, "Palmprint recognition using eigenpalms features", *Pattern Recog. Letters*, vol. 24, no. 9, pp. 1463–1467, June 2003.
- [36] X. Wu, D. Zhang, K. Wanga, "Fisherpalms based palmprint recognition", *Pattern Recog. Letters*, vol. 24, no. 15, pp. 2829–2838, Nov. 2003.
- [37] J. Wang, W. Yau, A. Suwandy, E. Sung, "Fusion of palmprint and palm vein images for person recognition based on laplacian palm feature", in *Proc. Comp. Vision and Pattern Recog.*, 2007, pp. 1–8.
- [38] A.W.-K. Kong, D. Zhang, "Competitive coding scheme for palmprint verification", in *Proc. Int. Conf. on Pattern Recog.*, pp. 520–523.
- [39] Z. Sun, T. Tan, Y. Wang, S. Z. Li, "Ordinal palmprint representation for personal identification", in *Proc. Computer Vision and Pattern Recog.*, 2005, pp. 279–284.
- [40] X. Wu, K. Wang, D. Zhang, "Palmprint texture analysis using derivative of Gaussian filters", in *Proc. Int. Conf. on Computational Intelligence and Security*, 2006, pp. 751–754.
- [41] Y. Zhou, A. Kumar, "Contactless palm vein identification using multiple representations", in *Proc. Int. Conf. on Biometrics: Theory Applications and Systems (BTAS)*, 2010, pp. 1–6.
- [42] Z. Khan, A. Mian, Y. Hu, "Contour code: Robust and efficient multispectral palmprint encoding for human recognition", in *Proc. Int. Conf. on Computer Vision (ICCV)*, 2011, pp. 1935–1942.
- [43] P. R. Hill, N. Anantrasirichai, A. Achim, M. E. Al-Mualla, D. R. Bulla, "Undecimated Dual-Tree Complex Wavelet Transforms", *Signal Processing: Image Communication*, vol. 35, pp. 61–70, July 2015.
- [44] "CASIA Multispectral Palmprint Database." [Online]. Available: <http://biometrics.idealtest.org>, accessed Oct. 2018.
- [45] "PolyU Multispectral Palmprint Database." [Online]. Available: <https://www4.comp.polyu.edu.hk/~biometrics/MultispectralPalmprint/MSP.htm>, accessed Oct. 2018.
- [46] I. W. Selesnick, R. G. Baraniuk, N. C. Kingsbury, "The dual tree complex wavelet transform", *IEEE Signal Processing Magazine*, vol. 22, no. 6, pp. 123–151, Nov. 2005.

## BIOGRAPHIES



**BURCIN OZMEN** received his BSc. degree in Electrical and Electronics Engineering from Eastern Mediterranean University, Gazimagusa, North Cyprus, in 1999, the M.Sc. degree in Electrical and Electronic Engineering from Eastern Mediterranean University, Gazimagusa, North Cyprus, in 2001. Ozmen was awarded the PhD degree in 2007 for his work in the area of signal processing. Presently, he is working as an Assistant Professor in European University of Lefke, Lefke, Northern Cyprus. His research interests include signal and image processing, computer vision, and sparse representation.



**OLAYINKA JOHN OLALEYE** received MSc. degree in Electrical and Electronics Engineering from the Cyprus International University, Lefkoşa, North Cyprus, in the year 2016. Presently, he is pursuing his PhD. in Electrical and Electronics Engineering Department of the Cyprus International University.

# Poultry Feed Dispensing System Control: A Case between Fuzzy Logic Controller and PID Controller

J.A. BALA, O.M. OLANIYI, T.A. FOLORUNSO and O.T. ARULOGUN

**Abstract**—The application of precision agriculture in farming practices results in higher yield and productivity with lower costs. Several works have applied this concept to poultry farming in an attempt to reduce human involvement, stress, fatigue, wastage of poultry feed as well as provided a high return on investment. A number of these systems lack control techniques to improve the system performance. A few works exist that implemented control techniques to improve system response, but different systems were implemented and therefore, a comparison cannot be made. In this paper the performance comparison of the Fuzzy Logic Controller (FLC) and the PID Controller on the Poultry Feed Dispensing System was evaluated in a quest to determine the more efficient and effective controller. The system was modelled and simulated using MATLAB SIMULINK and the performance was evaluated based on the rise time, settling time, overshoot and Integrated Absolute Error (IAE). The results showed that the system implemented with the PID and FLC performed better than the system without a control technique. The PID gave a faster system response than the FLC in the solid feed subsystem with a difference in rise time, settling time and IAE of 9.72 seconds, 11.68 seconds and 4.74 respectively. The FLC performed better in the liquid feed subsystem with a difference in rise time, settling time, overshoot and IAE of 9.22 seconds, 33.07 seconds, 13.92% and 7.18 respectively. This shows that the PID controller is more suitable in the solid feed subsystem and the FLC is more effective in the liquid feed subsystem.

**Index Terms**—Precision Agriculture, PID Controller, Fuzzy Logic Controller, Poultry, Feed Dispensing.

**J.A. BALA**, is with the Department of Mechatronics Engineering, Federal University of Technology, Minna, Nigeria, (e-mail: [jibril.bala@futminna.edu.ng](mailto:jibril.bala@futminna.edu.ng)).

 <https://orcid.org/0000-0003-4886-3924>

**O.M. OLANIYI**, is with the Department of Computer Engineering, Federal University of Technology, Minna, Nigeria, (e-mail: [mikail.olaniyi@futminna.edu.ng](mailto:mikail.olaniyi@futminna.edu.ng)).

 <https://orcid.org/0000-0002-2294-5545>

**T.A. FOLORUNSO**, is with the Department of Mechatronics Engineering, Federal University of Technology, Minna, Nigeria, (e-mail: [funso.taliha@futminna.edu.ng](mailto:funso.taliha@futminna.edu.ng)).

 <https://orcid.org/0000-0002-9373-6679>

**O.T. ARULOGUN**, is with the Department of Computer Science and Engineering, Ladoko Akintola University of Technology, Ogbomosho, Nigeria, (e-mail: [otarulogun@lautech.edu.ng](mailto:otarulogun@lautech.edu.ng)).

 <https://orcid.org/0000-0003-0254-4944>

Manuscript received March 5, 2019; accepted April 17, 2019.

DOI: [10.17694/bajece.536026](https://doi.org/10.17694/bajece.536026)

## I. INTRODUCTION

**P**RECISION AGRICULTURE is an information and technology based farm management practice. It is mainly used in farm analysis, variability identification and management for optimum sustainability and profitability. It serves as a feasible alternative for land resource protection and productivity [1]. Site specific management (SSM) requires doing the right thing, at the right place and at the right time. Precision Agriculture makes it possible for SSM to be applied to farms using information technology. Precision agriculture uses agricultural practices to alter inputs to produce the desired outputs as well as monitor those outputs [2]. Precision agriculture results in a higher or equal yield with lower costs in production thereby having a positive impact on farm economics and productivity [3].

Due to the increase in the demand for poultry products, there is a need for poultry farmers to meet the demand of their customers. These poultry farmers need to produce poultry birds that meet the high standards of the market within the shortest time possible [4]. The major problem associated with poultry farming especially in developing countries is that the feeding of the poultry birds is done manually which leads to contamination of the feed, wastage, stress and fatigue on the side of the farmers. These pitfalls result in poultry farming being carried out in the tropics at a high cost with a little return on investment [5]. Due to these shortcomings, there is a need to employ the principles of precision agriculture to develop systems that automate the process of poultry feeding.

The Proportional-Integral-Derivative (PID) controller is a feedback control mechanism which is widely used in the control industry. Its high demand is as a result of its control capabilities for a wide range of industrial applications such as DC motors, automotive and flight control. About 95% of control loops in process control are implemented with a PID controller due to their simplicity in structure and robust performance in a wide range of applications. [6]. Fuzzy logic control is often seen as an alternative to PID control. This is because the use of rules and membership functions in parameterization makes it easier to add logic, non-linearities and additional input signals in control applications. As a result of this, fuzzy logic controllers have recently been widely used in industrial processes due to their simplicity and effectiveness in dealing with both linear and non-linear systems [7].

In order to achieve a system with high performance and robustness, a suitable controller needs to be used. However, the tuning of control parameters to achieve optimum performance is a tedious task. Fuzzy logic blurs the line between control

engineering and artificial intelligence which makes it a suitable option. However, PID controllers are widely used in control applications due to their efficiency, ease of implementation and robustness [8].

Several works have been carried out in the area of poultry feeding systems. [9] designed a self-propelled poultry feed dispensing system. The system had feed level sensing capabilities and employed a parallel port connection with a computer. However, this system had no control technique implemented, had a limited range due to the parallel port and incurred a high cost of parallel port maintenance. [10] developed a mobile intelligent poultry feeding system with obstacle detection and avoidance. The system dispensed solid feed but had no liquid feed dispensing capabilities. Also, no control technique was employed in the development. [4] developed a mechanical poultry feeder which limited the feed dispensed based on the weight of feed on the trough. The system was not intelligent, had no liquid feed dispensing capabilities and employed no control technique.

The absence of control techniques in [10], [9] and [4] was addressed in [11]. Here, an intelligent poultry liquid feed dispensing system was developed using fuzzy logic. The system also had feed sensing capabilities to limit the time in which the feed was dispensed. However, the system could not dispense solid feed and the fuzzy logic control was designed and limited to feed dispensing and was not designed to improve system response. [12] developed a mobile intelligent poultry feed dispensing system using a PID controller tuned with Genetic Algorithm (GA). The results showed that the system response with the GA based PID controller performed better than the system implemented without a controller. The system however could not dispense solid feed. [5] developed a mobile intelligent poultry feed dispensing system using a PID controller tuned with Particle Swarm Optimization (PSO). This system dispensed both solid and liquid feed. The results showed that the PSO based PID system performed better than the system implemented without a control technique.

Due to the shortcomings of the works presented above such as absence of control techniques, undesirable system response, susceptibility to instability and disturbances (such as noise and vibrations), this paper presents a performance evaluation of a poultry feeding system implemented with a Fuzzy Logic Controller (FLC) and a PID controller in a quest to determine the more suitable, effective and efficient control technique in the poultry feed dispensing system. The paper adopts the system model in [5] and was simulated using MATLAB/SIMULINK. The Fuzzy Logic Controller was designed using the Fuzzy Logic Designer toolbox provided by MATLAB while the PID controller was designed and tuned using the PID tuner, also provided by MATLAB. The system performance was evaluated in terms of its system response parameters such as rise time, settling time, overshoot and Integrated Absolute Error (IAE).

The remaining parts of the paper are organized into four sections. Section 2 gives a background on fuzzy logic and PID control. Section 3 gives a description of the system modelling, design and simulation. The results and discussion are presented in section 4 while the conclusion and recommendations for future works are presented in section 5.

## II. BACKGROUND OF THE STUDY

### A. Proportional-Integral-Derivative Control

Proportional Integral and Derivative controllers have been around for a very long time, and despite being used in industrial control applications for a while, they are still widely used today. This is due to their simplicity, low cost, robustness and ease of re-tuning [8], [13]. PID controllers calculate the error value based on a measured process variable and the desired set point. The controller attempts to minimize or eliminate the error by adjusting the controller parameters [6].

The PID controller consists of three terms: the proportional term, integral term and the derivative term. These terms depend on the error value between the input and output. The equation of a PID controller can be represented as shown in equation 1.

$$u(t) = K_p e(t) + K_i \int_0^t e(t) dt + K_d \frac{d}{dt} e(t) \quad (1)$$

Where  $u(t)$  represents the control signal given as the output of the controller,  $K_p$  represents the proportional gain parameter,  $K_i$  represents the integral gain parameter,  $K_d$  represents the derivative gain parameter and  $e(t)$  represents the error signal. From equation 1, it can be seen that the output of the controller depends on the values of  $K_p$ ,  $K_i$  and  $K_d$ . Therefore, changes in the values of these terms produce a change in the value of the final output.

The proportional gain increases the speed of the system as the output is proportional to the error value. The integral gain reduces the steady state error of the system while the derivative gain improves the transient response of the system by reducing the overshoot [13]. The proportional term depends on the present error, the integral term depends on past error values while the derivative term predicts future error values. These parameters are adjusted to obtain a control signal that will improve the system performance by reducing the rise and settling times as well as reducing the steady state error and overshoot [6]. The transfer function of a PID controller is represented by equation 2.

$$K(S) = K_p + \frac{K_i}{s} + K_d s \quad (2)$$

The selection of  $K_p$ ,  $K_i$  and  $K_d$  are called tuning of the PID controller. There are two major categories of tuning which are the classical method and the computational or optimization method. The classical method is a traditional method of PID control which makes assumptions regarding the plant and attempts to tune the parameters analytically. This method is computationally fast but not always accurate as assumptions are made. Examples are the Ziegler-Nichols method and Cohen-Coon Method. The computational or optimization methods aim to tune the control parameters by optimizing a cost function by the use of artificial intelligent techniques, optimization algorithms or software packages. Examples include genetic algorithm, artificial neural networks and particle swarm optimization [13]. In this study, the PID tuner provided by MATLAB was used in tuning the PID controller. It is a custom PID tuning algorithm developed by Mathworks<sup>®</sup> which attempts to tune the controller gains to improve the system performance.

### B. Fuzzy Logic

Fuzzy Logic was introduced by Lofti Zadeh at the University of California, Berkley, in the 1960s to model the uncertainty of natural language [14]. Fuzzy Logic is a method that provides a definite solution from imprecise and vague information. It achieves that by using a set of mathematical principles used to represent knowledge based on degrees of membership [15]. Fuzzy Logic has widespread applications in control engineering, signal processing, artificial intelligence. Fuzzy Logic control was first used in the controller design for the steam engine in 1974. Fuzzy Logic can model human experience accurately and provides an efficient way to implement intelligent control in industrial applications [16]. Fuzzy logic implementation in control engineering is based on designing a self-adapting control system which maintains a particular closed loop performance by learning about changes that might affect the process behavior[14].

The fuzzy logic approach is made up of five steps:

1. Define all input and output variables.
2. Define the subset interval.
3. Choose the membership function.
4. Define the IF-THEN rules.
5. Perform calculations and adjust the rules [12].

Fuzzy logic is widely used due to its flexibility, ease of understanding, tolerance of imprecise data and its ability to be blended with other conventional control techniques [14]. Figure 1 shows a basic fuzzy logic system.

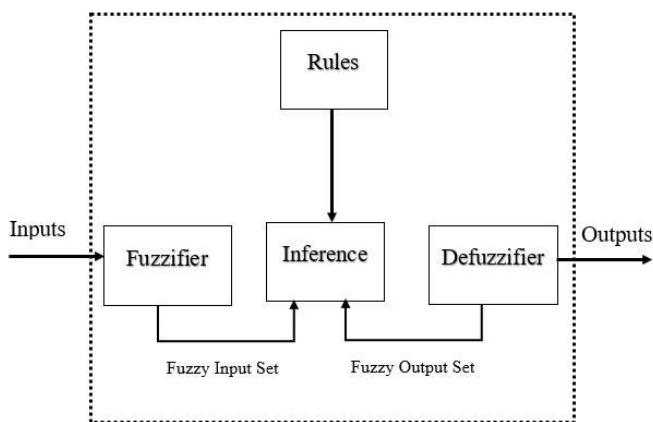


Figure 1: Fuzzy Logic System

## III. METHODOLOGY AND CONTROLLER DESIGN

### A. System Description

The mobile intelligent poultry feed dispensing system developed in [5] serves as the baseline for this work. This paper implements the models of the two subsystems of the poultry feeding system using a PID controller and also a fuzzy logic controller. The system consists of a power supply unit, an embedded unit, a solid and liquid feed dispensing unit as well as a mechanical unit. The power supply unit comprises of a 12V DC battery which powers the entire system. The embedded unit consists of an Arduino mega microcontroller which is

connected to the feed dispensing units and the mechanical unit. The feed dispensing units consist of a DC motor and a DC pump to dispense solid and liquid feed from the trough to the feeder/drinker. The mechanical unit consists of the wheels which enables the system to move within a deep litter poultry farm.

Figure 2 shows a diagram of the developed mobile intelligent poultry feed dispensing system. The system is modelled in terms of a DC motor and the flow rate of the liquid feed system. The system is modelled from first principle and presented in equations (3) and (4) [5]. The system is simulated using the Fuzzy Logic Controller and PID Controller in MATLABSIMULINK (R2018b version) and the performance is evaluated based on the system response parameters (rise time, settling time and overshoot).

$$G_{liquid}(s) = \frac{8.5}{s+0.07142} \quad (3)$$

$$G_{solid}(s) = \frac{3.475}{0.00374^2s^2 + 0.515995s + 12.33831} \quad (4) [5]$$



Figure 2: Mobile Intelligent Poultry Feed Dispensing System [5]

### B. Fuzzy Logic Control Development

#### I. Fuzzy Inference System (FIS)

The Fuzzy Inference System (FIS) is designed using the fuzzy logic toolbox provided by MATLAB. The Mamdani FIS is used in this study due to its widespread acceptance, intuitiveness and suitability for human inputs. The FIS comprised of two inputs (error and change in error) and one output (change in control signal). Defuzzification is achieved using the centroid technique which evaluates the area under a curve. This converts the fuzzy outputs to a crisp output. The output (change in error) is then integrated to provide the final control signal.

#### II. Membership Functions

The triangular membership function (MF) is implemented for all the inputs and the output due to its simplicity, wide use and ease of implementation. The input variables are error and change in error (or error variation). The output variable is the change in control signal. All the variables (error, change in error and change in control signal) have a range of -2 to 2 consisting of three MFs. The MFs were Negative (neg), Zero (zer) and

Positive (pos) with values of [-2, -1, 0], [-1, 0, 1] and [0, 1, 2] respectively. Figures 3, 4 and 5 show the input and output variables with the corresponding membership functions.

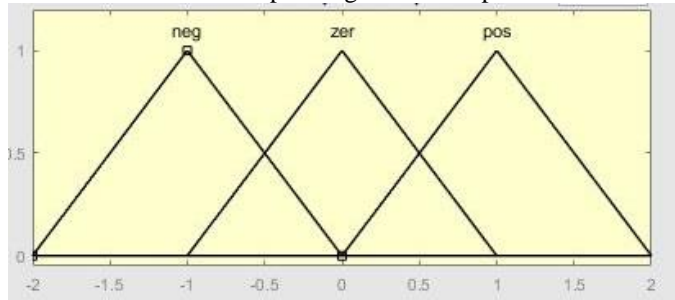


Figure 3: Membership Function for Error Input

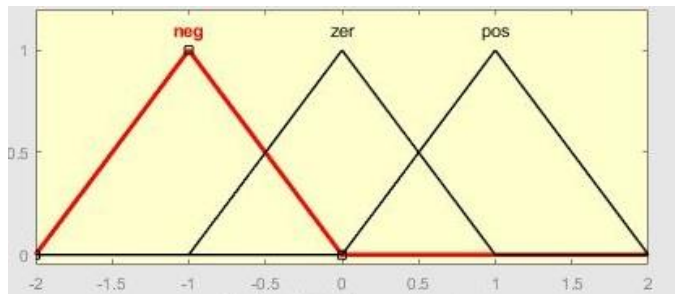


Figure 4: Membership Function for Change in Error Input

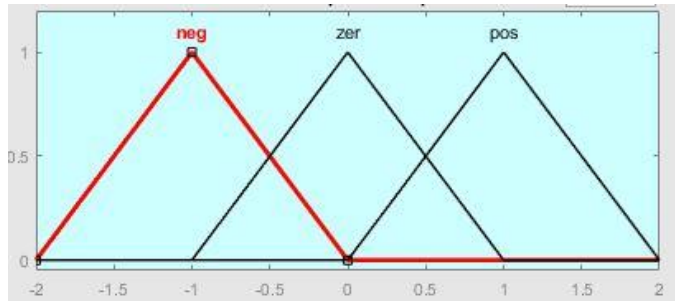


Figure 5: Membership Function for Change in Control Output

**III. Fuzzy Rules**

The fuzzy rules are designed based on the following considerations:

- i. If the error and change in error is zero, maintain the current output.
- ii. If the error is not zero but approaching zero, maintain current control output.
- iii. If the error is not zero and growing, change the control output based on the magnitude of the error.

The fuzzy rules are implemented based on the considerations above and the designed fuzzy rules are listed below. Figures 6 and 7 show the rule viewer and the surface viewer which provide a graphical representation of the implemented fuzzy rules.

1. If (error is neg) and (change\_in\_error is neg) then (change\_in\_control is neg)
2. If (error is neg) and (change\_in\_error is zer) then (change\_in\_control is neg)

3. If (error is neg) and (change\_in\_error is pos) then (change\_in\_control is zer)
4. If (error is zer) and (change\_in\_error is neg) then (change\_in\_control is neg)
5. If (error is zer) and (change\_in\_error is zer) then (change\_in\_control is zer)
6. If (error is zer) and (change\_in\_error is pos) then (change\_in\_control is pos)
7. If (error is pos) and (change\_in\_error is neg) then (change\_in\_control is zer)
8. If (error is pos) and (change\_in\_error is zer) then (change\_in\_control is pos)
9. If (error is pos) and (change\_in\_error is pos) then (change\_in\_control is pos)

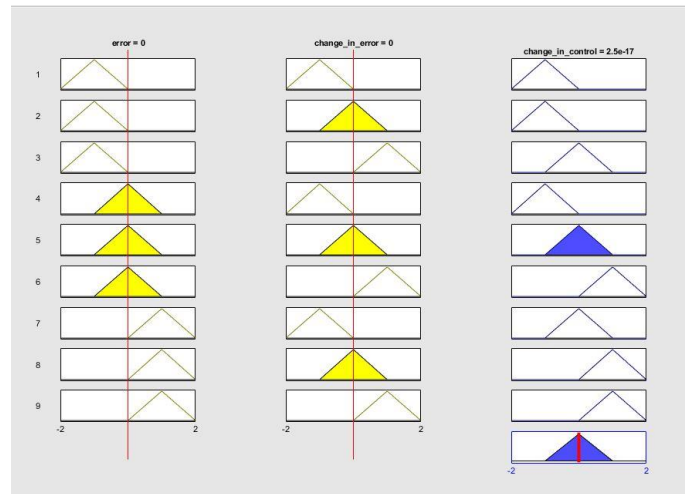


Figure 6: Fuzzy Logic Rules (Rule Viewer)

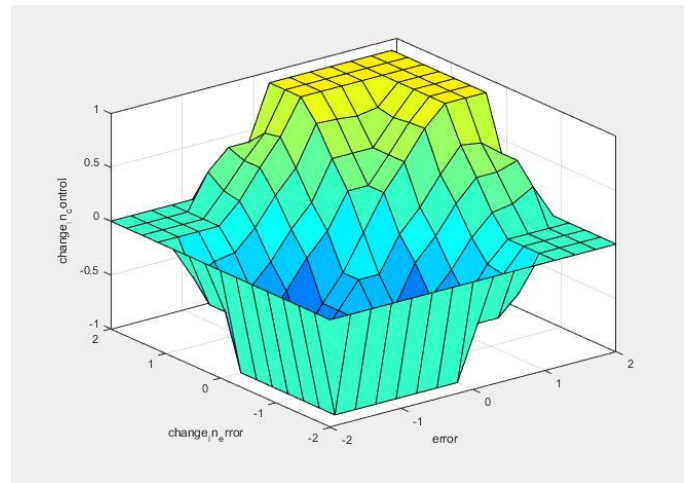


Figure 7: Fuzzy Logic Rules (Surface Viewer)

**C. PID Controller Development**

A closed loop control technique is used in the design. The PID controller is tuned using the PID tuner provided by the MATLAB software. The system is connected in series with a PID controller and a step input is fed into the system. From equations (3) and (4), it can be seen that the different subsystems of the poultry feeding system (solid and liquid)

have different transfer functions and therefore the PID controller design will vary in both cases. In the case of the solid feed subsystem, the proportional, integral and derivative gains are obtained as 7.0678, 271.2664 and 0.03372 respectively. On the other hand, the liquid feed subsystem is a first order system and therefore, a PI controller is used by setting the derivative gain to 0. This is because the derivative term has no significant effect on first order systems and increases the system complexity without significantly improving the performance. The proportional gain is obtained as 0.0088 and the integral gain is obtained as 0.0019.

The SIMULINK block diagram of the solid and liquid subsystems implemented with both the Fuzzy Logic Controller and PID controller are shown in figures 8 and 9. The outputs of both systems are connected to a single scope to visualize the varying effects of the different controllers on the system.

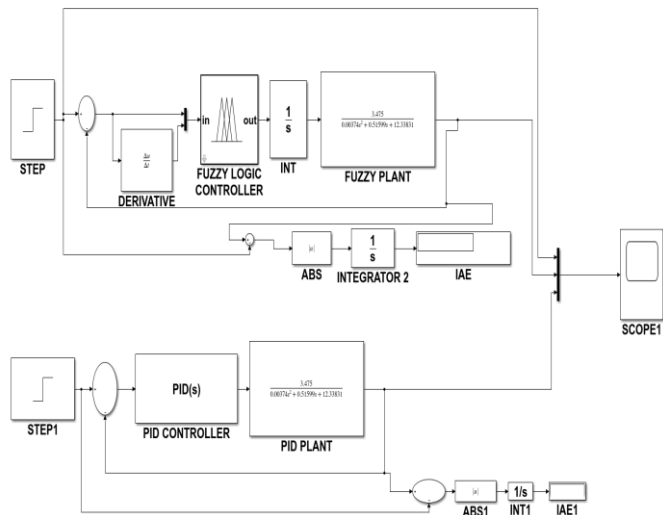


Figure 8: SIMULINK model of the solid feed subsystem with FLC and PID controller

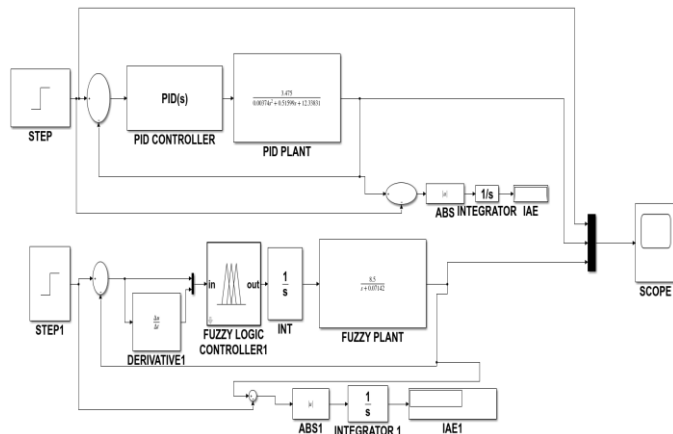


Figure 9: SIMULINK model of the liquid feed subsystem with FLC and PID controller

IV. RESULTS AND DISCUSSION

The system models are simulated using MATLAB/SIMULINK (R2018b version). The performance of each system is evaluated based on the rise time, settling time, overshoot and the

Integrated Absolute Error (IAE). The subsystems are modelled separately due to the difference in order and controller design.

A. Solid Feed Subsystem

The solid feed subsystem is connected in series with the fuzzy logic controller as well as the PID controller. Figure 10 shows the response of the solid feed subsystem.

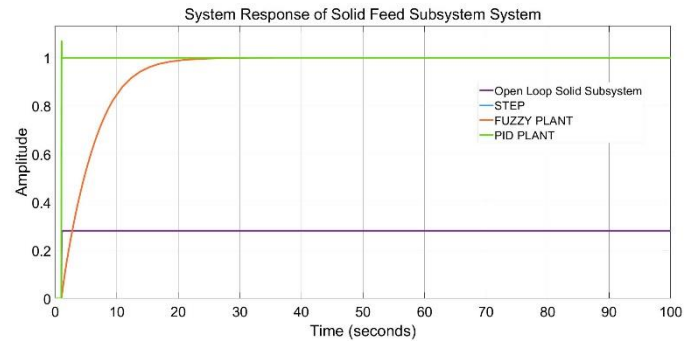


Figure 10: System Response of Solid Feed Subsystem

As shown in figure 10, the open loop system (without a controller) has a rise time of 0.076 seconds, a settling time of 0.100 seconds and an overshoot of 0.505%. However, the system has an IAE of 71.13 which is too high and unfavourable. In addition, the system’s output never reaches the reference input as it is less than 30% of the input. This indicates that without a control mechanism, the system response is quite poor due to the large error value. The PID controlled system has a rise time of 0.0281 seconds, a settling time of 0.0879 seconds and an overshoot of 6.989%. The system has an IAE of 0.0195. On the other hand, the fuzzy logic controlled system has a higher rise time, settling time and IAE of 9.748 seconds, 11.769 seconds and 4.759 respectively. However, the overshoot is much lower than that of the PID controlled system with a value of 0.505%.

B. Liquid Feed Subsystem

The liquid feed subsystem is connected in series with the fuzzy logic controller as well as the PID controller, as in the case of the solid feed subsystem. Figure 11 shows the response of the liquid feed subsystem.

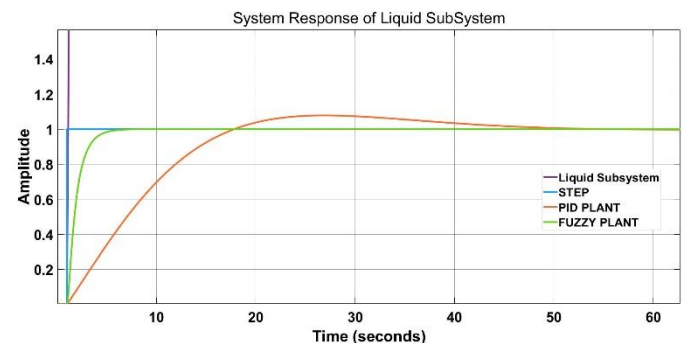


Figure 11: System Response of Liquid Subsystem

From figure 11, it can be seen that the open loop system (without a controller) has a rise time of 30.086 seconds, a settling time of 42.156 seconds and an overshoot of 0.501%.

However, the system has an IAE of 10020 which is extremely high. In addition, the system's output is about 120 times the reference input. This indicates that without a control mechanism, the system response is very unfavourable. The PID controlled system has a rise time of 11.209 seconds, a settling time of 35.906 seconds and an overshoot of 14.368 %. The system has an IAE of 8.213. On the other hand, the fuzzy logic controlled system has a lower rise time, settling time and IAE of 1.990 seconds, 2.838 seconds and 1.033 respectively. The overshoot is also much lower than that of the PID controlled system with a value of 0.446%. Table 1 shows a summary of the results obtained from all the subsystems.

Table 1: Summary of System Response Results

System/ System Response Parameter	Rise Time (seconds)	Settling Time (seconds)	Overshoot (%)	IAE
No Controller (Solid)	0.076	0.101	0.505	71.13
No Controller (Liquid)	30.086	42.156	0.501	1.002 $\times 10^4$
Solid Feed Subsystem (PID)	0.028	0.088	6.989	0.019
Solid Feed Subsystem (Fuzzy)	9.748	11.769	0.505	4.759
Liquid Feed Subsystem (PID)	11.209	35.906	14.368	8.213
Liquid Feed Subsystem (Fuzzy)	1.99	2.838	0.446	1.033

From Table 1, it can be seen that without any control mechanism, both subsystems gave a poor performance. In the case of the solid subsystem, the output never reaches the reference input while in the case of the liquid subsystem, the output is much larger than the reference input. In addition, the IAE is large in both subsystems.

In the case of the solid feed subsystem, the PID controller gives a faster response than the Fuzzy Logic Controller (FLC) as the rise time and settling time are lower than the FLC. The IAE is also lower than the FLC. However, the overshoot of the PID is higher than the FLC. This implies that in the case of the solid feed subsystem, the PID provides a faster response and more accurate response than the FLC but with a drawback of overshooting. In the liquid subsystem, the PID controller has higher rise time, settling time, overshoot and IAE than the FLC. The FLC gives a faster and more accurate response than the PID. This implies that the FLC performs better than the PID in the case of the liquid feed subsystem.

## V. CONCLUSION AND RECOMMENDATIONS

The poultry feed dispensing system was simulated with a fuzzy logic controller and a PID controller. The system response was evaluated based on its rise time, settling time, overshoot and IAE. From the results obtained and the comparisons made, it can be seen that both the PID controller and the fuzzy logic controller give a better performance than the system implemented without a controller. However, the PID controller gives a faster and more accurate response than the FLC in the solid feed subsystem, although the overshoot is higher in the PID controller. The FLC gives a better performance in the liquid feed subsystem in all the system response parameters evaluated.

Future works can attempt integrating multiple control techniques such as Fuzzy-PID and Neuro-Fuzzy control techniques.

## REFERENCES

- [1] S. Banu, "Precision Agriculture: Tomorrow's Technology for Today's Farmer," *J. Food Process. Technol.*, vol. 06, no. 08, pp. 8–13, 2015.
- [2] R. Bongiovanni and J. Lowenberg-Deboer, "Precision Agriculture and Sustainability," *Precis. Agric.*, vol. 5, pp. 359–387, 2004.
- [3] A. Balafoutis *et al.*, "Precision agriculture technologies positively contributing to ghg emissions mitigation, farm productivity and economics," *Sustain.*, vol. 9, no. 8, pp. 1–28, 2017.
- [4] V. I. Umogbai, "Development of a Mechanical Family Poultry Feeder," *J. Emerg. Trends Eng. Appl. Sci.*, vol. 4, no. 6, pp. 837–846, 2013.
- [5] O. M. Olaniyi, T. A. Folorunso, K. J.G., and J. A. Bala, "A Mobile Intelligent Poultry Feed Dispensing System Using Particle Swarm Optimized PID Control Technique," in *Proceedings of ISTEAMS Multidisciplinary Cross Border Conference, University of Professional Studies, Accra, Ghana*, 2016, pp. 185–194.
- [6] P. Mohindru, G. Sharma, and P. Pooja, "Simulation Performance of PID and Fuzzy Logic Controller for Higher Order System," *Commun. Appl. Electron.*, vol. 1, no. 7, pp. 31–35, 2015.
- [7] E. Yesil, M. Guzelkaya, and I. Eksin, "Fuzzy PID controllers: An overview," in *The 3rd Triennial ETAI International Conference on Applied Automatic Systems, At Ohrid, Macedonia*, 2003.
- [8] V. Kumar, B. Nakra, and A. Mittal, "A review of classical and fuzzy PID controllers," *Int. J. Intell. Control Syst.*, vol. 16, no. 3, pp. 170–181, 2011.
- [9] B. Omosebi, "Development of a self-propelled poultry feed dispenser with Feed level detector," Ladoke Akintola University of Technology, Nigeria, 2006.
- [10] O. T. Arulogun, O. M. Olaniyi, A. O. Oke, and D. O. Fenwa, "Development of Mobile Intelligent Poultry Feed Dispensing System," *Medwell J. Eng. Appl. Sci.*, vol. 5, no. 3, pp. 229–233, 2010.
- [11] O. M. Olaniyi, O. F. Salami, O. O. Adewumi, and O. S. Ajibola, "Design of an Intelligent Poultry Feed and Water Dispensing System Using Fuzzy Logic Control Technique," *Control Theory Informatics*, vol. 4, no. 9, pp. 61–72, 2014.
- [12] A. Adejumo, "Design and Development of a Mobile Intelligent Poultry Liquid Feed Dispensing System using GA Tuned PID Control Technique," Federal University of Technology, Minna, Nigeria, 2015.
- [13] H. O. Bansal, R. Sharma, and P. R. Shreeraman, "PID Controller Tuning Techniques : A Review," *J. Control Eng. Technol.*, vol. 2, no.

4, pp. 168–176, 2012.

- [14] B. Singh and A. K. Mishra, “Fuzzy Logic Control System and its Applications,” *Int. Res. J. Eng. Technol.*, vol. 2, no. 8, pp. 742–746, 2015.
- [15] A. S. Omar, M. Waweru, and R. Rimiru, “Application of Fuzzy Logic in Qualitative Performance Measurement of Supply Chain Management,” *Int. J. Inf. Commun. Technol. Res.*, vol. 5, no. 6, 2015.
- [16] Y. Luo *et al.*, “Fuzzy-Logic-Based Control, Filtering, and Fault Detection for Networked Systems: A Survey,” *Math. Probl. Eng.*, vol. 2015, 2015.



**Oladiran T Arulogun** is an Associate Professor in the Department of Computer Science and Engineering, Ladoke Akintola University of Technology, Ogbomosho, Nigeria. He was a visiting Research scholar at Hasso-Plattner Institute, Potsdam, Germany in 2012. He has published in reputable journals and learned conferences. His research interests include Networks Security, Wireless Sensor Network, Intelligent Systems and its applications.

## BIOGRAPHIES



Embedded Systems.

**Jibril Abdullahi Bala** is a Graduate Assistant with the Department of Mechatronics Engineering, Federal University of Technology, Minna, Nigeria. He obtained his Bachelor’s degree in Computer Engineering from Federal University of Technology, Minna, Nigeria. His area of interests are Control, Artificial Intelligence and



He had his Ph.D. in Computer Security from Ladoke Akintola University of Technology, Ogbomosho, Oyo State, Nigeria. He has published in reputable journals and learned conferences. His areas of research include Computer Security, Intelligent/Embedded Systems design and Applied Medical Informatics.

**Olayemi Mikail Olaniyi** is a Senior Lecturer in the Department of Computer Engineering at Federal University of Technology, Minna, Niger State, Nigeria. He obtained his B.Tech. and M.Sc. in Computer Engineering and Electronic and Computer Engineering respectively. He



He completed in Bachelor’s degree of Engineering in Electrical/Electronics Engineering at the Prestigious Ladoke Akintola University of Technology Ogbomosho Nigeria and proceeded to the famous Universiti Teknologi Malaysia for his Master’s Degree in Mechatronics and Automatic Control Engineering. He has published in reputable journals and learned conferences. His areas of research include: Control system, systems identification and estimation, Embedded Systems and Precision Agriculture.

**Folorunso Taliha Abiodun** is a Lecturer in the Department of Mechatronics Engineering Federal University of Technology Minna. He

# Fate of Entanglement for Initial Separable States in Quantum Neural Network

U. KORKMAZ

**Abstract**—This study is related to the fate of entanglement for initial separable states in a quantum neural network (QNN) model, which is in contact with the data environments locally. The duration of entanglement in quantum systems becomes extremely important when we consider it as a valuable resource. Thus, the effects of various initial states on the occurrence or decay of entanglement are investigated in the presence of information reservoirs. Especially in this study, central spin model has been examined as a quantum version of neural networks by taking inspiration from the biological models. Our model consists of a central spin system with two nodes to which the nodes are coupled to independent spin baths. Numerical results clearly show that different initial states have a profound effect on the fate of the entanglement. It also shows that the entanglement lifetime can be adjusted by regulating the reservoir states. The results can be used in realistic communication network situations to improve the performance of entanglement formation or distribution.

**Index Terms**— Entanglement, Information reservoir, Central spin model, Quantum neural network.

## I. INTRODUCTION

IN RECENT studies in the field of artificial intelligence, especially machine learning and artificial neural networks (ANN) have become popular. Machine learning, a field of computer science at the beginning of ANN, provides the ability to learn without explicit programming to computers [1-3]. Neural networks, which are interconnected computing structures based on binary McCulloch-Pitts neurons, are inspired by biological foundations [2]. The Hebb's learning rule, based on biological and neurophysiological basis, aims to obtain the best learning by changing the weight of the relevant units [4]. When classical learning rules address the dynamics in a statistical information environment, they manage them in the form of probability density functions [5]. Thus, the formulations and constraints of learning laws are based on the relationships between the global and local information environments of each transaction item.

UFUK KORKMAZ, is with Department of Electrical Engineering University of Istanbul Technical University, Istanbul, Turkey,(e-mail: [ufukkorkmaz@itu.edu.tr](mailto:ufukkorkmaz@itu.edu.tr)).

 <https://orcid.org/0000-0001-5836-5262>

Manuscript received January 12, 2019; accepted April 26, 2019.

DOI: [10.17694/bajece.541444](https://doi.org/10.17694/bajece.541444)

Networks that contain quantum material are known as quantum networks, which are important for the distribution of quantum resources and quantum communication [6]. The use of these quantum networks as neural networks has triggered several studies, including attempts to implement QNN suggestions in the context of quantum computations [7-18]. In this respect, quantum systems make the applications more attractive than classical communication tasks. In particular, one of the most interesting features of quantum mechanics is the entanglement. [19-21]. For this reason, it is important to understand their properties and dynamics for a number of applications in quantum mechanics. There are also many areas where entanglement plays a central role. For example, the transmission of unknown quantum data, quantum cryptography, secure communication, quantum measurement and quantum information processing [20-24]. In spite of these effective applications, because of the fragile nature of the entanglement, it is an important challenge to maintain and distribute entanglement for a sufficient amount of time.

When entangled system units come into contact with environmental degrees of freedom, entanglement decays to zero within a finite period. This is referred to as entanglement sudden death (ESD) [20, 25-27]. It was also observed experimentally by Almeida et al [28]. The entanglement dynamics in the common and independent reservoirs vary dramatically depending on the initial conditions of the system in the Markovian information environment [21]. In some cases, entanglement can be lost for a limited period of time, and then can revive again. The reason for this is that the common reservoirs tend to create entanglement instead of destroying completely it as a result of combining the qubits indirectly. Due to the correlation created by the environment, even if qubits are initially prepared in a factorized condition, may lead to a phenomenon known as entanglement sudden birth (ESB) [20, 29].

In this study, entanglement dynamics are investigated after creating a simple QNN architecture [30]. Although the dynamic behavior of quantum entanglement under certain assumptions in QNN architecture has been well studied for a few qubits scales, it should be reassessed for the sake of using quantum resources. Moreover, due to the rapid advances in technology, the entanglement production has been achieved more rapidly than the entanglement decay [31]. In particular, we investigate the dynamics of a small QNN unit in contact with the quantum information reservoir. In the Ref. [21], the information store concept was initially introduced in a classical style and was studied for quantum systems. We simulate the proposed quantum system up to three input nodes with different states

and examine the open system dynamics. This study relates to the numerical simulation of the dynamic evolution of an open QNN that is initially separated. The basic assumption of this paper is that QNNs in information environments are considered as open quantum systems. Therefore, the purpose of the study is to examine the dynamics of entanglement based on the quantum data of QNNs. Open system dynamics are modeled by repeated interactions [32,33] between the local nodes of the network and the units representing the reservoir. These repeated types of interactions have been shown to be dynamic maps equivalent to the Markovian principal equation approach, using the divisibility of quantum channels [34]. We have found that the initial states of the quantum network are strongly related to the entanglement dynamics. Both asymptotic decay and the decay of entanglement in finite time have been observed due to diversity in environmental states.

This paper is organized as follows: In Sec. II, we present the physical model and system dynamics. In Sec. III, we analyze the QNN as a system that interacts weakly with the information reservoir in the Markov approach. Finally, we conclude this work in Sec. IV.

## II. PHYSICAL MODEL AND SYSTEM DYNAMICS

One of the most important factors in the emergence of neural networks is the studies to perform advanced cognitive tasks [5]. Perceptron is the most simple neural network unit. And inspired by perceptron, we created the QNN model as equivalent to the central spin model (also known as the spin-star network) which has with various applications such as the decay of quantum coherence [35] and quantum communication [36]. In Ref. [37], the dynamic evolution of central spin quantum consistency based on different spin binding types with Markov Dynamics was investigated. It has also been shown that this model may have advantages on the quantum scale for thermodynamic studies [38]. In this study, the central spin model inspired by biological models (Fig. 1 (a)) was examined as a quantum version of neural networks.

The system of interest is treated as an open quantum system and consists of three interactive qubits with a flip-flop type Hamiltonian. The time-independent Hamiltonian representing system dynamics can also be used for quantum effects in biological systems [39]. This is expressed as follows

$$H = \frac{\omega}{2} \left( \sum_i^N \sigma_i^z + \sum_{i=1}^{N-1} \sigma_{u_i}^z \right) + \left( \sum_{i=1}^{N-1} J_i \sigma_i^+ \sigma_{out}^- + \sum_{i=1}^{N-1} J_i \sigma_{u_i}^+ \sigma_i^- + H.c. \right) \quad (1)$$

where  $\omega$ ,  $\sigma^z$ ,  $\sigma^+$ ,  $\sigma^-$  and  $\sigma_{out}^-$  are Bohr frequency each spin and single qubit information unit has been taken equal for simplicity, Pauli-z, raising and lowering operators for the qubits and Pauli operator for output qubit, respectively. Also,  $J_i$  is the coupling coefficient between input units and the output node,  $\sigma_i$  is the Pauli operator representing an individual node in contact with the information reservoir and  $\sigma_{u_i}$  is the Pauli operator of the individual unit representing the information reservoir.

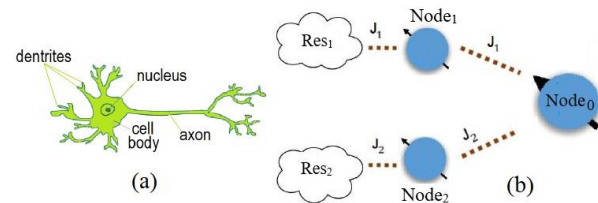


Fig.1. In (a) a biological neuron. In (b) unitary dynamics of a QNN unit with two input nodes

In this study, we use density matrix formalism to represent the quantum states of the relevant system. The quantum neurons are initially assumed to be in a product state as  $\rho(0) = \rho_{Res} \otimes \rho_{Sys}(0)$ , where  $\rho_{Res} = \rho_{Res1} \otimes \rho_{Res2}$  and  $\rho_s(0) = \rho_1(0) \otimes \rho_2(0) \otimes \rho_{out}(0)$  are Reservoir units and System units, respectively. Individual qubit states were chosen as  $\rho(0) = |\uparrow\rangle\langle\uparrow|$  in order to initially provide a blank memory. Here,  $\rho_{up} = |\uparrow\rangle\langle\uparrow|$ ,  $\rho_{dn} = |\downarrow\rangle\langle\downarrow|$ ,  $|\bar{\uparrow}\rangle = \frac{1}{\sqrt{2}}(|\uparrow\rangle - |\downarrow\rangle)$  are the cat states where  $|\uparrow\rangle$ ,  $|\downarrow\rangle$  are orthogonal spin states known as computational basis in quantum computing language.

Open system dynamics has been discussed by adopting a repetitive interaction process, also known as a collision model [40]. Fig. 1 (b) represents the open dynamics of the network to illustrate the specific use of the collision model. The initially and identically arranged qubit states that interact with the nodes of the neural network are obtained by tracing out the reservoir (environment) degrees of freedom as

$$\rho_s(t + \tau) = \text{Tr}_{u_i} [U(\tau) \rho_s(t) \otimes \rho_{u_i} U(\tau)^\dagger] \quad (2)$$

where,  $\text{Tr}_{u_i}$  stands for partial trace over environmental degrees of freedom,  $U(\tau) = e^{-iH\tau}$  is the unitary operator representing the system plus environment dynamics for time independent Hamiltonians and  $\tau$  is the duration of each unit-node interaction. Calculations were made using exact diagonalization. In our model,  $\rho_s$  the state of the system of interest (QNN) and  $\rho_{Res} = \rho_{u_i}$  represents the quantum state of each single qubit environment unit.

The aim of our study is to examine the change in the entanglement according to various initial states. That's why we are investigating that there is no initial entangled between the readout node and one of the input nodes in contact with the environment. After the system interacts with the information reservoir, the environment needs to send information to the system so that the system can be balanced with the environment carrying the quantum information content. Concurrence is a scalar function. It is used to measure the entanglement of density matrices that initially define the mixed states of a system [41]. In this paper concurrence is accepted as a measure of entanglement and calculated as  $C = \max[0, \lambda_1 - \lambda_2 - \lambda_3 - \lambda_4]$  where  $\lambda_i$  are the square roots of non-Hermitian matrix  $\rho \tilde{\rho}$ ,  $\rho$  is the density matrix to be calculated and  $\tilde{\rho}$  is its spin flipped from such as  $\tilde{\rho} = (\sigma_y \otimes \sigma_y) \rho^* (\sigma_y \otimes \sigma_y)$  where  $\rho^*$  is the complex conjugated from of  $\rho$ , the descending order [42].

## III. RESULTS

We analyze QNN, which we consider as a system that interacts weakly with the information store in the Markov approach. Due to this approach, the temporal evolution of the system only depends on the current state of the system. That is,

the quantum state of the system is lost irreversibly with reservoir degrees of freedom. In our scenario, each of the quantum information reservoirs interacts weakly with one of the input nodes (local subsystems) of the QNN unit. Pure single qubit states ( $|\uparrow\rangle\langle\uparrow|$  and  $|\downarrow\rangle\langle\downarrow|$ ) can represent information environments. The initial quantum state of the environment plus system is represented by  $\rho(0) = \rho_{\text{env}} \otimes \rho_{\text{sys}}(0)$  where  $\rho_{\text{sys}}(0) = \rho_1(0) \otimes \rho_2(0) \otimes \rho_0(0)$ . Here,  $\rho_1, \rho_2$  are the quantum states of the input nodes ( $Node_1, Node_2$ ) and  $\rho_0$  stands for the output node ( $Node_0$ ). Also, quantum state of the environmental qubit states are  $\rho_{\text{env}} = \rho_{\text{Res1}} \otimes \rho_{\text{Res2}}$  and fixed. Then, the concurrence time evolution between the two specific qubits of the three-qubit QNN system will be examined according to various initial states.

Fig. 2 represents the evolution of concurrence for initial separable states of the quantum neuron depending on the number of collisions (nc). In Fig. 2, the initial system plus environment states are **a)**  $\rho(0) = \rho_{dn} \otimes \rho_{up}(0) \otimes \rho_{|+\rangle}(0) \otimes \rho_{up}(0) \otimes \rho_{dn}$ , **b)**  $\rho(0) = \rho_{dn} \otimes \rho_{up}(0) \otimes \rho_{dn}(0) \otimes \rho_{up}(0) \otimes \rho_{dn}$ , **c)**  $\rho(0) = \rho_{dn} \otimes \rho_{dn}(0) \otimes \rho_{up}(0) \otimes \rho_{dn}(0) \otimes \rho_{dn}$  and **d)**  $\rho(0) = \rho_{up} \otimes \rho_{up}(0) \otimes \rho_{|+\rangle}(0) \otimes \rho_{up}(0) \otimes \rho_{dn}$ . In Fig. 2 **a)**, despite there is no initial entangled between the nodes of the QNN, during the early evolution of concurrence a rapid formation of entanglement between the nodes is evident. The observed entanglement rapidly decays as the system evolution continues (Fig. 2 **a)**, **b)** (between  $Node_1$  and  $Node_2$  ( $C_{21}$ )) and **d)**). More interestingly in the later evolution, a sudden birth of entanglement between  $Node_1$  and  $Node_2$  ( $C_{21}$ ) was observed where the nodes do not directly interact (Fig. 2 **a)** and **b)**). However, the revival scheme of Fig. 2 **b)** is slightly weaker than that observed in Fig. 2 **a)**. In Fig 2 **c)**, a rapid formation of entanglement in the very beginning of the evolution is appear for both  $C_{20}$  and  $C_{21}$  despite there is no initial entangled between the nodes of the QNN. As obvious they initial entangled decays exponentially and oscillatory. This applies to  $C_{21}$  in Fig. 2 **b)**. Especially in Fig. 2 **d)** initial entangled decays fast and end up in finite time [43].

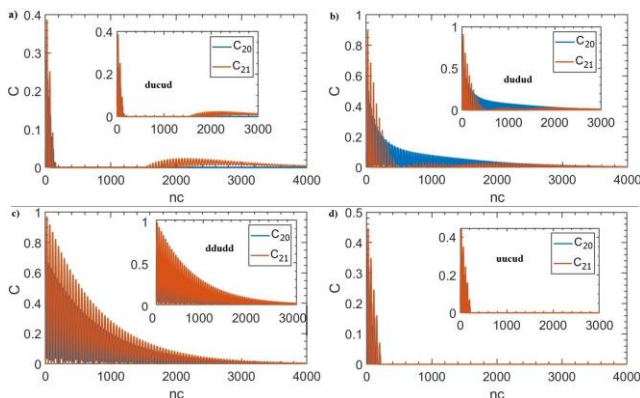


Fig.2. represents the evolution of concurrence for initial separable states of the quantum neuron depending on the number of collisions (nc).. **a)** The quantum state of the quantum neuron as  $Node_1 = \rho_{up}$ ,  $Node_2 = \rho_{up}$  and  $Node_0 = \rho_{|+\rangle}$  states. The state of the units representing the environment were set as  $\rho_{dn}$  for both of them. **b)** The quantum state of the quantum neuron  $Node_1 = \rho_{up}$ ,  $Node_2 = \rho_{up}$  and  $Node_0 = \rho_{|dn}\rangle$  states. The state of the units representing the environment were set as  $\rho_{dn}$  for both of them. **c)** The quantum state of the quantum  $Node_1 = \rho_{dn}$ ,  $Node_2 = \rho_{dn}$  and  $Node_0 = \rho_{up}$  states. The state of the units representing the environment were set as  $\rho_{dn}$  for both of them. **d)** The

quantum state of the quantum neuron as  $Node_1 = \rho_{up}$ ,  $Node_2 = \rho_{up}$  and  $Node_0 = \rho_{|+\rangle}$  states. The state of the units representing the environment were set as  $Res_1 = \rho_{up}$  and  $Res_2 = \rho_{dn}$ . The coupling between the environment unit and the input node is equal to the coupling between the input and the readout node  $J_1 = J_2 = J = 0.1$ . The duration of the each unit interaction  $\tau$  between the units and the input node is  $\tau = 5 \times 10^{-2}/J$

#### IV. CONCLUSION

We have connected the QNN unit, which we consider as open system dynamics, to two reservoirs by the conventional flip-flop Hamiltonian. We analyze QNN, which we consider as a system that interacts weakly with the information store in the Markov regimes. Each of the quantum information reservoirs interacts weakly with one of the input nodes (local subsystems) of the QNN unit. We adopt a collisional model to simulate open system quantum dynamics. The study also examines the generation of entanglement due to initially separable states. Numerical results clearly show that different initial states have a profound effect on the fate of the entanglement. We show that both entanglement revival (ESB) and entanglement sudden death (ESD) occur in the separable initial states. The results can be used to evolve the QNNs to distribute or connect the entanglement resource.

#### REFERENCES

- [1] S. Russell, P. Norvig, *Artificial Intelligence: A Modern Approach*. USA: Pearson, Upper Saddle River, 2009.
- [2] W.S. McCulloch, W. Pitts, "A logical calculus of the ideas immanent in nervous activity" *The bulletin of mathematical biophysics*, Vol.5, 4, 1943, pp.115-133.
- [3] F. Rosenblatt, "The perceptron: A probabilistic model for information storage and organization in the brain" *Psychological Review*, Vol.65, 6, 1958, pp.386-408.
- [4] D. O. Hebb, *The Organization of Behavior: A Neuropsychological Theory*, Psychology Press, Mahwah NJ, 2002.
- [5] R. Hecht-Nielsen, *Neurocomputing*, Boston, MA, USA: Addison-Wesley, 1990.
- [6] J. I. Cirac, P. Zoller, H. J. Kimble, H. Mabuchi, "Quantum state transfer and entanglement distribution among distant nodes in a quantum network" *Physical Review Letters*, Vol.78, 16, 1997, p. 3221.
- [7] M. Lewenstein, M. Olko, "Quantum neural networks" *Network: Computation in Neural Systems*, Vol.2, 1, 1991, pp.207-230.
- [8] S. Kak, "On quantum neural computing" *Information Sciences*, Vol.83, 3-4, 1995, pp.143-160.
- [9] M. Lewenstein, "Quantum Perceptrons" *Journal of Modern Optics*, Vol.41, 12, 1994, pp.2491-2501.
- [10] I. E. Lagaris, A. Likas, D. I. Fotiadis, "Artificial neural network methods in quantum mechanics" *Computer Physics Communications*, Vol. 104, 1-3, 1997, pp.1-14.
- [11] M. Zak, C. P. Williams, "Quantum Neural Nets" *International Journal of Theoretical Physics*, Vol.37, 2, 1998, pp.651-684.
- [12] A. Narayanan, T. Menneer, "Quantum artificial neural network architectures and components" *Information Sciences*, 2000; Vol.128, 3-4, 2000, pp.231-255.
- [13] D. Ventura, T. Martinez, "Quantum associative memory" *Information Sciences*, 2000; Vol. 124, 1-4, 2000, pp.273-296.
- [14] S. Gupta, R. K. P. Zia, "Quantum Neural Networks" *Journal of Computer and System Sciences*, Vol.63, 3, 2001, pp.355-383.
- [15] M. Panella, G. Martinelli, "Neural networks with quantum architecture and quantum learning" *International Journal of Circuit Theory and Applications*, Vol.39, 1, 2011, pp.61-77.
- [16] R. Zhou, H. Wang, Q. Wu, Y. Shi, "Quantum Associative Neural Network with Nonlinear Search Algorithm" *International Journal of Theoretical Physics*, Vol.51, 3, 2012, pp.705-723.
- [17] M. Schuld, I. Sinayskiy, F. Petruccione, "Simulating a perceptron on a quantum computer" *Physics Letters A*, 2015; Vol.379, 7, 2015, pp.660-663.

- [18] L. Banchi, N. Pancotti, S. Bose, "Quantum gate learning in qubit networks: Toffoli gate without time-dependent control" *npj Quantum Information*, Vol.2, 2016, p.16019.
- [19] R. Horodecki, P. Horodecki, M. Horodecki, K. Horodecki, "Quantum entanglement" *Reviews of Modern Physics*, Vol.81, 2, 2009, p.865.
- [20] L. Mazzola, S. Maniscalco, J. Piilo, K. A. Suominen, B. M. Garraway, "Sudden death and sudden birth of entanglement in common structured reservoirs" *Physical Review A*, Vol.79, 4, 2009, p.042302.
- [21] D. Türkpençe, "Disentanglement Dynamics of a Data Driven Quantum Neural Network" *NeuroQuantology*, Vol.16, 10, 2018, pp.14-19.
- [22] C. H. Bennett, G. Brassard, C. Crépeau, R. Jozsa, A. Peres, W. K. Wootters, "Teleporting an unknown quantum state via dual classical and Einstein-Podolsky-Rosen channels" *Physical Review Letters*, 1993; Vol.70, 13, 1993, pp.1895-1899.
- [23] V. Scarani, H. Bechmann-Pasquinucci, N. J. Cerf, M. Dušek, N. Lütkenhaus, M. Peev, "The security of practical quantum key distribution" *Reviews of Modern Physics*, Vol.81, 3, 2009, p.1301.
- [24] A. Galindo, M. A. Martin-Delgado, "Information and computation: Classical and quantum aspects" *Reviews of Modern Physics*, Vol.74, 2, 2002, p.347.
- [25] A. Al-Qasimi, D. F. V. James, "Sudden death of entanglement at finite temperature" *Physical Review A*, Vol.77, 1, 2008, p.012117.
- [26] T. Yu, J. H. Eberly, "Sudden Death of Entanglement" *Science*, Vol.323, 5914, 2009, pp.598-601.
- [27] J. León, C. Sabín, "Photon exchange and correlation transfer in atom-atom entanglement Dynamics" *Physical Review A*, Vol.79, 1, 2009, p.012301.
- [28] M. P. Almeida, F. de Melo, M. Hor-Meyll, A. Salles, S. P. Walborn, et al., "Environment-Induced Sudden Death of Entanglement" *Science* Vol.316, 5824, 2007, pp.579-582.
- [29] Z. Ficek, R. Tanaś, "Delayed sudden birth of entanglement" *Physical Review A*, Vol.77, 5, 2008, p.054301.
- [30] M. Schuld, I. Sinayskiy, F. Petruccione, "The quest for a quantum neural network" *Quantum Information Processing*, Vol.13, 11, 2014, pp.2567-86.
- [31] P. C. Humphreys, N. Kalb, J. P. Morits, R. N. Schouten, R. F. Vermeulen, et al., "Deterministic delivery of remote entanglement on a quantum network" *Nature*, Vol.558, 7709, 2018, p.268.
- [32] M. Ziman, P. Štelmachovič, V. Bužek, M. Hillery, V. Scarani, et al., "Diluting quantum information: An analysis of information transfer in system-reservoir interactions" *Physical Review A*, Vol.65, 4, 2002, p.042105.
- [33] V. Scarani, M. Ziman, P. Štelmachovič, N. Gisin, V. Bužek, "Thermalizing Quantum Machines: Dissipation and Entanglement" *Physical Review Letters*, Vol.88, 9, 2002, p.097905.
- [34] M. M. Wolf, J. I. Cirac, "Dividing quantum channels" *Communications in Mathematical Physics*, Vol.279, 1, 2008, pp.147-68.
- [35] W. H. Zurek, "Decoherence, einselection, and the quantum origins of the classical" *Reviews of Modern Physics*, Vol.75, 3, 2003, p.715.
- [36] Q. Chen, J. Cheng, K. L. Wang, J. Du, "Optimal quantum cloning via spin networks" *Physical Review A*, Vol.74, 3, 2006, p.034303.
- [37] D. Türkpençe, T. C. Akıncı, S. Şeker, "Decoherence in a quantumneural network" *NeuroQuantology*, Vol.16, 6, 2018, pp.1-5.
- [38] D. Türkpençe, F. Altıntaş, M. Patemostro, O. E. Müstecaplıoğlu, "A photonic Carnot engine powered by a spin-star network" *EPL (Europhysics Letters)*, Vol.117, 5, 2017, p.50002.
- [39] E. J. O'Reilly, A. Olaya-Castro, "Non-classicality of the molecular vibrations assisting exciton energy transfer at room temperature" *Nature Communications*, Vol.5, 3012, 2014.
- [40] D. Türkpençe, T. C. Akıncı, S. Şeker, "A steady state quantum classifier" *Physics Letters A*, 2019; In Press. doi: 10.1016/j.physleta.2019.01.063
- [41] R. Hildebranda, "Concurrence revisited" *Journal of Mathematical Physics*, Vol.48, 10, 2007, p.102108.
- [42] S. Hill, W. K. Wootters, "Entanglement of a Pair of Quantum Bits" *Physical Review Letters*, Vol.78, 26, 1997, p.5022.
- [43] T. Yu, J. H. Eberly, "Finite-time disentanglement via spontaneous emission" *Physical Review Letters*, Vol.93, 14, 2004, p.140404.

## BIOGRAPHIES



**UFUK KORKMAZ** was born in Turkey. He received the BSc, MSc and PhD degrees from the Ondokuz Mayıs University (OMU), Physics Department, in 2006, 2010 and 2014 respectively. He starting researches as Post-Doc in Istanbul Technical University (ITU) in 2018. His research interests are IR and UV spectroscopy, X-ray single crystal diffraction, Understanding the nature of H bonds in supramolecular structure, Quantum Mechanics and Quantum information theory.

# A Meta-Ensemble Classifier Approach: Random Rotation Forest

E. TAŞCI

**Abstract**—Ensemble learning is a popular and intensively studied field in machine learning and pattern recognition to increase the performance of the classification. Random forest is very important for giving fast and effective results. On the other hand, Rotation Forest can get better performance than Random Forest. In this study, we present a meta-ensemble classifier, called Random Rotation Forest to utilize and combine the advantages of two classifiers (e.g. Rotation Forest and Random Forest). In the experimental studies, we use three base learners (namely, J48, REPTree, and Random Forest) and two meta-learners (namely, Bagging and Rotation Forest) for ensemble classification on five datasets in UCI Machine Learning Repository. The experimental results indicate that Random Rotation Forest gives promising results according to base learners and bagging ensemble approaches in terms of accuracy rates, AUC, precision, recall, and F-measure values. Our method can be used for image/pattern recognition and machine learning problems.

**Index Terms**— Ensemble learning, Machine learning, Pattern recognition, Data mining, Classification, Rotation forest.

## I. INTRODUCTION

**E**NSSEMBLE SYSTEMS, MULTIPLE CLASSIFIER systems aim to combine individual decisions of a set of classifiers in some way typically by weighted or unweighted voting to classify new examples as an active research area of machine learning [1]. These systems specifically focus on obtaining a better classification performance than using a single model.

In recent years, ensemble learning has been extensively employed in a variety of subjects such as image classification, pattern recognition, remote sensing, text mining for its outstanding results [2-5]. Ensemble methods are composed of many base (weak) learners to provide data and model diversity. Types of decision tree such as CART [6], J48, REPTree [7] are commonly utilized as a base learner.

Random Forest, introduced by Breiman [8], is an extension of a bagging method and is a competitor to boosting such as AdaBoost. Thanks to its relatively fast and highly accurate

prediction, measures of variable importance, it is very attractive for classification problems. Random Forest can also deal with missing values.

On the other hand, Rotation Forest, proposed by Rodriguez et al. [9], generates classifier ensembles based on feature extraction. This ensemble learning method produces more accurate results than AdaBoost and Random Forest. It constructs individual classifiers more diverse than Bagging [9].

When both ensemble methods are compared, rotation forest applies Principal Component Analysis (PCA) on randomly selected feature subsets to reconstruct full feature space, promote the diversity and increase the accuracy of classifiers. In random forest, random selection of features to split each node provides error rates that compare favorably to AdaBoost [10].

The main contribution of this paper is summarized as follows: i) A meta-ensemble method which uses Random Forest as a base learner in the Rotation Forest ii) A comparative analysis of three base learners and two meta-ensemble learners on five datasets in UCI Machine Learning Repository in terms of five evaluation criteria: accuracy, weighted area under curve (AUC), precision, recall and F-measure.

The remainder of this paper is organized as follows: In Section II, related works specific to rotation forest are presented. In Section III, the proposed method is described in detail. Definition of the datasets, experimental process and results are given in Section IV. Finally, Section V mentions the conclusion and direction of future works.

## II. RELATED WORK

Classifications based on rotation forest method are commonly used in various fields such as machine learning, image recognition. Researchers developed improved versions of this ensemble method in their studies.

In [2], a new weight-based rotation forest (WRoF) ensemble algorithm is proposed for the classification of the hyperspectral image. Experimental results on two real hyperspectral datasets demonstrate that the WRoF algorithm results in significant improvement compared with random forests and rotation forest.

In [3], GA feature selection and Rotation Forest are used for Breast cancer diagnosis. Feature selection stage aims to reduce the computational complexity and speed up the data mining process. Their proposed approach yields the enhancement in performances.

**ERDDAL TASCI**, is with Department of Computer Engineering, Ege University, Izmir, Turkey, (e-mail: [arif.erdal.tasci@ege.edu.tr](mailto:arif.erdal.tasci@ege.edu.tr)).

 <https://orcid.org/0000-0001-6754-2187>

Manuscript received December 25, 2018; accepted April 2, 2019.  
DOI: [10.17694/bajece.502156](https://doi.org/10.17694/bajece.502156)

In [11], PCA, non-parametric discriminant analysis (NDA), random projections (RP) and independent component analysis (ICA) are applied to feature transformation in the original Rotation Forest for microarray dataset based cancer classification. According to the results, ICA improves the performance of Rotation Forest compared with the other transformation methods.

In [12], an ensemble classifier, called RotBoost, is proposed by combining Rotation Forest and AdaBoost. They used 36 real-world data sets from the UCI repository, among which a classification tree is adopted as the base learning algorithm. Their results show that RotBoost can generate ensemble classifiers with significantly lower prediction error than either Rotation Forest or AdaBoost.

In [13], firstly correlation-based feature selection (CFS) algorithm is performed for feature reduction. Then, ensemble methods are applied to medical datasets to increase classification accuracy.

In [14], Random Forest and Rotation Forest are applied to fully polarized SAR image classification using polarimetric and spatial features. Then, they conclude that Rotation Forest can get better accuracy than SVM and Random Forest, whereas Random Forest is much faster than Rotation Forest.

In [15], a classification method, called improved Rotation Forest (ROF) is proposed. In this method, Non-negative matrix factorization (NMF) is used to do feature segmentation to get more effective data. Then, kernel extreme learning machine (KELM) is chosen as a base classifier. Q-statistic is used to select base classifiers.

In [16], rotation forest is investigated for problems with continuous features whether this method is the best classifier or not.

### III. METHODOLOGY

This section presents the overview of the proposed system and describes data preprocessing stage, classification algorithms, ensemble learning methods and the algorithmic complexity of the method used in this study in detail.

#### A. Overview of the Proposed System

Overview of the proposed system is shown in Fig. 1. This system consists of several stages: datasets, base, and meta-learners, comparative analysis of results, conclusion and future work. In addition, 10-fold cross validation used for all learners and datasets to obtain generalization performance of the system is shown.

#### B. Data Preprocessing

In this stage, the ranges of the values of the data from diverse machine learning datasets may be high. In this case, some features can affect classification algorithms significantly or negatively. Therefore, data values are normalized to [0,1] range using min-max normalization technique [17]. For mapping a value, of a feature  $x_i$  from the range  $[\min(x_i), \max(x_i)]$  to a new range  $[\min x_{new}, \max x_{new}]$ , the normalized feature  $\hat{x}_i$  is computed as Eq. 1.

$$\hat{x}_i = \frac{x_i - \min_{x_i}}{\max_{x_i} - \min_{x_i}} (\max x_{new} - \min x_{new}) + \min x_{new} \quad (1)$$

#### C. Classification Algorithms

In this study, three base learners including J48, REPTree, and Random Forest are employed.

The J48 classifier is the extension of decision tree ID3 and straightforward C4.5 algorithms with additional features like accounting for missing values, continuous attribute value, and derivation of rules [18,19]. This classifier utilizes top-down and greedy search through all possible branches to construct a decision tree [19].

REPTree is a fast decision tree classifier algorithm. It constructs the decision tree using entropy and information gain of the attribute with reduced error pruning technique [18]. It builds multiple trees and selects the best tree from the generated list of trees [18]. This algorithm prunes the tree with the back fitting method.

The Random Forest classifier includes a set of tree classifiers. Each classifier is generated independently using randomly selected subspaces of data. Then, each tree assigns a unit vote for the most popular class to classify an input pattern with majority voting. Tree randomly samples the attributes, chooses and calculates the best split among those variables instead of the best split among all attributes in the training set [14]. The tree is grown using CART methodology to maximum size, without pruning [20].

Random Forest is considered to be one of the most accurate general-purpose learning techniques [20]. This algorithm is simple, easily parallelized, robust to outliers and noise, faster than bagging and boosting [8].

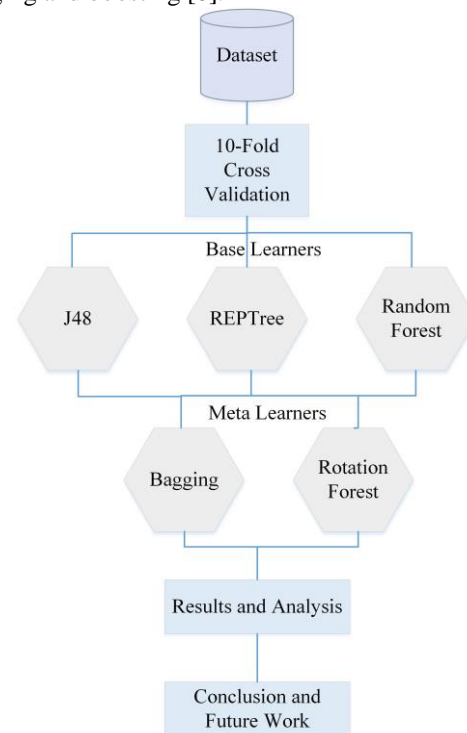


Fig.1. Overview of the proposed system

#### D. Ensemble Learning Methods

To evaluate the predictive performance, two ensemble algorithms consisting of Bagging and Rotation Forest are utilized. In addition, we introduce a forest-in-forest or meta

ensemble learning method (e.g. Random Rotation Forest) for effective classification results.

Bagging (short for bootstrap aggregating) algorithm is one of the earliest, simple, effective and popular ensemble learning approach. This algorithm generates an ensemble of independent models in which each base learner is trained using a sample of instances taken from the original dataset with replacement [21]. Bagging can be easily parallelized due to the fact that base learners are independently trained. It is best suited for problems with relatively small available training datasets [22].

Rotation Forest is an ensemble learning method that trains base learners on the whole dataset in a rotated feature space [21]. In this method, the features are randomly split into  $K$  subsets and PCA is applied to each subset for each base classifier in the ensemble [9]. The average confidence for each class and all classifiers are calculated. Then, the final class label is determined to the one with the highest confidence value [14].

#### E. The Algorithmic Complexity of the Proposed Method

The time complexity of Random Forest depends on the number of randomized trees ( $M$ ), samples ( $N$ ), and variables ( $p$ ) randomly drawn at each node. Accordingly, the time complexity for building Random Forest is  $O(MKN^2\log\tilde{N})$  [23].  $\tilde{N} = 0.632N$ , owing to the fact that bootstrap samples draw, on average, 63.2% of unique samples [23].

Similar to Random Forest, the time complexity of Rotation Forest depends on the number of PCA ( $P$ ) for randomly splitting feature subsets, the number of iterations ( $I$ ) and base learners ( $B$ ) [9]. For the proposed method, the time complexity of Random Rotation Forest can be calculated as  $O(PIMKN^2\log\tilde{N})$  due to the fact that we use Random Forest as a base learner.

The memory requirement of the proposed algorithm is directly proportional to the number of iterations ( $I$ ), the number of trees ( $T$ ), selected feature counts ( $F$ ) and the size of the dataset ( $S$ ). So, the proposed algorithm can use the space of  $(I*T*F*S)$ .

## IV. EXPERIMENTAL DESIGN

We describe and present the experimental process, evaluation measures and experimental results for this study in the subsections.

### A. Experimental Process

In this study, five datasets from UCI Machine Learning Repository [24] were utilized for classification schemes. These datasets are commonly used for machine learning problems. They also have numerical attributes and no missing values. The characteristics of these datasets are illustrated in Table I.

TABLE I  
CHARACTERISTICS OF THE DATASETS USED IN THIS STUDY

Dataset	Size	Features	Classes
diabetes	768	8	2
heart-statlog	270	13	2
ionosphere	351	34	2
messidor_features	1151	19	2
wifi	2000	7	4

In all experiments, J48, REPTree and Random Forest are chosen as base classifiers. In addition, bagging and rotation forest are used as meta-learners. All experiments are performed on total 9 schemes including base and ensemble learners by using WEKA (Waikato Environment for Knowledge Analysis) machine learning toolkit and JAVA programming language. We utilized default parameter values for all classifiers in WEKA.

We carry out a 10-fold cross validation to all datasets to yield reliable results for unseen data. For 10-fold cross-validation, the original dataset is randomly partitioned into 10 equally sized sets, one of which is used as a validation for testing, while the remaining sets are used for training operations. The process is repeated 10 times and calculated the averages of the results.

### B. Evaluation Measures

To evaluate the performance of the proposed method, we employed 5 different evaluation measures including accuracy rate, weighted AUC, weighted precision, weighted recall, and weighted F-measure.

Classification accuracy (ACC) is represented as the proportion of the total number of true positives and true negatives over the total number of instances. The equation of accuracy rate is shown in Eq. 2.

$$ACC = \frac{TP + TN}{TP + TN + FP + FN} \quad (2)$$

where TP, TN, FP, and FN denote the number of True Positives, True Negatives, False Positives, and False Negatives, respectively.

AUC is the area under the ROC curve for classifier performance. Its value will always be between 0.0 and 1.0. ROC graphs are two-dimensional graphs. In this curve, TP rate is plotted on the Y-axis and FP rate is plotted on the X-axis [25]. If AUC value is close to 1, the classifier is stronger and better than random classifier.

Precision is the positive predictive value [25]. It is the ratio of the number of true positives to the total number of true positives and false positives. The equation is illustrated in Eq. 3.

$$Precision = \frac{TP}{TP + FP} \quad (3)$$

Recall is the true positive rate or hit rate [25]. It is the ratio of the number of true positives to the total number of true positives and false negatives (e.g. total number of positives). The equation is illustrated in Eq. 4.

$$Recall = \frac{TP}{TP + FN} \quad (4)$$

F-measure is defined in Eq. 5 [25]. This measure depends on precision and recall values.

$$F\text{-measure} = \frac{2}{1/precision + 1/recall} \quad (5)$$

In the weighting operation, these criteria are adjusted by the reference class's prevalence proportionally in the data [26].

### C. Experimental Results

Table II presents classification accuracies for all datasets, base and ensemble learners. As it can be observed from Table II, Random Rotation Forest gives highly accurate results than other approaches except for heart-statlog dataset. In addition to the fact that Random forest produces more accurate results than J48 and REPTree, Rotation Forest is suitable for meta-learner.

In Table III, weighted AUC values are introduced for all datasets, base and ensemble classifiers. According to Table III, Random Rotation Forest gives the best results very close or equal to 1.0. So, it can be concluded that Random Rotation Forest is very strong and effective classifier for machine learning tasks used in this study.

In Table IV, weighted precision values obtained by all base and ensemble classifiers for all datasets are presented. As it can be observed from Table IV, Random Rotation Forest produces similar results to Table II. When this meta ensemble learning method is used, the performance of the system increases significantly.

In Table V and VI, weighted recall and weighted F-measure values are illustrated for all datasets, base and ensemble classifiers, respectively. These values give similar results compared to Table II and IV.

As well as these given tables, to show the effects of the classifiers and datasets, the charts are given in Fig. 2-6.

TABLE II  
CLASSIFICATION ACCURACIES (%) FOR UCI DATASETS

Datasets	Base Learner			Meta Learner Bagging			Meta Learner Rotation Forest		
	J48	REPTree	Random Forest	J48	REPTree	Random Forest	J48	REPTree	Random Forest
diabetes	72.01	73.70	75.78	74.22	75.78	76.43	75.78	76.95	<b>77.47</b>
heart-statlog	79.26	76.30	<b>83.33</b>	79.63	81.48	82.59	80.37	81.11	81.85
ionosphere	90.31	89.74	93.73	92.31	90.88	93.73	93.45	93.16	<b>94.87</b>
messidor_features	65.33	63.42	69.42	66.38	66.81	68.20	68.72	72.81	<b>73.76</b>
wifi	97.40	97.20	98.30	97.65	97.10	98.45	98.40	98.00	<b>98.55</b>

TABLE III  
WEIGHTED AUC VALUES FOR UCI DATASETS

Datasets	Base Learner			Meta Learner Bagging			Meta Learner Rotation Forest		
	J48	REPTree	Random Forest	J48	REPTree	Random Forest	J48	REPTree	Random Forest
diabetes	0.74	0.78	0.83	0.82	0.83	0.83	0.82	0.83	<b>0.83</b>
heart-statlog	0.77	0.80	0.90	0.88	0.87	0.90	0.88	0.88	<b>0.90</b>
ionosphere	0.90	0.90	0.98	0.95	0.94	0.98	0.97	0.97	<b>0.99</b>
messidor_features	0.68	0.66	0.76	0.74	0.73	0.76	0.74	0.81	<b>0.82</b>
wifi	0.99	0.99	1.00	1.00	1.00	1.00	1.00	1.00	<b>1.00</b>

TABLE IV  
WEIGHTED PRECISION VALUES FOR UCI DATASETS

Datasets	Base Learner			Meta Learner Bagging			Meta Learner Rotation Forest		
	J48	REPTree	Random Forest	J48	REPTree	Random Forest	J48	REPTree	Random Forest
diabetes	0.72	0.73	0.75	0.74	0.75	0.76	0.75	0.76	<b>0.77</b>
heart-statlog	0.79	0.76	<b>0.83</b>	0.80	0.82	0.83	0.80	0.81	0.82
ionosphere	0.90	0.90	0.94	0.92	0.91	0.94	0.94	0.93	<b>0.95</b>
messidor_features	0.65	0.64	0.70	0.67	0.67	0.69	0.70	0.73	<b>0.74</b>
wifi	0.97	0.97	0.98	0.98	0.97	0.98	0.98	0.98	<b>0.99</b>

TABLE V  
WEIGHTED RECALL VALUES FOR UCI DATASETS

Datasets	Base Learner			Meta Learner Bagging			Meta Learner Rotation Forest		
	J48	REPTree	Random Forest	J48	REPTree	Random Forest	J48	REPTree	Random Forest
diabetes	0.72	0.74	0.76	0.74	0.76	0.76	0.76	0.77	<b>0.77</b>
heart-statlog	0.79	0.76	<b>0.83</b>	0.80	0.81	0.83	0.80	0.81	0.82
ionosphere	0.90	0.90	0.94	0.92	0.91	0.94	0.93	0.93	<b>0.95</b>
messidor_features	0.65	0.63	0.69	0.66	0.67	0.68	0.69	0.73	<b>0.74</b>
wifi	0.97	0.97	0.98	0.98	0.97	0.98	0.98	0.98	<b>0.99</b>

TABLE VI  
WEIGHTED F-MEASURE VALUES FOR UCI DATASETS

Datasets	Base Learner			Meta Learner Bagging			Meta Learner Rotation Forest		
	J48	REPTree	Random Forest	J48	REPTree	Random Forest	J48	REPTree	Random Forest
diabetes	0.72	0.73	0.75	0.74	0.75	0.76	0.75	0.76	<b>0.77</b>
heart-statlog	0.79	0.76	<b>0.83</b>	0.80	0.81	0.83	0.80	0.81	0.82
ionosphere	0.90	0.90	0.94	0.92	0.91	0.94	0.93	0.93	<b>0.95</b>
messidor_features	0.65	0.63	0.69	0.66	0.67	0.68	0.69	0.73	<b>0.74</b>
wifi	0.97	0.97	0.98	0.98	0.97	0.98	0.98	0.98	<b>0.99</b>

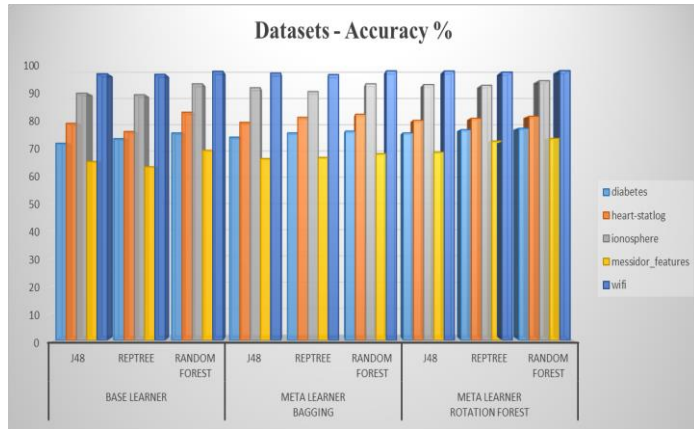


Fig.2. The chart showing the effects between datasets and accuracies

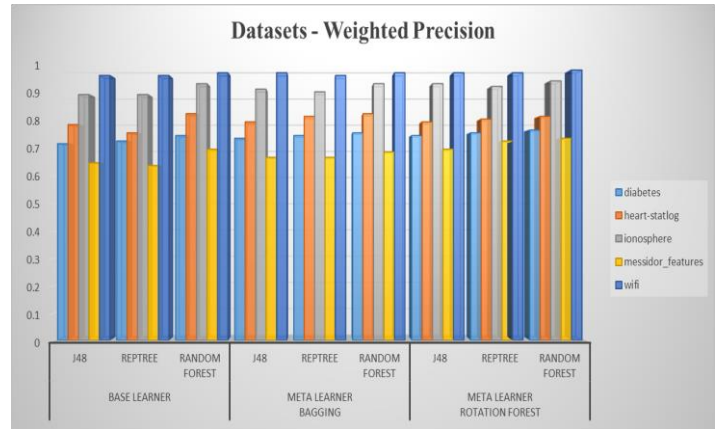


Fig.4. The chart showing the effects between datasets and weighted precision values

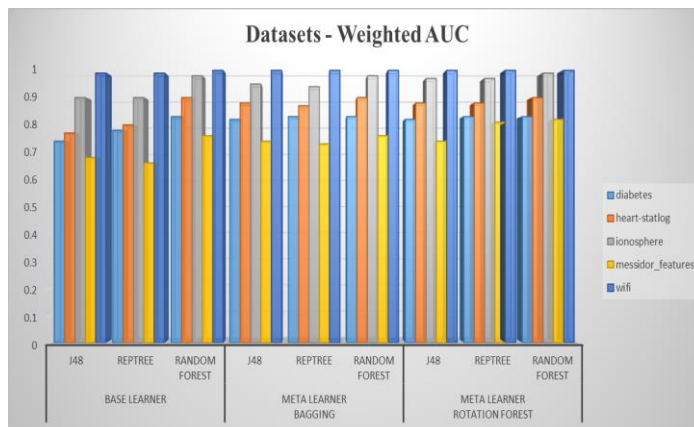


Fig.3. The chart showing the effects between datasets and weighted AUC values

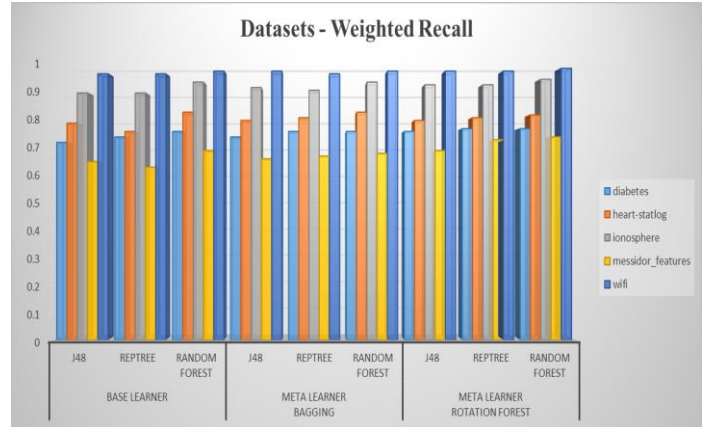


Fig.5. The chart showing the effects between datasets and weighted recall values

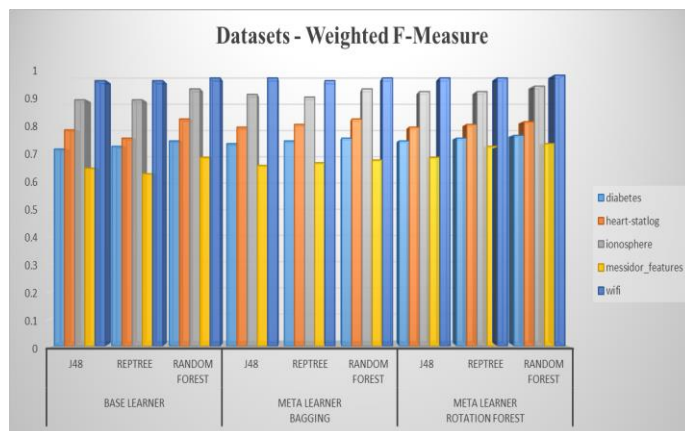


Fig.6. The chart showing the effects between datasets and weighted F-measure values

## V. CONCLUSION AND FUTURE WORK

Nowadays, the use of the ensemble classifier is becoming more common due to its effectiveness and high performance for various fields such as machine learning and pattern recognition. In this study, a meta-ensemble learning method (Random Rotation Forest) based on Random Forest and Rotation Forest is proposed. Despite the fact that Random Rotation Forest can take more space and time for computations, this method yields more efficient results by using hybrid advantages of both algorithms.

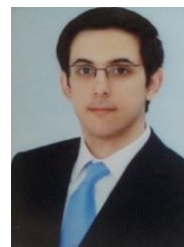
As a future work, other hybridization of ensemble learning methods can be obtained. In addition, classifier weighting for base and meta-learners can be provided for improving classification. Feature weighting approaches can also be tried with diverse optimization algorithms [27].

## REFERENCES

- [1] T.G. Dietterich, Ensemble methods in machine learning. In International workshop on multiple classifier systems, Springer, Berlin, Heidelberg, 2000, pp. 1-15.
- [2] W. Feng, W. Bao, Weight-Based Rotation Forest for Hyperspectral Image Classification, *IEEE Geoscience and Remote Sensing Letters*, 14(11), 2017, pp. 2167-2171.
- [3] E. Aličković, A. Subasi, Breast cancer diagnosis using GA feature selection and Rotation Forest, *Neural Computing and Applications*, 28(4), 2017, pp. 753-763.
- [4] M. Pal, Random forest classifier for remote sensing classification, *International Journal of Remote Sensing*, 26(1), 2005, pp. 217-222.
- [5] A. Onan, Sentiment Analysis on Twitter Based on Ensemble of Psychological and Linguistic Feature Sets, *Balkan Journal of Electrical and Computer Engineering*, 6(2), 2018, pp. 1-9.
- [6] W. Y. Loh, Classification and regression trees, *Wiley Interdisciplinary Reviews: Data Mining and Knowledge Discovery*, 1(1), 2011, pp. 14-23.
- [7] W.N.H.W. Mohamed, M.N.M. Salleh, A.H. Omar, A comparative study of reduced error pruning method in decision tree algorithms, In *Control System, Computing and Engineering (ICCSCE)*, 2012 IEEE International Conference on, 2012, pp. 392-397.
- [8] L. Breiman, Random forests, *Machine learning*, 45(1), 2001, pp. 5-32.
- [9] J.J. Rodriguez, L.I., Kuncheva, C.J. Alonso, Rotation forest: A new classifier ensemble method, *IEEE transactions on pattern analysis and machine intelligence*, 28(10), 2006, pp. 1619-1630.
- [10] Y. Freund, R.E. Schapire, Experiments with a new boosting algorithm, In *Icml*, 96, 1996, pp. 148-156.
- [11] K.H. Liu, D.S. Huang, Cancer classification using rotation forest, *Computers in biology and medicine*, 38(5), 2008, pp. 601-610.
- [12] C.X. Zhang, J.S. Zhang, RotBoost: A technique for combining Rotation Forest and AdaBoost. *Pattern recognition letters*, 29(10), 2008, pp. 1524-1536.

- [13] A. Ozcift, A. Gulden, Classifier ensemble construction with rotation forest to improve medical diagnosis performance of machine learning algorithms, *Computer methods and programs in biomedicine*, 104(3), 2011, pp. 443-451.
- [14] P. Du, A. Samat, B. Waske, S. Liu, Z. Li, Random forest and rotation forest for fully polarized SAR image classification using polarimetric and spatial features, *ISPRS Journal of Photogrammetry and Remote Sensing*, 105, 2015, pp. 38-53.
- [15] F. Lv, M. Han, Hyperspectral image classification based on improved rotation forest algorithm, *Sensors*, 18(11), 2018, 3601.
- [16] A. Bagnall, A. Bostrom, G. Cawley, M. Flynn, J. Lines, Is rotation forest the best classifier for problems with continuous features?, 2018, arXiv preprint arXiv:1809.06705.
- [17] B.K. Singh, K. Verma, A.S. Thoke, Investigations on impact of feature normalization techniques on classifier's performance in breast tumor classification, *International Journal of Computer Applications*, 116(19), 2015, pp. 11-15.
- [18] C.L. Devasena, Comparative analysis of random forest, REP tree and J48 classifiers for credit risk prediction, In *International Journal of Computer Applications (0975-8887)*, International Conference on Communication, Computing and Information Technology (ICCCMIT-2014), 2014, pp. 30-36.
- [19] P. Hamsagayathri, P. Sampath, Decision tree classifiers for classification of breast cancer, *Int. J. Curr. Pharm. Res*, 9(2), 2017, 31.
- [20] G. Biau, Analysis of a random forests model, *Journal of Machine Learning Research*, 13(Apr), 2012, pp. 1063-1095.
- [21] O. Sagi, L. Rokach, Ensemble learning: A survey, *Wiley Interdisciplinary Reviews: Data Mining and Knowledge Discovery*, 8(4), e1249, 2018, pp. 1-18.
- [22] C. Zhang, Y. Ma, Ensemble machine learning: methods and applications, Springer Science & Business Media, 2012.
- [23] G. Louppe, Understanding random forests: From theory to practice, arXiv preprint arXiv:1407.7502, 2014.
- [24] UCI Machine Learning Repository, 2018, <https://archive.ics.uci.edu/ml/datasets.html>
- [25] T. Fawcett, An introduction to ROC analysis, *Pattern recognition letters*, 27(8), 2006, pp. 861-874.
- [26] T. Fawcett, ROC graphs: Notes and practical considerations for researchers, *Machine learning*, 31(1), 2004, pp. 1-38.
- [27] E. Taşçı, O. Gökalp, A. Uğur, Development of a novel feature weighting method using CMA-ES optimization, In *2018 26th Signal Processing and Communications Applications Conference (SIU)*, IEEE, 2018, pp. 1-4.

## BIOGRAPHIES



**ERDAL TAŞCI** was born in 1989. He received the BS, MSc and PhD degrees from the Ege University, Computer Engineering Department, Izmir, Turkey, in 2011, 2013 and 2018, respectively. He has been working as teaching assistant at the Department of Computer Engineering of Ege University, Izmir, Turkey. He has been reviewing for various journals including *IEEE Transactions on Systems, Man, and Cybernetics: Systems*, *Computer Methods and Programs in Biomedicine* and *IET Image Processing*. His research interests are pattern recognition, machine learning, image processing and data mining.

# Minimizing Mutually Coupled Switched Reluctance Machine's Stator Volume by Stator Yoke Modification

C. SAHIN, M. KARACOR and A. E. AMAC

**Abstract**—In parallel with the increased production of electric vehicles, the research on electric motors has become very popular. Switched Reluctance Machines (SRMs) have been widely preferred in these investigations. Mutually Coupled Switched Reluctance Machine (MCSRМ) has higher torque performances than conventional SRMs have. In this study, it is aimed to reduce the weight of MCSRМ by geometric arrangement. For this purpose, the MCSRМ's stator yoke is minimized without deteriorating the flux distribution. Various geometrical changes are performed on the stator yoke of the MCSRМ. Each of the obtained motor models is magnetostatic analyzed in different currents by finite-element analysis. From comparison of the results of the analysis, it is seen that the proposed MCSRМ models show reduction in the stator volumes between 11.31% and 14.17%. This reduction leads to a reduction in the overall weight of the MCSRМ.

**Index Terms**—Mutually Coupled Switched Reluctance Machine (MCSRМ), stator yoke, volume, weight.

## I. INTRODUCTION

THE STUDIES OF advanced traction motors generally focus on efficiency, high power density, higher torque, lower noise, and cost [1]. Permanent magnet (PM) motors have high efficiency, high torque density, and compactness. Because of these features, they are widely used in hybrid and electric vehicles. But, the magnet is a rare element in nature. For this reason, the magnet is still one of the main concerns for hybrid and electric vehicle manufacturers. In this case,

**CIHAN SAHIN**, is with Department of Control and Automation of University of Bilecik Seyh Edebali, Bilecik, Turkey, (e-mail: [cihan.sahin@bilecik.edu.tr](mailto:cihan.sahin@bilecik.edu.tr)).

 <https://orcid.org/0000-0001-6430-7827>

**MEVLUT KARACOR**, is with Department of Mechatronic Engineering of University of Celal Bayar, Turgutlu, Turkey, (e-mail: [mevlut.karacor@cbu.edu.tr](mailto:mevlut.karacor@cbu.edu.tr)).

 <https://orcid.org/0000-0001-5408-9117>

**AYSE ERGUN AMAC**, is with Department of Energy Systems Engineering of University of Kocaeli, Kocaeli, Turkey, (e-mail: [ayseergun@kocaeli.edu.tr](mailto:ayseergun@kocaeli.edu.tr)).

 <https://orcid.org/0000-0003-3215-0129>

Manuscript received December 27, 2018; accepted April 13, 2019.  
DOI: [10.17694/bajece.503752](https://doi.org/10.17694/bajece.503752)

SRMs can be considered as one of the alternative solutions [2-3].

SRMs consist of a stator with windings and a rotor with saliency. They have no winding or permanent magnet on rotor [4-5]. Since SRMs do not need PM, they have low cost and work even in high temperature conditions created by internal-combustion engines [6]. SRMs are ideal for adjustable speed applications because of these properties [7]. They have stronger structure compared to PM motors, although they are produced simpler and at cheaper cost [8]. Although PM motors are preferred for specific applications, they might not be cost effective for mass production in certain applications [9]. SRMs also offer high efficiency and extended-speed constant power operation [10]. Because of all these advantages, SRMs are useful and attractive for electric vehicles as well as they have high competitive power in transportation applications [11-14].

High torque ripple is one of the major disadvantages of SRMs due to their high nonlinearity of torque production [15-16]. For the purpose of the torque ripple reduction, the researchers have improved the motor magnetic design and have used complex control algorithms for the motor [17-18]. In recent years, many studies have been devoted to different rotor or stator configurations with specific properties to improve the performance of SRMs [19-20].

In conventional SRMs, the windings are located on opposite poles of the stator. They are connected as series to form a phase of the machine. The asymmetric-half-bridge type converter is commonly used in SRM drives [21]. When a suitable phase in the machine is excited with DC voltage, the moving rotor begins to rotate in the direction that reduces the reluctance of the magnetic circuit. The continuity in turning of the rotor is obtained by energizing the phases respectively. Fig. 1 shows the 3-phase, 6/4-pole stator-rotor structure of conventional SRMs.

Torque characteristics of SRM are highly nonlinear and dependent on the rotor position and phase current [22]. SRMs operate based on reluctance torque and have a "minimum reluctance" rule. In addition, they cannot be easily applied to traditional power equations [23]. In SRMs, as the air gap between the stator and rotor pole heads increases, the reluctance of the magnetic circuit also grows. The machine structure tends to reduce this high reluctance and produces a torque for this. With the production of torque, the stator and rotor pole heads close up. As a result, the reluctance of the magnetic circuit is reduced. Thus, as a result of the request to

reduce the reluctance, the continuity of the machine torque is generated.

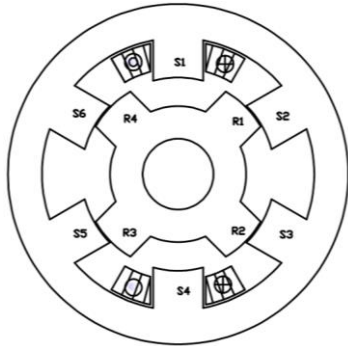


Fig.1. Conventional SRM

The winding structure of conventional SRMs is short pitched. Mecrow has changed the winding structure of classical SRM and placed windings as full pitched instead of short pitched [24]. It is called the ‘fully-pitched SRM’. The electromagnetic (EM) torque in fully-pitched SRM is formed entirely by the mutual inductance formed between the phases [25-26]. The fully-pitched SRMs are also known as MSCRM and are named accordingly [26]. MCSRMs could have 25% more output torque than conventional SRM could have [25]. These machines can be used in a variety of applications, using conventional 6 switch inverter or the asymmetric half-bridge converter [26].

In this study, the performance of MCSRM based on stator volume is proposed. For this aim, a MCSRM prototype and five different MCSRM models with modified stator yoke are developed. The only difference between the proposed models is the geometric arrangements on the stator yoke. The other parameters of the machine are kept constant. Therefore, they have not been observed in this study.

II. STRUCTURE OF MCSRM

The phase coupling in the conventional SRMs is very small and can be neglected, but it cannot be neglected for MCSRM. Therefore, the phases are coupled by the nature of MSCRM operation [27]. The torque in MCSRMs is produced by the changing of the mutual coupling that occurs between phases according to the rotor position [25]. As a result; torque is produced by energizing more than one phase at the same time. Fig. 2 shows the structure of MCSRM.

In SRMs, torque is produced by controlling each phase independently. Thus, torque generation is transferred from the active phase to the other phase. Consequently, torque vibrations become important in these switching moments [28]. Eq. (1) shows the general torque expression in a SRM.

$$T = \frac{1}{2} i_a i_b \frac{\partial M_{ab}}{\partial \theta} + \frac{1}{2} i_b i_c \frac{\partial M_{bc}}{\partial \theta} + \frac{1}{2} i_c i_a \frac{\partial M_{ca}}{\partial \theta} + \frac{1}{2} i_a^2 \frac{\partial L_a}{\partial \theta} + \frac{1}{2} i_b^2 \frac{\partial L_b}{\partial \theta} + \frac{1}{2} i_c^2 \frac{\partial L_c}{\partial \theta} \quad (1)$$

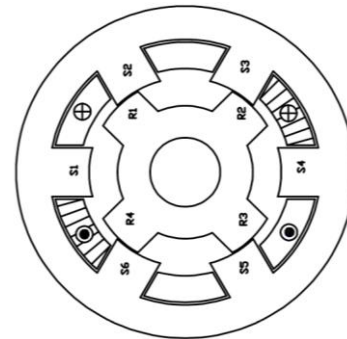


Fig.2. Mutual Coupled SRM

Where T is the total torque;  $i_a, i_b, i_c$  are the phase currents;  $L_a, L_b, L_c$  are the phase inductances; and  $M_{ab}, M_{bc}, M_{ac}$  are the mutual inductances between the phases. Since the torque in MCSRM is produced with the mutual inductance between the phases and self inductances are neglected in MCSRMs, the torque can be denoted as in equation (2) [26].

$$T = \frac{1}{2} i_a i_b \frac{\partial M_{ab}}{\partial \theta} + \frac{1}{2} i_b i_c \frac{\partial M_{bc}}{\partial \theta} + \frac{1}{2} i_c i_a \frac{\partial M_{ca}}{\partial \theta} \quad (2)$$

Since two phases are active in MCSRM (assume phase ‘a’ and phase ‘b’ are active, and phase ‘c’ is passive), Eq. (2) turns into Eq. (3).

$$T = \frac{1}{2} i_a i_b \frac{\partial M_{ab}}{\partial \theta} \quad (3)$$

III. DESIGN OF MCSRM

The only feature which distinguishes the five proposed MCSRM models from the basic MCSRM model is the stator yoke structures. For the comparison of the machines, the basic model MCSRM is called MCSRM-0 in this study. Fig. 3 denotes the geometric structure of the 6/4 MCSRM-0.

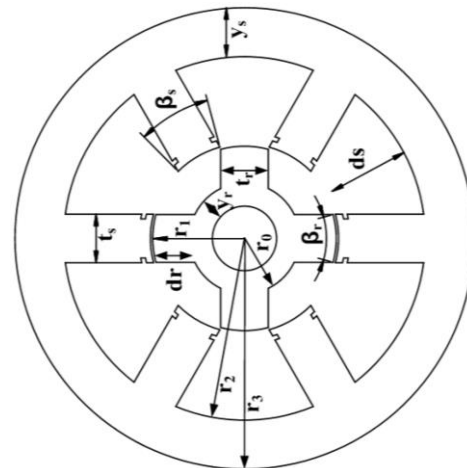


Fig.3. Geometric structure of the MCSRM-0

Where  $\beta_r$  is the rotor pole arc (degree),  $\beta_s$  is the stator pole arc (degree),  $t_s$  is the stator pole width,  $t_r$  is the rotor pole

width,  $d_s$  is the stator pole height,  $d_r$  is the rotor pole height,  $y_s$  is the stator yoke thickness,  $y_r$  is the rotor yoke thickness, and  $g$  is the air-gap length. Table 1 presents the dimensions of the 6/4 MCSRM-0.

TABLE I  
GEOMETRIC DIMENSIONS OF THE MCSRM-0

Symbol	Value	Symbol	Value
$r_0$	12.00 (mm)	$y_s$	10.60 (mm)
$r_1$	20.00 (mm)	$y_r$	05.00 (mm)
$r_2$	39.40 (mm)	$d_s$	18.90 (mm)
$r_3$	50.00 (mm)	$d_r$	08.00 (mm)
$t_s$	10.50 (mm)	$\beta_r$	$30^\circ$
$t_r$	10.50 (mm)	$\beta_s$	$30^\circ$
$g$	0.50 (mm)	depth	40.00 (mm)

IV. PROPOSED MCSRM STATOR YOKE MODELS

In the study, first, the MCSRM-0 is magnetostatic analyzed with 2D finite element method (FEM) at different currents. In addition, flux density is examined. 2D (FEM) analysis is sufficient to obtain the required results [29]. Geometric regulation is realized in regions where flux density is decreased. For the comparison of the machines, proposed models are called MCSRM-1, MCSRM-2, MCSRM-3, MCSRM-4, and MCSRM-5 respectively. The proposed five stator yoke models are shown in Fig.4.

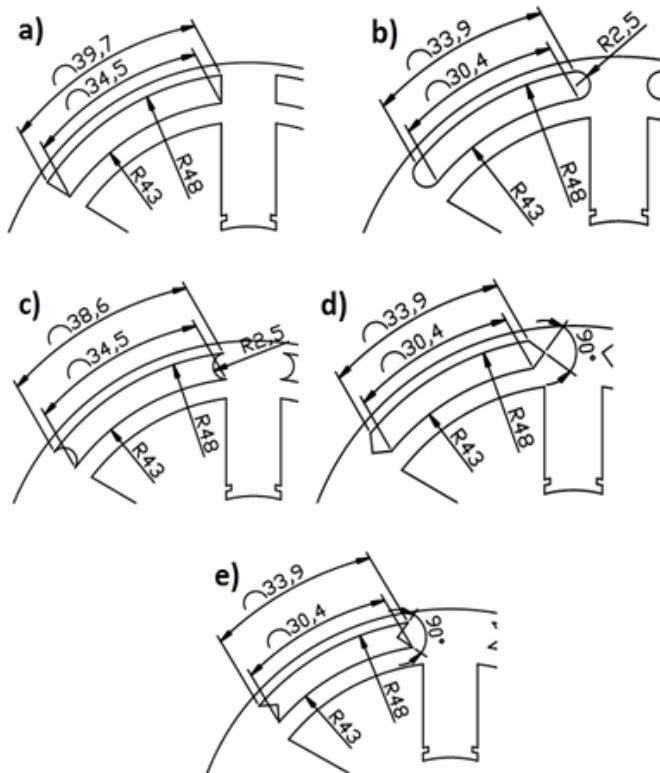


Fig.4. Proposed stator yoke models a) MCSRM-1, b) MCSRM-2, c) MCSRM-3, d) MCSRM-4, and e) MCSRM-5

V. SUBMISSION RESULTS AND DISCUSSIONS

Each of the obtained motor models is analyzed at different currents through the 2D finite-element analysis. Firstly, the MCSRM-0 is analyzed for the comparison of the proposed models. The curves of mutual inductance and torque obtained from the analysis results are plotted for MCSRM-0 as shown in Fig.5. The distribution of the flux for MCSRM-0 at 10Amps is denoted in Fig.6.

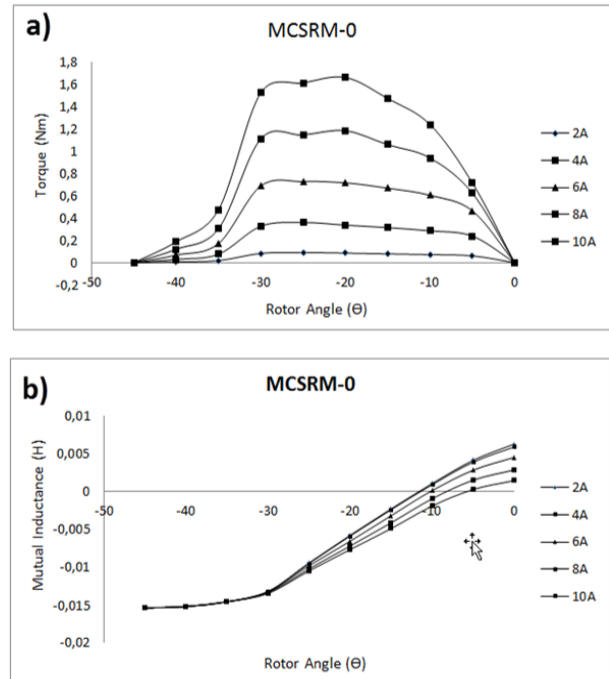


Fig.5. Curves of MCSRM-0 a) Torque curves of MCSRM-0 and b) Mutual inductance curve of MCSRM-0

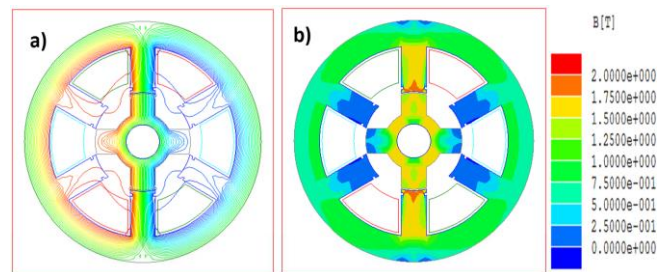


Fig.6. Flux distribution and b) flux density of MCSRM-0 at 10 Amps

The proposed MCSRM-1...MCSRM-5 are obtained through an optimization study on MCSRM-0. The same rotor is used in all MCSRMs and just a simple modification is performed on its stator yoke. It is presented in Fig.4. The geometric arrangements of the proposed MCSRM models are based on the flux distribution of the basic model (MCSRM-0). The flux distribution of the MCSRM-0 in Fig.6 is dealt with and intensive regions are determined. In regions where the flux density shows decrease, the thickness of the stator yoke is thinned and MCSRM-1 model is formed. In the MCSRM-1 model, the ends of this region, which is extracted from the stator yoke region, are cut flat. The end points of this region are near the stator pole. Therefore, the 'flux linkages' can occur

at the end points of the region. For this reason, the end points of these regions are studied in five different basic geometric shapes such as straight, convex, concave, outer triangle, and inner triangle. According to the results of the analysis, despite the five different geometric structures, flux distributions and flux densities are very close to each other.

The MCSRМ-0 and the five proposed models are analyzed in the range of 1-10 amps with 1 amp step. In order to compare the proposed models to the performance of MCSRМ-0, the curves obtained from the analyses performing at 5 Amps and 10 Amps are used. The purpose of comparing the 5 Amps and 10 Amps can be seen clearly on the graph that similar results are obtained in different currents. The comparison of the torque curves of the five proposed models with the torque curves of MCSRМ-0 is shown in Fig.7.

When the torque curves of the MCSRМ-0 and the proposed models obtained from the analyses are compared, they show a very similar characteristic to each other. Fig.7-a shows the comparison of the torque curves of MCSRМ-0 and MCSRМ-1 at 5 Amps and 10 Amps. When the  $T_{max}$  value of the MCSRМ-0 is 1.66 Nm at 10 Amps, the  $T_{max}$  value of MCSRМ-1 is 1.56 Nm. Similarly, when the  $T_{max}$  value of MCSRМ-0 is 0,55 Nm at 5 Amps, the  $T_{max}$  value of MCSRМ-1 is 0,52 Nm. When the  $T_{max}$  values are compared with the analysis results obtained at 5 Amps and 10 Amps, it can denote that the difference is very small. The torque characteristics of both models are also quite similar.

Fig.7-b shows the comparison of the torque curves of MCSRМ-0 and MCSRМ-2 at 5 Amps and 10 Amps. The  $T_{max}$  values of MCSRМ-2 are 1.57 Nm at 10 Amps and 0.52 Nm at 5 Amps. When  $T_{max}$  values are evaluated,  $T_{max}$  values of MCSRМ-2 and MCSRМ-0 are very close to each other. The torque characteristics of both models are also quite similar.

When the torque curves of MCSRМ-3, MCSRМ-4, and MCSRМ-5 in Fig.7-c-d-e are evaluated, there are very small decreases in  $T_{max}$  values compared to MCSRМ-0 as in the previous three models. The torque characteristic of all three models is also very close to the MCSRМ-0. When all torque curves are evaluated together, it is seen that the peak values and the characteristic curves of all the models are very close to each other.

When the flux distributions of the basic model and the proposed MCSRМ models are evaluated, it appears that the values are very small. The flux in regulated regions completes the flow from the stator yoke region near the coil which has a lower resistance compared to the high resistance of the air. Thus, the density of the flux increases in those regions. The flux distributions of the proposed models are given in Fig.8. The density of the flux in the near-winding region seems to be more intense when compared to the MCSRМ-0's given in Fig.6. Since the total flux density does not change too much, the engine performance is not adversely affected. The distribution of the flux for proposed MCSRМ models at 10 Amps is shown in Fig.8.

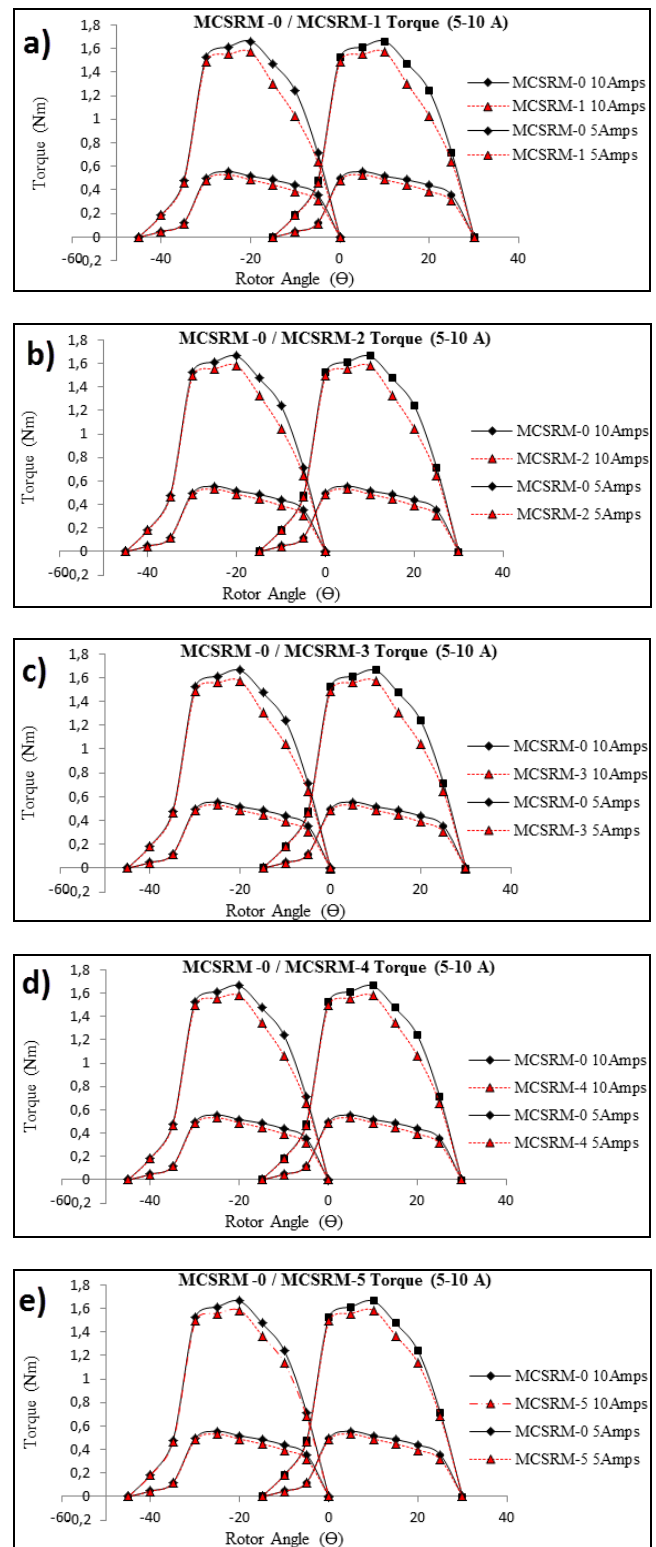


Fig.7. Comparisons of the curves of torque a) MCSRМ-0 and MCSRМ-1, b) MCSRМ-0 and MCSRМ-2, c) MCSRМ-0 and MCSRМ-3, d) MCSRМ-0 and MCSRМ-4, and e) MCSRМ-0 and MCSRМ-5

In the proposed models, the flux which flows on the stator yoke is forced to flow through a narrow path by being compressed. Thus, there is no significant change in the total flux value. The small changes in the torque values of the proposed models are due to the resistance difference of the geometric regions. Therefore, there are very small differences

in the areas of the proposed geometric regulations.

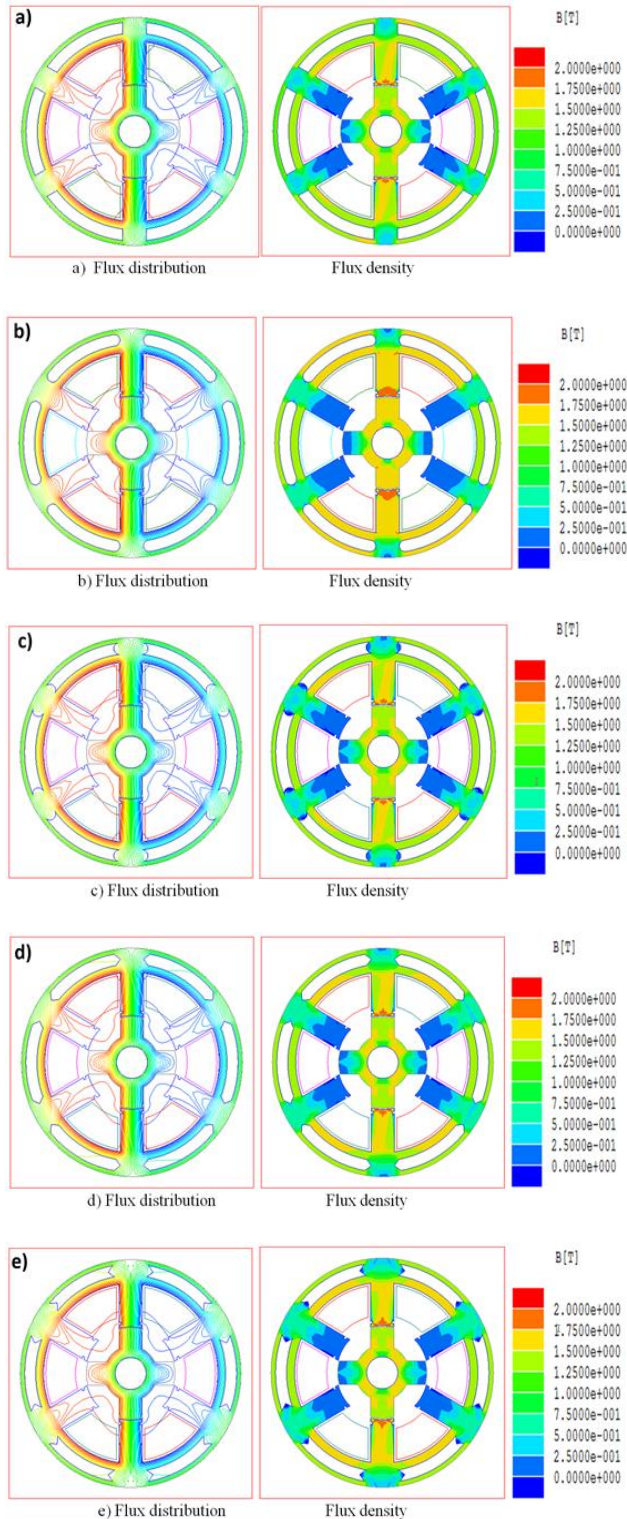


Fig.8. Flux distribution and Flux density of recommended MCSRMs a) MCSRM-1, b) MCSRM-2, c) MCSRM-3, d) MCSRM-4, and e) MCSRM-5

The torque in MCSRM is produced depending on mutual inductance. Hence, the mutual inductance curves of the proposed models are evaluated and given in Fig.9. The mutual inductance curves of the five proposed models are quite close when compared to the mutual inductance curves of MCSRM-0

given in Fig.9. The close proximity of mutual inductance curves are proofs of the proximity of the motor torque curves.

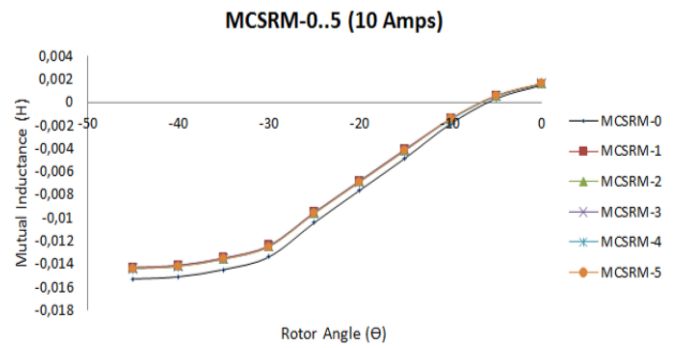


Fig.9. Proposal structure of Salesbury Screen Mutual inductance curves of proposed MCSRMs and MCSRM-0

The average torque value and torque ripple ratio are also very important for the performance comparison of an electric machine. For this reason, the geometric regulations in electric machines should not adversely affect the machine performance. In this study, the average torque values and torque ripple ratios of the proposed models are calculated and compared with the basic model.

The difference between the maximum and minimum instantaneous torque expressed as a percentage of average torque at steady-state operation is called torque ripple [30].

$$T_{ripple} = \frac{T_{ins(max)} - T_{ins(min)}}{T_{avg}} \times 100 \% \quad (4)$$

The average torque can be derived mathematically through integration:

$$T_{avg} = \frac{1}{T} \int_0^T T_{ins} dt. \quad (5)$$

Torque ripple ratios of all models are calculated using Equations (4) - (5) at 5 Amps and 10 Amps. The basic model MCSRM-0 has a value of  $T_{avg} = 1,13$  Nm at 10 Amps. On the other hand, in the proposed models,  $T_{avg}$  decreases to 1.08 Nm at 10 Amps. The average torque difference at 10 Amps of the MCSRM-0 and of the proposed models is about 0.05 Nm. This difference decreases to 0.03 Nm at 5 Amps. Since MCSRMs have high torque density, these values are quite small and negligible. The average torques and torque ripples rates of all MCSRM models are given in Table 2.

For the calculation of torque ripple, the instantaneous torque and average torque are determined. The obtained values at 10 Amps are replaced in (5). As a result, the torque ripple of the basic model MCSRM-0 is 46.2%. For the proposed model MCSRM-1, the attained values at 10 Amps are replaced in (5). Thus, the torque ripple is 44.9%. The results for the torque ripple rates of proposed MCSRM models are rather lower, yet acceptable. Moreover, in the arranged regions of the proposed models, the air circulation contributes to the cooling of the machine.

TABLE II  
THE AVERAGE TORQUES AND TORQUE RIPPLES RATES OF ALL  
MCSRMs MODELS

	MC SRM-0	MC SRM-1	MC SRM-2	MC SRM-3	MC SRM-4	MC SRM-5
10 A $T_{avg}$ (Nm)	1,13	1,08	1,09	1,08	1,08	1,09
10 A $T_{rp}$ (%)	46,2	44,9	45,8	46,5	46,5	45,8
5 A $T_{avg}$ (Nm)	0,4	0,37	0,37	0,37	0,38	0,38
5 A $T_{rp}$ (%)	37,5	38,6	38,6	40,5	39,4	39,4

Without minimizing the stator volume while maintaining the motor performance, the improvements at torque ripple are not very important. The improvements obtained from the stator volumes for the proposed MCSRMs models are given in Table 3. Small changes in torque performance are negligible when compared to the weight obtained from the stator volume.

TABLE III  
COMPARISON OF MCSRMs STATOR VOLUMES

	MC SRM-0	MC SRM-1	MC SRM-2	MC SRM-3	MC SRM-4	MC SRM-5
Volume (cm <sup>3</sup> )	314,16	269,62	270,91	274,4	272,62	278,62
Reduce (%)		14,17	13,76	12,65	13,22	11,31

Owing to the proposed geometric arrangements, the volume of the basic model MCSRMs-0 is decreased from 314.16 cm<sup>3</sup> to 269.69 cm<sup>3</sup>. When the values are generalized as a percentage, the stator volume decreases between 11.31% and 14.17% by stator yoke optimization. Depending on the density of the material used in the manufacture of the stator, the stator weight also decreases significantly. A lighter MCSRMs, which provides near-optimal performance in applications such as electric vehicles, is more preferable than the basic model. One of the important points to be considered here is the negative strength on the stator yoke. In order to avoid this situation, stator housing should be considered.

## VI. CONCLUSION

In this study, an approach is proposed for reducing the weight of MCSRMs without loss of performance. For this purpose, some modifications have been made to the geometry of the basic model of designed MCSRMs. The basic model and all proposed models are the same except for the changes made to the stator yoke. The geometric arrangements on the stator yoke are carried out in regions where the flux density shows a decrease. Thus, the loss of flux is prevented. All models are analyzed and the results of the proposed models are compared with the basic model at 5 Amps and 10 Amps. Due to the proposed geometric stator yoke models, the motor stator

volume decreases between 11.31% and 14.17%. Further, an additional torque ripple does not occur and the torque characteristic is not degraded. In the proposed models, the flux flows over the narrowed region through the stator. These regulations also support air circulation. As a result, the user can use a more lightweight MCSRMs. By this advantage, it will bring great benefits especially to electric vehicle works. In future research, the copper losses of the models can be studied, and the advantages and disadvantages of the models can be evaluated. As a result, a lightweight MCSRMs with high performance has been proposed for electric vehicles.

## REFERENCES

- [1] E. Bostanci, M. Moallem, A. Parsapour, B. Fahimi, "Opportunities and challenges of Switched Reluctance Motor drives for electric propulsion A comparative study", IEEE Transactions on Transportation Electrification, Vol.3, No.1, 2017, pp.58-75.
- [2] N. Kurihara, J. Bayless, H. Sugimoto, A. Chiba, "Noise reduction of Switched Reluctance Motor with high number of poles by novel simplified current waveform at low speed and low torque region", IEEE Transactions on Industry Applications, Vol.52, No.4, 2016, pp.3013-3021.
- [3] C. H. T. Lee, K. T. Chau, C. Liu, D. Wu, S. Gao, "Quantitative Comparison and Analysis of Magnetless Machines With Reluctance Topologies Christopher", IEEE Transactions on Magnetics, Vol.49, No.7, 2013, pp.3969-3972.
- [4] H. Makino, T. Kosaka, N. Matsui, "Digital PWM-control-based active vibration cancellation for Switched Reluctance Motors", IEEE Transactions on Industry Applications, Vol.51, No.6, 2015, pp.4521-4530.
- [5] J. Kartigeyan, M. Ramaswamy, "Effect of Material Properties on Core Loss in Switched Reluctance Motor using Non-Oriented Electrical Steels", Journal of Magnetics, Vol.22, No.1, 2017, pp.93-99.
- [6] K. Kiyota, T. Kakishima, A. Chiba, M.A. Rahman, "Cylindrical Rotor Design for Acoustic Noise and Windage Loss Reduction in Switched Reluctance Motor for HEV Applications", IEEE Transactions on Industry Applications, Vol.52, No.1, 2016, pp.154-162.
- [7] A. Shahabi, A. Rashidi, M. Afshoon, S. M. S. Nejad, "Commutation angles adjustment in SRM drives to reduce torque ripple below the motor base speed", Turkish Journal of Electrical Engineering and Computer Sciences, Vol.24, No.2, 2016, pp.669-682.
- [8] M. Tursini, M. Villani, G. Fabri, L.D. Leonardo, "A switched-reluctance motor for aerospace application: Design, analysis and results", Electric Power Systems Research, Vol.142, 2017, pp.74-83.
- [9] T.S. Chuang, "Acoustic noise reduction of a 6/4 SRM drive based on third harmonic real power cancellation and mutual coupling flux enhancement", Energy Conversion and Management, Vol.3, 2010, pp.546-552.
- [10] B. Fahimi, A. Emadi, B.R. Sepe, "A switched reluctance machine-based starter/alternator for more electric cars", IEEE Transactions on Energy Conversion, Vol.19, No.1, 2007, pp.116-124.
- [11] H. Cheng, H. Chen, Z. Yang, "Design indicators and structure optimisation of switched reluctance machine for electric vehicles", IET Electric Power Applications, Vol.9, No.4, 2015, pp.319-331.
- [12] M. Belhadia, G. Krebs, C. Marchanda, H. Hannounb, X. Miningera, "Evaluation of axial SRM for electric vehicle application", Electric Power Systems Research, Vol.148, 2017, pp.155-161.
- [13] J. Zhu, K. W. E. Cheng, X. Xue, Y. Zou, "Design of a New Enhanced Torque In-Wheel Switched Reluctance Motor With Divided Teeth for Electric Vehicles", IEEE Transactions on Magnetics, Vol.53, No.11, 2017.
- [14] S. Sadeghi, M. Mirsalim, "Dynamic Modeling and Simulation of a Switched Reluctance Motor in a Series Hybrid Electric Vehicle", Acta Polytechnica Hungarica, Vol.7, No.1, 2010, pp. 51-71.
- [15] J. Kim, Y. Jeong, Y. Jeon, J. Kang, S. Lee, J. Park, "Development of a Switched Reluctance Motor-based Electric AC Compressor Drive for HEV/EV Applications", Journal of Magnetics, Vol.19, No.3, 2014, pp.282-290.

- [16] D. Marcsa, M. Kuczmann, "Design and control for torque ripple reduction of a 3-phase switched reluctance motor", *Computers & Mathematics with Applications*, Vol.74, No.1, 2017, pp.89-95.
- [17] G. Li, J. Ojeda, S. Hlioui, E. Hoang, M. Lecrivain, M. Gabsi, "Modification in Rotor Pole Geometry of Mutually Coupled Switched Reluctance Machine for Torque Ripple Mitigating", *IEEE Transactions on Magnetics*, Vol.48, No.6, 2012, pp.2025-2034.
- [18] M. Asgar, E. Afjei, H. Torkaman, "A New Strategy for Design and Analysis of a Double-Stator Switched Reluctance Motor: Electromagnetics, FEM, and Experiment", *IEEE Transactions on Magnetics*, Vol.51, No.12, 2015.
- [19] W. Ding, Z. Yin, L. Liu, J. Lou, Y. Hu, Y. Liu, "Magnetic circuit model and finite element analysis of a modular switched reluctance machine with E-core stators and multi-layer common rotors", *IET Electric Power Applications*, Vol.8, No.8, 2014, pp.296-309.
- [20] E. Afjei, A. Siadatan, Hossein Torkaman, "Magnetic Modeling, Prototyping, and Comparative Study of a Quintuple-Set Switched Reluctance Motor", *IEEE Transactions on Magnetics*, Vol.51, No.8, 2015.
- [21] X. Cao, Q. Sun, C. Liu, H. Zhou, Z. Deng, "Direct control of torque and levitation force for dual-winding bearingless Switched Reluctance Motor", *Electric Power Systems Research*, Vol.145, 2017, pp.214-222.
- [22] J. E. Stephen, S. S. Kumar, J. Jayakumar, "Nonlinear Modeling of a Switched Reluctance Motor using LSSVM – ABC", *Acta Polytechnica Hungarica*, Vol.11, No.6, 2014, pp.143-158.
- [23] W. Hua, G. Zhao, H. Hua, M. Cheng, "General Power Equation of Switched Reluctance Machines and Power Density Comparison", *IEEE Transactions on Industry Applications*, Vol.53, No.5, 2017, pp.4298 – 4307.
- [24] X. Sun, Z. Xue, S. Han, X. Xu, Z. Yang, L. Chen, "Design and Analysis of a Novel 16/10 Segmented Rotor SRM for 60V Belt-Driven Starter Generator", *Journal of Magnetics*, Vol.21, No.3, 2016, pp.393-398.
- [25] B. G. Mecrow, "Fully pitched-winding switched-reluctance and stepping-motor arrangements", *IEE Proceedings-B*, Vol.140, No.1, 1993, pp.61-70.
- [26] Md. A. Kabir, I. Husain, "Design of Mutually Coupled Switched Reluctance Motors (MCSRMs) for Extended Speed Applications Using 3-Phase Standard Inverters", *IEEE Transactions on Energy Conversion*, Vol.31, No.2, 2016, pp.436-445.
- [27] W. Uddin, Y. Sozer, "Analytical modeling of Mutually Coupled Switched Reluctance Machines under saturation based on design geometry", *IEEE Int. Conf. Electr. Machines & Drives (IEMDC)*, 2015, pp.133-138.
- [28] Y. H. Kima, S. Kimb, J. H. Choic, J. Ahnd, C. H. Choe, J. Lee, "Direct torque control of switched reluctance motor for minimizing torque ripple", *International Journal of Applied Electromagnetics and Mechanics*, Vol.28, no.(1-2), 2008, pp.247-253.
- [29] T. Higuchi, T. Ueda, T. Abe, "Torque ripple reduction control of a novel segment type SRM with 2-steps slide rotor, *IEEE Int. Conf. The International Power Electronics Conference (ECCE ASIA)*, 2010, pp.2175-2180.
- [30] P. C. Desai, M. Krishnamurthy, N. Schofield, A. Emadi, "Novel Switched Reluctance Machine Configuration With Higher Number of Rotor Poles Than Stator Poles: Concept to Implementation, *IEEE Transactions on Industrial Electronics*", Vol.57, No.2, 2010, pp.649-659

### BIOGRAPHIES

**CIHAN SAHIN** was born İskenderun. He received B.S., M.S. and Ph.D degrees in Electrical Education from Kocaeli University, Kocaeli, Turkey, in 1999, 2007 and 2014 respectively. He is currently Asst. Prof. in Control and Automation Program of Vocational Scholl in Bilecik Şeyh Edebali University, Bilecik, Turkey. His research interests are



automation systems (PLC, SCADA, etc...), power electronics and electric machines.



**MEVLUT KARACOR** was born Eskişehir. He received M.S. and the Ph.D. degrees in electrical education from Kocaeli University, Kocaeli, Turkey in 2004 and 2010 respectively. Since 2013, he has been working as an Asst. Prof. in Engineering of Mechatronic, Faculty of Technology, Manisa Celal Bayar University, Turkey. His research interests are automation systems (PLC, SCADA, etc...), power electronics and electric machines.



**AYSE ERGUN AMAC** was born İzmit. She received B.S. degree (with honors) in electrical education from Marmara University, Istanbul, Turkey in 1994 and the M.S. and the Ph.D. degrees in electrical education from Kocaeli University, Kocaeli, Turkey in 1997 and 2003 respectively. From 1995 to 2003, she was a research and teaching assistant in Department of Electrical Education, in Kocaeli University, Technical Education Faculty. From 2002 to 2004, she was in the Electric and Power Electronics Center and the Grainger Laboratories, Illinois Institute of Technology, Chicago as a research scholar to study on active filters and uninterruptible power supplies. Since 2014, she has been with the Energy Systems Engineering, Faculty of Technology, University of Kocaeli, as an Associate Professor. Dr. Amac's current research interests are hybrid electrical vehicles and computer based learning approaches in teaching power electronics courses.

# Lip Reading Using Convolutional Neural Networks with and without Pre-Trained Models

T. OZCAN and A. BASTURK

**Abstract**—Lip reading has become a popular topic recently. There are widespread literature studies on lip reading in human action recognition. Deep learning methods are frequently used in this area. In this paper, lip reading from video data is performed using self designed convolutional neural networks (CNNs). For this purpose, standard and also augmented AvLetters dataset is used in train and test stages. To optimize network performance, minibatchsize parameter is also tuned and its effect is investigated. Additionally, experimental studies are performed using AlexNet and GoogleNet pre-trained CNNs. Detailed experimental results are presented.

**Index Terms**—Convolutional neural networks, data augmentation, deep learning, human action recognition, human computer interaction, lip reading, transfer learning

## I. INTRODUCTION

**H**UMAN ACTION RECOGNITION is an important phase for human computer interaction [1]. Lip reading, a subcategory of human action recognition, has begun to be used in various applications [2-6].

Sound and image assisted features can be used for lip reading. In particular, data containing image-assisted features seem to have higher success rate in applications where they are used. Success rate of lip reading is also directly related to the classification techniques which are used extensively with feature selection. Hidden Markov models [7,8], support vector machines [7,9], k-nearest neighbor algorithm [7] are most basic conventional classification algorithms. After deep learning methods have been used frequently in classification problems [10-13], researchers have started to use them on lip reading which is another classification problem.

Lip reading process is applied at alphabet, word and sentence levels [14]. In alphabet level lip reading process, still image and time series classification methods can be used. On the other hand, classification methods such as long short-term

memory (LSTM), recurrent neural network (RNN), and so on are preferred in word and sentence level operations.

In this paper, we aim to classify an alphabet level lip reading dataset, AvLetters [15], by using a designed convolutional neural network (CNN) model and pre-trained model supported CNNs. A CNN model with 3 convolution layers, 3 max pooling layers, and 3 regularization layers is designed. On the other side, AlexNet [16] and GoogleNet [17] supported CNN structures are employed to compare performance with designed CNN model. Dataset size also affects performance as much as the classification model. In this study, data augmentation is also addressed by using data augmentation techniques. Experimental studies, which are based on CNN models with and without augmented dataset depends on different “minibatchsize” values, are performed. The contributions of this study are as follows:

- To the best of our knowledge, transfer learning supported CNN using AlexNet was used for the first time on the AvLetters dataset.
- By using some techniques, the problem is converted to a still image based lip reading from time series data.
- A CNN architecture is proposed and compared with transfer learning supported CNNs.
- The proposed methods in this study, not only have better performance than some methods used in [18] in the literature but also are easy to develop.

The presentation of this paper will be as follows: Section 2 provides a literature review on the subject. Section 3 describes the information of CNN and pre-trained models used through the study. In section 4, experimental studies are presented and in conclusion section, which is the last section of this paper, success rate results obtained from experiments and future studies are reviewed.

## II. RELATED WORK

Garg et al. [2], combined CNN and LSTM deep learning methods and applied it on lip reading problem. In this combination, CNN was used for feature extraction and LSTM was used for classification. MIRACL-VC1 [7] dataset which consists words and phrases was used for testing the model. Li et al. [3], who performed classification with CNN using the dynamic feature image instead of original image, tested the model with ATR Japanese speech dataset. Petridis et al. developed an LSTM supported work on visual speech recognition [4]. The model consisted of two streams. The first was feature extraction from mouth and the second was the change between images. The temporal dynamics of each stream were performed with LSTM. Proposed method was

**TAYYIP OZCAN**, is with Department of Computer Engineering University of Erciyes, Kayseri, Turkey, (e-mail: [tozcan@erciyes.edu.tr](mailto:tozcan@erciyes.edu.tr)).

 <https://orcid.org/0000-0002-3111-5260>

**ALPER BASTURK**, is with Department of Computer Engineering University of Erciyes, Kayseri, Turkey, (e-mail: [ab@erciyes.edu.tr](mailto:ab@erciyes.edu.tr)).

 <https://orcid.org/0000-0001-5810-0643>

Manuscript received December 7, 2018; accepted April 3, 2019.

DOI: [10.17694/bajece.479891](https://doi.org/10.17694/bajece.479891)

tested with OuluVS2 [19] and CUAVE [20] datasets. A model using LSTM with 5 convolution layers and 256 hidden units was developed by Dong and his team [21]. The method's performance was tested by combining 2 datasets. Word-level visual speech recognition models using deep learning was proposed by Stafylakis and Tzimiropoulos [22]. The proposed method was combined with CNN, ResNet and bi-directional LSTM. The model tested on LRW [23] dataset and experimental results were presented. Takashima et al. [5] developed a deep learning-supported speech recognition system for people with severe hearing loss. Both voice and visual data were used in the method and extracted features were included in system for classification. In another work, Takashima et al. [24] proposed a new approach for lip reading using the combination of lip image and sound features by using deep learning. The proposed method was tested on ATR Japanese speech dataset. A method which classifies the dataset consisting of Turkish color names by taking image and angle values with Kinect device was proposed by Yargic and Dogan [6]. Authors, who took the knowledge of lip co-ordinates from Kinect camera, used the angles between the points and classify them with k-nearest neighbor search algorithm.

### III. METHODS

#### A. Convolutional Neural Networks

CNN is a type of artificial neural network (ANN) specialized to handle multi-dimensional, large data. Convolutional networks are neural networks that use at least one layer of convolution processing instead of general matrix multiplication [25-27].

Basic components of CNNs are; convolution layer, pooling layer, activation functions, fully connected layers, loss layer, regularization, and optimization.

The convolution layer includes a learnable filter set. This layer is the structure of convolutional network that has the ability to learn along like as fully connected layer. The parameters that are important for this layer are spatial extent, number of filters and stride [25].

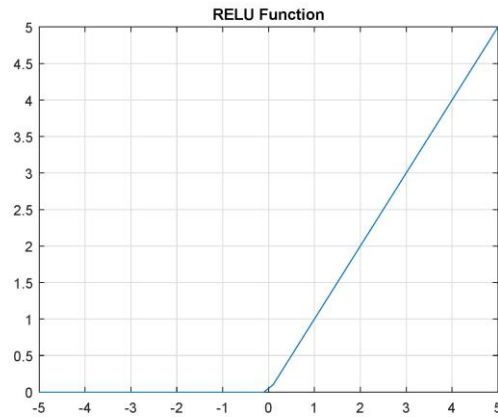
Another important structure that reduces the network model's cost is the pooling layer. In this layer, which makes the system resistant to small position changes, pooling process usually uses operations such as sum, maximum, average, etc.

Choice of activation functions such as ReLU, ELU, sigmoid etc., significantly affects the performance of CNN. ReLU, which is a piecewise linear function, is an activation function that returns negative inputs to zero, and positive inputs to output without changing them. The ReLU function graph is shown in Figure 1a. ELU is an activation function that allows neural networks to learn faster and achieve higher classification accuracy [28]. The ELU function graph is shown in Figure 1b. The sigmoid function is a continuous and derivable function and is frequently used. The Sigmoid function graph is shown in Figure 1c.

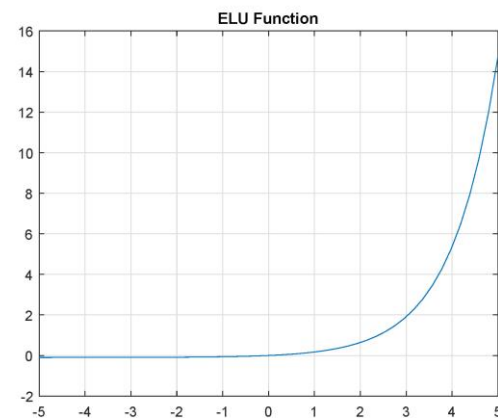
Fully connected layer comes after convolution and pooling layers in CNN. In this layer, neurons have full contact with the previous layer.

Loss layer, which is the last layer of CNN, determines how the difference is to be evaluated between predicted and actual labels during training. Softmax is the most commonly used loss function.

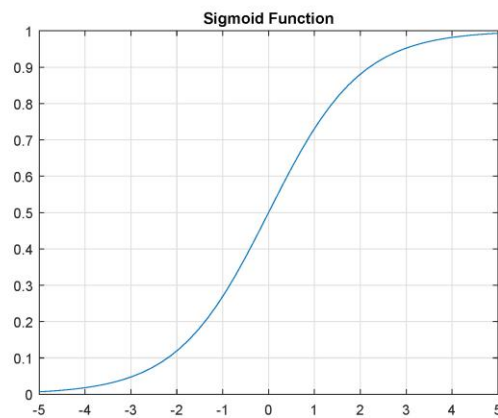
Regularization techniques prevent the overfitting problem, which is an important problem for deep neural networks. Dropout and Dropconnect are two most important regularization techniques [25].



(a) ReLU activation function.



(b) ELU activation function



(c) Sigmoid activation function

Fig.1. Activation functions

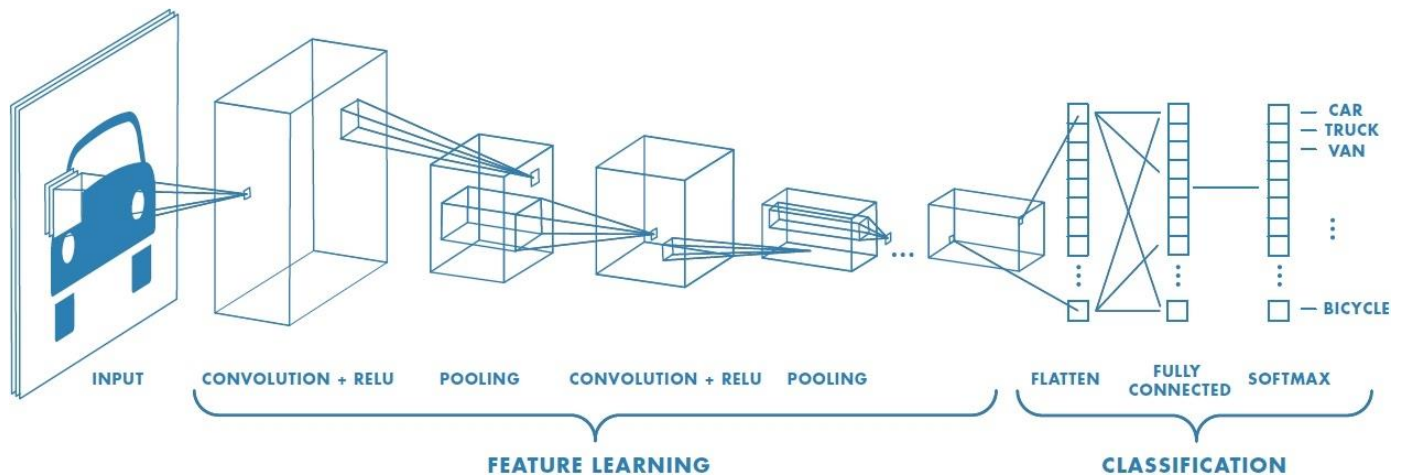


Fig.2. Convolutional Neural Network architecture [25]



Fig.3. AlexNet architecture

### B. Pre-Trained Models

The easier and faster option than developing a new model is using pre-trained networks. Pre-trained networks are used for purposes such as classification, transfer learning, and feature extraction.

Figure 2 presents the architecture of a typical neural network with basic components. The most commonly used pre-trained CNN architects are AlexNet [16], VGG16 [29], VGG19 [29], GoogleNet [17] and ResNet 50 [30]. In this paper, AlexNet and GoogleNet will be used for experiments.

#### 1) AlexNet

Transfer learning or feature extraction can be applied to different problems with AlexNet, which is trained with a large library of images and performs powerful feature extraction. A subset of ImageNet dataset was used to train this network model. AlexNet, which has 8 learnable layers, 5 convolution layers, and 3 fully connected layers, won first place in 2012 ImageNet Large Scale Visual Recognition Competition (ILSVRC). The architecture of AlexNet model is shown in Figure 3.

#### 2) GoogleNet

GoogleNet model, which won the 2014 ILSVRC competition, has a smaller and faster network structure than the VGG models. GoogleNet has a higher performance than AlexNet on ILSVRC dataset. It has a more complex structure than AlexNet and VGG models. The architecture of the GoogleNet model is shown in Figure 4.

## IV. EXPERIMENTAL STUDIES

Two different methods have been applied to study on with and without augmented AvLetters dataset. The first of these methods is developing a user-designed CNN model. Another

method is using AlexNet and GoogleNet pre-trained models instead of a user-designed one.

#### A. AvLetters Dataset

Lip reading is studied under the heading of human action recognition. AvLetters dataset, which consists of both video and audio recordings, was created by repeating the 10 alphabet letters in 3 different trials [15]. Visual data will be used in the study. Therefore, the Matlab mat data file containing image information of the dataset is handled. Numerical information of image frames formed during each alphabetical pronunciation is kept in mat files. For example, 'R3\_Kate-lips.mat' file holds the frame information of 3rd pronouncement of the letter R of Kate.

In AvLetters dataset, 10 subjects repeated 26 letters 3 times. "TrainData" and "TestData" folders have been created by the way first two pronunciations are recorded for training and the last pronouncement is recorded for testing.

#### 1) Data Pre-processing

Duration of each letter for each trial may vary. This situation causes the number of different frames to be formed between samples. As the first step in dataset preparation, average number of frames is set to 20, and adding image process for below 20 and deleting image process is performed for above 20. After each letter is formed in 20 frames, lip images are rendered as still images in 5x4 format. By this way, the dataset consisting of the time series is transformed into a structure composed of still images. A sample image of the pre-processed dataset is shown in Figure 5.



Fig.4. GoogleNet architecture [31]

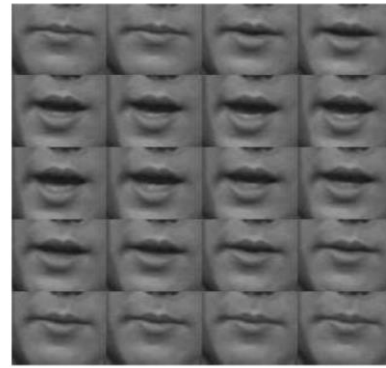
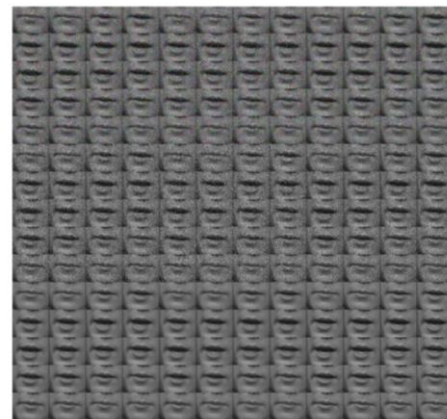


Fig.5. Avletters, pre-processed data - letter A

2) Data Augmentation

520 samples can be regarded as a small number for training in deep learning. Data augmentation (DA) can be used to increase the size of samples. The training dataset is increased using various DA methods. Adding noise with “gaussian”, “salt and pepper” and “speckle”, sharpening with “unsharp” and softening with “median” filtering are the operations of DA used in this paper. Also, RGB and grayscale format of noised images are used additionally. Therefore, eight different types of original images are replicated. An example for DA is presented in Figure 6a and augmented data matrix is depicted in Figure 6b.



(a) Avletters, augmented data - letter A

Gaussian RGB Image	Salt & pepper RGB Image	Speckle RGB Image
Gaussian Grayscale Image	Salt & pepper Grayscale Image	Speckle Grayscale Image
Original Image	Median Filtered Image	Unsharp Filtered Image

(b) Avletters, augmented data matrix

Fig.6. Data augmentation structure

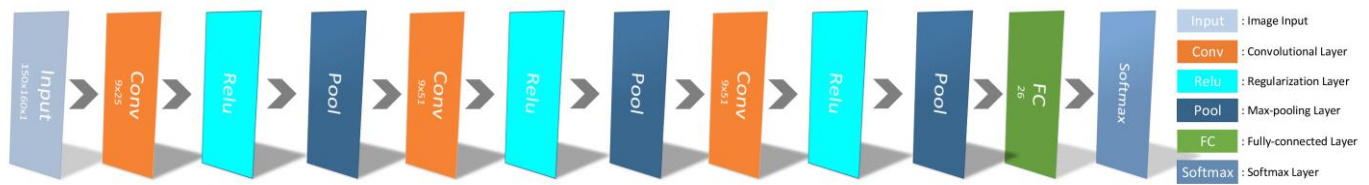


Fig.7. Designed CNN architecture

**B. Proposed CNN Model**

Deep learning methods have recently been used frequently in classification problems. CNN, which is a deep learning method, is accepted as a popular method in classification problems. A CNN model that separates from ANN models because of the number of layers is designed for lip reading problem. Designed CNN model is presented in Figure 7. This model, consisting of 3 convolution layers, 3 max pooling layers, 3 regularization layers, achieved 54.23% success rate on augmented AvLetters dataset with '8' value of minibatchsize parameter. A confusion matrix graph is presented in Figure 8.

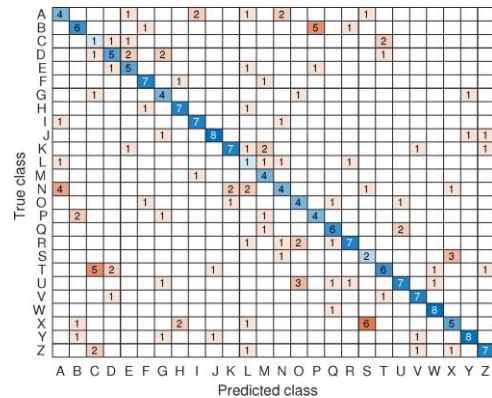


Fig.8. Confusion matrix for best result of designed CNN

**C. Pre-Trained Model Supported CNN**

Developing a new CNN model is a challenging task. Transfer learning from pre-trained models is an easier and faster way.

Designed CNN architecture is compared with AlexNet and GoogleNet supported CNN on with and without augmented AvLetters dataset. The presentation of results obtained with different “minibatchsize” values is done and presented in Table I. According to this table, when the “minibatchsize” value is 8, AlexNet supported CNN + DA is more successful than other models with 54.62% success rate. Designed CNN model has the highest accuracy rate when “minibatchsize” value is equal to 16. Designed CNN + DA model achieves better success rate when “minibatchsize” value is equal to 32. One of the main reasons for the low achievement success rates is needing more data for training in deep learning. Another important factor that may increase success rate is the choice of the correct initial parameters. The success of deep learning based models used in this study and available in the literature is presented in Table II. The studies in this table use standardized split training and test data. The autoencoder based method gave the best result. On the other hand, the success of studies in literature has been achieved with our methods. Although the proposed methods are less successful than the most successful method, architectural installation is simpler and more flexible by using transfer learning supported CNN. Confusion matrix figures for AlexNet and GoogleNet supported CNN are shown as in Figure 9 and Figure 10.

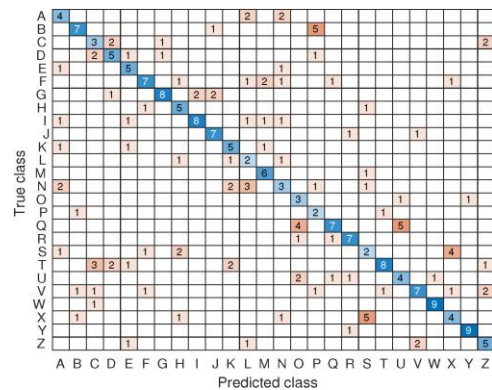


Fig.9. Confusion matrix for best result of AlexNet supported CNN

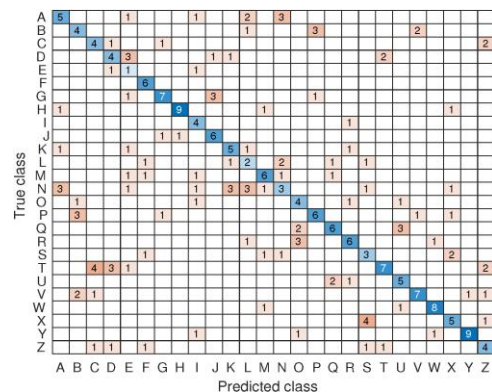


Fig.10. Confusion matrix for best result of GoogleNet supported CNN

TABLE I

## ACCURACY COMPARISON OF DESIGNED, ALEXNET AND GOOGLNET SUPPORTED CNN MODELS

CNN Models	Initial Parameters			Accuracy
	MiniBatchSize	InitialLearnRate	MaxEpochs	
Designed CNN	8	0.0001	100	0.0346
Designed CNN + DA	8	0.0001	100	0.5423
AlexNet Supported CNN	8	0.0001	100	0.4769
AlexNet Supported CNN+ DA	8	0.0001	100	<b>0.5462</b>
GoogleNet Supported CNN	8	0.0001	100	0.3692
GoogleNet Supported CNN+ DA	8	0.0001	100	0.5231
Designed CNN	16	0.0001	100	<b>0.5231</b>
Designed CNN + DA	16	0.0001	100	0.4808
AlexNet Supported CNN	16	0.0001	100	0.4423
AlexNet Supported CNN+ DA	16	0.0001	100	0.4808
GoogleNet Supported CNN	16	0.0001	100	0.5192
GoogleNet Supported CNN+ DA	16	0.0001	100	0.5192
Designed CNN	32	0.0001	100	0.4885
Designed CNN + DA	32	0.0001	100	<b>0.5385</b>
AlexNet Supported CNN	32	0.0001	100	0.4577
AlexNet Supported CNN+ DA	32	0.0001	100	0.4500
GoogleNet Supported CNN	32	0.0001	100	0.3962
GoogleNet Supported CNN+ DA	32	0.0001	100	0.5000

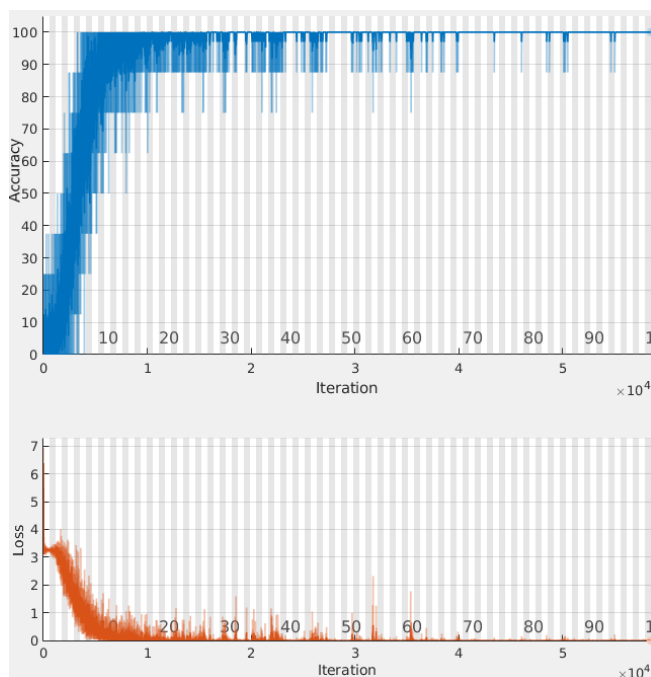


Fig.11. Training progress of AlexNet supported CNN

TABLE II  
ACCURACY COMPARISON BETWEEN USED IN THIS PAPER AND APPLIED DEEP LEARNING MODELS

Methods	Accuracy
Deep auto-encoder [32]	<b>64.40%</b>
CNN [18]	49.90%
CNN & LSTM [18]	57.70%
CNN & bidirectional LSTM [18]	49.40%
Designed CNN & DA	54.23%
AlexNet supported CNN & DA	<b>54.62%</b>
GoogleNet supported CNN & DA	52.31%

## V. CONCLUSION

Lip reading, which is a human action recognition subcategory, may be used on various applications such as interaction with deaf people, intelligence services, detection of swearing people in football stadiums and so on. Alphabet level can be acceptable for the first step of lip reading. In this paper, the success of the CNN models supported by the user-designed and pre-trained model on AvLetters dataset has been investigated. Selecting different initial parameters gives different results and there is not an absolute winning model. Using data augmentation increases the success rate generally. In experiments, 8 simple methods are also used for data augmentation on Avletters dataset. Experimental results show that data augmentation is a good way of getting more successful results.

For future studies, other pre-trained models supported CNN can be run on both AvLetters and different datasets. Also, other data augmentation methods can be used for getting a larger dataset.

## REFERENCES

- [1] S. Agrawal, V. R. Omprakash, Ranvijay, "Lip reading techniques: A survey," in 2016 2nd International Conference on Applied and Theoretical Computing and Communication Technology (iCATccT), pp. 753–757, July 2016.
- [2] A. Garg, J. Noyola, S. Bagadia, "Lip reading using CNN and LSTM," in Technical Report, 2016.
- [3] Y. Li, Y. Takashima, T. Takiguchi, Y. Ariki, "Lip reading using a dynamic feature of lip images and convolutional neural networks," in 2016 IEEE/ACIS 15th International Conference on Computer and Information Science (ICIS), pp. 1–6, June 2016.
- [4] S. Petridis, Z. Li, M. Pantic, "End-to-end visual speech recognition with LSTMs," CoRR, vol. abs/1701.05847, 2017.
- [5] Y. Takashima, Y. Kakihara, R. Aihara, T. Takiguchi, Y. Ariki, N. Mitani, K. Omori, K. Nakazono, "Audio-visual speech recognition using convolutional bottleneck networks for a person with severe hearing loss," IPSJ Transactions on Computer Vision and Applications, vol. 7, pp. 64–68, 2015.
- [6] A. Yargic, M. Dogan, "A lip reading application on MS Kinect camera," in 2013 IEEE INISTA, pp. 1–5, June 2013.

- [7] A. Rezik, A. Ben-Hamadou, W. Mahdi, "A new visual speech recognition approach for RGB-D cameras," in *Image Analysis and Recognition* (A. Campilho and M. Kamel, eds.), (Cham), pp. 21–28, Springer International Publishing, 2014.
- [8] A. Rezik, A. Ben-Hamadou, W. Mahdi, "Human machine interaction via visual speech spotting," in *Advanced Concepts for Intelligent Vision Systems* (S. Battiato, J. Blanc-Talon, G. Gallo, W. Philips, D. Popescu, and P. Scheunders, eds.), (Cham), pp. 566–574, Springer International Publishing, 2015.
- [9] A. Rezik, A. Ben-Hamadou, W. Mahdi, "Unified system for visual speech recognition and speaker identification," in *Advanced Concepts for Intelligent Vision Systems* (S. Battiato, J. Blanc-Talon, G. Gallo, W. Philips, D. Popescu, P. Scheunders, eds.), (Cham), pp. 381–390, Springer International Publishing, 2015.
- [10] M. Emin Yuksel, N. Sarikaya Basturk, H. Badem, A. Caliskan, A. Basturk, "Classification of high resolution hyperspectral remote sensing data using deep neural networks," *Journal of Intelligent & Fuzzy Systems*, vol. 34, pp. 2273–2285, 04 2018.
- [11] A. Caliskan, M. Yuksel, H. Badem, A. Basturk, "Performance improvement of deep neural network classifiers by a simple training strategy," *Engineering Applications of Artificial Intelligence*, vol. 67, pp. 14 – 23, 2018.
- [12] H. Badem, A. Basturk, A. Caliskan, M. E. Yuksel, "A new efficient training strategy for deep neural networks by hybridization of artificial bee colony and limited-memory bfgs optimization algorithms," *Neurocomputing*, vol. 266, pp. 506 – 526, 2017.
- [13] A. Caliskan, M. Yuksel, H. Badem, A. Basturk, "A deep neural network classifier for decoding human brain activity based on magnetoencephalography," *Elektronika ir Elektrotechnika*, vol. 23, no. 2, 2017.
- [14] A. Fernandez-Lopez, F. M. Sukno, "Survey on automatic lip-reading in the era of deep learning," *Image and Vision Computing*, vol. 78, pp. 53 – 72, 2018.
- [15] I. Matthews, T. Cootes, J. A. Bangham, S. Cox, R. Harvey, "Extraction of visual features for lipreading," *IEEE Transactions on Pattern Analysis and Machine Intelligence*, vol. 24, p. 2002, 2002.
- [16] A. Krizhevsky, I. Sutskever, G. Hinton, "Imagenet classification with deep convolutional neural networks," *NIPS*, vol. 25, pp. 1106–1114, 2012.
- [17] C. Szegedy, W. Liu, Y. Jia, P. Sermanet, S. E. Reed, D. Anguelov, D. Erhan, V. Vanhoucke, A. Rabinovich, "Going deeper with convolutions," *CoRR*, vol. abs/1409.4842, 2014.
- [18] W. Feng, N. Guan, Y. Li, X. Zhang, Z. Luo, "Audio visual speech recognition with multimodal recurrent neural networks," in *2017 International Joint Conference on Neural Networks (IJCNN)*, pp. 681–688, May 2017.
- [19] I. Anina, Z. Zhou, G. Zhao, M. Pietikainen, "Ouluvs2: A multi-view audiovisual database for non-rigid mouth motion analysis," in *2015 11th IEEE International Conference and Workshops on Automatic Face and Gesture Recognition (FG)*, vol. 1, pp. 1–5, May 2015.
- [20] E. K. Patterson, S. Gurbuz, Z. Tufekci, J. N. Gowdy, "Moving talker, speaker-independent feature study, and baseline results using the CUAVE multimodal speech corpus," *EURASIP J. Appl. Signal Process.*, vol. 2002, pp. 1189–1201, Jan. 2002.
- [21] W. Dong, R. He, S. Zhang, "Digital recognition from lip texture analysis," in *2016 IEEE International Conference on Digital Signal Processing (DSP)*, pp. 477–481, Oct 2016.
- [22] T. Stafylakis, G. Tzimiropoulos, "Combining residual networks with LSTMs for lipreading," *CoRR*, vol. abs/1703.04105, 2017.
- [23] J. S. Chung, A. Zisserman, "Lip reading in the wild," in *Asian Conference on Computer Vision*, pp. 87–103, Springer, 2016.
- [24] Y. Takashima, R. Aihara, T. Takiguchi, Y. Arika, N. Mitani, K. Otori, K. Nakazono, "Audio-visual speech recognition using bimodal trained bottleneck features for a person with severe hearing loss," in *INTERSPEECH*, 2016.
- [25] E. Kilic, "Classification of Mitotic figures with convolutional neural networks." M.Sc. thesis, Erciyes University, Graduate School of Natural and Applied Sciences, 2016.
- [26] H. S. Nogay, T. C. Akinci, "A convolutional neural network application for predicting the locating of squamous cell carcinoma in the lung," *Balkan Journal of Electrical and Computer Engineering*, vol. 6, pp. 207 – 210, 2018.
- [27] H. S. Nogay, "Classification of different cancer types by deep convolutional neural networks," *Balkan Journal of Electrical and Computer Engineering*, vol. 6, pp. 56 – 59, 2018.
- [28] J. Gu, Z. Wang, J. Kuen, L. Ma, A. Shahroudy, B. Shuai, T. Liu, X. Wang, G. Wang, "Recent advances in convolutional neural networks," *CoRR*, vol. abs/1512.07108, 2015.
- [29] K. Simonyan, A. Zisserman, "Very deep convolutional networks for large-scale image recognition," *CoRR*, vol. abs/1409.1556, 2014.
- [30] K. He, X. Zhang, S. Ren, J. Sun, "Deep residual learning for image recognition," *CoRR*, vol. abs/1512.03385, 2015.
- [31] S. Das, "CNNs architectures: LeNet, AlexNet, VGG, GoogLeNet, ResNet and more . . . ." <https://medium.com/@siddharthdas-32104>, 2017.
- [32] J. Ngiam, A. Khosla, M. Kim, J. Nam, H. Lee, A. Y. Ng, "Multimodal deep learning," in *Proceedings of the 28th international conference on machine learning (ICML-11)*, pp. 689–696, 2011.

## BIOGRAPHIES



**TAYYIP OZCAN** received his B.S. degree in Computer Engineering from Istanbul Kultur University, Istanbul, Turkey, in July 2010. He then joined as a research assistant to the Dept. of Computer Engineering of Erciyes University in 2013. He received his M.Sc. degree in 2016 from Computer Engineering, Erciyes University. He is currently Ph.D. candidate in Erciyes University, Department of Computer Engineering, Kayseri, Turkey. His research areas are intelligent optimization algorithms, image processing, machine learning, deep learning and Kalman filter. Lip reading, hand gesture recognition, human action recognition and human computer interaction are the main topics of his applications.



**ALPER BASTURK** received his B.S. degree in Electronics Engineering from Erciyes University, Kayseri, Turkey, in July 1998. He then joined as a research assistant to the Dept. of Electronics Eng. of Erciyes University. He received his M.S. and Ph.D. degrees in both of Electronics Engineering from Erciyes University in August-2001 and November 2006, respectively. In 2006, he joined the Computer Hardware Division, Department of Computer Engineering, Erciyes University, where he is currently an Associate Professor. Between 2010 and 2011, he was a visiting scholar to the Department of Electrical, Computer, and Systems Engineering, Rensselaer Polytechnic Institute, Troy, New York, USA. He guest-edited several special issues for various journals and has published more than fifty articles in leading journals and conferences. His research areas are digital signal and image processing, machine learning, deep learning, neural networks, fuzzy and neuro-fuzzy systems, intelligent optimization and applications of these techniques.

# Direction of Arrival Estimation in Multiple Antenna Arrays by Using Power Delay Profile for Random Access Performance in 5G Networks

O. AYDIN and T. AKYÜZ

**Abstract**—In the transition from 4G to 5G, various solutions are being developed to improve performance for features such as data rates, latency, connectivity density and reliability. One of these features is Random Access Procedure because of the increasing number of users in 5G networks. In the random access method, user equipment performs a random access to the base station with a preamble and thus registers itself to the base station. However, if more than one user equipment use the same preamble at the same time, collision occurs and the registration process in the base station could be halted. In this paper, a new method is proposed which can be used to calculate Direction of Arrival between adjacent antenna signals in the antenna array with the help of the phase differences. Thus, the collision can be avoided by using the beamforming technique of the MIMO system using the calculated arrival angle of the user equipment. The proposed method is verified for two and three user equipment placed at different angles, at different distances to an antenna array consisting of 10 antennas.

**Index Terms**—Direction of Arrival (DOA), Power Delay Profile, Preamble, Zadoff-Chu.

## I. INTRODUCTION

IT IS EXPECTED that in the Fifth Generation (5G) wireless communication systems, the connection density will increase more than tenfold compared to the Fourth Generation (4G) systems [1]. As a result of this increase, it is clear that user elements (UE) will cause significant congestion in accessing LTE services. To meet this demand, one of the solutions is the using location division multiplexing systems which is supported with multi input multi output (MIMO) antenna systems in addition to time and frequency division

OMER AYDIN, is with the Department of Research and Development, Netas, 34912, Turkey, (e-mail: [aydin@netas.com.tr](mailto:aydin@netas.com.tr)). Also with Department of Electrical and Electronics Engineering, Istanbul Technical University, Istanbul, Turkey.

 <https://orcid.org/0000-0002-1519-6937>

TUĞRUL AKYÜZ, is with the Department of Research and Development, Netas, 34912, Turkey (e-mail: [tugrulvega@gmail.com](mailto:tugrulvega@gmail.com)).

 <https://orcid.org/0000-0001-8297-8720>

Manuscript received March 8, 2019; accepted May 25, 2019.  
DOI: [10.17694/bajece.537262](https://doi.org/10.17694/bajece.537262)

multiplexing structures with the intelligent deployment of Resource Elements (RE) [1]. Furthermore, Random Access (RA) that UEs use for the first access to base station is one of the bottlenecks that make LTE services difficult to access and the number of preambles, already used in 4G networks to solve the Random Access collision problem seems to be insufficient. It is clear that solutions that solve this congestion will enable more UEs to be registered to the base station more quickly.

Registration of the UE to the base station is done over the Random Access Channel (RACH) in Long Term Evolution (LTE) networks. However, concurrent access of UEs to the same channel causes signal collision. To overcome this problem, a preamble structure was introduced in 4G. With the help of the preamble, the randomly selected Zadoff Chu sequences are being used to eliminate the effects of collisions at the base station [2], [3].

Since the number of users in 5G networks is expected to be much more than the 4G network, the number of Zadoff Chu series may be insufficient for the first registration of the UEs. Reusing the same Zadoff Chu series on the random access channels which are multiplexed in the 3D space with the help of MIMO antenna system might be a solution to the this problem. To do this efficiently, it is very important to correctly calculate the Direction of Arrival (DoA) of the different UEs in the coverage area of the base station. Using angular position information, the initial registration and channel allocation procedures for UEs can be performed using the same Zadoff Chu series with the help of the RACH Procedure.

DoA resolution algorithms have been extensively investigated and in a variety of solutions were proposed in the literature. Delay and Collection techniques such as Bartlett method tries to magnify the signals from certain direction by compensating the phase shift [4], [5]. The Capon method is a minimum variance method that estimates direction of arrival by changing weight to minimize the array power subject to unity gain [6]. MUSIC (MULTiple SIGNAL Classification) and ESPRIT (Estimation of Signal Parameters via Rotational Invariance Technique) algorithm, which are based on the subspace method, are developed based on eigenvectors, eigenvalues and spectral matrix theories [7]. The above algorithms use the correlation of the signals received by the

different antennas in the multi-antenna structure. Apart from these studies, subcarrier-based beamforming methods and multi-level beamforming approaches for more efficient operation are available [8]. Some studies also use two dimensional antenna arrays [9]. Other recent studies on DOA estimation are using MUSIC algorithm after rejecting interferences [10], wideband DOA estimation by using adaptive array technique [11], DOA estimation in cyclic prefix OFDM systems by using mono pulse ratio [12]. The estimation of the reception angle is proposed in [13] based on the distribution characteristics using power delay profile.

The above-mentioned methods evaluate the correlation of all incoming signals; therefore, they also take into account the signals of the UEs having different input preamble. These algorithms have an upper limit on the number of source UEs to be calculated depending on the number of antennas used in the array antenna structure of the base station [9]. Therefore, the use of these algorithms at the receiver input gives the main difficulty in accurately determining the desired arrival angle of a large number of UEs.

In this paper, a new method is proposed to overcome the above-mentioned problem, which is based on using the phase differences of the peak values in the Power Delay Profile array, which is already calculated in the receiver stage of OFDM layer, used LTE systems [1], [2].

## II. PROPOSED METHOD

### A. Preamble and Zadoff Chu Sequence

The RACH is the channel (Random Access Channel) for mobile users to access the base station. Physical structure of the RACH, Physical Random Access Channel (PRACH) is shown in the Fig. 1.

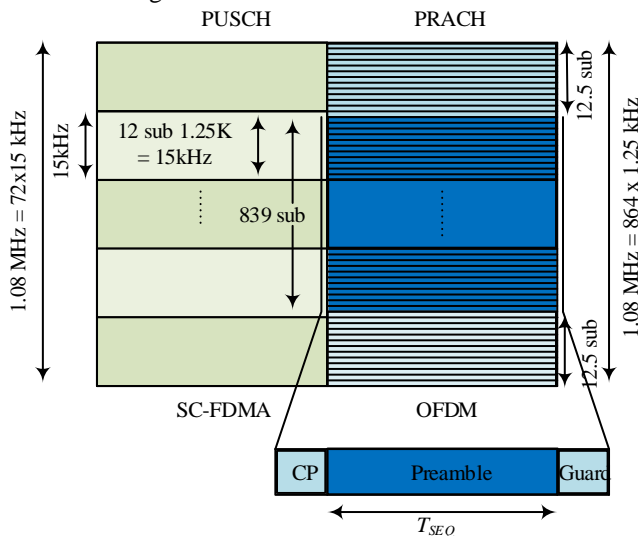


Fig.1. Structure of the Physical Random Access Channel (PRACH)

Access through this channel continues with the mutual acknowledgment mechanisms and the mobile device receives the configuration of the resource blocks (RB) that it needs from the base station. The Random Access of the UEs to the base station is achieved by preamble signatures produced

using Zadoff Chu arrays which are perpendicular to each other, that provides the detection of UEs by the base station.

The Zadoff Chu sequence  $z_u$  is obtained from the following formula.

$$z_u(n) = e^{-\frac{j\pi un(n+1)}{N_{zc}}} \quad n = 0, 1, 2, \dots, N_{zc} - 1 \quad (1)$$

where  $u \in \{1, 3, 5, \dots, U - 1\}$ ,  $U$  is the root index and  $N_{zc}$  length of the Zadoff Chu sequence [2].

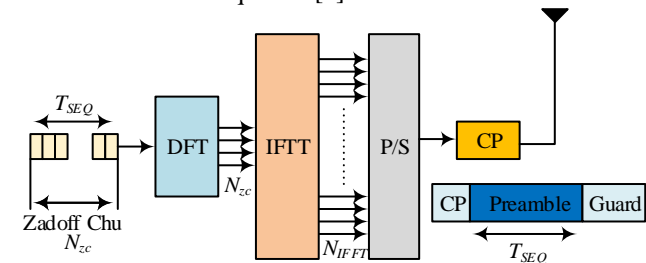


Fig.2. Transmitter side of the OFDM random access channel (DFT: Discrete Fourier Transform, IFFT: Inverse Fourier transform, P/S: parallel/serial, CP: Cyclic Prefix)

As shown in Fig. 2, the user terminal initially selects a Zadoff Chu sequence. Afterwards, Discrete Fourier Transform (DFT) is performed to the Zadoff Chu series which has a sequence length of  $N_{zc}$ . The array of frequency signals of DFT output is then located at the 1.08 MHz range in the middle region of the Orthogonal Frequency Division Multiplexing (OFDM) band according to carrier frequencies of 1.25 kHz as shown in Fig. 1 [2]. Then, Inverse Fast Fourier Transform (24576 point IFFT) is applied to the carrier frequencies of 1.25 kHz (Fig. 2). The preamble signal of 0.8 ms long is then converted from the parallel to the serial by adding the cyclic prefix (CP) and guard time, and then sent to the antennas [2]. In the receiver part, as shown in Fig. 3, the inverse of the sending procedure is applied, and the preamble is obtained.

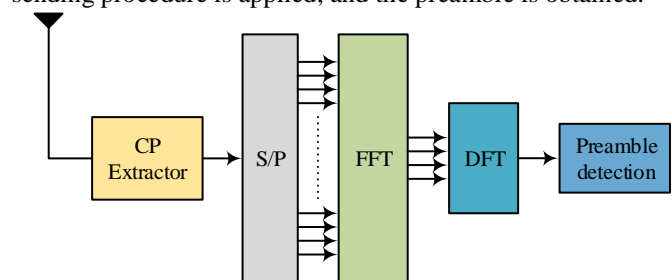


Fig.3. OFDM random access receiver channel

### B. Power Delay Profile and DoA

The signal sent from the UEs received from the PRACH channel is pre-processed and preamble detection is performed according to the defined standards as shown in Fig. 4.

Assumed that  $x(n)$  is to be the sequence of the signal received, the Power-Delay Profile,  $PDP(l)$  is calculated by the following formula:

$$PDP(l) = |p(l)|^2 = \left| \sum_n^{N_{zc}-1} x(n) z_u^*[(n+l) \bmod N_{zc}] \right|^2 \quad (2)$$

where  $z_u(n)$  is the reference Zadoff Chu for the root index  $u$  and  $z_u(n)^*$  indicates the complex conjugate of  $z_u(n)$ .

As a result of this process which is shown in the block diagram in Fig. 4b, peak values occur only when the Zadoff

Chu series generated from the root index selected by the corresponding UE to generate the preamble for the same root index. The distance between the peaks of this array to the reference point gives the time of arrival (ToA) of signals sent by the UEs. For example, if there are two UEs, two peaks are formed in the array for each UE as can be seen from Fig. 5. The signal from an UE sometimes reaches to the receiver after being reflected from an obstacle; in this case, a relatively weak peak may be seen with a delay as shown from the figure.

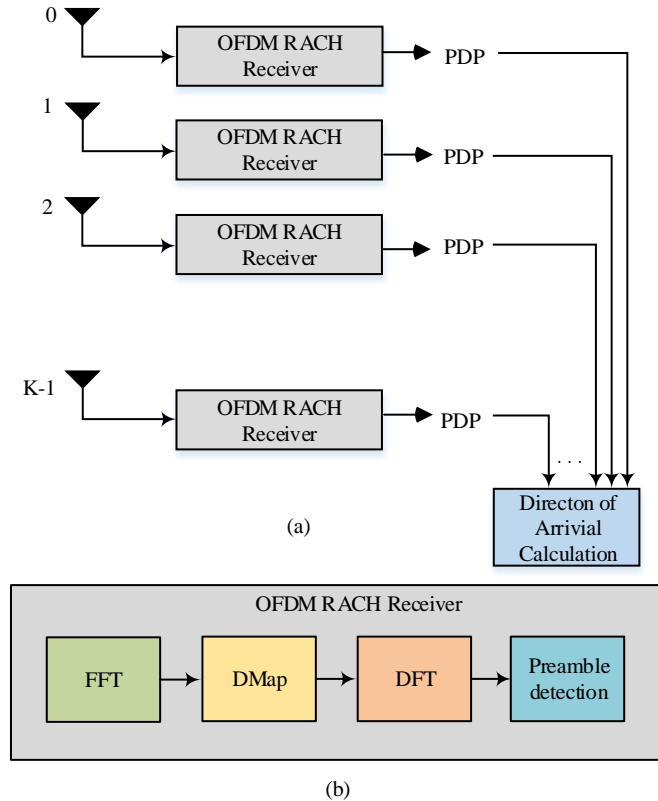


Fig.4. Block diagram of the receiver part with the antenna array and pre-processor blocks which calculate PDP (a) and sub-blocks of the OFDM RACH receiver (b)

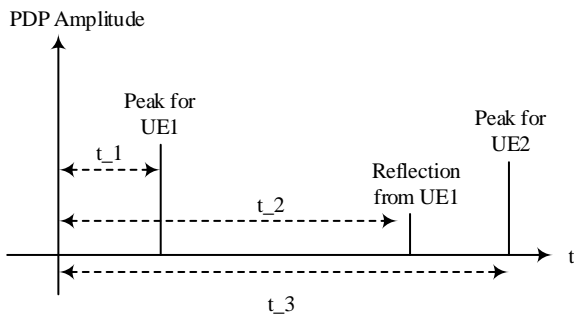


Fig.5. Depending on the distance of the UEs from antenna, the signals reach the receiver at different time, and peaks are formed at these points; the reflected signals form relatively low peaks

In the case of multiple antenna structures, this process is applied on every antenna. The resulting Power Delay Profile sequences can be used for the direction of the arrival detection method. Obtaining the UE's signal input angles, gives the possibility to the base station to continue to perform the RACH procedure differently for each of the mobile terminals by using beam forming with the help of the antenna array.

### III. PHASE DIFFERENCE IN POWER DELAY PROFILE

The signal from one UE to each antenna will come with a certain phase difference, both depending on the angle of arrival of the signal to the antenna array and the distance between the antennas. As can be seen in Fig. 6, time delays occur in the signals sent by the UEs at a certain angle relative to the range  $d$  between the antennas. The constant  $c$  defines propagation waves at light speed.  $\Delta_{tk}$  is  $k$ th antenna signal arriving delay time. Assuming that  $s_b(t)$  is a narrow base band signal and  $f_c$  is the carrier frequency, the real part of this signal becomes  $s(t) = \text{Re}\{s_b(t)e^{-j2\pi f_c t}\}$ .

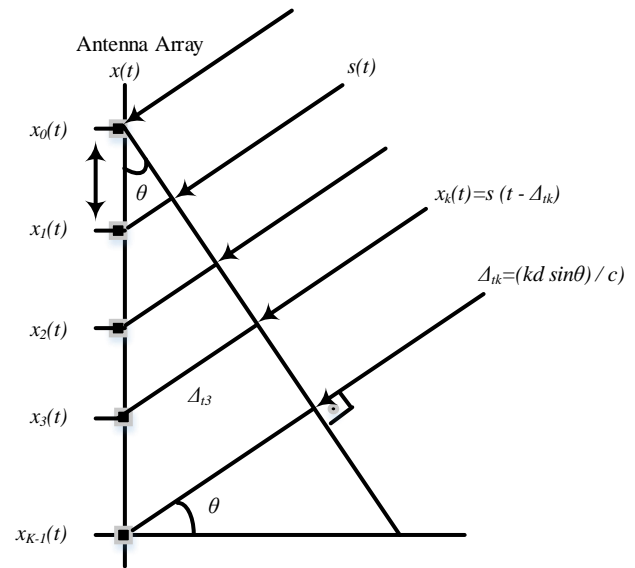


Fig.6. UE signal to the antenna array with the angle of  $\theta$

We can write  $x_k(t)$  at the receiver such that:

$$x_k(t) = \text{Re}\{s_b(t - \Delta_{tk})e^{-j2\pi f_c(t - \Delta_{tk})}\} \quad (3)$$

$$x_k(t) = \text{Re}\{s_b(t - \Delta_{tk})e^{-j2\pi f_c \Delta_{tk}}e^{-j2\pi f_c t}\} \quad (4)$$

and for the base band, we can write

$$x_k(t) = s_b(t - \Delta_{tk})e^{-j2\pi f_c \Delta_{tk}} \quad (5)$$

and then, when we put  $nT$  instead of  $t$ , we get

$$x_k(nT) = s_b(nT - \Delta_{tk})e^{-j2\pi f_c \Delta_{tk}} \quad (6)$$

where  $T$  is the sampling period. Assuming that  $T \gg \Delta_{tk}$ , we get

$$x_k(nT) \cong s_b(nT)e^{-j2\pi f_c \Delta_{tk}} \quad (7)$$

We have  $\Delta_{tk} = kd \sin \theta / c$  and  $f_c \lambda = c$ , so when we select  $d = \lambda/2$  we get;

$$x_k(nT) = s_b(nT)e^{-j2\pi f_c \frac{kd \sin \theta}{c}} \quad (8)$$

$$x_k(nT) = s_b(nT)e^{-j\pi k \sin \theta} \quad (9)$$

In discrete domain for  $k$ th antenna we can write:

$$x_k[n] = s[n]e^{-j\pi k \sin \theta} \quad (10)$$

We get  $p_k(l)$  as below after the cross correlation by substituting Equation (10) into Equation (2):

$$p_k(l) = e^{-j\pi k \sin \theta} \sum_n^{N_{zc}-1} s[n] z_u^*[(n+l) \bmod N_{zc}] \quad (11)$$

In each  $p_k(l)$  series for each  $k$ th antenna there is a phase difference angle of  $\pi k \sin \theta$ . If we consider the peaks in the  $p_k(l)$  series that indicate the signal from a UE, there is a phase difference between the  $p_k(l_{peak})$  of the  $k$ th antenna and the  $p_{k+1}(l_{peak})$  of the  $(k + 1)$ th antenna. The phase difference  $\phi$  can be calculated as:

$$\phi = \angle(p_k(l_{peak})p_{k+1}(l_{peak})) \quad (12)$$

and direction of arrival  $\theta$  is

$$\theta = \sin^{-1} \frac{\phi}{\pi} \quad (13)$$

assuming that phase difference between adjacent antennas less than  $180^\circ$ .

#### IV. SIMULATION RESULTS

The simulation was performed in MATLAB using two UEs positioned against to the base station at a distance of 357 m and 2145 m with the angle of  $30^\circ$  and  $-10^\circ$  degrees to the linear antenna array respectively.

The antenna array consists of  $K = 10$  antennas spaced at distance  $d = \lambda/2$ . As shown in Fig. 7, when the broadcast frequency is selected as 3GHz, this spacing distance  $d$  should be about 5 cm.

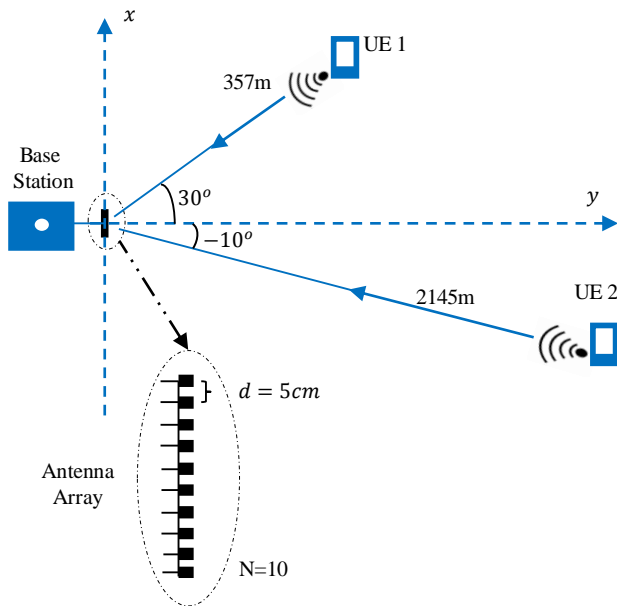


Fig.7. Configuration of the UEs and antenna array to simulate proposed DoA calculation method

The preamble index of the two UEs in RACH channel was chosen as one. As a result, when the same Zadoff Chu sequence is used in the two UEs for random access, in the Power Delay Profile series, two peaks are formed as shown in Fig. 8.

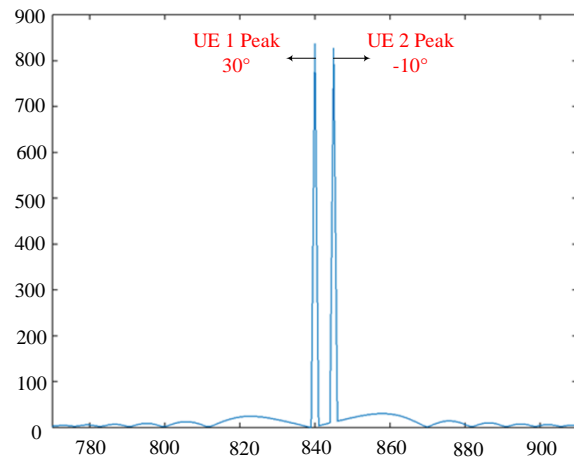


Fig.8. Peak values of the Power Delay Profile, UE 1 and UE 2 obtained as a result of the preamble detection. The horizontal axis shows the sampled data index

To find the direction of arrival, the phase shifts at the peak complex values are used. These phase shifts are shown in Fig. 9 for the fifth and sixth antennas of the antenna array in the base station. As mentioned above,  $\theta$  is the direction of arrival to be found, and the phase shift is  $\phi = \pi \sin \theta$  as from the Equation (13). Since the phase in each consecutive adjacent antenna is approximately  $\theta$ , the average of this values increase the accuracy. The average is calculated as follows:

$$\phi = \frac{1}{K-1} \sum_{k=1}^{K-1} \tilde{\phi} \quad (14)$$

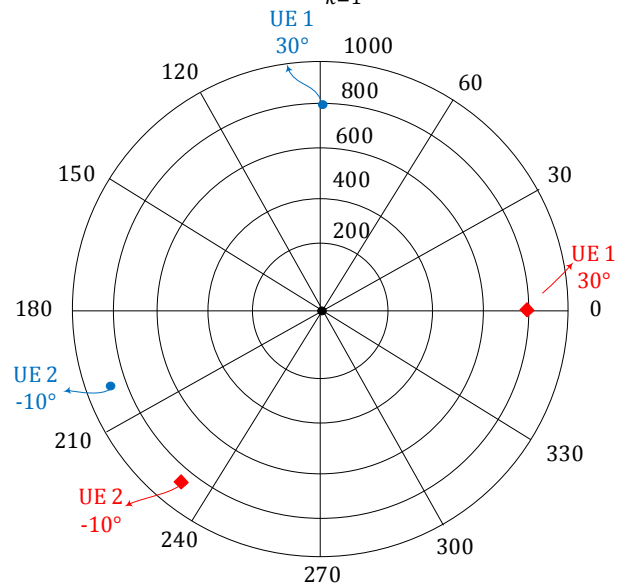


Fig.9. Peak values of Power Delay Profile for the fifth (red rectangular) and sixth (blue circles) antenna view in the polar coordinate

The second simulation is made by adding a third UE with same Zadoff Chu sequence, in addition to the previous two UEs and positioned at an angle of  $-20^\circ$  at a distance of 3576 m. With this simulation, the effect of the third UE which uses the same Zadoff Chu sequence, on the results obtained in the previous simulation is examined. Peak values of the Power Delay Profile for three UEs are shown in Fig. 10.

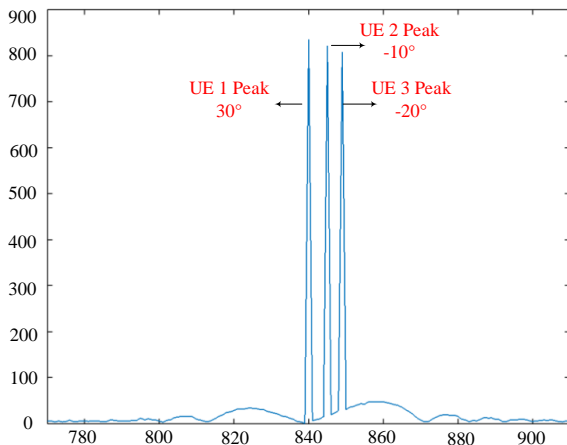


Fig.10. Peak values of the Power Delay Profile for three UEs using same Zadoff Chu sequence.

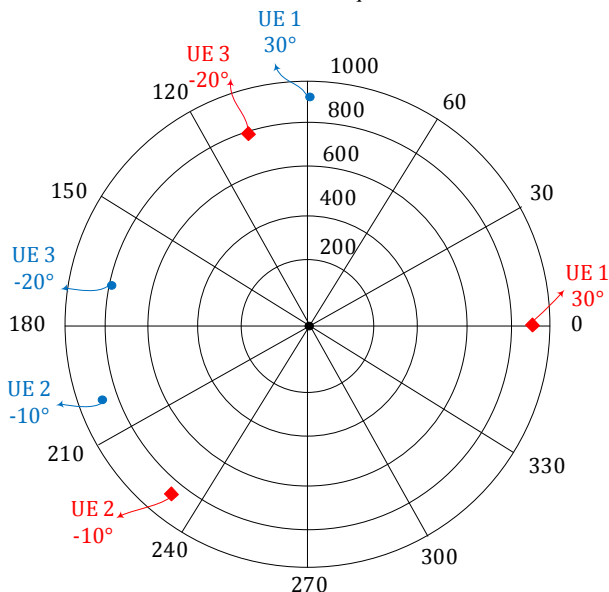


Fig.11. Peak values of Power Delay Profile for the fifth (red rectangular) and sixth (blue circles) antenna for three UEs

As can be seen from Fig. 11, the positions calculated in the first simulation for the first and second UE are not affected by the third UE. The location of the UE 3 is also calculated correctly.

## V. CONCLUSION

It is expected that the number of users in 5G networks will be much higher than the number of preambles that can ensure that the UEs are successfully registered to the base station. In this paper, a solution is proposed that allows the simultaneous use of same preambles to increase the registration performance. For this purpose, using the power delay profile, the angle of receiving signal sent by the UE can be calculated to enable beam-forming functionality, which can be performed with the help of the antenna array. The phase difference of the incoming signals from the neighbouring antennas is calculated by using peak values which are already calculated OFDMA layers with the help of Zadoff Chu series in 4G networks.

The success of the proposed method verified by using MATLAB with an antenna array consisting 10 antennas. Simulations are made for two different configurations, first

consists two UEs and the second with third UE additional to the first configuration. All UEs which use same Zadoff Chu sequences in the preamble are located at different distance and angles. Simulation result proves that, the proposed method can be a candidate method for solving the simultaneous registration problem of multiple UEs in 5G systems.

## REFERENCES

- [1] A. Gupta, R. K. Jha, "A Survey of 5G Network: Architecture and Emerging Technologies", *IEEE Access*, vol. 3, 2015, pp.1206-1232.
- [2] 3<sup>rd</sup> Generation Partnership Project; Technical Specification Group Radio Access Network; Evolved Universal Terrestrial Radio Access (E-UTRA); Physical Channels and Modulation (Release 10), 2011.
- [3] H. J. Zepernick, A. Finger, *Pseudo Random Signal Processing: Theory and Application*, John Wiley & Sons, 2013.
- [4] V. Krishnaveni, T. Kesavamurthy, B. Apama, "Beamforming for Direction-of-Arrival (DOA) Estimation-A Survey", *International Journal of Computer Applications*, vol. 61, 11, 2013, pp.4-11.
- [5] Y. Khmou, S. Safi, M. Frikel, "Comparative Study between Several Direction Of Arrival Estimation Methods", *Journal of Telecommunications and Information Technology*, vol. 1, 2014, pp.41-48.
- [6] R. J. Weber, Y. Huang, "Analysis for Capon and MUSIC DOA estimation algorithms", *IEEE Antennas and Propagation Society International Symposium*, June 2009.
- [7] J. S. Jeong, K. Sakaguchi, J. I. Takada, K. Araki, "Performance of MUSIC and ESPRIT for joint estimation of DOA and angular spread in slow fading environment", *IEICE Transactions on Communications*, vol. E85-B, 5, 2002.
- [8] A. Abdelkader, S. Shahbazpanahi, S. Gershman, "Joint subcarrier power loading and distributed beamforming in OFDM-based asynchronous relay networks", *3rd IEEE International Workshop on Computational Advances in Multi-Sensor Adaptive Processing (CAMSAP)*, 2009.
- [9] S. Sesia, I. Toufik, M. Baker, *LTE – The UMTS Long Term Evolution From Theory to Practice*, John Wiley & Sons, 2013.
- [10] K. Kataoka, N. Kikuma, K. Sakakibara, "DOA Estimation of Desired Wave with Interference Rejection Using BeamSpace Root-MUSIC", *International Symposium on Antennas and Propagation (ISAP)*, 2018.
- [11] B. Yin, "Wideband Signal Direction-of-Arrival Estimation by Using Steered Adaptive Array Technique", *IEEE International Conference on Signal Processing, Communications and Computing (ICSPCC)*, 2018.
- [12] H. Kim, J. Kim, K. H. Lee, K. S. Kim, "DOA estimation in Cyclic Prefix OFDM Systems in LOS mmWave Channel using Monopulse Ratio", *International Conference on Information and Communication Technology Convergence (ICTC)*, 2018.
- [13] C. ZióBkowski, J. M. Kelner, "Estimation of the Reception Angle Distribution Based on the Power Delay Spectrum or Profile", *Hindawi Publishing Corporation International Journal of Antennas and Propagation*, vol. 2015.

## BIOGRAPHIES



**OMER AYDIN** has received his B.Sc. and M.Sc. in Electronics Engineering from Istanbul Technical University in 1982, 1985, respectively. He has completed his PhD on 4G and 5G radio power frequency amplifiers in 2016 in Istanbul Technical University. He is now working in Netas R&D. He has more than 20 scientific papers on 5G communication systems. His research interests include 5G communication systems, theoretical and practical aspects of radio frequency power amplifier designs.



**TUĞRUL AKYÜZ** has received his B.Sc. in Electronics Engineering from İstanbul Technical University (İTÜ) in 1992 and M.Sc. in Electronics and Telecommunication Engineering from Boğaziçi University (BÜ) in 1996. He is working in Netas R&D as S/W design

engineer since 1996.

# An Approximate Error Expression for RQAM Scheme under $\alpha$ - $\eta$ - $\mu$ Fading Conditions

N. KAPUCU

**Abstract**— In this paper, average symbol error rate (ASER) performance of rectangular quadrature amplitude modulation (RQAM) scheme is analyzed over  $\alpha$ - $\eta$ - $\mu$  fading channels. First, an ASER expression is derived based on Chernoff approximation of Gaussian  $Q$ -function. Then, an asymptotic ASER formula is obtained for analyzing system behavior at high signal-to-noise ratio (SNR) regime. The ASER performance is presented for different modulation levels and fading parameter values. In addition, relative truncation error (RTE) is illustrated in order to determine how many terms are needed for the computation of proposed expression. It is shown that analytical results are in close agreement with exact results.

**Index Terms**— Error analysis,  $\alpha$ - $\eta$ - $\mu$  distribution, RQAM, Gaussian  $Q$ -function.

## I. INTRODUCTION

QUADRATURE amplitude modulation (QAM) which is known as efficient modulation method for bandwidth has an important role in digital multimedia transmission since it achieves high data rates. Rectangular QAM (RQAM), cross QAM (XQAM) and square QAM (SQAM) are popular QAM methods that are used in high speed communications. RQAM is considered as a generic modulation type and it has practical applications in the field of high speed mobile communications and microwave communications [1].

A number of studies which focus on the performance for RQAM schemes under different fading conditions, have been presented in the literature [2-7]. In [2], a lower bound ASER expression was derived for cooperative diversity systems with RQAM technique over Rayleigh fading channels. In addition, symbol error probability (SEP) and average symbol error rate (ASER) expressions were proposed for RQAM modulated systems under Nakagami- $m$  fading conditions [3-6]. In [3], the SEP of RQAM modulation was presented over Nakagami- $m$  fading channels in terms of the product of two Gaussian  $Q$ -functions. The authors in [4] studied the performance of  $L$ -branch communication system with RQAM scheme in the presence of Nakagami- $m$  fading and they proposed an

expression for the SEP of the considered system. In [5] and [6], RQAM technique was applied to multiple relay networks and two-way relaying systems operating under Nakagami- $m$  fading conditions. Asghari *et al.* analyzed the SEP of RQAM scheme with maximum ratio combining over  $\eta$ - $\mu$  fading channels [7]. In [8], the ASER of RQAM and XQAM modulations were investigated based on moment generating function over two-wave with diffuse power fading channels. Lower bound ASER expressions of RQAM and XQAM for AF relaying systems were presented in Rayleigh fading with maximum ratio combining in [9]. In another work [10], the authors derived ASER formulas for hexagonal and rectangular QAM based on cumulative distribution function over Nakagami- $m$  fading channels.

In wireless communications, it is important to take the composite fading channels into consideration such as in [11-15] for performance analysis since these fading models are generalized distributions which provide flexibility for reducing other well-known fading channels. However, as far as we know, error performance of RQAM modulated wireless communication systems over  $\alpha$ - $\eta$ - $\mu$  fading channels does not exist in literature.  $\alpha$ - $\eta$ - $\mu$  fading can be employed in order to reflect small variations in the signal strength and it has special cases including popular fading distributions such as Rayleigh, Nakagami- $m$ , Weibull,  $\eta$ - $\mu$ ,  $\alpha$ - $\mu$ . Motivated by this, for the first time in the literature, we analyze ASER performance of RQAM scheme over  $\alpha$ - $\eta$ - $\mu$  fading channels. Here, we derive a novel ASER expression based on Chernoff approximation of Gaussian  $Q$ -function. Then, we also obtain an asymptotic ASER expression in order to evaluate the system behavior at high signal-to-noise ratio (SNR) region.

## II. SYSTEM AND CHANNEL MODELS

We consider a single-input single-output wireless communication system that sends a signal  $x$  which is modulated according to RQAM scheme. The received signal,  $y$  is defined as

$$y = xG + N_0 \quad (1)$$

where  $G$  is the fading coefficient of the channel and  $N_0$  is spectral density of noise power. The probability density function (PDF) of instantaneous SNR,  $\gamma$ , for  $\alpha$ - $\eta$ - $\mu$  distribution is expressed by

NURİ KAPUCU, is with Department of Electrical and Electronics Engineering, Hitit University, Turkey, (e-mail: [nurikapucu@hitit.edu.tr](mailto:nurikapucu@hitit.edu.tr)).

 <https://orcid.org/0000-0002-8399-5546>

Manuscript received September 28, 2018; accepted March 29, 2019.  
DOI: [10.17694/bajece.465158](https://doi.org/10.17694/bajece.465158)

$$f_\gamma(\gamma) = A \exp\left(-\frac{2\mu h \gamma^{\frac{\alpha}{2}}}{\bar{\gamma}^{\frac{\alpha}{2}}}\right) \gamma^{\frac{\alpha(\mu+0.5)}{2}-1} I_{\mu-\frac{1}{2}}\left(\frac{2\mu H \gamma^{\frac{\alpha}{2}}}{\bar{\gamma}^{\frac{\alpha}{2}}}\right) \quad (2)$$

$$A = (\sqrt{\pi} \alpha \mu^{\mu+0.5} h^\mu) / (\Gamma(\mu) H^{\mu-0.5} \bar{\gamma}^\lambda) \quad (3)$$

where  $\alpha$ ,  $\eta$ ,  $\mu$  are fading parameters,  $\lambda = \alpha(\mu+0.5)/2$ ,  $\Gamma(\cdot)$  is Gamma function,  $I_\nu(\cdot)$  is the modified Bessel function of the first kind,  $\bar{\gamma}$  is the average SNR defined by  $\bar{\gamma} = E(\gamma)$  and  $E(\cdot)$  denotes expectation.  $h$  and  $H$  parameters are defined in two different formats, respectively, as

$$h = \frac{(1+\eta)^2}{4\eta}, H = \frac{1-\eta^2}{4\eta}, \quad 0 < \eta < \infty, \text{ Format 1} \quad (4)$$

$$h = \frac{1}{1-\eta^2}, H = \frac{\eta}{1-\eta^2}, \quad -1 < \eta < 1, \text{ Format 2}$$

### III. AVERAGE SYMBOL ERROR RATE ANALYSIS

Mathematically, the ASER for any kind of modulation method is evaluated by integrating the conditional symbol error rate (SER) of additive White Gaussian noise (AWGN) channels over the PDF of instantaneous SNR as follows

$$P_s(e) = \int_0^\infty P_s(e|\gamma) f_\gamma(\gamma) d\gamma \quad (5)$$

where  $P_s(e|\gamma)$  is the conditional SER expression of AWGN channels and  $f_\gamma(\gamma)$  is the PDF of the instantaneous SNR. General order RQAM constellations can be obtained by combining two pulse amplitude modulation (PAM) signals as  $M_I$ -PAM (in-phase) and  $M_Q$ -PAM (quadrature). For  $M$ -ary RQAM, the conditional SER in AWGN channels is expressed as

$$P_s(e|\gamma) = 2(pQ(a\sqrt{\gamma}) + qQ(b\sqrt{\gamma}) - 2pqQ(a\sqrt{\gamma})Q(b\sqrt{\gamma})) \quad (6)$$

where  $M = M_I \times M_Q$ ,  $p = 1 - (1/M_I)$ ,  $a = \sqrt{6/((M_I^2 - 1) + (M_Q^2 - 1)\beta^2)}$ ,  $q = 1 - (1/M_Q)$ ,  $b = \beta a$ ,  $\beta = d_Q/d_I$  is the decision distance ratio of quadrature-to-in-phase components ( $d_I$  is the in-phase decision distance and  $d_Q$  is the quadrature decision distance) and  $Q(\cdot)$  is Gaussian  $Q$ -function. Inserting (6) into (5), the ASER can be rewritten as

$$P_s(e) = \underbrace{\int_0^\infty 2pQ(a\sqrt{\gamma}) f_\gamma(\gamma) d\gamma}_{I_1} + \underbrace{\int_0^\infty 2qQ(b\sqrt{\gamma}) f_\gamma(\gamma) d\gamma}_{I_2} - \underbrace{\int_0^\infty 4pqQ(a\sqrt{\gamma})Q(b\sqrt{\gamma}) f_\gamma(\gamma) d\gamma}_{I_3} \quad (7)$$

The integral in (7) is in an intractable format because of including Gaussian  $Q$ -function. Therefore, we utilize an upper bound approximation of the Gaussian  $Q$ -function which is defined by

$$Q(x) \approx \frac{1}{2} \exp\left(-\frac{x^2}{2}\right) \quad (8)$$

The approximate form given in (8) is known as Chernoff approximation [16]. This approximation facilitates the integration and ASER analysis over fading channels. First, we start by solving  $I_1$  for ASER analysis. By inserting the Chernoff approximation and (2) into the first integral in (7),  $I_1$  can be reexpressed as follows

$$I_1 = pA \int_0^\infty \exp\left(-\frac{a^2\gamma}{2}\right) \exp\left(-\frac{2\mu h \gamma^{\frac{\alpha}{2}}}{\bar{\gamma}^{\frac{\alpha}{2}}}\right) \times \gamma^{\lambda-1} I_{\mu-0.5}\left(\frac{2\mu H \gamma^{\frac{\alpha}{2}}}{\bar{\gamma}^{\frac{\alpha}{2}}}\right) d\gamma \quad (9)$$

Now using the infinite series representations of exponential function [17, (1.211.1)] and  $I_\nu(\cdot)$  [17, (8.445)] in (9), we have

$$I_1 = Ap \sum_{k=0}^\infty \frac{(-1)^k}{k!} \left(\frac{2\mu h}{\bar{\gamma}^{\frac{\alpha}{2}}}\right)^k \sum_{m=0}^\infty \frac{(\mu H)^u}{m! \Gamma(\mu + m + 0.5)} \times \frac{1}{(\bar{\gamma}^{\frac{\alpha}{2}})^u} \int_0^\infty \exp\left(-\frac{a^2\gamma}{2}\right) \gamma^{v-1} d\gamma \quad (10)$$

where  $v = \lambda + (\alpha k/2) + (\alpha u/2)$  and  $u = \mu + 2m - 0.5$ . After some algebra and by using [17, (3.381.4)],  $I_1$  is derived as

$$I_1 = Ap \sum_{k=0}^\infty \frac{(-1)^k}{k!} \left(\frac{2\mu h}{\bar{\gamma}^{\frac{\alpha}{2}}}\right)^k \sum_{m=0}^\infty \frac{(\mu H)^u \Gamma(v) (a^2/2)^{-v}}{m! \Gamma(\mu + m + 0.5) (\bar{\gamma}^{\frac{\alpha}{2}})^u} \quad (11)$$

Then,  $I_2$  and  $I_3$  are obtained by using the same analytical steps as used for  $I_1$ , respectively, as

$$I_2 = Aq \sum_{k=0}^{\infty} \frac{(-1)^k}{k!} \left( \frac{2\mu h}{\bar{\gamma}^{(\alpha/2)}} \right)^k \sum_{m=0}^{\infty} \frac{(\mu H)^u}{\Gamma(\mu + m + 0.5)} \times \frac{\Gamma(v)}{m! (\bar{\gamma}^{(\alpha/2)})^u (b^2/2)^v} \tag{12}$$

$$I_3 = Apq \sum_{k=0}^{\infty} \frac{(-1)^k}{k!} \left( \frac{2\mu h}{\bar{\gamma}^{(\alpha/2)}} \right)^k \sum_{m=0}^{\infty} \frac{(\mu H)^u}{\Gamma(\mu + m + 0.5)} \times \frac{\Gamma(v)}{m! (\bar{\gamma}^{(\alpha/2)})^u ((a^2 + b^2)/2)^v} \tag{13}$$

Finally, the ASER expression is found as

$$P_s(e) = A \sum_{k=0}^{\infty} \frac{(-1)^k}{k!} \left( \frac{2\mu h}{\bar{\gamma}^{(\alpha/2)}} \right)^k \sum_{m=0}^{\infty} \frac{(\mu H)^u \Gamma(v)}{m! \Gamma(\mu + m + 0.5) (\bar{\gamma}^{(\alpha/2)})^u} \times \left\{ \frac{p}{(a^2/2)^v} + \frac{q}{(b^2/2)^v} - \frac{pq}{((a^2 + b^2)/2)^v} \right\} \tag{14}$$

Concerning about the truncation error which arises from the infinite series involved in (14), we evaluated the ASER expression in (14) for several values of the upper limits of infinite summations. Table I tabulates the ASER values and relative truncation error (RTE) for 4X2 QAM at  $\bar{\gamma} = 20$  dB when  $K$  and  $M$  terms are used.

TABLE I  
ASER AND RTE VALUES FOR 4X2 QAM WITH  $\alpha = 1.5, \eta = 0.5, \mu = 1.5$   
AND  $\beta = 1$

M	K	ASER	RTE
24	2	<b>0.016957241605913</b>	$2.8012 \times 10^{-4}$
24	3	<b>0.016957295835405</b>	$3.1980 \times 10^{-6}$
24	4	<b>0.016957296375839</b>	$3.1870 \times 10^{-8}$
24	5	<b>0.016957296380701</b>	$2.8671 \times 10^{-10}$
24	6	<b>0.016957296380741</b>	$2.3755 \times 10^{-12}$
24	7	<b>0.016957296380742</b>	$1.8369 \times 10^{-14}$
24	8	<b>0.016957296380742</b>	$1.3382 \times 10^{-16}$

RTE can be evaluated by following the same procedure in [18]. In Table I, one can see that the decimal places remained same even if the upper limits were increased. Hereby, Table I shows that the number of enough terms in order to compute the derived ASER expression in (14) with a negligible truncation error are  $M = 24$  and  $K = 8$ . In Table II, we illustrate the ASER and RTE values for 8X4 QAM scheme at  $\bar{\gamma} = 40$  dB. Again, it can be easily seen that fewer terms are enough to evaluate the derived ASER expression at high SNR.

From Table II, only  $K=4$  terms are needed for the evaluation of infinite series when  $M=8$  where the RTE value decreases to  $7.5473 \times 10^{-16}$ . For all practical cases, (14) can be computed with a negligible truncation error without compromising numerical precision. Table I and Table II state that the derived expression is in rapidly convergent form.

TABLE II  
ASER AND RTE VALUES FOR 8X4 QAM WITH  $\alpha = 1.5, \eta = 0.5, \mu = 1.5$   
AND  $\beta = 1$

M	K	ASER	RTE
8	2	<b>3.688777670667582</b> $\times 10^{-5}$	$4.5747 \times 10^{-8}$
8	3	<b>3.688777670690955</b> $\times 10^{-5}$	$6.3366 \times 10^{-12}$
8	4	<b>3.688777670690958</b> $\times 10^{-5}$	$7.5473 \times 10^{-16}$
8	5	<b>3.688777670690958</b> $\times 10^{-5}$	$8.0208 \times 10^{-20}$

IV. ASYMPTOTIC ANALYSIS

To analyze system behavior at the high SNR regime ( $\bar{\gamma} \rightarrow \infty$ ), we derive an asymptotic ASER expression for the considered system. Firstly, we expand the infinite series of exponential function and  $I_\nu(\cdot)$  at zero point as

$$\exp\left(-2\mu h \bar{\gamma}^{(\alpha/2)} / \bar{\gamma}^{(\alpha/2)}\right) \approx 1 \tag{15}$$

$$I_{\mu-1/2} \left( \frac{2H\mu\gamma^{(\alpha/2)}}{\bar{\gamma}^{(\alpha/2)}} \right) \approx \frac{(H\mu\gamma^{(\alpha/2)} / \bar{\gamma}^{(\alpha/2)})^{\mu-0.5}}{\Gamma(\mu+0.5)} \tag{16}$$

Thus, the asymptotic PDF expression becomes

$$f_\gamma^a(\gamma) = \frac{A \gamma^{\left(\frac{\alpha(\mu+0.5)}{2} - 1\right) \left(\frac{\alpha(\mu-0.5)}{2}\right)}{\Gamma(\mu+0.5)} (\mu H \bar{\gamma}^{-(\alpha/2)})^{\mu-0.5} \tag{17}$$

Then, substituting (17) and Chernoff approximation of Gaussian  $Q$ -function into (7), we have

$$P_s^a(e) = \frac{A}{\Gamma(\mu+0.5)} \left( \frac{\mu H}{\bar{\gamma}^{(\alpha/2)}} \right)^{\mu-0.5} \left\{ p \int_0^\infty \exp\left(-\frac{\gamma a^2}{2}\right) \gamma^{\mu-1} d\gamma + q \int_0^\infty \exp\left(-\frac{\gamma b^2}{2}\right) \gamma^{\mu-1} d\gamma - pq \int_0^\infty \exp\left(-\frac{\gamma(a^2 + b^2)}{2}\right) \gamma^{\mu-1} d\gamma \right\} \tag{18}$$

By using [17, (3.381.4)], the asymptotic ASER expression results in

$$P_s^a(e) = \frac{A\Gamma(\alpha\mu)}{\Gamma(\mu+0.5)} \left( \frac{\mu H}{\gamma^{(\alpha/2)}} \right)^{\mu-0.5} \left\{ \frac{p}{(a^2/2)^{\alpha\mu}} + \frac{q}{(b^2/2)^{\alpha\mu}} - \frac{pq}{((a^2+b^2)/2)^{\alpha\mu}} \right\} \quad (19)$$

V. RESULTS

Here, ASER performance results are illustrated based on the proposed analytical expressions in comparison with exact results to validate the ASER expressions derived in this paper. The derived ASER expression includes convergent infinite series, which is truncated by  $K$  and  $M$  number of finite terms. Analytical results of (14) were obtained by setting the upper limits of the infinite summations to  $K = 10$  and  $M = 30$ . Fig. 1 shows the ASER performance of 4X2 QAM scheme for several values of fading parameters. As can be seen from Fig. 1, the analytical results of (14) match closely with the exact results while the asymptotic results are very tight at high SNR regime. A transition from  $\alpha = 1, \eta = 0.5$  and  $\mu = 1.5$  to  $\alpha = 1.5, \eta = 0.3$  and  $\mu = 1.5$  provides a considerable performance improvement which is more than 5 dB even if the value of  $\eta$  decreases from 0.5 to 0.3 with fixed value of  $\mu$ .

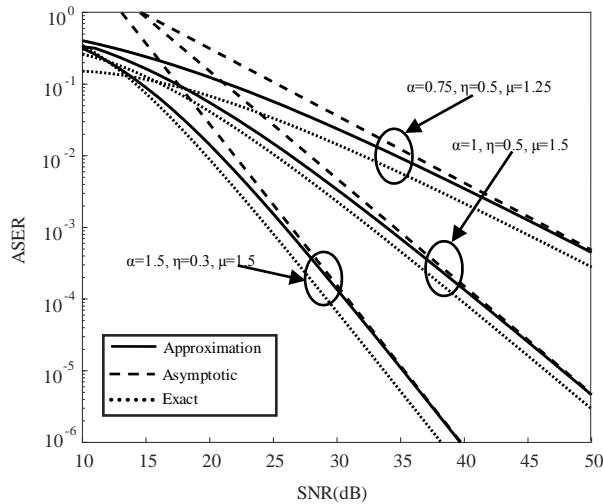


Fig. 1. ASER performance of 4X2 QAM scheme with  $\beta=1$

In Fig. 2, the ASER performance of 8X4 QAM modulated wireless systems is presented. Again, it can be seen that the exact results and approximated results are in close agreement. Moreover, the asymptotic results become tight with the approximate results at high SNR regime. For the case of  $\alpha = 1.5, \eta = 0.3$  and  $\mu = 1.5$ , 4X2 QAM scheme provides  $P_s(e) = 10^{-6}$  at 40 dB while the same ASER value is obtained at 46 dB with 8X4 QAM scheme. As expected, when the constellation size increases, the performance decreases.

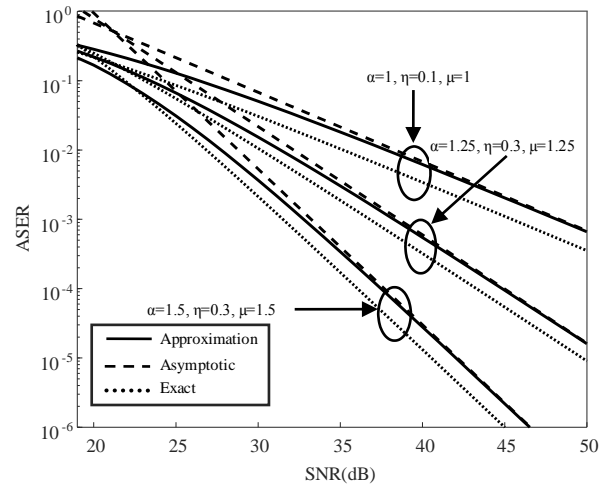


Fig.2. ASER performance of 8X4 QAM scheme with  $\beta=1$ .

VI. CONCLUSION

We have derived approximated and asymptotic ASER expressions for wireless communication systems using RQAM scheme over  $\alpha-\eta-\mu$  fading channels. The proposed approximate expression is in rapidly convergent form and its analytical results show close agreement to the exact ones. In addition, the asymptotic results are also tight with the approximate results at high SNR. In addition, it should be highlighted that using more terms for the infinite series does not have any influence in the 15th decimal place of the results and RTE values are decreasing rapidly to the negligible levels as given in Table I and Table II. As a result, one can easily obtain the ASER performance of the considered system over well-known fading channels such as Rayleigh, Nakagami- $m$ , Weibull and so on by using the flexibility of  $\alpha-\eta-\mu$  fading.

REFERENCES

- [1] D. Dixit, P.R. Sahu, "Performance analysis of rectangular QAM with SC receiver over Nakagami- $m$  fading channels", IEEE Communications Letters, Vol.18, No.7, 2014, pp.1262-1265.
- [2] D. Dixit, P. R. Sahu, "Symbol error rate of rectangular QAM with best-relay selection in cooperative systems over Rayleigh fading channels", IEEE Communications Letters, Vol.16, No.4, 2012, pp.466-469.
- [3] G. K. Karagiannidis, "On the symbol error probability of general order rectangular QAM in Nakagami- $m$  fading", IEEE Communications Letters, Vol.10, No.11, 2006, pp.745-747.
- [4] X. Lei, P. Fan, L. Hao, "Exact symbol error probability of general order rectangular QAM with MRC diversity reception over Nakagami- $m$  fading channels", IEEE Communications Letters, Vol.11, No.12, 2007, pp.958-960.
- [5] N. Kumar, P. K. Singya, V. Bhatia, "ASER analysis of hexagonal and rectangular QAM schemes in multiple-relay networks", IEEE Transactions on Vehicular Technology, Vol.67, No.2, 2018, pp.1815-1819.
- [6] N. Kumar, V. Bhatia, "Exact ASER analysis of rectangular QAM in two-way relaying networks over Nakagami- $m$  fading channels", IEEE Wireless Communications Letters, Vol.5, No.5, 2016, pp.548-551.
- [7] V. Asghari, D.B. da Costa, S. Aissa, "Symbol error probability of rectangular QAM in MRC systems with correlated  $\eta-\mu$  fading channels", IEEE Transactions on Vehicular Technology, Vol.59, No.3, 2010, pp.1497-1503.

- [8] D. Dixit, P.R. Sahu, "Performance of QAM signaling over TWDP fading channels", IEEE Transactions on Wireless Communications, Vol.12, No.4, 2013, pp.1794-1799.
- [9] N. Kumar, V. Bhatia, D. Dixit, "Performance analysis of QAM in amplify-and-forward cooperative communication networks over Rayleigh fading channels", AEU-International Journal of Electronics and Communications, Vol.72, 2017, pp.86-94.
- [10] P. R. Singya, N. Kumar, V. Bhatia, "Impact of imperfect CSI on ASER of hexagonal and rectangular QAM for AF relaying network", IEEE Communications Letters, Vol.22, No.2, 2018, pp.428-431.
- [11] N. Kapucu, M. Bilim, I. Develi, "Outage performance of cooperative DS-CDMA systems with best path selection over  $\alpha$ - $\eta$ - $\mu$  fading channels", Electronics Letters, Vol.53, No.11, 2017, pp.752-754.
- [12] O.S. Badarneh, M.S. Aloqlah, "Performance analysis of digital communication systems over  $\alpha$ - $\eta$ - $\mu$  fading channels", IEEE Transactions on Vehicular Technology, Vol.65, No.10, 2016, pp.7972-7981.
- [13] J. M. Moualeu, D. B. da Costa, W. Hamouda, U. S. Dias, R. A. A. de Souza, "Physical layer security over  $\alpha$ - $\kappa$ - $\mu$  and  $\alpha$ - $\eta$ - $\mu$  fading channels", IEEE Transactions on Vehicular Technology, Vol.68, No.1, 2019, pp.1025-1029.
- [14] A. M. Magableh, T. Aldalgamouni, S. Mater, O. S. Badarneh, "Ergodic capacity and SNR analysis for dual hop amplify and forward cooperative communication systems over  $\alpha$ - $\eta$ - $\mu$  channels", IEEE Transactions on Vehicular Technology, Vol.67, No.12, 2018, pp.12384-12388.
- [15] N. Kapucu, M. Bilim, "Analysis of analytical capacity for Fisher-Snedecor  $F$  fading channels with different transmission schemes", Electronics Letters, Vol.55, No.5, 2019, pp.283-285.
- [16] M.K. Simon, M.-S. Alouini, *Digital Communication over Fading Channels*, John Wiley & Sons, 2000.
- [17] I.S. Gradshteyn, I.M. Ryzhik, *Table of Integrals, Series and Products*, Academic Press, 2000.
- [18] S.S. Soliman, N.C. Beaulieu, "The bottleneck effect of Rician fading in dissimilar dual-hop AF relaying systems", IEEE Transactions on Vehicular Technology, Vol.63, No.4, 2014, pp.1957-1965.

#### BIOGRAPHIES



**Nuri Kapucu** received the B.Sc., M.Sc. and Ph.D. degrees in Electrical and Electronics Engineering from Erciyes University, Turkey, in 2010, 2012 and 2017, respectively. From 2011 to 2018, he was a Research

Assistant in the department of Electrical and Electronics Engineering at Erciyes University. Currently, he is an assistant professor in the department of Electrical and Electronics Engineering at Hitit University. His current research interests include performance analysis over fading channels, cooperative communications, two-way relaying, and multiple access techniques.

# Publication Ethics

The journal publishes original papers in the extensive field of Electrical-electronics and Computer engineering. To that end, it is essential that all who participate in producing the journal conduct themselves as authors, reviewers, editors, and publishers in accord with the highest level of professional ethics and standards. Plagiarism or self-plagiarism constitutes unethical scientific behavior and is never acceptable.

By submitting a manuscript to this journal, each author explicitly confirms that the manuscript meets the highest ethical standards for authors and coauthors

**The undersigned hereby assign(s) to *Balkan Journal of Electrical & Computer Engineering* (BAJECE) copyright ownership in the above Paper, effective if and when the Paper is accepted for publication by BAJECE and to the extent transferable under applicable national law. This assignment gives BAJECE the right to register copyright to the Paper in its name as claimant and to publish the Paper in any print or electronic medium.**

Authors, or their employers in the case of works made for hire, retain the following rights:

1. All proprietary rights other than copyright, including patent rights.
2. The right to make and distribute copies of the Paper for internal purposes.
3. The right to use the material for lecture or classroom purposes.
4. The right to prepare derivative publications based on the Paper, including books or book chapters, journal papers, and magazine articles, provided that publication of a derivative work occurs subsequent to the official date of publication by BAJECE.
5. The right to post an author-prepared version or an official version ( preferred version) of the published paper on an internal or external server controlled exclusively by the author/employer, provided that (a) such posting is noncommercial in nature and the paper is made available to users without charge; (b) a copyright notice and full citation appear with the paper, and (c) a link to BAJECE's official online version of the abstract is provided using the DOI (Document Object Identifier) link.



ISSN: 2147- 284X  
Year: April 2019  
Volume: 7  
Issue: 2

### CONTENTS

<b>S. Karagöl, D. Yıldız;</b> Linear Block Coding and Discrete Wavelet Transform Based Audio Signal Transmission over AWGN and Rician Fading Channels,.....	104-114
<b>S.M. Çürük;</b> Impulsive Noise Models Used in Power Line Communications, .....	115-122
<b>F. Asadi, K. Eguchi;</b> On the extraction of input and output impedance of PWM DC-DC converters, .....	123-130
<b>M. Taştan;</b> Adaptive Notch Filter Bank Based Power Quality Analysis of an Ultra-High Frequency Induction.....	131-136
<b>E. Aydemir, F. Toslak;</b> Unlock A Device with Pressure and Rhythm Based Password, .....	137-142
<b>R. Çelikel;</b> Speed Control of BLDC Using NARMA-L2 Controller in Single Link Manipulator, .....	143-148
<b>M. İnci;</b> Performance Analysis of T-type Inverter Based on Improved Hysteresis Current Controller, .....	149-155
<b>Y. Acar;</b> Subblock Aided OFDM with Index Modulation, .....	156-161
<b>B. Ozmen, O.J. Olaleye;</b> Multispectral Palmprint Recognition Based on Multidirectional Transform, .....	162-170
<b>J. Bala, O. Olaniyi, T. Folorunso, O.Arulogun;</b> Poultry Feed Dispensing System Control: A Case between Fuzzy Logic Controller and PID Controller, .....	171-177
<b>U. Korkmaz;</b> Fate of Entanglement for Initial Separable States in Quantum Neural Network, .....	178-181
<b>E. Taşçı;</b> A Meta-Ensemble Classifier Approach: Random Rotation Forest, .....	182-187
<b>C. Şahin, M. Karaçor, A.E. Amaç;</b> Minimizing Mutually Coupled Switched Reluctance Machine's Stator Volume by Stator Yoke Optimization,.....	188-194
<b>T. Ozcan, A. Basturk;</b> Lip Reading Using Convolutional Neural Networks with and without Pre-Trained,....	195-201
<b>O. Aydın;</b> Direction of Arrival Estimation in Multiple Antenna Arrays by Using Power Delay Profile for Random Access Performance in 5G Networks, .....	202-207
<b>N. Kapucu;</b> An Approximate Error Expression for RQAM Scheme under $\alpha$ - $\eta$ - $\mu$ Fading Conditions,.....	208-212

## BALKAN JOURNAL OF ELECTRICAL & COMPUTER ENGINEERING

(An International Peer Reviewed, Indexed and Open Access Journal)

### Contact

Batman University  
Department of Electrical-Electronics Engineering  
Bati Raman Campus Batman-Turkey

Web: <http://dergipark.gov.tr/bajece>  
<http://www.bajece.com>  
e-mail: [bajece@hotmail.com](mailto:bajece@hotmail.com)

